Residual Strains in Thick Thermoplastic Composites

an Experimental Approach

Proefschrift

ter verkrijging van de graad van doctor
aan de Technische Universiteit Delft,
op gezag van de Rector Magnificus prof.ir. K.C.A.M. Luyben,
voorzitter van het College voor Promoties,
in het openbaar te verdedigen op donderdag 18 februari 2010 om 10:00 uur
door

Patricia Pauline PARLEVLIET

ingenieur Materials Science and Engineering
geboren te Leidschendam.

Dit proefschrift is goedgekeurd door de promotor:
Prof.ir. A. Beukers

Copromotor:
Dr.ir. H.E.N. Bersee

Samenstelling promotiecommissie:

Rector Magnificus, voorzitter
Prof.ir. A. Beukers, Technische Universiteit Delft, promotor
Dr.ir. H.E.N. Bersee, Technische Universiteit Delft, copromotor
Prof.dr. S.J. Picken, Technische Universiteit Delft
Prof.dr.ir. R. Akkerman, Universiteit Twente
Prof.Dr.-Ing. P. Mitschang, Technische Universität Kaiserslautern, Duitsland
Prof.dr. V. Michaud, École Polytechnique Fédérale de Lausanne, Zwitserland
Prof.dr. A. Torres Marques, Universidade do Porto, Portugal

ISBN: 978-94-6113-0051

Cover photos:
Carbon fibre fabric and polarised optical micrograph of microcracks in CF/PEI composites.

Printed at Haveka, the Netherlands

Residual Strains in Thick Thermoplastic Composites

an Experimental Approach

Residual Strains in Thick Thermoplastic Composites

an Experimental Approach

Summary

Thermoplastic composites are currently investigated for application in windmill turbine blades for their recyclability. A suitable manufacturing technology for these thick structures is liquid resin infusion followed by in-situ polymerisation. Anionic polyamide-6 (APA-6) is a thermoplastic matrix that is currently further developed at Delft University of Technology for this process. During manufacturing of thick composite structures, temperature variations arise through the thickness, which can result in residual strains and through-the-thickness variations of properties, such as degrees of cure and crystallinity. The aim of this thesis is to develop experimental techniques that can be used to investigate these important effects of thermal gradients in thick glass fibre reinforced (GF) APA-6 laminates.

Optic fibres with Bragg gratings (FBGs) were used to investigate the polymer matrix shrinkage contribution to residual strain formation. It was demonstrated that strain development starts at the crystallisation temperature of ~185°C. For higher polymerisation temperatures the residual strains were found to increase, because of the increased thermal contraction during cooling from the polymerisation temperature. Thermal treatment of APA-6 and composites thereof had no effect on the final strain at room temperature as detected with embedded FBGs. A thermosetting polyurethane that was used as reference material however, did show significant strain relaxation during thermal treatment. A strain-free temperature could also be established for this material.

A volumetric dilatometry test based on the buoyancy principle was set-up to determine the polymer volumetric shrinkage during the processing cycle. The test showed significant shrinkage of APA-6 due to polymerisation and crystallisation (15-20 vol%). This resulted for example in many shrinkage voids in the woven fabric composites.

The microVickers indentation test showed a clear relation between the polymerisation temperature of GF/APA-6 composites and the hardness. Lower polymerisation temperatures result in higher degrees of crystallinity and corresponding hardness. The microVickers

hardness test is presented as a useful tool for detection of matrix property variations through the thickness.

During processing of thick GF/APA-6 laminates, significant temperature variations were found through the thickness. Embedded FBGs showed that polymerisation had started already during heating from the infusion temperature to the polymerisation temperature. This resulted in outside-in polymerisation, which did however not cause a significant strain gradient through the thickness. Explanations can be found in the significant strain relaxation of the APA-6 matrix, aided by the presence of voids, and the self-regulating crystallisation mechanism during the polymerisation dwell time. In addition, no significant variation in matrix properties was indicated by the hardness test, except for the plies close to the tool plate. Also, the final strain values were similar for 2 mm and 25 mm thick laminates. These findings lead to believe that scaling up of GF/APA-6 composites in the thickness direction has no significant effect on their properties.

Patricia P. Parlevliet,
February 2010

Restrekken in dikwandige thermoplastische composieten

een experimentele benadering

Samenvatting

Momenteel wordt aan de Technische Universiteit Delft onderzoek gedaan naar recyclebare composiet windmolenbladen d.m.v. toepassing van een thermoplastische kunststof matrix. Een zeer geschikte technologie om deze dikwandige structuren te produceren is het vacuüm injectie proces. Hierbij worden vloeibare kunststof componenten tussen de versterkingsvezels geïnjecteerd, gevolgd door polymerisatie (uitharding). Anionisch polyamide-6 (APA-6) is een goedkoop en veelbelovend thermoplastisch polymeer dat verder onderzocht wordt voor dit proces.

Tijdens het productieproces kunnen temperatuurverschillen door de dikte leiden tot (rest)rekken en variaties in eigenschappen, zoals kristalliniteit en uithardingsgraad. Het doel van het onderzoek zoals beschreven in dit proefschrift is dan ook om experimentele technieken te ontwikkelen die gebruikt kunnen worden om deze belangrijke effecten in dikke glasvezel (GV) versterkte APA-6 composieten te onderzoeken.

De bijdrage van het polymeer aan het ontstaan van restrekken bestaat uit de polymerisatiekrimp vanaf het punt waarop het genoeg stijfheid heeft om krachten te kunnen overdragen, en de thermische krimp vanaf de productietemperatuur naar de gebruiks-temperatuur. Voor het bepalen van deze bijdrage zijn optische vezels met Bragg roosters (fibre Bragg gratings – FBGs) gepositioneerd in de te polymeriseren vloeistof. Met deze sensoren is aangetoond dat de restrekken ontstaan op het moment dat kristallisatie van het gevormde polymeer optreedt rond een kristallisatietemperatuur van ~185°C. Daarnaast zijn grotere restrekken gemeten voor hogere productietemperaturen van APA-6. Dit komt met name door de grotere thermische krimp tijdens het afkoelen naar kamertemperatuur. Met de FBGs is geen effect gemeten van een thermische nabehandeling op de uiteindelijke restrekken in APA-6 op kamertemperatuur. Voor een thermohardende polyurethaan polymeer, wat als referentie diende, werd wel significante relaxatie waargenomen. Er kon zelfs een rekvrije temperatuur worden vastgesteld.

Naast de lineaire krimpmeting m.b.v. de FBGs, is een meetopstelling gebouwd voor het bepalen van volumetrische krimp van het polymeer tijdens de productiecyclus. Deze volumetrische methode is gebaseerd op de opwaartse druk van een vloeistof en maakt gebruik van een ondergedompeld rubber zak met daarin het uithardende polymeer. Met deze test is aangetoond dat het APA-6 polymeer ten gevolge van polymerisatie en kristallisatie significante krimp vertoont (15-20 vol%). Dit resulteerde o.a. in een grote hoeveelheid krimpholtes in de met glasweefsel versterkte composieten.

De microVickers hardheid test is gebruikt om een relatie aan te tonen tussen de productietemperatuur van GV/APA-6 composieten en de hardheid van de APA-6 matrix. Een lagere polymerisatie of productietemperatuur leidt tot een hogere kristallisatiegraad en daarmee tot een hogere hardheid. Geconcludeerd is dat de microVickers hardheid test een geschikte methode is om variaties in matrixeigenschappen door de dikte te bepalen die ontstaan zijn door temperatuurverschillen .

Tijdens de productie van dikwandige GV/APA-6 composieten zijn grote temperatuur-verschillen door de dikte gemeten. Ingebedde FBGs toonden aan dat polymerisatie van de APA-6 matrix al begon tijdens het opwarmen van de injectietemperatuur naar de polymerisatietemperatuur. Dit veroorzaakte heterogene polymerisatie door de dikte. Echter, dit leidde niet tot de verwachte grote restrekken in het composiet. De reden hiervoor ligt waarschijnlijk in het significante relaxatiegedrag van APA-6, wat versterkt wordt door het ontstaan van krimpholtes. Daarnaast zijn er m.b.v. de microVickers hardheid test geen grote verschillen in matrixeigenschappen waargenomen door de dikte. Alleen het materiaal dichtbij het maloppervlak vertoonde andere eigenschappen. De uiteindelijke restrekken waren ongeveer gelijk voor 2 mm en 25 mm dikke proefstukken. Hiermee lijkt het opschalen van GV/APA-6 composieten in de dikterichting weinig invloed te hebben op de eigenschappen.

Patricia P. Parlevliet,
februari 2010

Contents

Nomenclature

Abbreviation	Expression
APA-6	Anionic polyamide-6
Approx.	approximately
CCD	Charge coupled device
CF	Carbon fibre
CL	Constitutive Laminate
CL	Caprolactam
CLT	Classical laminate theory
CR	Cooling rate
CRM	Cure Reference Method
CT	Computer Tomography
CTE	Coefficient of thermal expansion
Dilato	Dilatometry
DM(T)A	Dynamic Mechanical (Thermal) Analyser
DoC	Degree of conversion
DSC	Differential Scanning Calorimetry
DTG®	Draw Tower Grating
EFPI	Extrinsic Fabry-Perot Interferometry
Eq.	Equation
FBG	Fibre Bragg grating
Fig.	Figure
FOS	Fibre optic sensor
FTIR	Fourier Transformed Infrared
GF	Glass fibre
GI	Gravimetric immersion
HPA	Hydrolytic polyamide-6
HS	Harness Satin
IR	Infrared
LCM	Liquid composite moulding
LVDT	Linear variable differential transformer
min	Minute(s)
MMU	Mini Mixing Unit
MRS	Micro (laser) Raman spectroscopy
PA-6	Polyamide 6
PC	Personal computer
PEEK	Polyetheretherketone
PEI	Polyetherimide
PEK	Polyetherketone
PEKK	Polyetherketoneketone
PET	Polyethyleneterephtalate
PI	Polyimide
Poly	Polymerisation
PPS	Polyphenylenesulfide
PSF	Polysulfone
PSL	Process Simulated Laminate
PVT	Pressure-volume-temperature
Resp.	Respectively
RTV	Room temperature vulcanising
SEM	Scanning Electron Microscope

SFT	Stress (or strain) free temperature
SI	International System of Units
SiC	Silicium carbide
T-FBG, T-sensor	FBG temperature sensor
TGA	Thermal gravimetric analysis
TMA	Thermal mechanical analysis
TPC	Thermoplastic composite
TPI	Thermoplastic polyimide
UD	Unidirectional
WAXS	Wide angle X-ray spectroscopy
XRD	X-Ray diffraction

Sub- and Superscripts	**Description**
$_0$	Initial reference point
$_{i,\ 1}$	Point of measurement
$_S$	Strain
$_T$	Temperature

Latin Symbol	**Unit**	**Description**
b	[mm]	Longitudinal ply thickness unsymmetrical laminate
d	[mm]	Transverse ply thickness unsymmetrical laminate
d_1	[µm]	Horizontal diagonal of Vickers indentation
d_2	[µm]	Vertical diagonal of Vickers indentation
E_{11}	[GPa]	Modulus parallel
E_{22}	[GPa]	Modulus perpendicular
E_f	[GPa]	Fibre modulus
E_m	[GPa]	Matrix modulus
F	[N]	Force
G	[GPa]	Shear modulus
g	[m/s^2]	Gravitational constant
h	[mm]	Longitudinal ply thickness symmetrical laminate
h	[m]	Chord length (in Eqs. 3-6, and 3-7)
HV	[MPa]	Vickers hardness
I	[-]	Intensity
ID	[mm]	Inner diameter
k	[mm]	Transverse ply thickness symmetrical laminate
L	[m]	Length
l	[mm]	Length
M	[Nm]	Bending moment
m	[g]	mass
m_{bag}^{bal}	[g]	(Empty silicone) submersed bag mass registered by balance
m_c	[g]	Composite mass
m_f	[g]	Fibre mass
m_{mon}	[g]	Monomer mass
m_{pol}, m_p	[g]	Polymer mass
m_{pol}^{bal}	[g]	(Theoretical) submersed polymer mass registered by balance
m_s	[g]	Specimen mass
m_{tot}^{bal}	[g]	Total submersed mass registered by balance
n_{eff}	[-]	Refractive index
OD	[mm]	Outer diameter

P	[-]	Strain-optic coefficient (in FBGs)
P	[kg]	Load (in hardness test)
p_{11}	[-]	Elastic-optic coefficient in 11-direction
p_{12}	[-]	Elastic-optic coefficient in 12-direction
S_T	[pm/°C]	FBG temperature sensitivity
S_ε	[pm/μm]	FBG strain sensitivity
t	[mm]	Thickness
T	[°C]	Temperature
T_0	[°C]	Reference or start temperature
T_c	[°C]	Crystallisation temperature
$T_{de\text{-}block}$	[°C]	De-blocking temperature of activator
T_g	[°C]	Glass transition temperature
T_m	[°C]	Melting temperature
T_p	[°C]	Polymerisation or processing temperature
T_{peak}	[°C]	Peak (maximum) temperature
T_{pol}	[°C]	Polymerisation temperature
V	[m^3]	Volume
V_{pol}	[m^3]	Polymer volume
w_m	[-]	Matrix weight fraction
X_c	[-]	Degree/ fraction of crystallinity

Greek Symbol	**Unit**	**Description**
α	[m m^{-1} °C^{-1}]	Coefficient of thermal expansion (CTE)
α_{11}	[m m^{-1} °C^{-1}]	CTE in longitudinal direction
α_{22}	[m m^{-1} °C^{-1}]	CTE in transverse direction
α_c	[m m^{-1} °C^{-1}]	Composite CTE
α_f	[m m^{-1} °C^{-1}]	Fibre CTE
α_{FBG}	[m m^{-1} °C^{-1}]	CTE of optic fibre
α_H	[m m^{-1} °C^{-1}]	Host structure CTE
α^l_f	[m m^{-1} °C^{-1}]	Fibre CTE in longitudinal direction
α^l_m	[m m^{-1} °C^{-1}]	Matrix CTE in longitudinal direction
α_n	[m m^{-1} °C^{-1}]	Fibre CTE
Δ	[-]	Difference
ΔH_0	[J/g]	Reference fusion enthalpy
ΔH_c	[J/g]	Composite enthalpy (during phase change)
ΔT	[°C]	Temperature difference
$\Delta\varepsilon$	[-]	Strain (difference)
$\Delta\varepsilon_{lin}$	[-]	Linear shrinkage
$\Delta\varepsilon_{pol}$	[-]	Polymer volumetric shrinkage
$\Delta\varepsilon_{vol}$	[-]	Volumetric shrinkage
$\Delta\lambda$	[nm]	Wavelength difference/ shift
ε	[-]	Strain
ε_{lin}	[-]	Linear strain
ε_{th}	[-]	Thermally induced axial strain
η	[Pa.s]	Viscosity
κ	[m^{-1}]	Curvature
λ	[nm]	wavelength
Λ	[nm]	Spacing
λ_B	[nm]	Bragg wavelength
λ_{ref}	[nm]	Reflected Bragg wavelength
λ_{trans}	[nm]	Transferred Bragg wavelength
ν	[-]	Poisson's ratio
ρ	[g/cm^3]	Density

ρ	[m]	Section 3.4.2: radius
ρ_{CL}	[g/cm^3]	Caprolactam density
ρ_{fl}	[g/cm^3]	Fluid density
σ	[MPa]	Stress
σ_{22}	[MPa]	Stress in perpendicular direction
σ^l_f	[MPa]	Fibre residual stress in longitudinal direction
σ_{max}	[MPa]	Maximum stress
σ_R	[MPa]	Residual stress
σ^t	[MPa]	Tensile strength
ω	[°]	Angle

Chapter 1: General Introduction – Residual Strains in Thick Thermoplastic Composites

1.1 Introduction

With the increasing demand for renewable energy, the number of windmill turbines rises accordingly. Locations for windmills are scarce, necessitating the increase in energy output per wind turbine. For example, new offshore windmill turbine blades are expected to reach lengths exceeding 100 meters, compared to the current 60 m [1]. Thicknesses of more than 10 centimetres will be required at the roots of these composite blades to maintain the structural performance.

Figure 1.1: 3.6 MW wind turbine at an offshore wind farm (courtesy Eurocopter Group [2]).

With the expected life of ~20 years for windmill turbines, and the forecasted production increase, a large amount of waste in the form of non-recyclable glass and carbon fibre reinforced epoxy and vinylester is expected in the coming decades. At Delft University of Technology a new resin system was developed for the production of thermoplastic composites based on the anionically polymerising polyamide-6 (APA-6) [3]. This novel system is characterised by its low material costs, short production cycles, recyclability [4], and above all, allows the manufacturing of thick thermoplastic composites, based on the widely used resin infusion technology [5].

During manufacturing of thick composite laminates, significant through-the-thickness gradients in temperatures can arise. In turn, these can result in residual strains as well as inhomogeneous properties, compromising the performance of the composite structure [6]. A knowledge gap exists on residual strain formation in thick composites manufactured with resin infusion and the effects thereof. This can be attributed to a lack of experimental techniques suitable for monitoring of residual strain formation during the entire processing cycle. Because resin infusion with thermoplastic polymer systems is a novelty [7], no information is available on parameters driving residual strain formation in composites manufactured with these systems. Therefore, the aim of this thesis is to develop experimental techniques that enable understanding of residual strain formation in thick thermoplastic composites manufactured with the resin infusion process.

1.2 Thick Thermoplastic Composites

1.2.1 Definition of thick composites

The first question that arises is 'what is considered a thick composite?' For an answer, two approaches can be used [8]: either a nominal composite thickness is arbitrarily chosen, such as from 10 mm, or a composite is considered thick when the through-the-thickness properties are significant. The first approach is easy to apply, while the second is of more technical importance. In this thesis, the focus is on the material properties, and therefore a composite shall be considered thick when any parameter or material property, such as temperature or degree of crystallinity, varies through the thickness. The corresponding nominal thickness thus depends on the material system and manufacturing process.

1.2.2 Thermoplastic composites

Thermoplastic polymers are characterised by their ability to soften and be shaped when heated, and harden upon cooling. This is opposed to thermoset polymers that require a chemical reaction to harden (cure) and cannot soften or melt when reheated [9]. A polymer in the liquid state (molten thermoplastics, uncured thermoset resins) can be used to impregnate continuous reinforcing fibres, such as carbon or glass, to construct a high-performance light-weight material.

Historically, the development of continuous fibre reinforced composites with thermoplastic matrices as a replacement for traditional thermoset resins started with high-performance polymers as polyetheretherketone (PEEK). The driving force for the development of these thermoplastic composites lies in the advantages found in both the mechanical properties and in new processing opportunities, such as rapid press forming and welding [1]. During their service life, thermoplastic composites offer many advantages over the for windmill blades

commonly used composites with thermoset matrices, such as epoxy and polyester. These advantages include [10]:

- weldability, enabling automated assembly;
- higher toughness, resulting in better damage tolerance;
- semi-crystalline thermoplastics offer better chemical resistance;
- melting of the polymer enables (re-)forming and repair without significant loss of performance; and
- due to possibility of melt-processing, thermoplastic composites offer the possibility of recycling and reusing the material in other applications.

However, no solution is currently available for manufacturing of thick thermoplastic composites with a complex 3-dimensional shape, such as desired for wind turbine blades [7, 11]. Due to the high viscosity in the molten phase, relatively high pressures are required for high-quality composites, necessitating the use of expensive and energy consuming autoclaves or hot presses. A disadvantage is that the product size is then limited to the size of the press or autoclave.

For thick thermoset matrix composite structures, a cost effective manufacturing technology is presented by the resin infusion technology. Here, a pressure difference forces the uncured liquid polymer to flow around the dry fibrous reinforcement (preforms, see Figure 1.2) in a closed mould and is then allowed to polymerise at elevated temperatures under pressure for a certain time. As the polymer is in a liquid state during processing, this process is referred to as liquid moulding and allows the production of complex shaped and thick composite structures. For thermoplastics however, this technique is not possible, since the viscosity of the molten polymers is too high: the viscous flow would exert huge deformation forces on the fibre reinforcement.

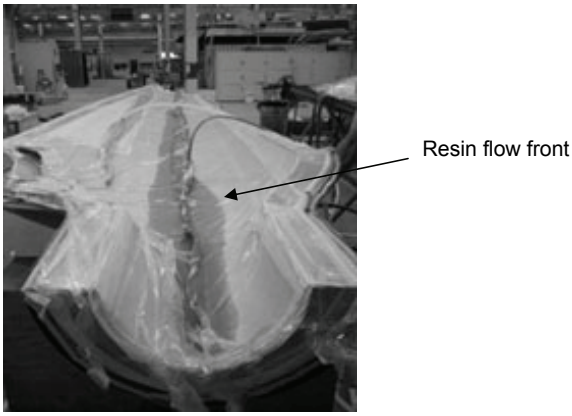

Figure 1.2: Resin infusion of a windmill turbine blade, from [12].

1.3 Anionic Polyamide-6

The high viscosity, processing temperatures in excess of 200°C, and cost of the high-performance thermoplastic polymers are a severe limitation for their large-scale use. For this reason a trend towards the use of more common and affordable engineering thermoplastics emerged. One group of engineering thermoplastics that is considered as a matrix for thermoplastic composites are polyamides, because of their low price, low viscosity, high toughness and high chemical resistance. Despite the low glass transition temperatures of these semi-crystalline resins, their high degree of crystallinity provides them with a useful service temperature range [3].

Anionic polymerisation of polyamide-6 (APA-6) was originally developed for casting of polyamide products in the early 1940s and from then on commercially exploited by BASF, Bayer, DSM and Monsanto. APA-6 is different from the common hydrolytically polymerised PA-6 (HPA-6), which is currently used as a matrix for composites in the automotive and sports industry. The main differences between hydrolytic polymerisation and anionic polymerisation of PA-6 can be summarised as follows [13]:

- The polymerisation temperature of HPA-6 is 240-285°C compared to 140-190°C for APA-6, with the latter being in the same range as aerospace-grade epoxy systems.
- The cure time is 12-30 hours for HPA-6 and 5 – 60 minutes for APA-6.
- After APA-6 processing a product is finished or semi-finished, such as a rod from which gears can be machined, whereas for HPA-6 only granules are obtained, that need to be converted to the final product by melt processing at ~260°C.

Besides, the molar mass of APA-6 is higher compared to HPA-6, increasing its toughness, glass transition temperature and elastic modulus, which is important for the design of slender constructions.

Before polymerisation, the reactive APA-6 mixture has a very low viscosity (10 – 50 mPa.s), which signifies the possibility of a thermoset processing route previously unavailable to thermoplastic composites: vacuum assisted resin infusion combined with in-situ polymerisation. This characteristic in combination with the proven suitability as a composite matrix, were the primary arguments for investigating this material system. One other important argument for this material system is that at the end of its service-life, the original components, i.e. monomer, initiator and activator, can be retrieved upon reheating [4], providing a durable alternative for the scrapping and burning of the fibre reinforced epoxy windmill blades.

Van Rijswijk *et al* started in 2003 the effort to find the most suitable chemistry and experimental set-up for successful reactive infusion of a glass fibre reinforced APA-6 composite windmill turbine blade [11], which is followed by the work of Teuwen *et al* [14, 15]. The goal of the ongoing research efforts is cost-effective and rapid manufacturing of high-

quality thick laminates with the relatively cheap and recyclable APA-6 matrix. In a comparative study with hydrolytic polyamide-6 (HPA-6) and nanoparticle filled HPA-6 [16], it was shown that APA-6 exhibits excellent mechanical properties and shows great potential as a composite matrix. Even though the moisture-conditioned mechanical properties do not yet match those of the standard epoxy-based composites, with further improvement of the chemistry and technology, liquid moulding of thick APA-6 composites seems a very promising technology for manufacturing of thermoplastic wind turbine blades [16].

1.4 Residual strains

Due to the significantly larger shrinkage of the polymer matrix compared to the reinforcing fibres, residual strains[1] arise in composites during processing and subsequent cooling from the processing to the service temperature. Owing to the composites inherent inhomogeneous nature, these process-induced residual strains occur in all fibre reinforced polymers and significantly influence the properties of the composite structures [18-21]. Therefore, it is important to take the residual strains and their effects into account during the design of composite structures, such as wind turbine blades. For engineering purposes, it is desired that the composite structure shows homogeneous and predictable behaviour over the entire structure. Many papers have hence been published on residual strains and stresses in thermoset and thermoplastic composites, with a main focus on predictive models [18, 22-25]. However, there is a fundamental lack in experimental studies on through-the-thickness residual strain formation in thick composites manufactured with liquid moulding. For example, many models predict how through-the-thickness temperature variations can lead to residual strain distributions as well as a variation in material properties [26], but experimental validation thereof is hardly available.

Since the APA-6 polymer system is still under development for use as a composite matrix, the parameters governing residual strain build-up and material properties in (thick) composites are still unknown. For successful application of APA-6 in windmill turbine blades, these need to be investigated. First however, suitable techniques to determine and quantify these parameters must be established.

[1] Residual strain is defined as “a strain that persists in a material that is free of external forces or temperature gradients” [17].

1.5 Thesis Outline

1.5.1 Research objective

The aim of this thesis is to develop experimental techniques that enable understanding of residual strain formation in thick thermoplastic composites during manufacturing with resin infusion. These techniques will be applied to the novel anionic polyamide-6 polymer system and composites made thereof.

1.5.2 Outline

To achieve this objective, the research is divided into three parts:

- First a literature review is conducted into the origins of residual strain formation and experimental techniques to measure residual strains and important matrix parameters, such as polymer shrinkage (Chapters 2 and 3).
- Then, experimental techniques are developed to study the polymer matrix behaviour and resulting residual strain formation during manufacturing of thick composites. In addition, techniques to study matrix property variations caused by thermal gradients through the thickness are investigated (Chapters 4 to 7).
- These techniques are subsequently applied to the APA-6 system and composites thereof to study the parameters influencing residual strain formation and through-the-thickness property variations (Chapters 9 to 11).

Finally, conclusions and recommendations for future research are presented in Chapter 12.

Figure 1.3: Windmill turbine blades, from [27].

References

1. Red, C., Wind turbine blades: Big and getting bigger, in Composites Technology. 2008.
2. Eurocopter UK receives first ever UK helicopter order for offshore wind farm maintenance. 2008 [cited 2 June 2009]. Available from: http://www.eurocopter.co.uk/index.php?page=news.
3. van Rijswijk, K., Joncas, S., Bersee, H.E.N., Bergsma, O.K.Beukers, A., Sustainable vacuum-infused thermoplastic composites for MW-size wind turbine blades - Preliminary design and manufacturing issues. Journal Of Solar Energy Engineering-Transactions Of The Asme, 127(4): 570-580, 2005.
4. Booij, M. Polyamide-6 Recycling to Caprolactam - DSM Closes the Loop. in Polyamide 2000 World Congress, Zurich, Switzerland, 2000.
5. Gardiner, G., Wind Blade Manufacturing, Part I: M and P innovations optimize production, in High Performance Composites.
6. Parlevliet, P.P., Bersee, H.E.N., Beukers, A., Residual Stresses in Thermoplastic Composites - A Study of the Literature - Part III: Effects of Thermal Residual Stresses. Composites Part A: Applied Science and Manufacturing, 38(6): 1581-1596, 2007.
7. Gardiner, G., Wind Blade Manufacturing, Part II: Are thermoplastic composites the future?, in High Performance Composites. 2008.
8. Goeke, E.C. Compression of "Thick" Composites: Two Test Methods. in Composite Materials: Testing and Design. 1993. Pittsburgh, PA: American Society for Testing and Materials.
9. Callister, W.D.J., Materials Science and Engineering - An Introduction. 5th ed. 2000: John Wiley & Sons, Inc. 871 pages.
10. Cogswell, F.N., Introduction - Thermoplastic Composite Materials, in Thermoplastic Composite Materials, Carlsson, L.A., Editor. 1991, Elsevier Science Publishers, B.V.: Amsterdam. p.1-25.
11. van Rijswijk, K., Thermoplastic Composite Wind Turbine Blades. 2007. PhD thesis Aerospace Engineering, Delft University of Technology, Delft. 249 pages.
12. Tygavac. Wind Energy. [cited 2 June 2009]. Available from: http://www.tygavac.co.uk/markets/wind-energy.html.
13. van Geenen, A.A., Anionic Polyamide - Chemistry and processing. 2007, AvG Consultancy.
14. Teuwen, J.J.E., Gillis, J.H.A.M., Bersee, H.E.N. Optimisation of infusion temperature for anionic polyamide-6 composites. in AIAA, 2008.
15. Teuwen, J.J.E., van Rijswijk, K., Bersee, H.E.N., Beukers, A. Effect of fibre textile reinforcement on anionic polyamide-6 composite properties. in ICCM-16, Kyoto, Japan, 2007.
16. van Rijswijk, K., Lindstedt, S., Vlasveld, D.P.N., Bersee, H.E.N.Beukers, A., Reactive processing of anionic polyamide-6 for application in fiber composites: a comparative study with melt processed polyamides and nanocomposites. Polymer Testing, 25(7): 873-887, 2006.
17. Callister, W.D.J., Materials Science and Engineering - An Introduction. 3rd ed. 1994: John Wiley & Sons, Inc. 811 pages.
18. Favre, J.P., Residual thermal stresses in fibre reinforced composite materials - A review. Journal of the Mechanical Behavior of Materials, 1(1-4): 37-53, 1988.
19. Adams, M.E., Campbell, G.A., Cohen, A., Thermal-Stress Induced Damage in a Thermoplastic Matrix Material for Advanced Composites. Polymer Engineering and Science, 31(18): 1337-1343, 1991.
20. Unger, W.J., Hansen, J.S., Method to predict the effect of thermal residual stresses on the free-edge delamination behavior of fibre reinforced composite laminates. Journal of Composite Materials, 32(5): 431-459, 1998.
21. Kim, J.-K., Mai, Y.-W., Residual Stresses, in Engineered Interfaces in Fiber Reinforced Composites. 1998, Elsevier Science Ltd.: Oxford. p.308-320.
22. Eijpe, M.P.I.M., A Modified Layer Removal Method for Determination of Residual Stresses in Polymeric Composites. 1997 Mechanical Engineering, University Twente, Enschede. 170 pages.
23. Nairn, J.A., Residual stress effects in fracture of composites and adhesives. 2003, University of Utah: http://www.eng.utah.edu/~nairn/papers/ElRSE.pdf. p. 6.
24. Nairn, J.A., Zoller, P. The Development of Residual Thermal Stresses in Amorphous and Semicrystalline Thermoplastic Matrix Composites. in Toughened Composites. 1987. Houston, Texas; USA: ASTM, 1916 Race Street, Philadelphia, Pennsylvania 19103, USA.
25. Wisnom, M.R., Gigliotti, M., Ersoy, N., Campbell, M.Potter, K.D., Mechanisms generating residual stresses and distortion during manufacture of polymer-matrix composites structures. Composites Part A: Applied Science and Manufacturing, 37(4): 522-529, 2006.
26. Ruiz, E., Trochu, F., Multi-criteria thermal optimization in liquid composite molding to reduce processing stresses and cycle time. Composites Part A: Applied Science and Manufacturing, 37(6): 913-924, 2006.
27. Max_Energy_Ltd. Wind Turbines Explained. [Website] 2005 [cited 25 May 2009]. Available from: http://www.solarnavigator.net/wind_turbines_how_they_work.htm.

Chapter 2: Formation of Residual Strains in Composites – an Overview of the Literature

2.1 Introduction

The goal of this Chapter is to identify parameters governing residual strain formation in thick composites manufactured with liquid composite moulding, by reviewing the available literature. Special attention is paid to important parameters for thermoplastics and reactive (thermoset) polymers. The reason for this is that APA-6 is a thermoplastic matrix suitable for reactive processing and a study on residual strains of such a system has no precedent. The material properties of the composites' constituents as well as processing parameters governing strain build-up are emphasised, and special attention is paid to parameters that inflict residual strain variations through the thickness. Mechanisms for alleviation of residual strains are briefly touched upon.

In the literature, the terms residual stress and residual strain are often used interchangeably. It is the effect of such *strains* on the developed *stresses* in a composite laminate, which may affect the composite properties. In principle, it is the strain that can be measured experimentally and is related to stress through the elastic coefficients. Therefore, the focus of this thesis is on residual strains rather than stresses. When the term 'stress' is used in this thesis, it likely refers to publications where residual stresses are studied.

In the last two decades several literature reviews have been published in which the one by Favre from 1988 [1] can be regarded as base literature when studying residual stresses in continuous fibre reinforced polymers (thermosets as well as thermoplastics). Favre covered the origins and magnitudes of the thermal residual stresses, temperature, moisture and time effects, and the effects of residual stresses themselves, such as geometrical distortions, microcracks and delaminations due to free edge effects. Included were the available predictive models and experimental techniques and proposals for reduction of residual stresses in composites. In the nineties, publications [1-4] appeared that summarised most of the work done earlier on the sources for internal stresses in composite materials, including composite intrinsic properties, processing conditions and environmental conditions. In 1985, Nairn and Zoller [5, 6] published the first experiment-based study on thermal residual stresses in thermoplastic composites.

2.2 Residual strain formation

Residual strains in continuous fibre reinforced polymers appear in the laminate or composite structure during processing. The main driving force is a mismatch in shrinkage behaviour between different constituents or components of a composite product and can be regarded on different levels based on their origins [1-4]:

- The mismatch in shrinkage between the fibres and the matrix is the main source for the development of residual strains on the micromechanical or constituent level [5-7]. During processing, the shrinkage of a polymer matrix is usually significantly higher than the fibre contraction. Assuming that a good fibre-matrix bonding is present during cooling, Figure 2.1 shows that a residual tensile strain develops in the polymer matrix along the fibre longitudinal axis and in the hoop direction [1, 7], and a compressive strain in the matrix in the radial direction [8] (indicated by the black arrows). The grey arrows indicate the direction of the matrix shrinkage. The physical nature of the constituents' shrinkage behaviour will be explained later.

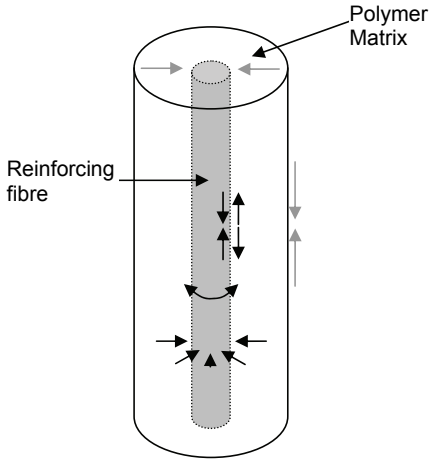

Figure 2.1: Schematic view of the effect of matrix shrinkage around a fibre, where ◄► and ►◄ represent tensile and compressive residual strains, respectively.

- When the reinforcing fibres and polymer matrix together form a composite ply, and several of these plies are stacked together at different angles to produce a composite laminate, residual stresses on a ply-to-ply scale arise due to an anisotropic difference in the transverse and longitudinal ply coefficients of thermal contraction[1] [8]. For example in

[1] In many publications, the term 'mismatch in coefficient of thermal expansion' is used. The term coefficient implies a constant parameter. However, for the polymer matrix the coefficient of thermal expansion, or rather 'coefficient of thermal contraction', varies with temperature and is therefore not a constant. Therefore, the term 'mismatch in thermal contraction' is used in this thesis instead.

cross-ply laminates, the 90° fibres impose a mechanical constraint on the 0° fibres during shrinkage and vice versa, because of the difference in thermal contraction direction [9], see Figure 2.2. The residual strains (ε) that develop due to this are called 'interlaminar' or 'lamination' [8] residual strains and are regarded on a macro-mechanical level. At fibre angles of $\omega \approx \pm 30°$, the interlaminar shear strains are maximum [10, 11]. The anisotropic contraction resembles the behaviour of a bi-metallic strip and, if unbalanced and unconstrained, a bending moment M may result in a deformation (curvature) of the laminate [12].

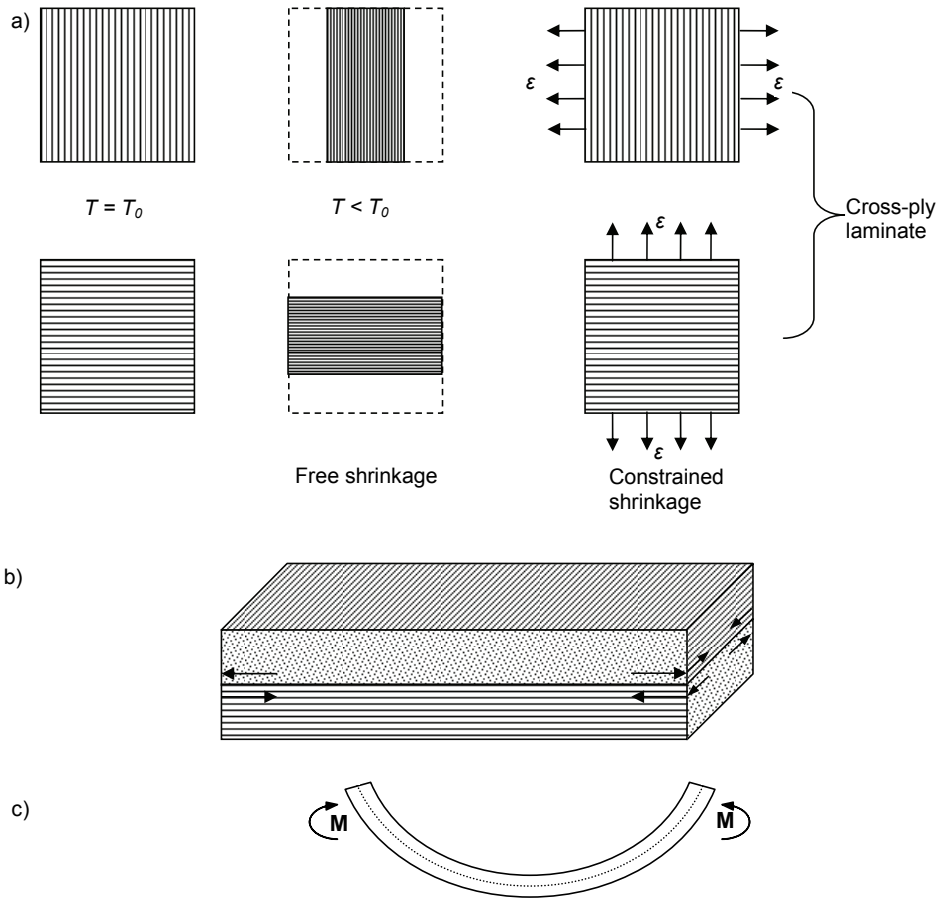

Figure 2.2: Schematic view of residual strain formation in an unbalanced cross-ply laminate (a), (b): residual strains when the laminate is constrained, (c): front view of out-of-plane deformation when unconstrained.

- Residual strains through the thickness of a composite laminate or structure (on a 'global' [1] mechanical level) can be the result of a variation in shrinkage through the thickness. For example, the centre plies may need a longer time to completely contract than the surface plies. Then at a certain time, the shrinkage of the centre plies may be restrained by the surface plies. This can result in a parabolic distribution of compressive residual strains in the surface (skin) plies and tensile strains in the centre (core) plies (Figure 2.3) [4, 5].

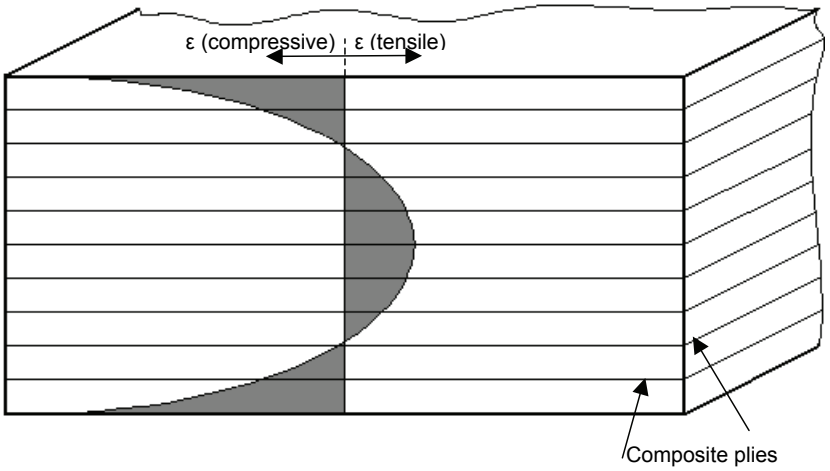

Figure 2.3: Laminate skin-core residual strain distribution (grey area), after [4].

Considering the above, these three levels would result in a complex three-dimensional residual strain state within a composite structure. Many micromechanical models have been developed to predict the magnitude of the corresponding stresses [3, 7, 8, 13-16]. But in a composite structure, the distinction between the three levels is not so clear. Especially, since additional sources for residual strain formation in composite products are angles and curvatures [2, 17-20], see for example Figure 2.4. The fibre-dominated in-plane contraction is for most composites much smaller than the out-of-plane matrix-dominated contraction [2, 21, 22] and therefore the axial contraction over the outer plies acts over a larger area compared to the inner plies during cooling. When the sheet is constrained, residual strains can form: the outside plies will suffer from a compressive strain while the inner layers undergo a tensile strain.

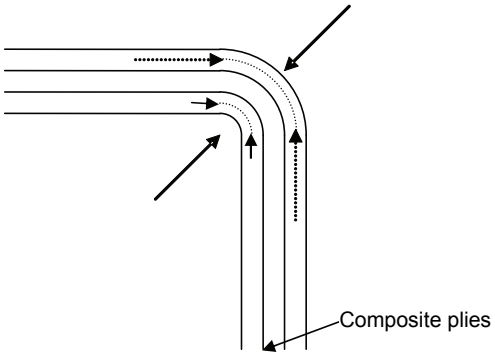

Figure 2.4: Schematic view of preferred contraction directions in angled composite structures.

According to Favre [3], if the long-term and environmental parameters are omitted, the magnitude of residual stresses[2] in composite structures depends on four parameters: shrinkage of the composites' constituents, temperature difference, elastic coefficients of the constituents, and fibre volume fraction. These parameters are, in turn, largely dependent on the matrix morphology (thermoset network or thermoplastic, semi-crystalline or amorphous), type of fibres, fibre-matrix interface properties, fibre morphology (woven fabric or unidirectional tape), and processing conditions. On top of this, residual stresses interact with the time-dependent (visco-elastic) behaviour of the matrix as well as environmental effects. These factors will be discussed separately.

2.3 Composites' constituents

2.3.1 Reinforcing fibres

For the temperature range between the processing and service temperature of composites, the thermal contraction behaviour of the fibres is linear, and therefore this can be described by a constant coefficient of thermal contraction that should be equal to the coefficient of thermal expansion (CTE). The CTE of the fibre is in general much lower than for the polymer matrices, which results in a large difference in expansion and shrinkage behaviour between the matrix and the reinforcing fibres.

Both aramid fibres and carbon fibres show highly anisotropic thermal expansion behaviour, with minor shrinkage in the fibre longitudinal direction and thermal expansion in the radial direction when heated [8, 23, 24]. Therefore in a composite, aramid and carbon fibres undergo higher residual strains in the longitudinal fibre direction than the radial direction [3],

[2] In this thesis, the strains and stresses are regarded far from free edges or ply interfaces.

but the latter was shown to provide a relatively insignificant contribution to the formation of residual strains [1]. For the isotropic glass fibres, there is no such difference.
For higher fibre volume fractions, the compressive fibre residual strains were found to be lower [25]. This can be attributed to a lower fraction of contracting polymer and the distribution of the strains over more fibres. For some composites, an optimum in fibre volume may exist at which the tensile strains in the matrix in between the fibres turn to compressive, depending on the fibre spacing [8, 26].
However, for cross-ply composites the interlaminar stresses increase with increasing fibre volume fraction [27] and with more plies the residual fibre strains are also higher [28-31].
The difference in effect of fibre morphology, i.e. unidirectional tapes or fabric reinforced, on the formation of residual stresses has barely been studied, even though fabric reinforced composites are currently applied more frequently [32].

2.3.2 Thermoplastic polymer matrix

Unlike a thermoset polymer matrix that requires a chemical reaction to form, a melt-processable thermoplastic matrix can be heated to a processing temperature above its glass or melting temperature and subsequently solidified upon cooling to the demoulding temperature. The cooling involves volumetric contraction of the thermoplastic matrix, which is significantly higher than the fibre contraction.

Shrinkage

The shrinkage in thermoplastic polymers depends on the matrix morphology, which can be either amorphous or semi-crystalline. In semi-crystalline thermoplastics, the volumetric shrinkage results from the densification upon crystallisation (because the crystalline structure has a higher density than the amorphous phase) in addition to the thermal contraction caused by the temperature drop between the processing and service temperature. In amorphous thermoplastics, the shrinkage is only due to the latter. Therefore, the total shrinkage for semi-crystalline matrices is much higher than for amorphous matrices, as can be seen in Figure 2.5, where T_g is the glass transition temperature, T_m is the melting temperature, and T_c is the crystallisation temperature on cooling from the melt (the portion of the curve that includes T_c is a representative plot during cooling) [12]. It must be noted that the thermal expansion and contraction behaviour is not linear for the thermoplastic polymer, i.e. the CTE varies at different temperatures [33, 34].

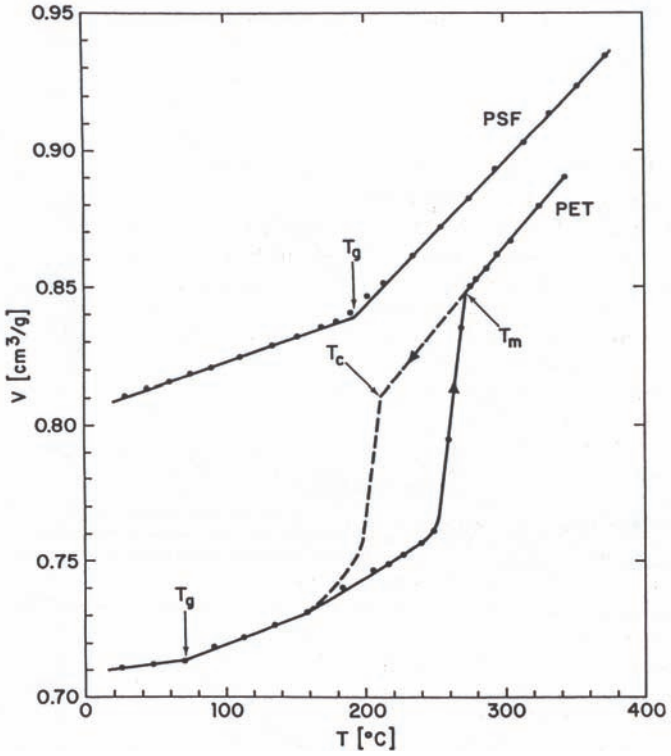

Figure 2.5: Specific volume of polysulfone (PSF, amorphous) and polyethyleneterephtalate (PET, semi-crystalline) as a function of temperature at atmospheric pressure [12].

Temperature difference

Upon cooling of amorphous thermoplastic composites between the processing temperature and the glass transition temperature (T_g), the amorphous matrix is in the visco-elastic state [35]. This means that possible stress build-up due to thermal shrinkage can still be relaxed, because the molecular chains possess sufficient energy for freedom of movement at high temperatures, especially at low cooling rates. When the T_g is reached, the amorphous polymer becomes glassy and residual stresses are formed and 'frozen in' upon subsequent cooling of the composite. Therefore, for amorphous matrix composites such as polyetherimide (PEI), thermoplastic polyimide (TPI), polyethersulfone (PES), and polysulfone (PSF) reinforced with carbon fibres, the temperature at which thermal stresses start building-up (defined as the 'stress-free' or 'strain-free' temperature) was found to be around the glass transition temperature [1, 36-39]. For semi-crystalline matrices such as polyetheretherketone (PEEK), the stress-free temperature (SFT) can be found near the peak crystallisation temperature [7, 40, 41], because of the load-bearing capability of the crystalline phases below that temperature [5].

A higher cooling rate results in a lower peak crystallisation temperature and a higher glass transition temperature in semi-crystalline and amorphous thermoplastics respectively, which in turn influence the stress-free temperatures [1, 5, 37, 40, 42]. Therefore, for amorphous polymer matrices, the faster the cooling rate in the glass transition region, the higher the residual stresses will be [37, 43]. For semi-crystalline thermoplastics, a higher cooling rate results in a lower peak crystallisation temperature and lower crystallinity levels [44-46]. This leads to a lower stress-free temperature and less shrinkage [2]. Therefore, it was concluded that residual stresses due to crystallisation could be reduced by increasing the cooling rate [44, 47], but this also depends on the visco-elastic behaviour and crystallisation kinetics, which is different for every polymer [30]. In addition, a low degree of crystallinity is often unwanted, due to a decreased solvent resistance [47, 48], and lower elastic modulus [49, 50].
Fibre properties that can influence the crystallisation are [51]: the nature of the fibre (presence of crystal nucleation sites on the fibre surface), surface roughness, thermal conductivity and fibre treatment.

2.3.3 Reactive thermoset polymer matrix

For composites manufactured with liquid moulding, the most important mechanisms governing residual strain formation are equal to those for thermoplastic composites: the mismatch in shrinkage behaviour between the reinforcing fibre and the polymer matrix from the point where the polymer matrix has sufficient mechanical properties for strain transfer [3, 52, 53]. However, for reactive polymers the physical origins of these parameters are different from those of melt-processable thermoplastic matrices: besides thermal contraction, in-situ polymerisation (curing) takes place. Curing is usually accompanied by significant volumetric shrinkage; for epoxies this is for example ~4–5% [54]. In addition, the point from where residual strains start to build up is different. For thermoplastic matrices suitable for LCM, these parameters are thus far unknown.
The shrinkage behaviour of a curing polymer will be explained with a schematic view in Figure 2.6.

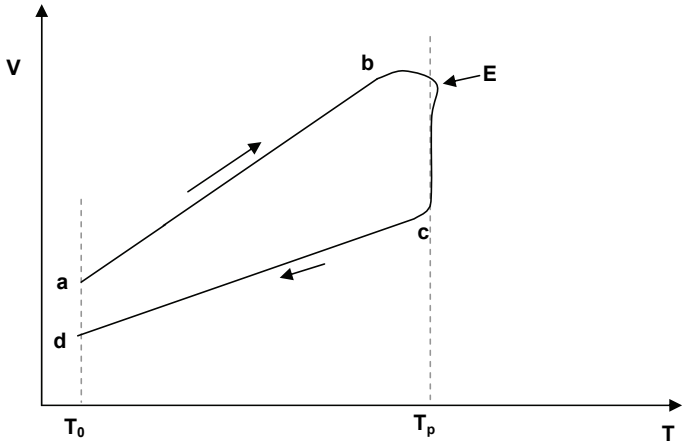

Figure 2.6. Schematic view of polymer volume during cure, after [53].

The following stages can be identified [53, 55, 56]:

a-*b*: The resin volume increases when heated from the reference temperature T_0 to the polymerisation (cure) temperature T_p, due to thermal expansion before any chemical shrinkage occurs.

b-*c*: Around the polymerisation temperature T_p, the resin volume starts to decrease due to cross-linking reactions resulting in significant chemical shrinkage, overtaking the thermal expansion. In the case of exothermic chemical reactions, an additional temperature peak may be observed (point *E*).

c-*d*: The volume decreases due to thermal contraction of the cured polymer during cooling to T_0 with a CTE that is proportional to the degree of conversion [53, 57, 58]. The slope between *c*-*d* is lower than for *a*-*b*, since the CTE in the glassy state (obtained after cure) is much lower than in the liquid state [58].

In trajectory *b*-*c* during the polymerisation reaction two points must be noted: the gel-point and the vitrification point. Gelation is usually defined by the point at which an infinite network of molecules is developed inside the polymer (gel point) with the characteristic of a sudden and irreversible transformation of the reacting mixture from a viscous liquid to a solid/ elastic gel which shows no tendency to flow [46, 59, 60]. Volume changes prior to polymer gelation are not expected to contribute to residual strain formation, since the polymer is still fluid. Most of the shrinkage is therefore wanted in the liquid state, since replenishment of the monomer or other reactive components can still occur [61]. The gel-point is where the resin has cured to such an extent that it has sufficient mechanical strength to transfer stresses and is therefore an important parameter for the prediction of residual strains [56, 62].

At the vitrification point the cure reaction will stop. This happens when the glass transition temperature of the reacting polymer equals the cure temperature [63]. This glass transition temperature increases as the molecular network builds-up and the modulus increases, that is, when the degree of cure increases [53, 64]. Beyond this point, molecular mobility is so reduced that curing is almost stopped [59]. Postcuring operations above T_g are sometimes necessary to complete the cure process and obtain the specified thermal and mechanical properties [60]. Many studies have shown that the T_g is often located a little below the (post-) curing temperature, which is similar for the 'stress-free' temperature [3, 65].

For all polymer matrix composites applies that the further the cool-down or service temperature from the SFT, the more residual stresses reside in the composite due to the mismatch in thermal contraction between the components [1, 7, 12, 36, 37, 40, 42, 49, 66]. The SFT can be determined by heating the composite until the residual stresses were found to be zero [1, 12], but this procedure will be explained in more detail in the next chapter.

2.3.4 Fibre-matrix interface

In thermoset composites, the fibre-matrix interface is formed with chemical bonds, whereas in thermoplastic composites (TPCs) the fibre-matrix adhesion primarily occurs due to the shrinkage of the matrix around the fibre and thereby increasing the Van der Waals bonds between the fibre and the matrix [66]. For APA-6 it is assumed that a chemical bond is formed between the APA-6 matrix and the glass fibre sizing [67]. The residual strains in the radial fibre direction offer a significant fraction of the fibre-matrix interfacial (shear) strength for thermoplastic composites, since it "provides one of the mechanisms whereby the matrix grips the fibres and allows stress transfer via the fibre-matrix interface" [8, 9]. It was indeed found that with increasing radial residual stresses the fibre-matrix interfacial bond became stronger [45, 68-71].

Treatments to improve the fibre-matrix bond strength in TPCs are based on chemical bonding (on a molecular level, often with a fibre coating or sizing) and mechanical interlocking [72], where the fibre surface may be treated to become "rougher". Arguments for the latter treatment are that stress transfer is governed by friction, and a linear relation can be assumed between the radial stress and the friction shear stress at the interface [43]. The mentioned treatments are synergistically enhanced by the radial residual stresses. A higher fibre-matrix interfacial bond strength by chemical treatment will increase the residual stresses [43, 45], because the residual stresses can be little relieved by interfacial debonding.

Another effect concerning the fibre-matrix interface is that in semi-crystalline composites the fibre surface may act as nucleation points for the crystalline spherulites [51, 73]. This can result in epitaxial spherulite growth from the fibre surface, giving a transcrystalline region

around the fibre, see Figure 2.7. This transcrystalline region was shown to cause additional radial residual stresses due to the local higher density [49, 68]. Nonetheless, the effect of transcrystallinity on the interfacial bond strength decreases as the composite fibre content increases [69, 74], and transcrystalline zones are scarcely observed in real composites [75].

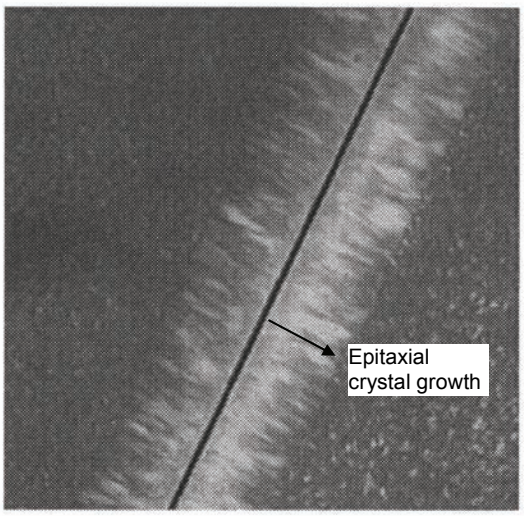

Figure 2.7: Microstructure of polypropylene sample isothermally crystallised around a carbon fibre followed by quenching [68].

2.4 Residual strains through the thickness

With increasing thickness the residual strain distribution through the thickness becomes more significant [76]. These strains can have several causes, including temperature gradients, material property variations and processing effects. One example is presented by through-the-thickness inhomogeneous distributions of fibre volume fraction or matrix rich layers (for example at the surface plies) that can induce additional residual stresses through the thickness due to a difference in shrinkage behaviour [66, 77].

Reactive polymers

During manufacturing of thick laminates with any reactive polymer matrix, thermal gradients through the thickness may arise due to non-homogeneous temperature fields and exothermic reactions. These temperature variations may result in residual strain gradients through the thickness as well as variations in polymer matrix properties, such as degree of cure [78, 79]. This can be explained as follows: In the likely event that in thick laminates the surface plies

reach the polymerisation temperature sooner than the centre plies, the polymerisation will start there and progress inwards. With gelation occurring at different points in time, residual strain variations through the thickness are then likely to be similar as in Figure 2.3.
Due to the exothermal reaction in combination with the insulating properties associated with polymer matrices, the centre plies can reach higher temperatures as the surface plies, leading to a higher vitrification temperature. This may lead to a higher T_g and degree of cure resulting in increased shrinkage in the centre plies. Therefore, it is very important that the temperature increase due to the exothermal reaction is controlled, also to prevent the temperature from reaching the polymer degradation temperature [78]. The reaction should thus not occur too fast, since the generated heat cannot be easily transferred to the surroundings due to the low heat conductivity, especially in a thick composite product. For economic reasons, the cure cycle should be as brief as possible and hence many models and curing strategies are currently being developed for determination, but also reduction of residual stresses through the thickness of thick thermoset laminates [57, 78, 80-85].

Thermoplastic polymers
In thermoplastic composites, cooling rate plays a significant role in the formation of residual stresses through the thickness ('global' residual stresses). High-performance melt-processable thermoplastic composites are inherently manufactured at high temperatures. Therefore, the complex and high variations in cooling rates within thick composite structures are typically unavoidable [5]. Often the surface plies cool down and reach the solidification temperatures sooner than the centre plies. Result is that the process leaves the surface regions in a state of compression balanced by interior tension (thermal skin-core residual stresses) [2], see Figure 2.3. With higher cooling rates, the residual stresses are higher and the distribution is more significant [2, 4, 5, 47, 86-88].
Crystallinity of semi-crystalline thermoplastic matrices plays an additional role in skin-core effects, when a non-uniform cooling rate through the thickness of the laminate exists. As stated before, a slower cooling rate (for example in the centre of a laminate) results in increased crystallinity levels and thus more shrinkage. Therefore, many studies regarding residual stress distributions focus on crystallinity distributions immediately after processing and subsequent annealing of the composite ('morphological skin-core stresses') [5, 86, 89]. Annealing is typically executed on thick laminates to reduce the skin-core residual stresses through relaxation.

2.4.1 Annealing and postcuring
In isotropic materials, residual stresses can be removed by annealing since their elastic expansion behaviour with temperature is uniform [37]. However, for anisotropic composites

this is not so straightforward. Annealing is often carried out on thermoplastic products or thermoplastic composites to relax the residual stresses, to minimise the residual strain gradient through the thickness [1, 4, 47, 49, 90], or simply to obtain optimal levels of crystallinity [49, 90, 91], but this requires additional time and resources [19]. Quenching of a semi-crystalline composite and subsequent annealing were shown to give similar results as slow cooling [4].

Annealing can be accomplished by raising the composites' temperature above the glass transition temperature of the matrix and allowing relaxation or crystallisation processes to take place [33]. In consequence, the stress-free temperature may effectively be altered by annealing [1, 91]. It must be noted however, that during cooling below the SFT strains reappear due to the shrinkage mismatch between the connected components [33].

For thermoset composites, the visco-elastic relaxation behaviour is less pronounced as for thermoplastics due to the network structure. Usually for thermoset composites, a postcure cycle or slow cooling trajectory is recommended for maximising the degree of cure and minimise the residual stress distribution.

2.4.2 Influence of processing mould material

Another processing parameter that influences residual stress formation, is the effect of mould materials during processing. The last few years, much effort is dedicated towards understanding the mechanisms of additional residual stress generation due to tool-part interaction and resulting deformations in thermoset composites [92-96]. Two types of interaction between the tools and the composite part can be distinguished: thermal and mechanical, and both can significantly influence the development of stresses in the composite [18, 97]. Thermal interaction was for example found due to differences in heating and cooling rate on the laminate surfaces [89]. This difference can originate from the heat transfer properties of different mould materials [97].

The mechanical interaction consists of the mismatch in CTE between the tool and the composite. Often the CTE of the tooling is higher than that of the composite [97]. This mismatch can result in significant residual stresses [6, 21, 98-105], or a through-the-thickness stress distribution in the composite part, depending on the interface conditions between the tool and the composite [18]. Interfacial stress transfer is determined by the friction between the tool and the composite material and it is conceivable that friction of the mould with the polymer composite in its solidifying state [106], induces additional compressive residual stresses in the surface plies due to forced shrinkage induced by the mould surface.

2.5 Mechanisms relieving residual strains

Besides annealing, other technologies and parameters influence the residual strain state of a composite structure significantly. These will be briefly discussed in this Section.

2.5.1 In-service environment

During its service life, temperature and moisture both influence the residual strain state of a composite structure significantly: at increased temperatures the residual stresses will be lower, due to thermal expansion of the matrix and a smaller difference with the actual and stress free temperature [9, 52, 66, 107]. For several thermoplastic composites the relation between temperature and residual stresses was found to be almost linear [1, 36, 49]. Matrix dominated moisture absorption was found to affect the residual stress state of the polymer composite significantly, e.g. due to swelling or plasticisation, which lowers the T_g of the matrix [23, 26, 35, 107-118].

In turn, the matrix-dominated environmental properties of a composite structure are themselves affected by residual stresses [39, 112, 119]. For example, for the amorphous PEI in a CF composite, a lower T_g was found compared to the pure polymer, corresponding to a lower temperature resistance. This was attributed to the residual strains induced by the carbon fibres [39]. In addition, higher residual strains were found to enhance the moisture uptake in a composite [112, 119].

Due to the time-dependent (visco-elastic) nature of the polymer matrix (and possibly also the fibre-matrix interphase), thermal residual stresses themselves prove to be time-dependent, viz. the matrix shows stress or strain relaxation or creep behaviour over time [9, 35, 36, 40, 41, 49, 66, 108, 120, 121]. Stress within a polymer resulting from a certain strain, is found to decrease with time due to molecular relaxation processes that take place within the polymer [46, 122]. Higher residual stresses result in a higher rate of relaxation. Environmental aspects, such as temperature and moisture, influence this relaxation behaviour. An annealing step is based on this effect. For increased temperatures, the relaxation rate of the residual stresses is higher [35, 39, 123-125] as well as the total relaxation [49]. Experimental studies have shown that residual stresses in composites arisen during manufacturing decrease significantly during storage under ambient hygrothermal conditions (room temperature ~23°C and ~50% relative humidity) [7, 9, 40, 66]. It must be made clear however, that residual stresses only relax to certain values, which results in a state where the remaining residual stresses still have a significant influence on the mechanical properties [36, 108, 126].

In addition to relaxation, another time-dependent mechanism affects the composites' residual strains: physical ageing of the polymer matrix [127]. Physical ageing occurs when a polymer is cooled below its T_g, and the material evolves towards thermodynamic equilibrium [39, 108].

This evolution will produce measurable changes over time of increasing modulus and yield strength and lower toughness [39, 125], thereby increasing the likelihood for failure initiation [128]. Due to physical ageing, the process of visco-elastic stress relaxation becomes much slower [120, 125]. Temperature and processing history have a strong influence on the rate of physical ageing, i.e. at higher temperatures (below T_g), the rate of physical ageing is higher [35]; hence for low cooling rates, the ageing effects are larger [129].
Excellent and extensive reviews have been published on visco-elastic behaviour in polymer matrix composites in relation with residual stresses, physical ageing and environment, and the reader is referred to these references for more background information on the exact mechanisms and modelling of this behaviour: [35, 108, 120, 130, 131].

2.5.2 Defects, damage and deformations

Residual stresses can be relieved by the occurrence of defects and deformations in composite laminates and structures, such as fibre waviness, transverse cracking, delamination and warpage:

- Fibre waviness occurs mostly in the surface plies due to the mismatch in CTE between the tool and the composite part. It can degrade the compressive strength as well as other aspects of the material performance, such as overall part quality [97, 132].
- Residual stresses can initiate transverse cracking (often referred to as microcracking) in a composite when exceeding the yield strength of the resin or the fibre-matrix bond strength, resulting in matrix cracking or fibre-matrix debonding [13, 66, 90, 133]. When residual stresses reach values in the order of the transverse ply strength, the ply may crack instantaneously during processing [7, 36, 124, 134, 135], see Figure 2.8. This was shown to depend on, among others, ply thickness [52, 136-138]. Cracking of the laminate provides an irreversible means for relief of the residual stresses by redistribution of the stresses [37, 41, 42, 44, 66], and results in a decrease in effective CTE of the composite [139-141] and deteriorates the composites' mechanical properties significantly [52, 136, 137]. External loading on top of residual stresses can also induce these types of defects.

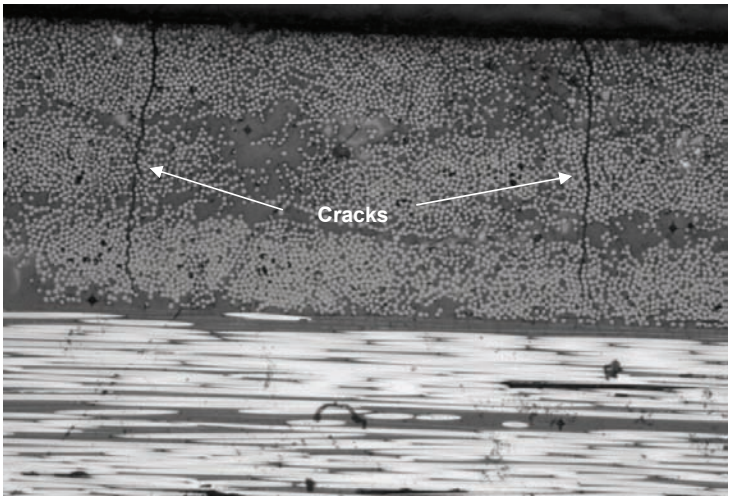

Figure 2.8: Transverse cracking in surface plies of a $0_3/90_9/0_3$ CF/PEI laminate.

- The discontinuity in residual stress level between the 0° and 90° plies in a cross-ply laminate could lead to premature interlaminar debonding in service [19], which is characterised by progressive delamination of composite plies, leading to a loss of stiffness and strength of the structure [142].
- One of the effects of interlaminar residual stresses, is that for relatively thin unsymmetrical laminates, a variety of curved shapes can be the result (warpage) [8, 37, 121, 143]. Non-symmetrical residual stresses through the thickness of a (balanced) composite can also result in dimensional instability of a composite structure. In addition, a non-uniform temperature distribution in press-plates or moulds can also induce warpage, see Figure 2.9.

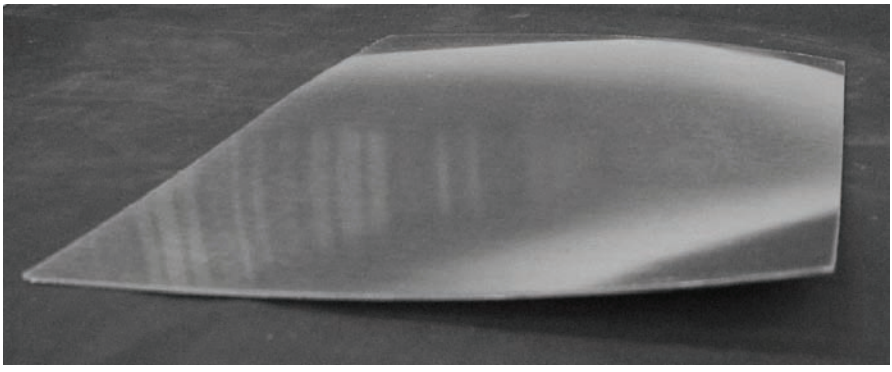

Figure 2.9: Distorted glass fibre fabric reinforced polyetherimide laminate due to non-uniform cooling of the hot platen press.

The most common way of residual stress relaxation in composite products is deformation of angled and curved parts (dimensional instability) [17, 144]. The change in shape during cooling of a composite structure is the result of the composites' anisotropy in contraction during cooling as described in Section 2.2 [2, 20, 145]. Upon demoulding, the sheet is instantaneously deformed because of residual stress relaxation (see Figures 2.9 and 2.10) and in a subsequent cooling stage, warpage is increased further [146]. The two sides of a curve often approach each other and this will result in a smaller enclosed angle. This change in enclosed angle is named the 'spring-in effect' [17, 20]. Tool-part interaction, fibre volume variations, ply stacking sequence, symmetry of lay-up and processing conditions may influence spring-in of the laminate, as well as environmental effects, such as moisture [2, 18, 19, 114]. Geometrical dimensions also play a role, such as enclosed angle, part thickness and tool radius [17].
The spring-in effect has implications for the production of three-dimensional, double curvature components [20]. Models based on classical laminate theory (CLT), thermo-elasticity as well as visco-elastic behaviour were developed to predict the final deformation, warpage or spring-in angle of a product [2, 17, 18, 20, 87, 145, 146] as well as the residual stress distribution [2, 17, 18, 146].

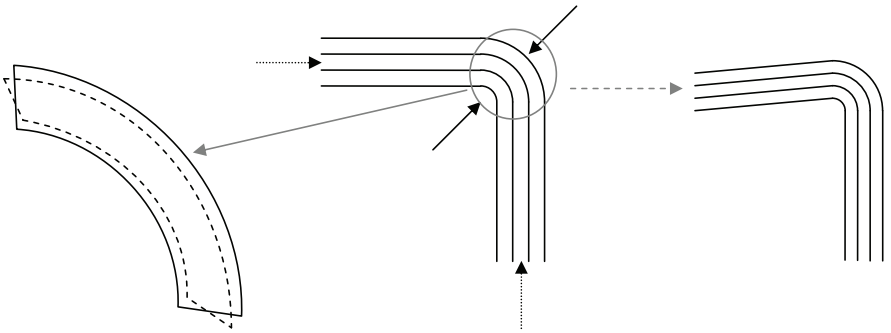

Figure 2.10: Schematic view of the spring-forward phenomenon, with the discontinuous lines depicting the deformation after processing.

One other mechanism whereby residual stresses can be relieved is to deliberately damage the composite material. For example, upon machining of the produced composite parts, such as drilling holes and cutting, deformations occur due to relaxation of these stresses. Many experimental techniques for determination of residual stresses through-the-thickness are based on this, as will be explained in the next chapter.

2.5.3 Modification of composite constituents

Since the above-mentioned means of stress relief are not always wanted, it is important to learn how to minimise the residual stresses. Several mechanisms were proposed in literature based on modification of the composite constituent materials. A careful design of the composite material by tailoring material properties such as fibre volume fraction, number of off-axis plies and thickness of plies is necessary to minimise (or optimise, depending on the desired structural behaviour of the composite product) residual stresses [52, 147, 148].

The temperature difference between the stress-free temperature and the service temperature is a major driving force for the formation of residual stresses. A polymer with a low stress-free temperature is therefore proposed as a matrix [7, 149] or, in the case that this is not desirable or possible, as a fibre-matrix interface [7, 15]. In addition, the application of a thin compliant layer (of pure polymer) between different plies was proposed to relieve residual strains and increase the impact toughness [8, 142, 147, 148]. Incorporation of glass fibres in a carbon fibre based composite, was also considered a good solution [148]. These solutions together with the use of a more resilient and toughened matrix, were also proposed to reduce the microcracking behaviour [147, 148, 150].

Another approach is to control the matrix shrinkage behaviour to decrease the mismatch between the fibres and the matrix [7, 8]. Addition of mineral fillers such as silica or low-profile additives to a polymer matrix usually reduces the thermal expansion coefficient considerably [133]. A development of the last 20 years concerns the production of nanocomposites, which can be used as a matrix for composite materials [151] and show a significantly reduced CTE compared to the pristine polymer matrix [152-154]. The fibre matrix adhesion and thermal properties were however also found to be affected.

2.5.4 Modification of processing parameters

The optimum processing cycle, giving the lowest residual stresses and maximising the mechanical properties of the composite, is different for each lay-up and material system [6]. Taking into account visco-elastic behaviour, cure and crystallisation kinetics, optimal temperature cycles can be found for obtaining the lowest possible residual stresses [124], while maintaining practical cycle times [57, 78, 80-85]. For thermoset matrix composites, an optimal cure path can be proposed based on step-wise curing during which the resin is partially cured at a lower dwell temperature [155]. The resin then expands during heating to the final cure temperature and thereby reduces the stress, provided that the mechanical properties of the resin are such that they can contribute to stress development.

Depending on the matrix crystallinity kinetics, it was proposed that fast cooling to the crystallisation temperature and then slow cooling to T_g would lower residual stresses in semi-

crystalline composites [30]. For amorphous thermoplastic composites, it is recommended to cool slowly in the temperature region of the rubber-to-glass transition [37, 43].

Thermal residual stresses were also found possible to be used advantageously, as several papers propose the prediction of deformed shapes of unsymmetrical laminates, to give them the shape that is necessary for certain applications [38, 156-158]. In addition, it was proposed to activate the snap-through moment of multi-stable unsymmetrical laminates with smart material fibres [158], see also Chapter 3.

2.6 Concluding remarks

From a literature study on residual strain formation during processing of composites, it can be concluded that the residual strains depend mostly on the shrinkage behaviour of the polymer matrix from the point where polymer shrinkage cannot be relaxed anymore, i.e. has sufficient stiffness for strain transfer. For prediction of the magnitude of residual stresses, not only the shrinkage behaviour of the composite constituents must be known, but also the quality of fibre-matrix adhesion is important, and the elastic moduli of the constituents must be identified as well as the fibre morphology.

In composites manufactured with a reactive polymer matrix, the polymer shrinkage contribution to residual strain formation consists of chemical shrinkage from the gel-point onwards and thermal contraction during cooling from the cure temperature to the service temperature, which in turn depends on the degree of cure.

For thermoplastics the shrinkage from the crystallisation and glass transition temperature in semi-crystalline and amorphous polymers, resp. is the principal factor governing residual strain formation.

Temperature variations proved to be the prime factor regarding residual strain variations through the thickness, as well as variations in matrix properties, such as degree of cure and crystallinity. Tool-part interaction also provides an important source for residual strain variations through the thickness.

The aim for every thick composite product is to have homogeneous properties through the thickness, including a known homogeneous residual strain distribution, without the defects generated by the composite itself to relieve the residual stresses, such as fibre waviness, transverse cracking and deformations. To achieve this, several mechanisms were proposed related to the material properties and processing cycle.

References

1. Barnes, J.A., Byerly, G.E., The Formation of Residual-Stresses in Laminated Thermoplastic Composites. Composites Science and Technology, 51(4): 479-494, 1994.
2. Trende, A., Astrom, B.T., Nilsson, G., Modelling of residual stresses in compression moulded glass-mat reinforced thermoplastics. Composites Part A-Applied Science and Manufacturing, 31(11): 1241-1254, 2000.
3. Favre, J.P., Residual thermal stresses in fibre reinforced composite materials - A review. Journal of the Mechanical Behavior of Materials, 1(1-4): 37-53, 1988.
4. Manson, J.A.E., Seferis, J.C., Process Simulated Laminate (Psl) - a Methodology to Internal-Stress Characterization in Advanced Composite-Materials. Journal of Composite Materials, 26(3): 405-431, 1992.
5. Chapman, T.J., Gillespie, J.W., Pipes, R.B., Manson, J.A.E.Seferis, J.C., Prediction of Process-Induced Residual-Stresses in Thermoplastic Composites. Journal of Composite Materials, 24(6): 616-643, 1990.
6. Li, M.C., Wu, J.J., Loos, A.C., Morton, J., A plane-strain finite element model for process-induced residual stresses in a graphite/PEEK composite. Journal of Composite Materials, 31(3): 212-243, 1997.
7. Nairn, J.A., Zoller, P., Matrix Solidification and the Resulting Residual Thermal-Stresses in Composites. Journal of Materials Science, 20(1): 355-367, 1985.
8. Kim, J.-K., Mai, Y.-W., Residual Stresses, in Engineered Interfaces in Fiber Reinforced Composites. 1998, Elsevier Science Ltd.: Oxford. p.308-320.
9. Harris, B., Residual Strains, in Engineering Composite Materials, Harris, B., Editor. 1999, IOM Communications: London. p.79-83.
10. Schwarz, G., Krahn, F., Hartwig, G., Thermal-Expansion of Carbon-Fiber Composites with Thermoplastic Matrices. Cryogenics, 31(4): 244-247, 1991.
11. Zhang, L., Time-Dependent Behaviour of Polymers and Unidirectional Polymeric Composites. 1995 Mechanical Engineering, Delft University of Technology, Delft. 174 pages.
12. Nairn, J.A., Zoller, P. The Development of Residual Thermal Stresses in Amorphous and Semicrystalline Thermoplastic Matrix Composites. in Toughened Composites. 1987. Houston, Texas; USA: ASTM, 1916 Race Street, Philadelphia, Pennsylvania 19103, USA.
13. Abedian, A., Szyszkowski, W., Influence of the free surface on the thermal stresses in unidirectional composites. Composites Part a-Applied Science and Manufacturing, 28(6): 573-579, 1997.
14. Meske, R., Schnack, E., Stress analysis of carbon-fiber reinforced polymeric materials by means of X-ray diffraction from fillers - micromechanical model and experimental results, in Ecrs 5: Proceedings of the Fifth European Conference on Residual Stresses. 2000. p.217-222.
15. Nairn, J.A., Thermoelastic Analysis of Residual-Stresses in Unidirectional, High-Performance Composites. Polymer Composites, 6(2): 123-130, 1985.
16. Zhao, L.G., Warrior, N.A., Long, A.C. A Micromechanical Study of Failure and Damage of Unidirectional Fibre-Reinforced Polymer Matrix Composites: Effect of Residual Stress. in Composites Europe 2005. 2005. Barcelona, Spain: Netcomposites.
17. Jain, L.K., Hou, M., Ye, L., Mai, Y.W., Spring-in study of the aileron rib manufactured from advanced thermoplastic composite. Composites Part a-Applied Science and Manufacturing, 29(8): 973-979, 1998.
18. Wijskamp, S., Shape Distortions in Composites Forming. 2005 Mechanical Engineering, Division of Design, Production and Manufacturing, University of Twente, Enschede, The Netherlands. 171 pages.
19. Kim, B.S., Bernet, N., Sunderland, P., Manson, J.A., Numerical analysis of the dimensional stability of thermoplastic composites using a thermoviscoelastic approach. Journal of Composite Materials, 36(20): 2389-2403, 2002.
20. Zahlan, N., Oneill, J.M., Design and Fabrication of Composite Components - the Spring-Forward Phenomenon. Composites, 20(1): 77-81, 1989.
21. Wisnom, M.R., Gigliotti, M., Ersoy, N., Campbell, M.Potter, K.D., Mechanisms generating residual stresses and distortion during manufacture of polymer-matrix composites structures. Composites Part A: Applied Science and Manufacturing, 37(4): 522-529, 2006.
22. Wang, J., Kelly, D., Hillier, W., Finite element analysis of temperature induced stresses and deformations of polymer composite components. Journal of Composite Materials, 34(17): 1456-1471, 2000.
23. Smith, P.A., Carbon Fiber Reinforced Plastics - Properties, in Polymer Matrix Composites, Talreja, R. and Manson, J.A., Editors. 2001, Elsevier Science Ltd.: Oxford. p.107-150.
24. Wardle, M.W., Aramid Fiber Reinforced Plastics - Properties, in Polymer Matrix Composites, Talreja, R. and Manson, J.A., Editors. 2001, Elsevier Science Ltd.: Oxford. p.199-229.
25. Wagner, H.D., Nairn, J.A., Residual thermal stresses in three concentric transversely isotropic cylinders: Application to thermoplastic-matrix composites containing a trans crystalline interphase. Composites Science and Technology, 57(9-10): 1289-1302, 1997.
26. Jones, F.R., Durability of reinforced plastics in liquid environments, in Reinforced plastics durability, Pritchard, G., Editor. 1999, Woodhead Publishing Limited: Cambridge, England. p.91-96.
27. Wang, S.K., Kowalik, D.P., Chung, D.D.L., Self-sensing attained in carbon-fiber-polymer-matrix structural composites by using the interlaminar interface as a sensor. Smart Materials and Structures, 13(3): 570-592, 2004.
28. Filiou, C., Galiotis, C., In situ monitoring of the fibre strain distribution in carbon-fibre thermoplastic composites 1. Application of a tensile stress field. Composites Science and Technology, 59(14): 2149-2161, 1999.
29. Galiotis, C., Melanitis, N., Batchelder, D.N., Robinson, I.M.Peacock, J.A., Residual Strain Mapping in Carbon-Fiber Peek Composites. Composites, 19(4): 321-324, 1988.
30. Nielsen, A.S., Pyrz, R., The effect of cooling rate on thermal residual strains in carbon/polypropylene microcomposites. Science and Engineering of Composite Materials, 7(1-2): 1-22, 1998.
31. Young, R.J., Day, R.J., Zakikhani, M., Robinson, I.M., Fibre Deformation and Residual Thermal Stresses in Carbon Fibre Reinforced PEEK. Composites Science and Technology, 34(3): 243-258, 1989.
32. van Barschot, J., Airbus en Boeing vliegen met Ten Cate, in NRC Handelsblad. 2005: Rotterdam. p. 17.
33. Barnes, J.A., Thermal-Expansion Behavior of Thermoplastic Composites .2. Journal of Materials Science, 28(18): 4974-4982, 1993.
34. Barnes, J.A., Simms, I.J., Farrow, G.J., Jackson, D., Wostenholm, G.Yates, B., Thermal Expansion Characteristics of PEEK Composites. Journal of Materials Science, 26(8): 2259-2271, 1991.
35. Brinson, L.C., Gates, T.S., Viscoelasticity and Aging of Polymer Matrix Composites, in Polymer Matrix Composites, Talreja, R. and Manson, J.A., Editors. 2001, Elsevier Science Ltd.: Oxford. p.333-368.

36. Cowley, K.D., Beaumont, P.W.R., The measurement and prediction of residual stresses in carbon-fibre/polymer composites. Composites Science and Technology, 57(11): 1445-1455, 1997.
37. Kim, K.S., Hahn, H.T., Croman, R.B., The Effect of Cooling Rate on Residual Stresses in a Thermoplastic Composite. Journal of Composite Technology & Research, 11(2): 47-52, 1989.
38. Peeters, L.J.B., Powell, P.C., Warnet, L., Thermally-induced shapes of unsymmetric laminates. Journal of Composite Materials, 30(5): 603-626, 1996.
39. D'Amore, A., Caprino, G., Nicolais, L., Marino, G., Long-term behaviour of PEI and PEI-based composites subjected to physical aging. Composites Science and Technology, 59(13): 1993-2003, 1999.
40. Jeronimidis, G., Parkyn, A.T., Residual-Stresses in Carbon Fiber-Thermoplastic Matrix Laminates. Journal of Composite Materials, 22(5): 401-415, 1988.
41. Youssef, Y., Denault, J. Residual stresses in continuous glass fiber/polypropylene composite thermoformed parts. in International SAMPE symposium. 1998.
42. Papadopoulos, D.S., Bowles, K.J. Use of Unbalanced Laminates as a Screening Method for Microcracking. in 35th International SAMPE Symposium. 1990. Anaheim, California.
43. DiLandro, L., Pegoraro, M., Evaluation of residual stresses and adhesion in polymer composites. Composites Part A-Applied Science and Manufacturing, 27(9): 847-853, 1996.
44. Guillen, J.F., Cantwell, W.J., The influence of cooling rate on the fracture properties of a thermoplastic-based fibre-metal laminate. Journal of Reinforced Plastics and Composites, 21(8): 749-772, 2002.
45. Youssef, Y., Denault, J., Thermoformed glass fiber reinforced polypropylene: Microstructure, mechanical properties and residual stresses. Polymer Composites, 19(3): 301-309, 1998.
46. Young, R.J., Lovell, P.A., Introduction to Polymers. Second ed. 1991, London: Chapman & Hall. 443 pages.
47. Deshpande, A.P., Seferis, J.C., Processing characteristics in different semi-crystalline thermoplastic composites using process simulated laminate (PSL) methodology. Journal of Thermoplastic Composite Materials, 9(2): 183-198, 1996.
48. Cogswell, F.N., Thermoplastic aromatic polymer composites; a study of the structure, processing and properties of the carbon fibre reinforced polyetheretherketone and related materials. 1992, Oxford: Butterworth-Heinemann. 277 pages.
49. Unger, W.J., Hansen, J.S., The effect of cooling rate and annealing on residual stress development in graphite fibre reinforced PEEK laminates. Journal of Composite Materials, 29: 108-137, 1993.
50. Young, R.J., Lovell, P.A., Degree of Crystallinity, in Introduction to Polymers. 1991, Chapman & Hall: London. p.263-267.
51. Quan, H., Li, Z.M., Yang, M.B., Huang, R., On transcrystallinity in semi-crystalline polymer composites. Composites Science and Technology, 65(7-8): 999-1021, 2005.
52. Parlevliet, P.P., Bersee, H.E.N., Beukers, A., Residual Stresses in Thermoplastic Composites - A Study of the Literature - Part I: Formation of Residual Stresses. Composites Part A-Applied Science and Manufacturing, , 37(11): 1847-1857, 2006.
53. Li, C., Potter, K., Wisnom, M.R., Stringer, G., In-situ measurement of chemical shrinkage of MY750 epoxy resin by a novel gravimetric method. Composites Science and Technology, 64(1): 55-64, 2004.
54. Morikawa, H., Sudo, A., Nishida, H., Endo, T., Volume-expandable monomer 5,5-dimethyl-1,3-dioxolan-2-one: Its copolymerization behavior with epoxide and its applications to shrinkage-controlled epoxy-curing systems. Journal of Applied Polymer Science, 96(2): 372-378, 2005.
55. Crasto, A.S., Kim, R.Y., Russell, J.D., In situ monitoring of residual strain development during composite cure. Polymer Composites, 23(3): 454-463, 2002.
56. Madhukar, M.S., Genidy, M.S., Russell, J.D., A new method to reduce cure-induced stresses in thermoset polymer composites, part I: Test method. Journal of Composite Materials, 34(22): 1882-1904, 2000.
57. Ruiz, E., Trochu, F., Multi-criteria thermal optimization in liquid composite molding to reduce processing stresses and cycle time. Composites Part A: Applied Science and Manufacturing, 37(6): 913-924, 2006.
58. Abou Msallem, Y., Boyard, N., Jaquemin, F., Poitou, A., Delaunay, D.Chatel, S. Identification of thermal and rheological properties of an aeronautic epoxy resin-simulation of residual stresses. in EsaForm 2008, Lyon, France, 2008.
59. Kim, D.H.K.a.S.C., Vitrification effect on the curing reaction of epoxy resin Polymer Bulletin 18(6): 533-539, 1987.
60. Kroschwitz, J.I., ed. Concise encyclopedia of polymer science and engineering. 1st ed. 1990, John Wiley & Sons, Inc.: New York. 1341.
61. Verstegen, E.J.K., Faasen, J.H.P., Stapert, H.R., Duineveld, P.C.Kloosterboer, J.G., Influence of the reaction mechanism on the shape accuracy of optical components obtained by photoreplication. Journal of Applied Polymer Science, 90(9): 2364-2376, 2003.
62. Antonucci, V., Cusano, A., Giordano, M., Nasser, J.Nicolais, L., Cure-induced residual strain build-up in a thermoset resin. Composites Part A-Applied Science And Manufacturing, 37(4): 592-601, 2006.
63. Gigliotti, M., Wisnom, M.R., Potter, K.D., Development of curvature during the cure of AS4/8552 0/90 unsymmetric composite plates. Composites Science and Technology, 63(2): 187-197, 2003.
64. Leroy, E., Dupuy, J., Maazouz, A., Seytre, G., Evolution of the coefficient of thermal expansion of a thermosetting polymer during cure reaction Polymer, 46(7): 9919-9927, 2005.
65. Timmerman, J.F., Hayes, B.S., Seferis, J.C., Cure temperature effects on cryogenic microcracking of polymeric composite materials. Polymer Composites, 24(1): 132-139, 2003.
66. Warnet, L., On the Effect of Residual Stresses on the Transverse Cracking in Cross-Ply Carbon-Polyetherimide Laminates. 2000 Mechanical Engineering, University of Twente, Enschede. 116 pages.
67. van Rijswijk, K., Thermoplastic Composite Wind Turbine Blades. 2007. PhD thesis Aerospace Engineering, Delft University of Technology, Delft. 249 pages.
68. Nielsen, A.S., Pyrz, R., A Raman study into the effect of transcrystallisation on thermal stresses in embedded single fibres. Journal of Materials Science, 38(3): 597-601, 2003.
69. Hsiao, B.S., Chen, E.J.H. Transcrystalline Interphase in Advanced Polymer Composites. in Controlled Interphases in Composite Materials. 1990. Cleveland, Ohio; USA: Elsevier Science Publishing Co , Inc , 655 Avenue of the Americas, New York, New York 10010, USA.
70. Kim, K.Y., Ye, L., Interlaminar fracture toughness of CF/PEI composites at elevated temperatures: roles of matrix toughness and fibre/matrix adhesion. Composites Part a-Applied Science and Manufacturing, 35(4): 477-487, 2004.
71. Walther, B.M., An Investigation of the Tensile Strength and Stiffness of Unidirectional Polymer-Matrix, Carbon-Fiber Composites under the Influence of Elevated Temperatures. 1998 Engineering Mechanics, Virginia Polytechnic Institute and State University, Blacksburg, Virginia. 112 pages.

72. Kim, J.-K., Mai, Y.-W., Engineered interfaces in fiber reinforced composites. First ed. 1998, Oxford: Elsevier Science Ltd. 401 pages.
73. Klein, N., Marom, G., Pegoretti, A., Migliaresi, C., Determining the role of interfacial transcrystallinity in composite materials by dynamic mechanical thermal analysis. Composites, 26(10): 707-712, 1995.
74. Chen, E.J.H., Hsiao, B.S., The Effects of Transcrystalline Interphase in Advanced Polymer Composites. Polymer Engineering and Science, 32(4): 280-286, 1992.
75. Spruiell, J., Janke, C., A review of the measurement and development of crystallinity and its relations to properties in neat poly(phenylene sulfide) and its fiber reinforced composites. 2004, Oak Ridge National Laboratory: Oak Ridge. p. 80.
76. Theriault, R., Osswald, T.A. Properties of Thermosetting Polymers during Cure. in ANTEC 97, 1997.
77. Ganley, J.M., Maji, A.K., Huybrechts, S., Explaining spring-in in filament wound carbon fiber/epoxy composites. Journal Of Composite Materials, 34(14): 1216-1239, 2000.
78. Hsiao, K.T., Little, R., Restrepo, O., Minaie, B., A study of direct cure kinetics characterization during liquid composite molding. Composites Part A-Applied Science And Manufacturing, 37(6): 925-933, 2006.
79. Boyard, N., Millischer, A., Sobotka, V., Bailleul, J.L.Delaunay, D., Behaviour of a moulded composite part: Modelling of dilatometric curve (constant pressure) or pressure (constant volume) with temperature and conversion degree gradients. Composites Science and Technology, 67(6): 943-954, 2007.
80. Jacquemin, F., Vautrin, A., Analytical calculation of the transient thermoelastic stresses in thick walled composite pipes. Journal of Composite Materials, 38(19): 1733-1751, 2004.
81. Lee, W., Myoung, J.M., Yoo, Y.H., Shin, H., Effect of thermal misfit stress on crack deflection at planar interfaces in layered systems. Composites Science and Technology, 66(3-4): 435-443, 2006.
82. Bogetti, T.A., Gillespie, J.W., McCullough, R.L., Influence of Processing on the Development of Residual Stresses in Thick Section Thermoset Composites. Int. J. Mater. Prod. Technol., 9(1-3): 170-182, 1994.
83. Bogetti, T.A., Gillespie, J.W., McCullough, R.L., Process-Induced Stress and Deformation in Thick-Section Thermoset Composite Laminates. Journal of Composite Materials 26(5): 626-660, 1992.
84. Huang, X.G., Gillespie, J.W., Bogetti, T., Process induced stress for woven fabric thick section composite structures. Composite Structures, 49(3): 303-312, 2000.
85. Guo, Z.S., Du, S.Y., Zhang, B.M., Temperature field of thick thermoset composite laminates during cure process. Composites Science And Technology, 65(3-4): 517-523, 2005.
86. Gillespie, J.W., Chapman, T.J., The Influence of Residual Stresses on Mode I Interlaminar Fracture of Thermoplastic Composites. Journal of Thermoplastic Composite Materials, 6(2): 160-174, 1993.
87. Sunderland, P., Yu, W.J., Manson, J.A., A thermoviscoelastic analysis of process-induced internal stresses in thermoplastic matrix composites. Polymer Composites, 22(5): 579-592, 2001.
88. Domb, M.M., Hansen, J.S., Development of Free-Edge Effect During Processing of Semicrystalline Thermoplastic Composites. Aiaa Journal, 32(5): 1029-1033, 1994.
89. Lawrence, W.E., Manson, J.A.E., Seferis, J.C., Thermal and Morphological Skin Core Effects in Processing of Thermoplastic Composites. Composites, 21(6): 475-480, 1990.
90. Shih, G.C., Tseng, W.W., Lou, A.Y., Evaluation of Test Methods in the Determination of Inplane Shear Modulus of Poly(Phenylene Sulfide) Matrix Composites. Polymer Composites, 15(1): 1-6, 1994.
91. Chung, D.D.L., Continuous carbon fiber polymer-matrix composites and their joints, studied by electrical measurements. Polymer Composites, 22(2): 250-270, 2001.
92. Wisnom, M.R., Gigliotti, M., Ersoy, N., Campbell, M.Potter, K.D., Mechanisms generating residual stresses and distortion during manufacture of polymer-matrix composites structures. Composites Part A: Applied Science and Manufacturing, in press: 1-8, 2005.
93. Twigg, G., Poursartip, A., Fernlund, G., Tool-part interaction in composites processing. Part I: experimental investigation and analytical model. Composites Part a-Applied Science and Manufacturing, 35(1): 121-133, 2004.
94. Twigg, G., Poursartip, A., Fernlund, G., An experimental method for quantifying tool-part shear interaction during composites processing. Composites Science and Technology, 63(13): 1985-2002, 2003.
95. Potter, K.D., Campbell, M., Wisnom, M.R. Investigation of tool/part interaction effects in the manufacture of composite components. in International Conference on Composite Materials. 2003. San Diego.
96. Ersoy, N., Potter, K., Wisnom, M.R., Clegg, M.J., An experimental method to study the frictional processes during composites manufacturing. Composites Part a-Applied Science and Manufacturing, 36(11): 1536-1544, 2005.
97. Kugler, D., Moon, T.J., Identification of the most significant processing parameters on the development of fiber waviness in thin laminates. Journal of Composite Materials, 36(12): 1451-1479, 2002.
98. Kugler, D., Moon, T.J., The effects of Mandrel material and tow tension on defects and compressive strength of hoop-wound, on-line consolidated, composite rings. Composites Part A-Applied Science And Manufacturing, 33(6): 861-876, 2002.
99. Sorensen, L., Gmur, T., Botsis, J., Residual strain development in an AS4/PPS thermoplastic composite measured using fibre Bragg grating sensors. Composites Part A: Applied Science and Manufacturing, 37(2): 270-281, 2006.
100. Kim, Y.K., Daniel, I.M., Cure cycle effect on composite structures manufactured by resin transfer molding. Journal of Composite Materials, 36(14): 1725-1743, 2002.
101. Cho, M., Kim, M.H., Choi, H.S., Chung, C.H., Ahn, K.J.Eom, Y.S., A study on the room-temperature curvature shapes of unsymmetric laminates including slippage effects. Journal of Composite Materials, 32(5): 460-482, 1998.
102. de Oliveira, R., Rakusa, F., Lavanchy, S., Chatton, R., Constantini, D., Michaud, V.Manson, J.A. Influence of the mould thermal expansion on composite stress build-up during cure. in ECCM-12: 12th European Conference on Composite Materials, Biarritz, France, 2006.
103. Ersoy, N., Garstka, T., Potter, K.D., Wisnom, M. Tests to measure the Material Properties Relevant to the Modelling of Process Induced Deformations in Composite Parts. in ICCM-15. 2005. Durban, South Africa: University of KwaZulu Natal, Durban.
104. Wisnom, M., Garstka, T., Ersoy, N., Potter, K.D. Mechanisms generating spring-in of curved composites. in ICCM-15. 2005. Durban, South Africa: University of KwaZulu Natal, Durban.
105. Wisnom, M.R., Gigliotti, M., Ersoy, N., Campbell, M.Potter, K.D., Mechanismsgenerating residual stresses and distortion during manufacture of polymer-matrix composites structures. Composites Part A: Applied Science and Manufacturing: 1-8, 2005.
106. Sorensen, L., Influence of mould friction on formation of residual stresses in thermoplastic composites, recipient: Parlevliet, P.P. November 2004.

107. Harris, B., Environmental Effects, in Engineering Composite Materials, Harris, B., Editor. 1999, IOM Communications: London. p.261-295.
108. Bradshaw, R.D., Brinson, L.C., Mechanical response of linear viscoelastic composite laminates incorporating non-isothermal physical aging effects. Composites Science and Technology, 59(9): 1411-1427, 1999.
109. Kim, H.W., Grayson, M.A., Nairn, J.A., The effect of hygrothermal aging on the microcracking properties of of some carbon fiber/polyimide laminates. Advanced Composites Letters, 4(6): 185-188, 1995.
110. Burcham, L.J., Vanlandingham, M.R., Eduljee, R.F., Gillespie, J.W., Moisture effects on the behavior of graphite/polyimide composites. Polymer Composites, 17(5): 682-690, 1996.
111. Jones, F.R., The effects of aggressive environments on long-term behaviour, in Fatigue in Composites, Harris, B., Editor. 2003, Woodhead Publishing Limited: Cambridge. p.117-146.
112. Sims, G.D., Broughton, W.R., Glass Fiber Reinforced Plastics - Properties, in Polymer Matrix Composites, Talreja, R. and Manson, J.A., Editors. 2001, Elsevier Science Ltd.: Oxford. p.151-197.
113. Weitsman, J., Effects of Fluids on Polymeric Composites - A Review, in Polymer Matrix Composites, Talreja, R. and Manson, J.A., Editors. 2001, Elsevier Science Ltd.: Oxford. p.369-401.
114. Cai, L.W., Weitsman, Y., Non-Fickian Moisture Diffusion in Polymeric Composites. Journal of Composite Materials, 28(2): 130-154, 1994.
115. Kriz, R.D., Stinchcomb, W.W., Effects of Moisture, Residual Thermal Curing Stresses, and Mechanical Load on the Damage Development in Quasi-Isotropic Laminates, in Damage in Composite Materials, Reifsnider, K.L., Editor. 1982, American Society for Testing and Materials. p.63-80.
116. Schnack, E., Meske, R., Eigenspannungen bei viskoelastischen Verbundwerkstoffen. 1996, Institut fuer Technische Mechanik/Festigkeitslehre, Universitaet Karlsruhe: Karlsruhe, Germany. p. 123.
117. Weitsman, Y.J., Anomalous fluid sorption in polymeric composites and its relation to fluid-induced damage. Composites Part A-Applied Science And Manufacturing, 37(4): 617-623, 2006.
118. Weitsman, Y.J., Guo, Y.J., A correlation between fluid-induced damage and anomalous fluid sorption in polymeric composites. Composites Science and Technology, 62(6): 889-908, 2002.
119. Gates, T.S., Grayson, M.A. On the use of accelerated aging methods for screening high temperature polymeric composite materials. in AIAA Structures, Dynamics and Materials Conference. 1999. St. Louis, MI: AIAA, Reston, VA.
120. Ogale, A.A., Creep Behavior of Thermoplastic Composites, in Thermoplastic Composite Materials, Carlsson, L.A., Editor. 1991, Elsevier Science Publishers, B.V.: Amsterdam. p.205-232.
121. Wang, C., Sun, C.T., Thermoelastic behavior of PEEK thermoplastic composite during cooling from forming temperatures. Journal of Composite Materials, 31(22): 2230-2248, 1997.
122. Callister, W.D.J., Materials Science and Engineering - An Introduction. 3rd ed. 1994: John Wiley & Sons, Inc. 811 pages.
123. Wang, C., Sun, C.T., Experimental characterization of constitutive models for PEEK thermoplastic composite at heating stage during forming. Journal of Composite Materials, 31(15): 1480-1506, 1997.
124. Lee, K., Weitsman, Y., Optimal cool down in nonlinear thermoviscoelasticity with application to graphite/PEEK (APC-2) laminates. Journal of Applied Mechanics (Transactions of the ASME), 61(2): 367-374, 1994.
125. Struik, L., Physical Ageing in amorphous polymers and other materials. 1st ed. 1978, Amsterdam: Elsevier Scientific Publishing Company. 230? pages.
126. Zhang, Y., Xia, Z., Ellyin, F., Evolution and influence of residual stresses/strains of fiber reinforced laminates. Composites Science and Technology, 64(10-11): 1613-1621, 2004.
127. Brinson, L.C., Gates, T.S., Effects of Physical Aging on Long-Term Creep of Polymers and Polymer Matrix Composites. International Journal of Solids and Structures, 32(6-7): 827-846, 1995.
128. Roy, S., Computer models for predicting durability, in Reinforced Plastics Durability, Pritchard, G., Editor. 1999, Woodhead Publishing Limited: Cambridge, England. p.352-354.
129. Meijer, H.E.H., Govaert, L.E., Multi-scale analysis of mechanical properties of amorphous polymer systems. Macromolecular Chemistry And Physics, 204(2): 274-288, 2003.
130. Tounsi, A., Bedia, E.A.A., Benachour, A., Stresses during moisture desorption in laminated composite plates with different degrees of anisotropy. Journal of Thermoplastic Composite Materials, 18(1): 37-58, 2005.
131. Akshantala, N.V., Brinson, L.C., A damage evolution model for viscoelastic composite laminates. Journal of Composites Technology & Research, 23(1): 3-14, 2001.
132. Karami, G., Garnich, A., Micromechanical study of thermoelastic behavior of composites with periodic fiber waviness. Composites Part B-Engineering, 36: 241-248, 2005.
133. Liggat, J.J., Pritchard, G., Pethrick, R.A., Temperature - its effects on the durability of reinforced plastics: Physical mechanisms, in Reinforced plastics durability, Pritchard, G., Editor. 1999, Woodhead Publishing Ltd.: Cambridge, England. p.115-125.
134. Nairn, J.A., Transverse Fracture in Unidirectional Graphite Polysulfone Composites. Journal of Composite Materials, 21(9): 798-808, 1987.
135. Parlevliet, P.P., Bersee, H.E.N. Effects of Impact Modifiers on Mechanical and Microcracking Properties of PPS Composites. in 25th Jubilee International SAMPE Europe Conference 2004. 2004. Paris EXPO, Porte de Versailles, Paris, France: SAMPE.
136. Nairn, J.A., Matrix microcracking in composites, in Polymer Matrix Composites, Talreja, R. and Manson, J.A., Editors. 2001, Elsevier Science Ltd.: Oxford. p.403-432.
137. Nairn, J.A., Hu, S., Matrix Microcracking, in Damage Mechanics of Composite Materials, Talreja, R., Editor. 1994, Elsevier Science B.V.: Amsterdam. p.187-243.
138. Parvizi, A., Garret, K.W., Bailey, J.E., Constrained Cracking in glass fibre reinforced epoxy cross-ply laminates. Journal of Materials Science, 13: 195-201, 1978.
139. Nairn, J.A., Fracture Mechanics of Composites with Residual Thermal Stresses. Journal of applied Mechanics - Transactions of the ASME, 64: 804-815, 1997.
140. Hashin, Z., Thermal-Expansion Coefficients of Cracked Laminates. Composites Science and Technology, 31(4): 247-260, 1988.
141. Baschek, G., Hartwig, G., Parameters influencing the thermal expansion of polymers and fibre composites. Cryogenics, 38(1): 99-103, 1998.
142. Unger, W.J., Hansen, J.S., Ko, H.Y.S., Method of Reducing Residual Stresses in Thermoplastic Laminates. 1993: USA; European patent.

143. Hyer, M.W., Some observations on the cured shape of thin unsymmetric laminates. Journal of Composite Materials, 15: 175-194, 1981.
144. Hsiao, S.W., Kikuchi, N., Numerical analysis of deep drawing process for thermoplastic composite laminates. Journal of Engineering Materials and Technology-Transactions of the Asme, 119(3): 314-318, 1997.
145. Spencer, A.J.M., Watson, P., Rogers, T.G., Mathematical Analysis of the Springback Effect in Laminated Thermoplastic Channel Sections. Composites Manufacturing, 2: 253-258, 1991.
146. Hsiao, S.W., Kikuchi, N., Numerical analysis and optimal design of composite thermoforming process. Computer Methods in Applied Mechanics and Engineering, 177(1-2): 1-34, 1999.
147. Harris, B., Transverse-Ply Cracking and Toughness of Practical Reinforced Plastic Laminates, in Engineering Composite Materials, Harris, B., Editor. 1999, IOM Communications: London. p.179-187.
148. Khatri, S.C., Koczak, M.J., Thick-section AS4-graphite/E-glass/PPS hybrid composites .1. Tensile behavior. Composites Science and Technology, 56(2): 181-192, 1996.
149. White, S.R., Processing-Induced Residual Stresses in Composites, in Processing of Composites, Dave, R. and Loos, A.C., Editors. 2000, Hanser Publishers: Munich. p.239-271.
150. Hiemstra, D.L., Sottos, N.R., Thermally-Induced Interfacial Microcracking in Polymer Matrix Composites. Journal of Composite Materials, 27(10): 1030-1051, 1993.
151. Vlasveld, D.P.N., Bersee, H.E.N., Picken, S.J., Nanocomposite matrix for increased fibre composite strength. Polymer, 46(23): 10269-10278, 2005.
152. Hine, P., Broome, V., Ward, I., The incorporation of carbon nanofibres to enhance the properties of self reinforced, single polymer composites. Polymer, 46(24): 10936-10944, 2005.
153. Hsu, S.L.C., Lin, C.Y., Chuang, S.W., Positive-working aqueous base developable photosensitive polybenzoxazole precursor/organoclay nanocomposites. Journal Of Applied Polymer Science, 97(6): 2350-2356, 2005.
154. Yoon, P.J., Fornes, T.D., Paul, D.R., Thermal expansion behavior of nylon 6 nanocomposites. Polymer, 43(25): 6727-6741, 2002.
155. Boogh, L., Mezzenga, R., Processing Principles for Thermoset composites, in Polymer Matrix Composites, Talreja, R. and Manson, J.A., Editors. 2001, Elsevier Science Ltd.: Oxford. p.27.
156. Potter, K.D., Weaver, P.M., A concept for the generation of out-of-plane distortion from tailored FRP laminates. Composites Part a-Applied Science and Manufacturing, 35(12): 1353-1361, 2004.
157. Gigliotti, M., Jacquemin, F., Vautrin, A., On the maximum curvatures of 0/90 plates under thermal stress. Composite Structures, 68(2): 177-184, 2005.
158. Hufenbach, W., Gude, M., Analysis and optimisation of multistable composites under residual stresses. Composite Structures, 55(3): 319-327, 2002.

Chapter 3: Experimental Techniques for Residual Strain Determination – an Overview of the Literature

3.1 Introduction

In Chapter 2 the material parameters governing the residual strain state in composites were identified. This chapter continues with a literature survey on experimental techniques to determine the magnitude of these parameters and the resulting residual strains. The purpose of this exercise is to identify techniques that can be used to reach the goal of this thesis as described in the Introduction of this thesis.

Many experimental techniques for residual strain determination in polymer matrix composites have been developed in the past [1-3], mostly based on methods applicable to metallic structures. A good summary of these methods was given by Kesavan *et al* [4], where the experimental techniques were categorised in two classes: destructive techniques and non-destructive techniques [4, 5].

New developments in the field of experimental residual strain determination for polymer-matrix composites provide the basis for this chapter, as an up-to-date summary of the available experimental techniques is currently not available. Moreover, LCM processing of thermoplastic composites may bring about different mechanisms of residual strain formation [6], such as crystallisation shrinkage in semi-crystalline thermoplastics additional to polymerisation shrinkage. This may lead to certain requirements for the experimental techniques, such as applicability to non-transparent matrix composites.

First, the experimental techniques using the intrinsic composite constituents' properties will be described, followed by techniques employing embedded (foreign) strain sensors. Techniques based on in-plane and out-of-plane deformations will be discussed, including a small section on determination of the relaxation behaviour, and another section is dedicated to destructive techniques. A short description of the techniques used to determine values for the material properties governing residual strain formation that are needed for estimation of residual stresses, concludes this chapter.

3.2 Techniques based on intrinsic material properties

Some material properties change when the material is exposed to strains or stresses, such as the electrical resistance in the metal wiring of a strain gauge. This section will describe the experimental techniques that detect the change in material properties due to residual strains in one of the composites' constituents. These include the change in refraction of light,

change in Raman peak position of the crystalline phase and the change in electrical conductivity. The applications thus far comprise only micromechanical and interlaminar residual stresses.

3.2.1 Photo-elasticity

Nairn and Zoller [9, 10] were (to the best of the authors' knowledge) in 1985 the first to publish an experimental study on thermal residual stresses in continuous fibre reinforced thermoplastics. They measured the stresses in the polysulfone matrix in a unidirectional (UD) graphite fibre tape by means of photo-elasticity. Photo-elasticity is a classical optical technique for static stress analysis, where a sample is rotated between crossed polarisers. For determination of stress fields in composites, a transparent or translucent matrix is required. Therefore, this method was applied to transparent thermoset matrix composites [11-16] and amorphous thermoplastic matrices [9, 17]. Strain alters the molecular orientation distribution, which affects the polarisation state of the light (photo-elasticity) [17], or in other words, strain results in anisotropic scattering of light and intensity measurements provide information on orientation. For determination of the magnitude of residual stresses, measurement of retardation (phase difference between two light vectors travelling at different velocities) is required, from which the residual stress components can be calculated by means of the Stress-Optic Law (or "Brewster's Law") [9, 18, 19].
In UD composites, maximum extinctions are found at 0° and 90° with respect to the direction of the fibres, meaning that the principal stress directions are parallel and perpendicular to the fibre direction. One drawback of this method is that thin composite layers with low fibre volume fractions (i.e. < 40Vol%) are required, to observe any effects in the matrix. To see the residual stress patterns in both matrix and reinforcing phase (usually glass fibres due to their transparency) in the cross-section of UD composites with a higher fibre volume fraction, a thin slice of the cross-section can be cut and examined [13].

3.2.2 Micro-Raman Spectroscopy

Another technique for residual strain determination based on an intrinsic material property is Micro (Laser) Raman Spectroscopy (MRS) [20-24]. This technique is based on the strain sensitivity of Raman vibrational modes of crystalline phases [25]. The difference in energy between the incident photon and the Raman scattered photon is equal to the energy of vibration of the scattering molecule. A plot of intensity of scattered light versus energy difference is a Raman spectrum [26]. Raman Spectroscopy is an established technique for measuring the state of strain in carbon fibres embedded in a translucent polymer matrix, since certain peak positions in the Raman spectrum of the fibre change with applied strain. The Raman peaks of the fibre in -for example- an unloaded PEEK prepreg shows a shift to

higher peak positions, which represents a compressive thermal residual strain imposed by the surrounding matrix, see Figure 3.1. First, a calibration curve on pure single fibres in air needs to be established to relate the Raman peak position to the magnitude of fibre strain within the composite. The composite types that were investigated are micro-composites[1] [23, 27, 28], single UD prepreg layers (PEEK) with common fibre volume fractions (60% or higher) [20, 22, 24] and more-ply UD composites [20]. A major advantage of the Micro (Laser) Raman Spectroscopy method is that residual strains can be directly measured in steps as small as 1-2 μm, and there is no need to resort to analytical models to calculate the macroscopic residual stresses of a laminate [21]. It must be made sure however, that the contribution of the matrix peaks is taken into account, otherwise this would yield a too high value for residual stresses in the fibre [29]. In addition, it must be noted that the Raman spectra are taken from the laminate or fibre surfaces only. To overcome this problem, remote laser Raman spectroscopy was developed [29]. This incorporates an optic fibre embedded in the bulk of the composite, through which the excited laser light is transported.

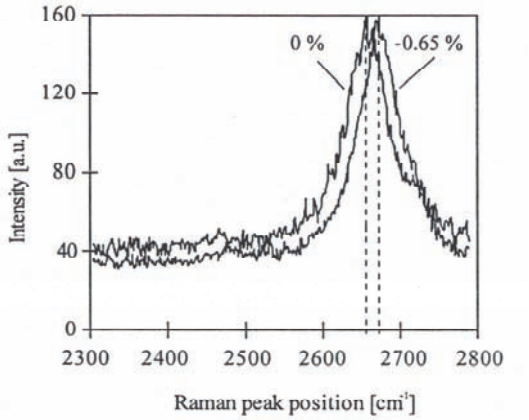

Figure 3.1: Compressive strain-induced shift of 2660 cm^{-1} Raman peak in AS4 carbon fibre embedded in a PEEK matrix [27].

Certain amorphous fibres, such as glass, have a very weak Raman response and can therefore not readily be used as intrinsic strain sensors [25]. Therefore, a small amount of aramid fibres, which due to their crystallinity exhibit a very strong Raman response, can be embedded in glass fibre reinforced laminates to act as strain Raman sensors [25, 29, 30]. This also enables the use of the Raman spectroscopy method to determine interlaminar stresses in cross-ply laminates [25, 30]. This requires a transparent composite, to enable the detection of strain fields in the aramid fibres at certain depths in the laminate. Nielsen & Pyrz

[1] Micro-composites are samples of polymer with one single fibre in it.

[17, 28] successfully combined the MRS and photo-elasticity methods, to determine the local strain state in amorphous polymers around an embedded fibre. Moreover, it was shown that by measuring the fibre strain, the residual fibre-matrix interfacial shear strain could be determined [21].

3.2.3 Electrical conductivity of carbon fibre reinforcement

In carbon fibre (CF) reinforced composites the electrical properties of the composite, such as electrical resistance, are affected by strain, damage and temperature [31]. The electrical resistance can therefore be monitored to indicate variations in these properties, without the need to embed 'foreign' sensors, which increase the cost and may weaken the structure. This gives the possibility to determine differences in the interlaminar residual stresses by means of electrical resistivity measurements of (cross-ply) laminates [31-35]. For example, it was found that upon curing of thermoset matrix composites with higher pressures the electrical conductivity barrier, measured as the activation energy, increased [34]. This was attributed to increased residual interlaminar stress, because of a higher fibre volume fraction achieved by the higher processing pressure. Due to these stresses, the quality of the interlaminar interface in angle-ply laminates is reduced [31]. Insufficient bonding between the plies results in a higher electrical resistance during cooling [33]. In order to quantify the residual stresses by means of this method, further development of this technique is needed.

3.3 Residual strain determination with extrinsic embedded strain sensors

Another method to follow strain build-up during processing is to embed strain sensors in the composite. One example was already described: embedded aramid fibres as Raman strain sensors in glass fibre reinforced composites. The sensors can be of any material or shape and currently used sensors are:

1. Strain gauges;
2. Fibre optic sensors (FOS); and
3. Embedded metallic particles in combination with X-ray diffraction.

These sensors show a measurable change in properties when exposed to (residual) strains, provided there is sufficient mechanical interaction between the composite and the sensors. Strain gauges as well as optic sensors have been applied to study interlaminar strains in angle-ply laminates as well as micromechanical strains in unidirectional laminates [36]. The metallic particles were inserted only in the resin-rich areas in between the plies; hence interlaminar strains were detected.

3.3.1 Embedded strain gauges

Unger and Hansen [37] employed strain gauges to directly measure residual strain development resulting from both thermal and crystallisation effects in unidirectional CF/PEEK laminates. A strain gauge was melt-embedded in the centre of the surface plies during a short melt time, because no strain gauges exist that can resist the high processing temperatures very well [38]. In thermoset composites, embedded strain gauges were shown to provide accurate measurements of residual strain build-up during the cure cycle, including the tool effect [36, 39-41].

3.3.2 Embedded fibre optic sensors

Recent developments show that fibre optical sensors (FOSs) can be applied as internal 'strain gauges' to follow the development of residual strains inside a composite laminate, even during processing at the high temperatures needed for thermoplastic composites [42, 43]. Applications were found in unidirectional laminates as well as in angle-ply laminates. A number of different fibre optic sensors exist [44], of which the Fibre Bragg Grating (FBG) and Extrinsic Fabry-Perot Interferometric (EFPI) sensors were most often applied for detection of residual strain formation in composites. The working principle of both sensors is well explained by Zhou and Sim [44]. An EFPI sensor measures strain through a change in cavity length, which is related to a phase change between the input and output signals, and the reflection of the optical fibre [44], see Figure 3.2. Residual strain development during curing of thermoset laminates was successfully monitored using EFPI sensors [36, 45-47] and a hybrid FBG/EFPI sensor [48, 49]. EFPI optical fibres were found not to measure any strain until the matrix was solidified [36]. Disadvantages are that with the EFPI sensor a cavity (and correspondingly a weakness) is included in the laminate and the diameter of the sensor is quite large, through which stress concentrations may arise. In addition, the EFPI sensor showed being prone to failure due to residual stresses alone [50].

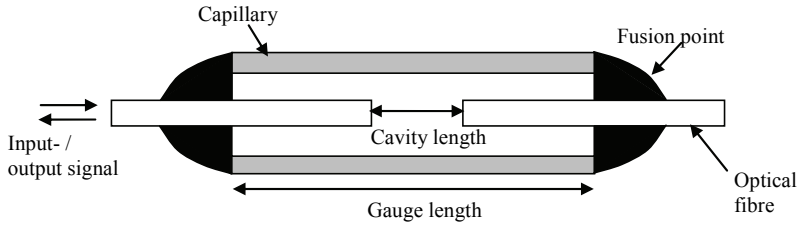

Figure 3.2: Schematic view of EFPI sensor, after [48, 49].

The latest publications on residual strain monitoring during processing of composites by means of embedded fibre optic sensors, show a clear trend in favour of the FBG sensors due

to their small diameter and accuracy [42, 51-56]. The working principle of a Bragg grating within an optical fibre is schematically explained in Figure 3.3.

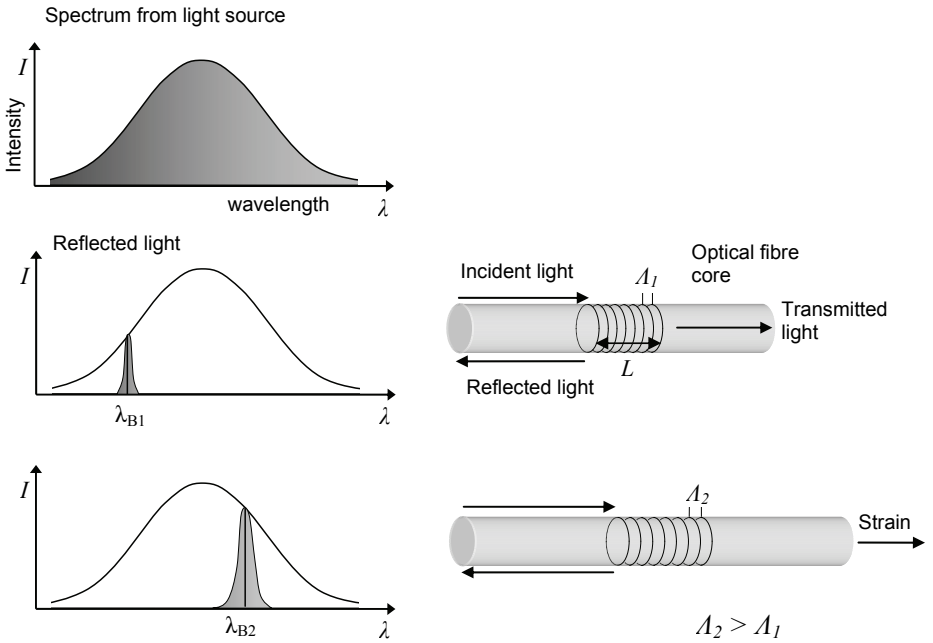

Figure 3.3: Schematic view of working principle of a fibre Bragg grating in an optic fibre, after [57, 58].

When broadband light with a wide range of wavelengths travels through the optic fibre core containing a Bragg grating (viz. a “periodic modulation of the refractive index” [59]), a narrow band of wavelengths is reflected (λ_{ref}), while the others pass through the grating (λ_{trans}). The central wavelength of the reflected light is called the Bragg wavelength λ_B. This is shown in Figure 3.4.

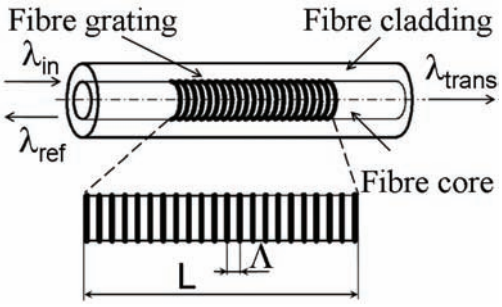

Figure 3.4: Bragg grating detail, from [58].

The strain[2] sensing effect of the grating is based on the change in spacing Λ, which is affected by strain as well as temperature variations. The parameter that is actually measured is a change in Bragg wavelength λ_B and this is related to the spacing Λ with the Bragg relation, where n_{eff} is an averaged refractive index over the length L of the grating [57]:

$$\lambda_B = 2n_{eff}\Lambda \tag{3-1}$$

Assuming that the refractive index n_{eff} does not vary with strain, a difference in Bragg wavelength $\Delta\lambda$ varies linearly with the imposed strain according to relations based on the photo-elastic constants and effective refractive index of the optic fibre [55, 58, 60, 61]. Hence, differences in Bragg wavelength before and after embedding in a composite laminate can directly be related to, for example, residual strains.
It can occur that the reflection spectra of the optical sensors split into two peaks due to non-axisymmetric residual stresses in the composite [42, 55, 62, 63]; hence polarisation effects and strain differences throughout the length of the specimen can be detected, see Figure 3.5.

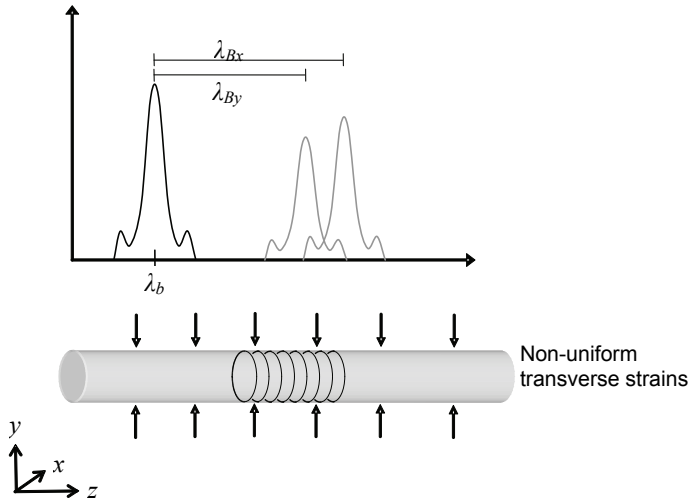

Figure 3.5. Non-symmetric Bragg reflection, after [42].

Advantages of employing fibre Bragg gratings as sensors in composites are [44]:

- Fibre optic sensors are robust passive components resulting in a long life-span (> 25 years).

[2] Here, strain is defined in the axial direction, i.e. in the length-direction of the optic fibre.

- The fibre Bragg grating forms an intrinsic part of the optical fibre, with very small dimensions when compared to other types of sensors (thermocouples or strain gauges), which renders it very suitable for embedding in composite products.
- The sensors are minimally disruptive when embedded parallel to the reinforcing fibres (provided that the thickness of the ply in that direction matches the diameter of the optical fibre) and generally causes no degradation of macroscopic properties. When a FOS is embedded perpendicular to the fibre direction however, an eye-shaped defect is the result, which causes a severe stress concentration and decreases the mechanical properties [64].
- One optic fibre can contain many gratings ('multiplexing'), which gives the possibility of measuring at multiple locations with one optical fibre and connection [65]. An array of sensors can be embedded inside a laminate and give information on the residual strain distribution throughout the laminate [43] on a macro-mechanical as well as a global level.
- The strain resolution is higher than 1 $\mu\varepsilon$ [44], while the wavelength accuracy is ~10 pm (or 1%). This is without any fibre coating, but it also depends on humidity and temperature variations.
- The gratings are not sensitive to electromagnetic interference [66].
- They are relatively insensitive to fatigue and corrosion [58].

Some disadvantages are:

- Fibre optic technology is still relatively high-tech and therefore expensive, although the costs have dropped significantly over the past few years.
- The choice of fibre coating materials is limited when the optic fibre is embedded in high-performance thermoplastic composites, because of the high temperatures and pressures during manufacturing. For every composite system and optic fibre, the strain transfer must be ideal. When this is not possible, it is best to remove the coating at the location of the sensor to ensure proper strain transfer, but this leaves the optic fibre even more fragile [67].
- Because the optic fibres are made of glass and therefore are brittle, great caution must be expressed when handling the optic fibres, especially during embedding in composites (prevent sudden movements).

3.3.3 Embedded metallic particles

Another 'embedded-sensor' technique employs X-ray diffraction analysis of metallic particles that are embedded in the matrix (also named 'tracers' [68]) to detect their deformation imposed by residual strains in the polymer matrix [69-72]. Embedded aluminium [73-75], copper [76] and silver [71, 72, 75] particles show a deflection in peak angle when embedded

in a composite. Using Bragg's Law, this deflection is related to a change in crystal lattice spacing induced by the residual strain [75]. The measured strain can be related to the residual stress in the polymer matrix via a 'stress transmission tensor' [72] or using Hooke's law [75]. Regular shaped aluminium particles gave the highest accuracy [75]. The metal needs to be selected with care, since it should not yield when exposed to the residual strains of the composite [1]. This type of experiment was mainly performed on thermoset matrix materials, because thermosets do not have a crystalline structure that changes the X-rays' response when strained and therefore require crystalline fillers. In semi-crystalline thermoplastics however, the lattice spacing between the crystals and the change therein due to straining, can be followed by means of X-ray diffraction. This was shown to be possible for polyetherketone (PEK) reinforced with carbon and glass fillers [76], but this technique was not yet tested for continuous fibre reinforced thermoplastics. An overview of the application of this technique to polymers and their composites was given by Hauk [76]. The main disadvantage of this technique is that it either gives information on the surface properties of the sample only, or requires a thin specimen (0.3 - 0.5 mm) to measure through the thickness [77]. This disadvantage applies also to another technique based on embedded particles, namely the piezo-spectroscopy technique, which employs embedded fluorescent alumina fillers as a macroscopic stress sensor [78].

3.4 Experimental techniques based on in-plane and out-of-plane deformations

One technique based on in-plane deformations was presented by Reid *et al* [79], where the longitudinal expansion of unidirectional glass fibre composites was determined with a non-contact dilatometer as a function of temperature. By comparing this with the free expansion of glass fibres, the residual strain with temperature could be established for the glass fibres. Methods based on interferometry and warpage are more commonly used and are discussed below.

3.4.1 Interferometry based methods

A number of methods exist that utilise the phenomenon of interference of light waves reflecting from a sample. This interference causes a visual fringe pattern that can be used to determine deformations. For example, Moiré interferometry can be used to monitor both in plane and out-of-plane-displacements [80]. For in-plane measurements, a grating needs to be applied to the surface of the sample, while for out-of-plane displacements the grating can be projected onto the surface at an angle to the viewing direction (shadow moiré technique) [81].

A method named the Cure Reference Method (CRM) was developed to determine the strain development in thermoset composites with Moiré interferometry [2, 82, 83]. It is an accurate non-contact full-field laser based method to monitor in-plane displacements on the surface of a symmetric laminate during cooling [81]. From the displacements the residual stresses can be calculated using lamination theory [2]. The grating is applied during consolidation and acts as a reference to the stress-free condition prior to reaching the stress-free temperature. This technique possesses high displacement and strain sensitivity, high spatial resolution (in the order of 0.5 μm) and a high signal-to-noise ratio. However, it only gives information of the residual strain state on the surface and an interference image needs to be captured when no strains are present, which may prove to be difficult for thermoplastic composites and closed moulds. Even though other interferometry-based methods are currently investigated for characterisation of composite mechanical properties [84], thus far few studies have been published that utilise methods as shearography, speckle pattern interferometry [85] and holographic interferometry to study residual stress formation in composites [86].

3.4.2 Warpage of non-symmetrical laminates

A common manifestation of residual stresses is 'warpage' of laminates with unsymmetrical lay-up (see also Figure 2.2). Therefore, the simplest means that can be used to assess the magnitude of interlaminar residual stresses is the use of unsymmetrical cross-ply or angle-ply laminates [8], because the residual stresses are partially relieved by out-of-plane deformations [87]. Nairn and Zoller [88] were the first to apply this technique to thermoplastic composites, to study the build-up of residual stresses in amorphous and semi-crystalline matrix composites. This showed that the method is applicable to composites with any matrix. The out-of-plane deformations (curvatures) of a laminate can be determined during or after cooling from the processing temperature. The higher the curvature for a certain unsymmetrical laminate with a certain thickness, the higher the residual stresses are in a corresponding symmetrical laminate [88, 89]. At a certain temperature the interlaminar residual stress, σ_{22}, that would exist perpendicular to the fibres in a corresponding symmetrical cross-ply laminate, can be calculated from the curvature using equation (3-2) based on linear lamination theory:

$$\sigma_{22} = \frac{\left(E_{11} \times E_{22}\right)}{\left(E_{11} + E_{22}\right)} \cdot \frac{t}{\rho} \cdot \left(\frac{1}{2} + \frac{1}{24} \left(2 + \frac{E_{11}}{E_{12}} + \frac{E_{22}}{E_{21}} \right) \right) \tag{3-2}$$

where t is the thickness and ρ is the radius of curvature, E_{11} and E_{22} are the moduli of the ply in the longitudinal and transverse direction, respectively. The dimensionless curvature t/ρ

defined as the thickness *t* divided by the radius *ρ* is often used, because it directly relates to the amount of differential thermal shrinkage that can induce residual stresses. This eliminates the effects of thickness variation from specimen to specimen [88, 90, 91]. The thicknesses of the longitudinal and transverse plies need to be equal [38]. If this is not the case, the following equation [87, 89, 92, 93] can be used:

$$\sigma_{22} = \frac{(E_{11} \times E_{22})h}{(E_{11}h + E_{22}k)} \cdot \left(\frac{b+d}{2\rho} + \frac{E_{11}b^3 + E_{22}d^3}{6\rho(b+d)} \left(\frac{1}{E_{11}b} + \frac{1}{E_{22}d} \right) \right) \tag{3-3}$$

Where the thickness of the longitudinal and transverse plies in the unsymmetrical laminate are *b* and *d*, respectively and *h* and *k* are the corresponding thickness in the symmetrical lay-up. As a first approximation, instead of using the above equation, the maximum residual stress can be calculated from the cross-ply curvature using a linear elastic relation [94]:

$$\sigma_{max} = E \cdot \kappa \cdot t / 2 \tag{3-4}$$

where σ_{max} represents the maximum stress at the surface; *E* the modulus of the composite in the direction of measurement (90°), and *κ* the curvature equal to ρ^{-1}.
Another approach is to compare the obtained curvatures with curvature predictions based on the classical lamination theory (CLT) [3, 38, 87, 90, 95-100]. When the theory can accurately predict the curvatures, it may be assumed that the calculated residual stresses are also accurate and that correct thermo-elastic properties were used [38, 96]. These properties include the composite stiffness characteristics, thermal expansion coefficients and the difference between the service temperature and the temperature at which residual stresses start to build-up (stress-free temperature) [96]. The curvature can also be predicted by using a similar model as equations (3-2) and (3-3) [89], where ΔT represents the temperature difference between the stress-free temperature and the service temperature, and the coefficients of thermal expansion in the longitudinal and transverse fibre directions are α_{11} and α_{22}, respectively:

$$(\alpha_{22} - \alpha_{11})\Delta T = \frac{b+d}{2\rho} + \frac{E_{11}b^3 + E_{22}d^3}{6\rho(b+d)} \left(\frac{1}{E_{11}b} + \frac{1}{E_{22}d} \right) \tag{3-5}$$

It was shown that only few dimensions follow the predictions by CLT, and it was concluded that the thickness-to-length ratio and the width-to-length ratio determine the final room temperature shape of the laminate [38, 87, 95, 97, 99]. Instead of forming saddle shapes as

predicted by CLT, it was shown [95] that thin non-symmetric laminates form into a part of a cylinder upon curing. Especially if one dimension of the curved panel dominates [38, 90, 95, 96, 98], such as in a strip, only one curvature can be conveniently measured.
One drawback of the curvature method is that values of curvature may show large variations for equal laminates under similar conditions. This can be explained by a multitude of reasons, such as the limits in the precision of curvature measurement, but also fibre alignment, disorientation of the plies or non-symmetry of ply thickness [96, 101]. In addition, it does not provide any information regarding the spatial variation of residual stresses at the micromechanical level resulting from varying fibre distributions, variable thermal contraction, transcrystallinity, etc. [21].

Measurement of out-of-plane deformations
Curvature measurements can be performed in several ways, with the most common technique being cutting of the laminate in thin strips, and measuring the deflection in the centre of the specimen *h* and the chord length of the specimen *L*, see Figure 3.6 [8, 36, 87, 88, 90, 91, 96, 102-104]. The radius ρ and curvature $\kappa = \rho^{-1}$ [105] can then be calculated with:

$$\rho = \frac{L^2}{8h} + \frac{h}{2} \qquad (3\text{-}6), \qquad \kappa = \frac{8h}{L^2 + 4h^2} \qquad (3\text{-}7)$$

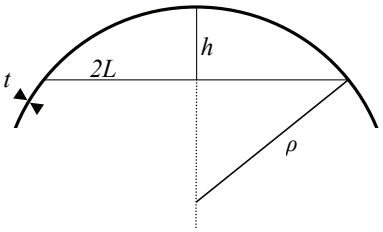

Figure 3.6: Measurement of radius of curvature, after [87].

The deflection of the strip was measured using a travelling microscope [8, 87, 88], measuring microscope [105], a cathetometer [104], or with a dial micrometer fixed between two pins [90]. The chord length was measured with a (steel) ruler [88]. Alternatively, it is possible to perform curvature measurements from digital scans or curvature tracings on a sheet of paper [106], as well as from photographs [91, 107] taken of the side of the deformed laminate. Determination of the shape of the whole composite laminate was also performed [95, 108] by measuring the out-of-plane displacement in the *x*- and *y*-directions with a dial gauge [81, 95], LVDT [3, 107], or with a non-contact technique to prevent deflection of the thin laminates [3].

For angle-ply laminates, Hyer [95] used the circle of Mohr for determination of the principal curvatures. It was observed [108] that the laminates were not perfectly cylindrical, because they showed some free-edge effects. In addition, it must be made sure that no anomalies, such as fibre flow or ridges are present in the laminates, hence curvature measurements were performed after sides were trimmed [91, 107].
Some investigators studied out-of-plane deflections with methods based on interferometry [18, 81, 109], one of which was the shadow moiré technique [81]. Comparison with the results obtained with the dial gauge showed excellent agreement between the techniques. In addition, time dependent warpage was measured using an ultrasonic contour scan technique [110]. One other method that can be used to determine the curvature of the cylinder is stereo-reconstruction based on square grid analysis as developed in-house at Delft University of Technology by Niño *et al* [107, 111, 112]. This method employs two photographs from different angles of the three-dimensional specimens, which have been prepared by applying a grid on the surface. In the photographs, a reference item (the target, such as a cube with a grid of known dimensions) is included. During analysis, the target is used to define a coordinate system and to calibrate the photographs for the dimensions. Then, the grid points on the sample are identified and computer analysis of the photographs results in the coordinates of the grid points, from which the curvatures can be determined. The curvatures obtained with this method were compared with those from the strip curvature method and a probe tip (measuring the height z on a x-y table) following the same grid lines. The strip curvature method was found to show most scatter, whereas the square grid analysis and the probe tip method showed similar accuracy, with the square grid method being the most user-friendly method.

Relaxation experiments
As explained in Chapter 2, residual stresses in thermoplastic composites can relax with time and temperature due to the visco-elastic behaviour of the matrix [38, 87, 91, 101, 113-119]. One method to determine the relaxation behaviour is to follow the curvature of unsymmetrical laminates [8]. At room temperature, a decrease of curvature with time due to relaxation of residual stresses was reported [9, 38, 117], although initially curved laminates do not completely turn flat due to relaxation. The reason is that no driving force in the deformed laminates exists to become flat, because part of the residual stresses are relieved by the curvature itself due to the absence of a constraint [8, 87, 91]. However, when curved specimens are clamped or restrained flat, the relaxation behaviour can be determined by periodically removing each specimen and measurement of the curvature [8, 87, 91, 117]. The stress relaxation in clamped off-axis unidirectional laminates at high temperatures was followed by recording the load change in the tensile test set-up [120].

3.5 Residual strain determination by means of destructive testing

Early-developed experimental techniques are mainly based on destructive evaluation of residual strains in composites. These techniques include first-ply failure and curvature methods for the interlaminar strains, and strain-relaxation based techniques (layer removal, etc.) for determination of global or skin-core residual strains.

3.5.1 First ply failure

Thermal contraction in a symmetrical cross-ply laminate creates a state of residual tensile stresses in the transverse 90° plies. When subsequently loading the laminate in the transverse direction the tensile strength of the laminate, $\sigma^{t}_{0/90}$ (where superscript *t* denotes the transverse direction), is measured to be lower as for transverse tensile strengths of unidirectional laminates, $\sigma^{t}_{0/0}$. This tensile strength can be recorded at the first audible crack (often determined by acoustic emission), hence the term first ply failure. The difference between these values provides an estimate for the interlaminar residual stress via: $\sigma_R = \sigma^{t}_{0/0} - \sigma^{t}_{0/90}$ [38, 87, 121]. It was remarked that crack suppression must be eliminated and for that reason the 90° plies should be positioned on the outside surfaces [38].

3.5.2 Relaxation based techniques

Thus far, techniques were discussed that are used to determine micromechanical and interlaminar residual strains and these techniques mostly relied on non-destructive evaluation. Disadvantages of the frequently used curvature method are that no information regarding (global) strain distribution through-the-thickness in the laminate can be obtained, nor on symmetrical laminates since they are flat [122]. Techniques to determine the residual strain distribution through the thickness are mostly based on destructive techniques that depend on releasing internal stresses by removing material. This causes deformations in the specimen, which can be measured and compared to the state before removal. Creation of additional free surface in the composite, i.e. damaging the composite, relaxes the residual stresses [123] and if this happens in a controlled manner and the released strains are measured, it is possible to calculate the residual stresses that were originally present in the laminate. These methods were also used to determine the interlaminar stresses [38, 87]. Techniques for determination of residual stress by relaxation include: layer removal of symmetric laminates, blind-hole drilling and grooving. The application of these relaxation based techniques is not restricted to continuous fibre reinforced polymers only, also in metals, unfilled polymers and in concrete they have proven their use [124, 125].

Layer removal of symmetrical laminates

A variation on the curvature technique as described in Section 3.4.2, is to obtain unsymmetrical laminates by removing one or more layers from a balanced (flat) laminate. The released strains can be detected by strain gauges and the resulting deformations monitored by for example Moiré interferometry [126]. Combined, these parameters can be used to calculate the residual stresses in the laminate before layer removal [127], often with CLT. Layer removal was usually accomplished by abrasion/ milling to remove the successive outer layers of the laminate [38, 87, 105]. This method proved not to be very accurate, because it is sensitive to heat generation and initiation of microcracking due to abrading, both of which may release the internal stresses under investigation [87, 105]. In addition, any irregularity in layer thickness due to abrasion will affect the resulting curvatures [38]. Another drawback is that the abrading technique eliminates any further structural and/or property evaluations to be performed. A method was proposed based on minimum energy potential [3, 97], which excluded the need for measuring the released strains for calculation of the residual stresses. In addition, refinements were proposed to take into account extension-bending coupling and variation of mechanical properties through the thickness of the angle-ply laminate.

To prevent damaging of the composite as in layer removal by abrasion, the concept of the Process Simulated Laminate (PSL) was described [105]. The PSL consists of several composite plies separated by thin release plies, such as polyimide foils. The composite plies between two separation films form a Constitutive Laminate (CL), and these CL's can be separated after processing and analysed. The analysis can be carried out in two ways:

- The constitutive laminate deformation technique, where the residual stress distribution is determined by measuring the dimensional changes (curvature) of the PSL and CL's before and after separation.
- The PSL-strain gauge technique, where after processing strain gages are applied on one laminate surface to monitor the strain changes during removal of the constitutive laminates from the other side of the laminate.

These two methods were compared with the layer abrasion method and the measured stress profiles were almost identical, with the PSL-strain gauge technique providing most accuracy. It was successfully applied to determine the residual stress distribution in unidirectional CF/PEEK laminates subjected to various cooling rates and annealing times [128] as well as for thermoset composites [129, 130]. It was shown [94] that the PSL technique did not influence the morphology (crystallinity) or transport processes in a CF/PEEK laminate. The separation film is the critical constituent in the PSL technique, because the film must enable 'perfect' adhesion to the composite for load transfer and it must allow separation from the composite after the processing step. In addition, it must not interfere in any way with residual

stress formation, through for example crystallinity effects, initiation of additional forces by friction, etc.

Other stress relaxation based techniques

One of the more common residual stress determination techniques that depend on stress relaxation is the frequently used and widely accepted blind-hole drilling technique. It is suitable for all types of material and can be performed based on ASTM testing standard E837 [131]. In this approach, a strain gauge rosette is fixed to the material area of interest and a small hole is drilled through the material in the centre of the rosette. Hole dimensions and geometry change due to the release of stresses when material is removed. The resultant strain changes are recorded and processed in a (semi-empirical) model to deduce the stresses present prior to the hole drilling [85, 122]. One drawback is that the size of a standard strain gauge rosette is two to four times the hole diameter, making the region covered by the rosette too large compared to the released strain field [132]. Also, the eccentric hole drilling error (i.e. the error caused when the hole is not drilled exactly in the centre of the rosette) is a commonly recognised problem with this method [132]. The hole-drilling method was therefore also employed in combination with Moiré interferometry [133-136], holographic interferometry [109] and speckle pattern interferometry [137], as well as measurement of hole diameter deformation due to external loading in combination with finite element modelling [138]. Incremental hole-drilling can be utilised to study residual stresses in between adjacent plies [122, 139, 140], but optimal drilling and translation speeds need to be found.

Another stress relaxation based technique is known as the crack compliance method or Successive Grooving Technique (slot drilling) in which single or multiple slots (also called grooves or slits) are incrementally cut into a specimen [85, 123, 141, 142]. Deformations due to stress relaxation are recorded with strain gauges to determine the residual stresses through the thickness. These techniques are destructive, but do not require specific specimen preparation and it was stated that they offer a high degree of accuracy.

3.6 Experimental determination of material properties

For determination of residual stresses with the abovementioned experimental techniques, as well as for prediction of residual stresses, values for material properties are needed to carry out the necessary calculations. The following is a short outline of the experimental techniques that are commonly used to determine these values.

3.6.1 Micromechanical strains

For prediction of the magnitude of residual strains in a single fibre micro-composite or UD ply, the following parameters are required (provided that the fibre-matrix interaction is sufficient):

- The shrinkage of the matrix α_m and fibre α_f upon cooling,
- over the temperature difference ΔT between the stress-free temperature and the service temperature.
- For the calculation of residual stresses resulting from the strains, the elastic moduli of both constituents E_m and E_f at the service temperature are necessary.

For example, the residual stress in the fibre in the longitudinal direction σ^l_f at a certain temperature can then be calculated with Eq. (3-8) [69, 116]:

$$\sigma_f^l = E_f^l \left(\alpha_f^l - \alpha_m^l\right)\Delta T \tag{3-8}$$

The fibre properties, such as modulus and thermal contraction, are linear in the applicable temperature range for processing of polymers and can be obtained from any fibre material datasheet [1].

Matrix shrinkage

The shrinkage of semi-crystalline thermoplastic composites depends on the level of crystallinity and can be calculated with a rules-of-mixtures approach between the amorphous and 100% crystalline properties [88, 143]. The experimental work consists of measuring the crystallinity levels for various cooling rates with differential scanning calorimetry (DSC) or wide angle x-ray spectroscopy (WAXS) [37]. The thermal contraction α_m for polymers with known crystallinity levels needs to be measured for the entire temperature range between the stress-free and service temperature, since it is a temperature-dependent property. Techniques to measure this include (Dynamic) Thermal Mechanical Analysis (TMA) [8, 42, 101, 141, 144], use of strain gauges in conjunction with a controlled temperature chamber [145] or during processing [37], speckle pattern interferometry [146-148], or fibre optic sensors [149].

For reactive polymer matrices, determination of the shrinkage is usually based on volumetric measurements, due to the low viscosity. These can be easily transformed into linear data when necessary, see Appendix A. One experimental technique to determine the total amount of volumetric shrinkage (*a*-*d* in Figure 2.6) is by determination of the liquid resin mass *m* before curing at room temperature by weighing a pipette before and after filling with a fixed volume of resin [16, 150]. The density ρ of the polymer after curing can be determined with

the immersion method as described in ISO standard 1183-1:2004. With the assumption of constant mass, the volume after curing can be calculated ($V = m/\rho$) and compared to the original volume in the pipette.

Experimental techniques for the monitoring of volumetric changes during the entire polymerisation cycle are mainly based on volumetric dilatometry [151]. Two categories of dilatometry equipment exist: the capillary type and the plunger type. The capillary type measures the curing shrinkage by determination of the linear height change of a column of liquid (or gas), which is connected to a reservoir of the liquid surrounding the test substance [150]. This is also referred to as a pycnometer [151], which is usually a glass instrument for measuring the density of a liquid. In essence, this type of dilatometer is a pycnometer equipped with instruments to study density as a function of temperature or time. The system is described as method B in ISO standard 1183-1:2004, but the direct contact with the fluid (often toxic mercury) may influence the curing reaction.

The resin system can also be sealed in a silicone rubber bag; preventing the chemical reaction from being disturbed by another medium. A prerequisite is that the bag follows closely the changing contours of the polymer resin sample. The change of buoyancy due to the density increase of the polymer is determined in comparison with the constant density of the surrounding fluid [150]. This technique is similar to the technique currently used for determination of the density of composites and polymers by means of the immersion method of ISO 1183-1:2004 [152]. The exact procedure with the silicone bag is described by Li *et al* [150].

The plunger type uses something similar to a syringe to contain and pressurise the sample [153, 154]. The equipment can also be referred to as a PVT (pressure-volume-temperature) apparatus [153, 155, 156]. The displacement of the plunger corresponds to the volume change [150].

Another approach is where the resin is contained in a test-tube: as soon as the polymer starts to solidify, a known amount of silicon oil is injected in the test tube. Reading the oil level enables calculation of the polymer volume as a function of time [157]. A variation to this is provided by a set-up that was used for determination of the diffusion constant of a gas into a liquid polymer [157], that might be suitable for determination of the polymerisation shrinkage. This set-up consists of an airtight container in which the polymer cures. A capillary is inserted with a drop of silicon oil. The level of silicon oil may decrease due to the total volume change in the container caused by polymerisation of the polymer.

Thermal mechanical analysis (TMA) was also used for assessing the linear expansion and shrinkage behaviour. The curing polymer was contained between two plates and the (linear) dimensional changes were monitored using a LVDT. Through comparison of the heat flows obtained with differential scanning calorimetry (DSC), cure shrinkage induced by the cross-

linking reaction was validated [158]. This technique seems however unsuitable for low-viscosity resins.

These mentioned techniques do not provide information regarding the gel-point or vitrification point, nor the melt crystallisation point, meaning that always more than one experiment is necessary to establish the matrix shrinkage behaviour responsible for residual strain formation [159]. For example, relations with the degree of cure can be achieved by rheometer experiments or Dynamic Mechanical Analysis (DMA), dielectric sensors [155, 160], DSC [161] and density gradient column monitoring [16].

FBGs

Recent publications describe the use of FBG sensors in 'single-fibre composites': a model composite with the optic fibre functioning as fibre reinforcement, while simultaneously detecting the strain development caused by the resin curing shrinkage and thermal contraction [162-164]. The gel-point was found to be the point were strain build-up was first detected by the FBG since the resin then has developed a network with sufficient stiffness to enable strain transfer to the optic fibre [165-172]. The vitrification point could be identified where the FBG did not register any curing shrinkage strains anymore, since the chemical reaction has stopped [171, 172]. After this point the FBGs were found suitable for detection of thermal contraction and expansion coefficients, by taking the slope of the strain versus temperature curves [165, 168, 172].

Giordano *et al* observed a dominating effect of the mismatch in thermal expansion and contraction behaviour between the mould and the resin on strain development [165, 166, 168, 172]. This contribution was represented by a jump in residual strain upon de-moulding, and during heating of the de-moulded polymer above T_g, significant strain relaxation behaviour occurred.

Simultaneously with the strain development, the development of degree of cure can be established based on the Fresnel's reflection at the cleaved fibre end [166, 173]: upon increasing degree of cure, the density of the resin increases, resulting in enhanced intensity of the reflected light. Regarding curing shrinkage, a linear relation was found between strain and degree of cure by Chehura [53] and Garstka *et al* [174].

The 3-dimensional strain state after curing of this single-fibre composite model was investigated by Colpo *et al* [162, 163], by using the FBG as a strain sensor in combination with the crack compliance method. A significant increase in residual strains was observed after post-curing of an epoxy resin. Residual strains for the several mentioned epoxy resin systems ranged from -2000 $\mu\varepsilon$ to -6000 $\mu\varepsilon$.

Concluding, it can be stated that the FBG sensors provide a powerful tool to establish the matrix contributions to residual strain development during cure. This technology will therefore be investigated in more detail in Chapter 4.

Temperature difference

The stress-free temperature is often taken as the glass transition temperature (T_g) for amorphous thermoplastics [9, 127] and the crystallisation peak temperature (T_c) for semi-crystalline thermoplastics [9, 38, 101]. These values can be determined using DSC or DMTA. The gel-point in thermosets can be established with several experimental techniques of which DSC and DMTA are used most frequently [175]. The photo-elasticity method in combination with a hot stage was also employed to find the stress-free temperature, which was determined as the temperature at which the retardation was zero [9].

Modulus

The modulus of semi-crystalline thermoplastic composites depends also on the level of crystallinity and can be calculated with a rules-of-mixtures approach. Determination of the modulus with temperature can be performed by means of a dynamic mechanical thermal analyser (DMTA) with the specimen preferably loaded in tension, or by static mechanical testing. The modulus of a reacting polymer depends on the degree of cure and can also be assessed with DMTA [151].

3.6.2 Interlaminar stresses

For calculation of the interlaminar residual stresses in cross-ply laminates at the service temperature, one needs similar values as for Eq. (3-8) for single composite plies in the transverse and longitudinal direction. The magnitude of the resulting stresses can be estimated by a one-dimensional linear elastic stress analysis [8, 9]:

$$\sigma_{22} = \frac{\left(E_{11} \times E_{22}\right)}{\left(E_{11} + E_{22}\right)} \times \left(\alpha_{22} - \alpha_{11}\right)\Delta T \qquad (3\text{-}9)$$

Where E_{11} = stiffness of the composite parallel to the fibres, E_{22} = stiffness of the composite transverse to the fibre direction, and the terms α denote the coefficients of thermal expansion in each of the major directions. For simplicity, α_{11} can be assumed zero for carbon fibre composites [8, 176].

The coefficients of thermal expansion and the moduli can also be calculated using the matrix and fibre properties, with for example a rule-of-mixtures based approach. Additional parameters then include the volume fractions and Poisson's ratios of the constituents [24,

177]. The Poisson's ratio can be obtained with a static tensile test [178, 179] and the volume fractions following ASTM standard D3171 [180]. Shear moduli are occasionally required for calculations and these can be obtained via calculation [142] ($G=E/2[1+v]$; where G is the shear modulus, E is the Young's modulus and v is the Poisson's ratio), strain gauge data obtained during a static mechanical test [181-183], or with a rheometric torsion test [87]. However, properties for woven fabric reinforcement are not easily found.

To determine the temperature difference ΔT for the calculations, some of the previously described experimental techniques were applied to determine the stress-free temperature. This was often performed by heating strips or cylinders of non-symmetric laminates in an oven and following the curvature. When the laminate became flat (infinite radius), it was assumed that at this temperature all residual stresses were removed [8, 38, 87, 88, 90, 91, 104, 129]. This type of test led to the consensus that for reactive systems, the stress-free temperature corresponds to the maximum cure temperature, which can be different than the gel-point [79, 129]. For thermoplastics, the stress-free temperatures were often found close to the glass transition and crystallisation temperature. This test was also carried out using DMTA with a three-point-bending set-up in a controlled force mode [89]. In general, determination of the precise point at which the strip becomes flat is difficult, and a rather wide range is frequently found. Evidently, determination of the stress-free temperature during the process is also possible: the temperature at which the non-symmetrical laminate starts to curve will be the temperature for onset of residual stresses [88].
A novel ply pull-out technique based on internal composite friction variations due to curing was proposed by Ersoy *et al* [159] to determine the gel-point.

3.6.3 Stresses through the thickness

For calculation of skin-core residual stresses due to temperature variations, material properties need to be known, such as heat transfer properties and crystallisation or cure kinetics [127, 128]. For the heat transfer properties of fibre reinforced reactive polymers, several temperature-dependent parameters are required, including degree of cure or crystallinity, density, specific heat and thermal conductivity [161]. The degree of cure can be established with (modulated) DSC, Fourier Transformed InfraRed (FTIR) and dielectric spectroscopy, and FBGs [166]. Density can be established using a PVT dilatometer [153] or pycnometer and the specific heat with a modulated DSC. For thermal conductivity measurements the temperature needs to be stable, which is difficult during a non isothermal cure cycle, exothermal reaction or during cooling. Suitable equipment is scarce and expensive, and include the hot disk® [184] or the Laser Flash® [185] technique from Netzsch.

Cure and crystallisation kinetics can be established using DSC. Visco-elastic behaviour needs also be taken into account [127], which was deduced from creep [186] and relaxation experiments. The latter was carried out with rheology measurements [177], using a dynamic torsion rheometer in rectangular torsion mode [142] and a DMA in three-point-bending mode [141].
Variations in material properties through the thickness were studied with the aid of the PSL method: the properties of the constitutive laminates, such as degree of cure or crystallinity and mechanical properties, were investigated after separation [94, 128].

Even though the knowledge is available on how to acquire values for material properties, there is still a fundamental lack of material properties accessible to the public, especially for thermoplastic composites. This restricts the validation of the techniques mentioned in this section, but also validation of predictive models for residual stresses in composite structures.

3.7 Concluding remarks

Table 3.1 and 3.2 show an overview of the discussed techniques categorised into non-destructive and destructive techniques and according to the specimen type and residual strain level they were used for. As can be seen in Table 3.1, photo-elasticity and Raman Spectroscopy can be employed for determination of residual strains in the matrix and the fibre, respectively. For determination of interlaminar residual strains and stresses, suitable techniques are embedded sensors, first ply failure and curvature measurements. The most-often used technique is the curvature method applied to unsymmetrical laminates, since this method is relatively easy to perform. For residual stresses through the thickness, mostly destructive techniques were employed (see Table 3.2), such as layer removal and hole drilling. The PSL method was successfully used; citing Lawrence et al. [94]: 'The PSL technique makes it possible to perform process, structure and property investigations on laminates as a function of thickness'.
Few non-destructive experimental techniques are available where residual strain values can be obtained directly, that is without further mathematical operations. Only Raman spectroscopy and embedded optic fibres require not much more than a calibration curve, but Raman spectroscopy is unsuitable for determination of strain variations through the thickness, as is the goal in this thesis. The fibre Bragg gratings have many advantages over EFPI sensors, but have not yet found application in studies on through-the-thickness strains. This technology seems capable of providing a three-dimensional profile of the stress distribution in composites by means of polarisation effects, but also by embedding several optical fibres through the thickness. In addition, the FBGs were shown to be capable of

Table 3.1: Overview of non-destructive experimental techniques for residual strain and stress determination in composites

Technique	Level of residual strain			Type of specimen					Specimen requirements/ Drawbacks
	Micro-mechanical	Inter-laminar	Through-thickness	Micro-composites	UD prepregs	Cross-ply prepregs	UD laminates	Angle-ply laminates	
Photo-elasticity	X			X	X				Transparent matrix, low V_f
Raman spectroscopy	X	X		X	X		X		Transparent matrix, measures only fibre surface, need aramid fibres in amorphous material
Electrical conductance		X				X			Need electrically conducting fibres, prevent short-circuiting, further development necessary
Embedded strain gauges	X	X					X	X	Compensation needed for gauge CTE
Embedded FOS	X	X	X	X			X	X	Polarisation effects
Embedded metallic particles	X	X					X	X	Particles need to be close to surface
Interferometry		X					X	X	Only surface information, grid is necessary
Warpage		X	X		X	X	X	X	Low accuracy

Table 3.2: Overview of destructive experimental techniques for residual strain and stress determination in composites.

Technique	Level of residual strain			Type of specimen					Specimen requirements/ Drawbacks
	Micro-mechanical	Inter-laminar	Through-thickness	Micro-composites	UD prepregs	Cross-ply prepregs	UD laminates	Angle-ply laminates	
First ply failure		X				X		X	Works best for $[0/90]_{ns}$ laminates
Layer removal		X	X				X	X	No high accuracy
Blind-hole drilling		X	X				X	X	Low accuracy
Successive grooving technique		X	X				X	X	Low accuracy, time consuming

determining the material properties responsible for residual strain formation. Therefore, the FBG technology will be investigated further for determination of residual strain formation through the thickness in thermoplastic composites as well as the responsible parameters.

References

1. Favre, J.P., Residual thermal stresses in fibre reinforced composite materials - A review. Journal of the Mechanical Behavior of Materials, 1(1-4): 37-53, 1988.
2. Schulz, W.A., *et al.*, Determination of residual stress and thermal history for IM7/977-2 composite laminates. Composites Science and Technology, 65(13): 2014-2024, 2005.
3. Eijpe, M.P.I.M., A Modified Layer Removal Method for Determination of Residual Stresses in Polymeric Composites. 1997 Mechanical Engineering, University Twente, Enschede. 170 pages.
4. Kesavan, K., *et al.*, Non destructive evaluation of residual stresses in welded plates using the Barkhausen noise technique. Experimental Techniques, 29(5): 17-21, 2005.
5. Dally, J.W., Riley, W.F., Residual Stress Determination, in Experimental Stress Analysis. 1991, McGraw-Hill, Inc: New York. p.329-334.
6. Parlevliet, P.P., Bersee, H.E.N., Beukers, A., Residual Stresses in Thermoplastic Composites - A Study of the Literature - Part I: Formation of Residual Stresses. Composites Part A-Applied Science and Manufacturing, , 37(11): 1847-1857, 2006.
7. Kim, J.-K., Mai, Y.-W., Residual Stresses, in Engineered Interfaces in Fiber Reinforced Composites. 1998, Elsevier Science Ltd.: Oxford. p.308-320.
8. Barnes, J.A., Byerly, G.E., The Formation of Residual-Stresses in Laminated Thermoplastic Composites. Composites Science and Technology, 51(4): 479-494, 1994.
9. Nairn, J.A., Zoller, P., Matrix Solidification and the Resulting Residual Thermal-Stresses in Composites. Journal of Materials Science, 20(1): 355-367, 1985.
10. Nairn, J.A., Thermoelastic Analysis of Residual-Stresses in Unidirectional, High-Performance Composites. Polymer Composites, 6(2): 123-130, 1985.
11. Pawlak, A., *et al.*, Photoelastic studies of residual stresses around fillers embedded in an epoxy matrix. Macromolecular Symposia, 169: 197-210, 2001.
12. Yan, X., Ohsawa, T., Measurement of the Internal Local Stress-Distribution of Composite-Materials by Means of Laser Imaging Methods. Composites, 25(6): 443-450, 1994.
13. Andersson, B., Sjogren, A., Berglund, L., Micro- and meso-level residual stresses in glass-fiber/vinyl-ester composites. Composites Science and Technology, 60(10): 2011-2028, 2000.
14. Sjögren, A., Matrix and interface effects on microcracking in polymer composites. 1999 Materials and Manufacturing Engineering / Polymer Engineering, Lulea University of Technology, Lulea.
15. Sjogren, A., *et al.*, Effects of fibre coating (size) on properties of glass fibre vinyl ester composites. Composites Part a-Applied Science and Manufacturing, 30(8): 1009-1015, 1999.
16. Howell, B.F., Effect of Expanding Monomer on Carbon Fiber-Reinforced Epoxy Composites. Journal of Composites Technology & Research, 14(3): 169-175, 1992.
17. Nielsen, A.S., Pyrz, R., A novel approach to measure local strains in polymer matrix systems using polarised Raman microscopy. Composites Science and Technology, 62(16): 2219-2227, 2002.
18. Dally, J.W., Riley, W.F., Optical Methods of Stress Analysis, in Experimental Stress Analysis. 1991, McGraw-Hill, Inc.: New York. p.343.
19. Ingersoll, J., Photoelastic Stress Analysis (§ 4.1.0). 2004, Shodor Education Foundation: Durham, NC.
20. Filiou, C., Galiotis, C., In situ monitoring of the fibre strain distribution in carbon-fibre thermoplastic composites 1. Application of a tensile stress field. Composites Science and Technology, 59(14): 2149-2161, 1999.
21. Filiou, C., Galiotis, C., Batchelder, D.N., Residual-Stress Distribution in Carbon-Fiber Thermoplastic Matrix Preimpregnated Composite Tapes. Composites, 23(1): 28-38, 1992.
22. Galiotis, C., *et al.*, Residual Strain Mapping in Carbon-Fiber Peek Composites. Composites, 19(4): 321-324, 1988.
23. Nielsen, A.S., Pyrz, R., The effect of cooling rate on thermal residual strains in carbon/polypropylene microcomposites. Science and Engineering of Composite Materials, 7(1-2): 1-22, 1998.
24. Young, R.J., *et al.*, Fibre Deformation and Residual Thermal Stresses in Carbon Fibre Reinforced PEEK. Composites Science and Technology, 34(3): 243-258, 1989.
25. Arjyal, B.P., *et al.*, Monitoring local strains in cracked cross-ply composites using an embedded aramid fibre strain sensor. Journal of Materials Science, 33(11): 2745-2750, 1998.
26. Raman Tutorial - A brief look at Raman scattering theory. 2006 [cited 2006. Available from: http://www.kosi.com/raman/resources/tutorial/.
27. Nielsen, A.S., Pyrz, R., In-situ observation of thermal residual strains in carbon/thermoplastic microcomposites using Raman spectroscopy. Polymers & Polymer Composites, 5(4): 245-257, 1997.
28. Nielsen, A.S., Pyrz, R., A Raman study into the effect of transcrystallisation on thermal stresses in embedded single fibres. Journal of Materials Science, 38(3): 597-601, 2003.
29. Arjyal, B., Galiotis, C., Localized Stress Measurements in Composite Laminates Using a Raman Stress Sensor. Advanced Composites Letters, 4(2): 47-52, 1995.
30. Arjyal, B.P., *et al.*, Residual strain and Young's modulus determination in cross-ply composites using an embedded aramid fibre strain sensor. Composites Part a-Applied Science and Manufacturing, 29(11): 1363-1369, 1998.
31. Chung, D.D.L., Continuous carbon fiber polymer-matrix composites and their joints, studied by electrical measurements. Polymer Composites, 22(2): 250-270, 2001.
32. Guerrero, V.H., Chung, D.D.L., Interlaminar interface relaxation upon heating carbon fiber thermoplastic-matrix composite, studied by contact electrical resistivity measurement. Composite Interfaces, 9(6): 557-563, 2002.

33. Mei, Z., Chung, D.D.L., Thermal stress-induced thermoplastic composite debonding, studied by contact electrical resistance measurement. International Journal of Adhesion and Adhesives, 20(2): 135-139, 2000.
34. Wang, S.K., Kowalik, D.P., Chung, D.D.L., Self-sensing attained in carbon-fiber-polymer-matrix structural composites by using the interlaminar interface as a sensor. Smart Materials and Structures, 13(3): 570-592, 2004.
35. Wang, S.K., Mei, Z., Chung, D.D.L., Interlaminar damage in carbon fiber polymer-matrix composites, studied by electrical resistance measurement. International Journal of Adhesion and Adhesives, 21(6): 465-471, 2001.
36. Kim, Y.K., Daniel, I.M., Cure cycle effect on composite structures manufactured by resin transfer molding. Journal of Composite Materials, 36(14): 1725-1743, 2002.
37. Unger, W.J., Hansen, J.S., The Effect of Thermal-Processing on Residual Strain Development in Unidirectional Graphite Fiber Reinforced Peek. Journal of Composite Materials, 27(1): 59-82, 1993.
38. Jeronimidis, G., Parkyn, A.T., Residual-Stresses in Carbon Fiber-Thermoplastic Matrix Laminates. Journal of Composite Materials, 22(5): 401-415, 1988.
39. Crasto, A.S., Kim, R.Y., Russell, J.D., In situ monitoring of residual strain development during composite cure. Polymer Composites, 23(3): 454-463, 2002.
40. Daniel, I.M., Liber, T., Lamination residual stresses in fiber composites. 1975, NASA Center for AeroSpace Information (CASI).
41. Wisnom, M.R., *et al.*, Mechanisms generating residual stresses and distortion during manufacture of polymer-matrix composites structures. Composites Part A: Applied Science and Manufacturing, 37(4): 522-529, 2006.
42. Sorensen, L., Gmür, T., Botsis, J. Residual Strain Development in Laminated Thermoplastic Composites Measured Using Fibre Bragg Grating Sensors. in CompTest 2004. 2004. Bristol, UK.
43. Vlekken, J., Fibre Bragg Grating sensors for monitoring thermoplastic composite processing, recipient: Parlevliet, P.P. November 2004. Telephone conversation.
44. Zhou, G., Sim, L.M., Damage detection and assessment in fibre-reinforced composite structures with embedded fibre optic sensors - review. Smart Materials & Structures, 11(6): 925-939, 2002.
45. Leng, J.S., Asundi, A., Real-time cure monitoring of smart composite materials using extrinsic Fabry-Perot interferometer and fiber Bragg grating sensors. Smart Materials & Structures, 11(2): 249-255, 2002.
46. Lawrence, C.M., *et al.*, An embedded fiber optic sensor method for determining residual stresses in fiber-reinforced composite materials. Journal of Intelligent Material Systems and Structures, 9(10): 788-799, 1998.
47. Lai, L., *et al.*, Processing Monitoring of Carbon Phenolic Composites Using Smart Sensors. Smart Materials & Structures, 4(2): 118-125, 1995.
48. Kang, H.K., *et al.*, Simultaneous monitoring of strain and temperature during and after cure of unsymmetric composite laminate using fibre-optic sensors. Smart Materials & Structures, 12(1): 29-35, 2003.
49. Kang, H.K., *et al.*, Cure monitoring of composite laminates using fiber optic sensors. Smart Materials & Structures, 11(2): 279-287, 2002.
50. Kalamkarov, A.L., Fitzgerald, S.B., MacDonald, D.O., The use of Fabry Perot fiber optic sensors to monitor residual strains during pultrusion of FRP composites. Composites Part B-Engineering, 30(2): 167-175, 1999.
51. Okabe, Y., *et al.*, Detection of transverse cracks in CFRP composites using embedded fiber Bragg grating sensors. Smart Materials & Structures, 9(6): 832-838, 2000.
52. O'Dwyer, M.J., *et al.*, Relating the state of cure to the real-time internal strain development in a curing composite using in-fibre Bragg gratings and dielectric sensors. Measurement Science and Technology, 9(8): 1153-1158, 1998.
53. Chehura, E., *et al.*, Strain development in curing epoxy resin and glass fibre/epoxy composites monitored by fibre Bragg grating sensors in birefringent optical fibre. Smart Materials & Structures, 14(2): 354-362, 2005.
54. Kuang, K.S.C., *et al.*, Process monitoring of aluminum-foam sandwich structures based on thermoplastic fibre-metal laminates using fibre Bragg gratings. Composites Science and Technology, 65(3-4): 669-676, 2005.
55. Okabe, Y., *et al.*, Effect of thermal residual stress on the reflection spectrum from fiber Bragg grating sensors embedded in CFRP laminates. Composites Part a-Applied Science and Manufacturing, 33(7): 991-999, 2002.
56. Okabe, Y., *et al.*, Detection of microscopic damages in composite laminates with embedded small-diameter fiber Bragg grating sensors. Composites Science and Technology, 62(7-8): 951-958, 2002.
57. FOS&S. Fibre Bragg Grating Technology. 2006 [cited. Available from: http://www.fos-s.be/fos%2Ds/.
58. de Waele, W.A.J., Structural monitoring of composite elements using optical fibres with Bragg-sensors. 2002. PhD thesis Faculty of Engineering, Department of Mechanical Construction and Production, Universiteit Gent, Ghent University. 420 pages.
59. Jung, K., Kang, T.J., Cure monitoring and internal strain measurement of 3-D hybrid braided composites using fiber Bragg grating sensor. Journal of Composite Materials, 41(12): 1499-1519, 2007.
60. Sorensen, L., Gmur, T., Botsis, J., Residual strain development in an AS4/PPS thermoplastic composite measured using fibre Bragg grating sensors. Composites Part A: Applied Science and Manufacturing, 37(2): 270-281, 2006.
61. Grattan, K.T.V., Meggitt, B.T., Optical fibre sensor technology: Fundamentals. 2000, Dordrecht: Kluwer academic publishers.
62. Sorensen, L.G., Thomas; Botsis, John Long FBG sensor characterization of residual strains in AS4/PPS thermoplastic laminates, in International Symposium on Smart Structures and Materials, Proceedings of SPIE, Vol 5384, pp. 267-278. 2004, SPIE: San Diego, CA; USA;.
63. Luyckx, G., *et al.*, Three-dimensional strain and temperature monitoring of composite laminates. Insight, 49(1): 10-16, 2007.
64. Shivakumar, K., Bhargava, A., Failure mechanics of a composite laminate embedded with a fiber optic sensor. Journal of Composite Materials, 39(9): 777-798, 2005.
65. Fernandez-Valdivielso, C., Matias, I.R., Arregui, F.J., Simultaneous measurement of strain and temperature using a fiber Bragg grating and a thermochromic material. Sensors and Actuators a-Physical, 101(1-2): 107-116, 2002.
66. Betz, D.C., *et al.*, Advanced layout of a fiber Bragg grating strain gauge rosette. Journal of Lightwave Technology, 24(2): 1019-1026, 2006.
67. Mostafa, M.A., Gmur, T., Botsis, J., Experimental study on the effects of the boundary conditions on the deformations of composite plates. Composites Science and Technology, 66(11-12): 1756-1765, 2006.
68. Campbell, D., Pethrick, R.A., White, J.R., Polymer Characterization - Physical Techniques. 2nd ed. 2000, Cheltenham: Stanley Thornes, Ltd. 481 pages.
69. Schnack, E., Meske, R., Eigenspannungen bei viskoelastischen Verbundwerkstoffen. 1996, Institut fuer Technische Mechanik/Festigkeitslehre, Universitaet Karlsruhe: Karlsruhe, Germany. p. 123.

70. Fenn, R.H., Jones, A.M., Wells, G.M., X-Ray-Diffraction Investigation of Triaxial Residual-Stresses in Composite-Materials. Journal of Composite Materials, 27(14): 1338-1351, 1993.
71. Meske, R., Schnack, E., Particular adaptation of X-ray diffraction to fiber reinforced composites. Mechanics of Materials, 35(1-2): 19-34, 2003.
72. Meske, R., Schnack, E., Stress analysis of carbon-fiber reinforced polymeric materials by means of X-ray diffraction from fillers - micromechanical model and experimental results, in Ecrs 5: Proceedings of the Fifth European Conference on Residual Stresses. 2000. p.217-222.
73. Kumosa, M.S., An investigation of damage initiation in woven graphite fiber/polyimide composites subjected to shear, in Advances in Fracture and Damage Mechanics. 2003. p.447-456.
74. Benedikt, B., *et al.*, The use of X-ray diffraction measurements to determine the effect of bending loads on internal stresses in aluminum inclusions embedded in a unidirectional graphite-fibre/PMR-15 composite. Composites Science and Technology, 61(14): 1995-2006, 2001.
75. Benedikt, B., *et al.*, An analysis of residual thermal stresses in a unidirectional graphite/PMR-15 composite based on X-ray diffraction measurements. Composites Science and Technology, 61(14): 1977-1994, 2001.
76. Hauk, V., Structural and residual stress analysis by X-ray diffraction on polymeric materials and composites. Materialwissenschaft Und Werkstofftechnik, 30(7): 377-384, 1999.
77. Mendes, E., Preparation of X-ray specimens, recipient: Parlevliet, P.P.
78. Muraki, N., *et al.*, Residual Stress Mapping of Epoxy Molding Compound in a Ball Grid Array Microelectronic Package Using a Fluorescent Sensor. Applied Spectroscopy, 58(2): 152-159, 2004.
79. Reid, R.G., Paskaramoorthy, R., A novel method to measure residual stresses in unidirectional GFRP Composite Structures, 88(4): 388-393, 2008.
80. Han, B., Post, D., Ifju, P., Moire interferometry for engineering mechanics: current practices and future developments. Journal of Strain Analysis for Engineering Design, 36(1): 101-117, 2001.
81. Li, M.C., *et al.*, A plane-strain finite element model for process-induced residual stresses in a graphite/PEEK composite. Journal of Composite Materials, 31(3): 212-243, 1997.
82. Ifju, P.G., *et al.*, A novel method to measure residual stresses in laminated composites. Journal of Composite Materials, 33(16): 1511-1524, 1999.
83. Ifju, P.G., *et al.*, Residual strain measurement in composites using the cure-referencing method. Experimental Mechanics, 40(1): 22-30, 2000.
84. Lee, J.R., *et al.*, Application of grating shearography and speckle shearography to mechanical analysis of composite material. Composites Part a-Applied Science and Manufacturing, 35(7-8): 965-976, 2004.
85. Pechersky, M.J., Determination of Residual Stresses by Thermal Relaxation and Speckle Correlation Interferometry. 2001, Westinghouse Savannah River Company: Aiken, South Carolina. p. 15.
86. Newman, J.W., Holographic and shearographic NDT applications in aerospace manufacturing. Materials Evaluation, 63(7): 746-750, 2005.
87. Cowley, K.D., Beaumont, P.W.R., The measurement and prediction of residual stresses in carbon-fibre/polymer composites. Composites Science and Technology, 57(11): 1445-1455, 1997.
88. Nairn, J.A., Zoller, P. The Development of Residual Thermal Stresses in Amorphous and Semicrystalline Thermoplastic Matrix Composites. in Toughened Composites. 1987. Houston, Texas; USA: ASTM, 1916 Race Street, Philadelphia, Pennsylvania 19103, USA.
89. Timmerman, J.F., Hayes, B.S., Seferis, J.C., Cure temperature effects on cryogenic microcracking of polymeric composite materials. Polymer Composites, 24(1): 132-139, 2003.
90. Kim, K.S., Hahn, H.T., Croman, R.B., The Effect of Cooling Rate on Residual Stresses in a Thermoplastic Composite. Journal of Composite Technology & Research, 11(2): 47-52, 1989.
91. Unger, W.J., Hansen, J.S., The effect of cooling rate and annealing on residual stress development in graphite fibre reinforced PEEK laminates. Journal of Composite Materials, 29: 108-137, 1993.
92. Penn, L.S., *et al.*, The Effect of Matrix Shrinkage on Damage Accumulation in Composites. Journal of Composite Materials, 23(6): 570-586, 1989.
93. Bailey, J.E., Curtis, P.T., Parvizi, A., Proceedings of the Royal Society in London, A, 366: 599, 1979.
94. Lawrence, W.E., Manson, J.A.E., Seferis, J.C., Thermal and Morphological Skin Core Effects in Processing of Thermoplastic Composites. Composites, 21(6): 475-480, 1990.
95. Hyer, M.W., Some observations on the cured shape of thin unsymmetric laminates. Journal of Composite Materials, 15: 175-194, 1981.
96. Youssef, Y., Denault, J., Thermoformed glass fiber reinforced polypropylene: Microstructure, mechanical properties and residual stresses. Polymer Composites, 19(3): 301-309, 1998.
97. Eijpe, M., Powell, P.C., Residual stress evaluation in composites using a modified layer removal method. Composite Structures, 37(3-4): 335-342, 1997.
98. Eijpe, M., Powell, P.C., Determination of residual shear stresses in composites by a modified layer-removal method. Journal of Materials Science, 33(8): 2019-2026, 1998.
99. Hufenbach, W., Gude, M., Analysis and optimisation of multistable composites under residual stresses. Composite Structures, 55(3): 319-327, 2002.
100. Hyer, M.W., Calculations of the room-temperature shapes of unsymmetric laminates. Journal of Composite Materials, 15: 296-310, 1981.
101. Youssef, Y., Denault, J. Residual stresses in continuous glass fiber/polypropylene composite thermoformed parts. in International SAMPE symposium. 1998.
102. Genidy, M.S., Madhukar, M.S., Russell, J.D., A new method to reduce cure-induced stresses in thermoset polymer composites, part II: Closed loop feedback control system. Journal of Composite Materials, 34(22): 1905-1925, 2000.
103. White, S.R., Processing-Induced Residual Stresses in Composites, in Processing of Composites, Dave, R. and Loos, A.C., Editors. 2000, Hanser Publishers: Munich. p.239-271.
104. Papadopoulos, D.S., Bowles, K.J. Use of Unbalanced Laminates as a Screening Method for Microcracking. in 35th International SAMPE Symposium. 1990. Anaheim, California.
105. Manson, J.A.E., Seferis, J.C., Process Simulated Laminate (Psl) - a Methodology to Internal-Stress Characterization in Advanced Composite-Materials. Journal of Composite Materials, 26(3): 405-431, 1992.
106. Twigg, G., Poursartip, A., Fernlund, G., Tool-part interaction in composites processing. Part I: experimental investigation and analytical model. Composites Part a-Applied Science and Manufacturing, 35(1): 121-133, 2004.

107. Parlevliet, P.P., Bersee, H.E.N., Beukers, A., Residual Stresses in Thermoplastic Composites: Experimental Techniques, in ICCM-15, Verijenko, V.E.A., S.; Morozov; E.; von Klemperer, C.J., Editor. 2005, University of KwaZulu Natal, Durban: Durban, South Africa.
108. Peeters, L.J.B., Powell, P.C., Warnet, L., Thermally-induced shapes of unsymmetric laminates. Journal of Composite Materials, 30(5): 603-626, 1996.
109. Makino, A., Nelson, D., Residual stress determination by single-axis holographic interferometry and hole drilling - Part I: Theory. Experimental Mechanics: 66-78, 1994.
110. Shrotriya, P., Sottos, N.R., Skipor, A.F., Residual stress development during relamination of woven composite circuit boards. Journal of Composite Materials, 35(10): 905-927, 2001.
111. Nino, G.F., Bergsma, O.K., Bersee, H.E.N. Evaluation of Intraply Shear in Thermoformed Composite Products. in ICCM-15. 2005. Durban, South Africa.
112. Nino, G.F., Bergsma, O.K., Bersee, H.E.N. Square Grid Analysis for Intraply Shear in Thermoformed Thermoplastic Composites. in CompTest 2004. 2004. Bristol, UK: University of Bristol.
113. Brinson, L.C., Gates, T.S., Viscoelasticity and Aging of Polymer Matrix Composites, in Polymer Matrix Composites, Talreja, R. and Manson, J.A., Editors. 2001, Elsevier Science Ltd.: Oxford. p.333-368.
114. Bradshaw, R.D., Brinson, L.C., Mechanical response of linear viscoelastic composite laminates incorporating non-isothermal physical aging effects. Composites Science and Technology, 59(9): 1411-1427, 1999.
115. Callister, W.D.J., Materials Science and Engineering - An Introduction. 3rd ed. 1994: John Wiley & Sons, Inc. 811 pages.
116. Harris, B., Residual Strains, in Engineering Composite Materials, Harris, B., Editor. 1999, IOM Communications: London. p.79-83.
117. Warnet, L., On the Effect of Residual Stresses on the Transverse Cracking in Cross-Ply Carbon-Polyetherimide Laminates. 2000 Mechanical Engineering, University of Twente, Enschede. 116 pages.
118. Ogale, A.A., Creep Behavior of Thermoplastic Composites, in Thermoplastic Composite Materials, Carlsson, L.A., Editor. 1991, Elsevier Science Publishers, B.V.: Amsterdam. p.205-232.
119. Wang, C., Sun, C.T., Thermoelastic behavior of PEEK thermoplastic composite during cooling from forming temperatures. Journal of Composite Materials, 31(22): 2230-2248, 1997.
120. Wang, C., Sun, C.T., Experimental characterization of constitutive models for PEEK thermoplastic composite at heating stage during forming. Journal of Composite Materials, 31(15): 1480-1506, 1997.
121. Kim, R.Y., Hahn, H.T., Effect of Curing Stresses on the First Ply-Failure in Composite Laminates. Journal of Composite Materials, 13(JAN): 2-16, 1979.
122. Sicot, O.*, et al.*, Determination of residual stress in composite laminates using the incremental hole-drilling method. Journal of Composite Materials, 37(9): 831-844, 2003.
123. Ersoy, N., Vardar, O., Measurement of residual stresses in layered composites by compliance method. Journal of Composite Materials, 34(7): 575-598, 2000.
124. Vincent, M., Giraud, T., Residual Stresses in Injection Molded Thermoplastics. Materials science forum, 404-407: 587-598, 2002.
125. McGinnis, M.J., Pessiki, S., Turker, H., Application of three-dimensional digital image correlation to the core-drilling method. Experimental Mechanics, 45(4): 359-367, 2005.
126. Gascoigne, H.E., Residual Surface Stresses in Laminated Cross-Ply Fiber-Epoxy Composite-Materials. Experimental Mechanics, 34(1): 27-36, 1994.
127. Chapman, T.J.*, et al.*, Prediction of Process-Induced Residual-Stresses in Thermoplastic Composites. Journal of Composite Materials, 24(6): 616-643, 1990.
128. Deshpande, A.P., Seferis, J.C., Processing characteristics in different semi-crystalline thermoplastic composites using process simulated laminate (PSL) methodology. Journal of Thermoplastic Composite Materials, 9(2): 183-198, 1996.
129. Crasto, A.S., Kim, R.Y., On the Determination of Residual-Stresses in Fiber-Reinforced Thermoset Composites. Journal of Reinforced Plastics and Composites, 12(5): 545-558, 1993.
130. Joh, D., Byun, K.Y., Ha, J., Thermal Residual-Stresses in Thick Graphite-Epoxy Composite Laminates - Uniaxial Approach. Experimental Mechanics, 33(1): 70-76, 1993.
131. ASTM_International, E837: Standard Test Method for Determining Residual Stresses by the Hole-Drilling Strain-Gage Method. 2001. p. 1-10.
132. Wu, Z., Lu, J., Study of surface residual stress by three-dimensional displacement data at a single point in hole drilling method. Journal of Engineering Materials and Technology-Transactions of the Asme, 122(2): 215-220, 2000.
133. Shankar, K.*, et al.*, A study on residual stresses in polymer composites using moire interferometry. Advanced Composite Materials, 13(3-4): 237-253, 2004.
134. Ambu, R., Ginesu, F., Residual stress analysis in graphite/PEEK composite laminates, in Experimental Techniques and Design in Composite Materials 5. 2002, TRANS TECH PUBLICATIONS LTD: Zurich-Uetikon. p.347-354.
135. Chen, J.B.*, et al.*, Measurement of residual stresses in fiber reinforced composite material, in Advances in Engineering Plasticity and Its Applications, Pts 1 and 2. 2004, TRANS TECH PUBLICATIONS LTD: Zurich-Uetikon. p.865-870.
136. Cardenas-Garcia, J.F.*, et al.*, Non-linear least-squares solution to the moire hole method problem in orthotropic materials. Part I: Residual stresses. Experimental Mechanics, 45(4): 301-313, 2005.
137. Schajer, G.S., Steinzig, M., Full-field Calculation of Hole Drilling Residual Stresses from Electronic Speckle Pattern Interferometry Data. Experimental Mechanics, 45(6): 526-532, 2005.
138. Bateman, M.G.*, et al.*, Measurement of residual stress in thick section composite laminates using the deep-hole method. International Journal Of Mechanical Sciences, 47(11): 1718-1739, 2005.
139. Montay, G.*, et al.*, Determination of the residual stresses in composite laminate using the compliance method, in Residual Stresses Vii, Proceedings. 2005, TRANS TECH PUBLICATIONS LTD: Zurich-Uetikon. p.533-538.
140. Sicot, O.*, et al.*, Influence of experimental parameters on determination of residual stress using the incremental hole-drilling method. Composites Science and Technology, 64(2): 171-180, 2004.
141. Sunderland, P., Yu, W.J., Manson, J.A., A thermoviscoelastic analysis of process-induced internal stresses in thermoplastic matrix composites. Polymer Composites, 22(5): 579-592, 2001.
142. Kim, B.S.*, et al.*, Numerical analysis of the dimensional stability of thermoplastic composites using a thermoviscoelastic approach. Journal of Composite Materials, 36(20): 2389-2403, 2002.
143. Lawrence, W.E., Seferis, J.C., Gillespie, J.W., Material Response of a Semicrystalline Thermoplastic Polymer and Composite in Relation to Process Cooling History. Polymer Composites, 13(2): 86-96, 1992.

144. Menard, K.P., Thermomechanical Analysis, in Dynamic Mechanical Analysis - A Practical Introduction. 1999, CRC Press LLC: Boca Raton, FA.
145. Kim, R.Y., Crasto, A.S., Schoeppner, G.A., Dimensional stability of composite in a space thermal environment. Composites Science and Technology, 60(12-13): 2601-2608, 2000.
146. Dudescu, C., *et al.*, Characterisation of thermal expansion coefficient of anisotropic materials by electronic speckle pattern interferometry. Strain, 42(3): 197-205, 2006.
147. Kim, K.S., *et al.*, Thermal strain analysis of composite materials by electronic speckle pattern interferometry. Ksme International Journal, 14(5): 477-482, 2000.
148. Aswendt, P., Hofling, R., Speckle Interferometry for Analyzing Anisotropic Thermal-Expansion - Application to Specimens and Components. Composites, 24(8): 611-617, 1993.
149. Menendez, Fernandez, Guemes, Sensing with embedded fiber bragg gratings in extreme mechanical conditions, in ICCM-16. 2007: Kyoto.
150. Li, C., *et al.*, In-situ measurement of chemical shrinkage of MY750 epoxy resin by a novel gravimetric method. Composites Science and Technology, 64(1): 55-64, 2004.
151. Schoch, K.F., Panackal, P.A., Frank, P.P., Real-time measurement of resin shrinkage during cure. Thermochimica Acta, 417(1): 115-118, 2004.
152. van Rijswijk, K., Thermoplastic Composite Wind Turbine Blades. 2007. PhD thesis Aerospace Engineering, Delft University of Technology, Delft. 249 pages.
153. van der Beek, M.H.E., Specific Volume of Polymers - influence of the thermomechanical history. 2005, Technische Universiteit Eindhoven, Eindhoven. 113 pages.
154. Yang, D.G., *et al.*, Micromechanical modeling of stress evolution induced during cure in a particle-filled electronic packaging polymer. Ieee Transactions On Components And Packaging Technologies, 27(4): 676-683, 2004.
155. Russell, J.D., *et al.*, A new method to reduce cure-induced stresses in thermoset polymer composites, part III: Correlating stress history to viscosity, degree of cure, and cure shrinkage. Journal of Composite Materials, 34(22): 1926-1947, 2000.
156. Zarrelli, M., Partridge, I.K., D'Amore, A., Warpage induced in bi-material specimens: Coefficient of thermal expansion, chemical shrinkage and viscoelastic modulus evolution during cure. Composites Part A-Applied Science And Manufacturing, 37(4): 565-570, 2006.
157. Zingraff, L., *et al.*, Resin transfer moulding of anionically polymerised polyamide 12. Composites Part A: Applied Science and Manufacturing, 36(12): 1675-1686, 2005.
158. Yu, H., Mhaisalkar, S.G., Wong, E.H., Effect of temperature on the cure shrinkage measurement of non-conductive adhesives for flip chip interconnects. Journal of Materials Research, 20(5): 1324-1329, 2005.
159. Ersoy, N., *et al.* Tests to measure the Material Properties Relevant to the Modelling of Process Induced Deformations in Composite Parts. in ICCM-15. 2005. Durban, South Africa: University of KwaZulu Natal, Durban.
160. Leroy, E., *et al.*, Evolution of the coefficient of thermal expansion of a thermosetting polymer during cure reaction Polymer, 46(7): 9919-9927, 2005.
161. Balvers, J.M., Determination of Cure-Dependent Properties for Thermo-Chemical Simulation of the Curing Process of Thick-walled RTM6 based Composites. 2007. MSc thesis Aerospace Engineering, Delft University of Technology, Delft. 124 pages.
162. Colpo, F., Humbert, L., Botsis, J., Characterisation of residual stresses in a single fibre composite with FBG sensor. Composites Science and Technology, 67(9): 1830-1841, 2007.
163. Colpo, F., *et al.*, Characterization of residual strains in an epoxy block using an embedded FBG sensor and the OLCR technique. Composites Part A: Applied Science and Manufacturing, 37(4): 652-661, 2006.
164. Yong, W., Bongtae, H. Measurement of effective chemical shrinkage of polymeric materials using fiber bragg grating sensor. in Proceedings of the International Symposium and Exhibition on Advanced Packaging Materials Processes, Properties and Interfaces. 2007.
165. Antonucci, V., *et al.*, Cure-induced residual strain build-up in a thermoset resin. Composites Part A-Applied Science And Manufacturing, 37(4): 592-601, 2006.
166. Antonucci, V., *et al.*, Real time monitoring of cure and gelification of a thermoset matrix. Composites Science and Technology, 66(16): 3273-3280, 2006.
167. Cusano, A., *et al.*, Chirped fiber-bragg grating as self-temperature referenced strain sensor in nonisothermal thermoset processing. IEEE Sensors Journal, 6(1): 111-117, 2006.
168. Giordano, M., *et al.*, Monitoring by a single fiber Bragg grating of the process induced chemo-physical transformations of a model thermoset. Sensors and Actuators a-Physical, 113(2): 166-173, 2004.
169. Giordano, M., *et al.*, Advanced cure monitoring by optoelectronic multifunction sensing system. Thin Solid Films, 450(1): 191-194, 2004.
170. Giordano, M., *et al.* Non isothermal monitoring of strain build up in thermoset processing by a single chirped fiber Bragg grating. in Proceedings of SPIE - The International Society for Optical Engineering. 2004.
171. Harsch, M., Karger-Kocsis, J., Herzog, F., Influence of cure regime on the strain development in an epoxy resin as monitored by a fiber Bragg grating sensor. Macromolecular Materials and Engineering, 292(4): 474-483, 2007.
172. Harsch, M., Karger-Kocsis, J., Herzog, F., Monitoring of cure-induced strain of an epoxy resin by fiber bragg grating sensor. Journal of Applied Polymer Science, 107(2): 719-725, 2008.
173. Vacher, S., *et al.*, A Fresnel's reflection optical fiber sensor for thermoset polymer cure monitoring. Polymers and Polymer Composites, 12(4): 269-276, 2004.
174. Garstka, T., *et al.*, In situ measurements of through-the-thickness strains during processing of AS4/8552 composite. Composites Part a-Applied Science and Manufacturing, 38(12): 2517-2526, 2007.
175. Kroschwitz, J.I., ed. Concise encyclopedia of polymer science and engineering. 1st ed. 1990, John Wiley & Sons, Inc.: New York. 1341.
176. Barnes, J.A., Thermal-Expansion Behavior of Thermoplastic Composites .2. Journal of Materials Science, 28(18): 4974-4982, 1993.
177. DiLandro, L., Pegoraro, M., Evaluation of residual stresses and adhesion in polymer composites. Composites Part A-Applied Science and Manufacturing, 27(9): 847-853, 1996.
178. ASTM_International, ASTM E132-04: Standard Test Method for Poisson's Ratio at Room Temperature. 2004, ASTM International: 100 Barr Harbor Drive, PO Box C700, West Conshohocken, PA 19428-2959, United States.

179. ASTM_International, ASTM D3039: Standard Test Method for Tensile Properties of Polymer Matrix Composite Materials. 2000, ASTM International: 100 Barr Harbor Drive, PO Box C700, West Conshohocken, PA 19428-2959, United States.
180. ASTM_International, D3171-99(2004): Standard Test Methods for Constituent Content of Composite Materials. 2004, ASTM International: 100 Barr Harbor Drive, PO Box C700, West Conshohocken, PA 19428-2959, United States.
181. ASTM_International, ASTM D6856-03 Standard Guide for Testing Fabric-Reinforced Textile Composite Materials. 2003, ASTM International: 100 Barr Harbor Drive, PO Box C700, West Conshohocken, PA 19428-2959, United States.
182. ASTM_International, ASTM D7078/D7078M-05 Standard Test Method for Shear Properties of Composite Materials by V-Notched Rail Shear Method. 2005, ASTM International: 100 Barr Harbor Drive, PO Box C700, West Conshohocken, PA 19428-2959, United States.
183. ASTM_International, ASTM D4762-04: Standard Guide for Testing Polymer Matrix Composite Materials. 2004, ASTM International: 100 Barr Harbor Drive, PO Box C700, West Conshohocken, PA 19428-2959, United States.
184. Hot_Disk. Hot Disk (R). [cited 11 June 2009]. Available from: http://www.hotdisk.se/.
185. Netzsch_Thermal_Analysis. Laser Flash. [cited 11 June 2009]. Available from: http://www.laserflash.com/.
186. ASTM_International, ASTM D2990-01 Standard Test Methods for Tensile, Compressive, and Flexural Creep and Creep-Rupture of Plastics. 2001, ASTM International: 100 Barr Harbor Drive, PO Box C700, West Conshohocken, PA 19428-2959, United States.

Chapter 4: Shrinkage Determination of a Reactive Polymer with the Fibre Bragg Grating Technology

4.1 Introduction

As described in Chapter 3, a micro-composite with a fibre Bragg grating can be used to detect the strain development due to polymer shrinkage, to identify gelation, vitrification and postcuring effects, and to sense the effects of tooling. A great benefit is that no further experiments are required to determine other material properties necessary for the calculation of residual strains. Consequently, the fibre Bragg grating technology seems perfect to determine the matrix properties governing residual strain formation in novel reactive systems for LCM, such as APA-6.

Composite processing with the APA-6 matrix is still under development, and the FBG technology is relatively new with the gratings still being expensive. Therefore, the FBGs are first tested in a micro-composite with a commercially available polymer of which the processing is more or less comparable to the APA-6 system [1]. The room temperature curing Daron® system (DSM Composite Resins, the Netherlands) is a thermosetting polyurethane (turane) and was chosen for its ease of processing. It can be demoulded within 90 minutes, has a significant exothermic reaction and is suitable for the production of thick composite laminates by means of the vacuum assisted resin infusion process because of its low viscosity [2].

A postcure cycle is recommended for this polymer system, and therefore the cured specimens with FBG sensors were exposed to another temperature cycle for postcuring. A second thermal cycle was carried out to identify differences in polymer properties after the postcuring cycle. For comparison with the FBG results, differential scanning calorimetry (DSC) tests were carried out to confirm thermal transitions in the cured and postcured polymer. In addition, the thermal expansion and contraction of the polymer was determined with thermal mechanical analysis (TMA), which can be compared with the FBG results to establish whether the strain transfer between the matrix and optic fibre is sufficient. First however, the working principle of the FBG technology are explained in more detail.

4.2 Fibre Bragg Gratings – working principle

4.2.1 Theory

The Bragg wavelength λ_B is related to the spacing of the grating Λ with the Bragg relation, where n_{eff} is the averaged refractive index of the grating [3]:

$$\lambda_B = 2 n_{eff} \Lambda \tag{3-1}$$

A shift in Bragg wavelength ($\Delta\lambda_B$) of the grating is caused by strain (ε) as well as temperature variations (T). This is expressed by differentiation of Eq. (3-1) over these two variables:

$$\Delta\lambda_B = 2\left[\frac{\partial n_{eff}}{\partial \varepsilon}\Lambda + n_{eff}\frac{\partial \Lambda}{\partial \varepsilon}\right]\Delta\varepsilon + 2\left[\frac{\partial n_{eff}}{\partial T}\Lambda + n_{eff}\frac{\partial \Lambda}{\partial T}\right]\Delta T \tag{4-1}$$

By combining Eqs. (3-1) and (4-1), Eq. (4-2) can be obtained:

$$\Delta\lambda_B = \lambda_B\left[\frac{1}{n_{eff}}\frac{\partial n_{eff}}{\partial \varepsilon} + \frac{1}{\Lambda}\frac{\partial \Lambda}{\partial \varepsilon}\right]\Delta\varepsilon + \lambda_B\left[\frac{1}{n_{eff}}\frac{\partial n_{eff}}{\partial T} + \frac{1}{\Lambda}\frac{\partial \Lambda}{\partial T}\right]\Delta T \tag{4-2}$$

With

$$\frac{\partial \Lambda}{\Lambda} = \partial\varepsilon\,, \tag{4-3}$$

and definition of the following constants [4]:

$$\begin{cases} P = -\dfrac{1}{n_{eff}}\dfrac{\partial n_{eff}}{\partial \varepsilon} = \dfrac{{n_{eff}}^2}{2}[p_{12} - \nu(p_{11} + p_{12})] \\ \alpha_n = \dfrac{1}{n_{eff}}\dfrac{\partial n_{eff}}{\partial T} \\ \alpha_f = \dfrac{1}{\Lambda}\dfrac{\partial \Lambda}{\partial T} \end{cases} \tag{4-4}$$

The resulting Equation is:

$$\Delta\lambda_B = \lambda_B(1 - P)\cdot\Delta\varepsilon + \lambda_B(\alpha_n + \alpha_f)\cdot\Delta T \tag{4-5}$$

where the wavelength difference $\Delta\lambda_B$ is an absolute value, since it only depends on the geometry of the grating and the opto-elastic constants of the glass [4]: P is the 'effective photo-elastic coefficient' or 'strain-optic coefficient', p_{11} and p_{12} are the 'elasto-optic coefficients' of the strain-optic tensor, v is the Poisson ratio of the fibre, α_n is the 'thermo-optic

constant' and α_f is the thermal expansion coefficient of the fibre [5]. Typical values for p_{11}, p_{12} and v for GeO_2 doped silica-fibres are 0.113, 0.252 and 0.16, respectively [4, 5]. With an effective refractive index n_{eff} of 1.456, this results in a value for P of ~0.204. Typical values for α_n and α_f for these fibres are $5.9 \cdot 10^{-6}$ °C^{-1} and $0.55 \cdot 10^{-6}$ °C^{-1}, respectively [6].
Eq. (4-5) can be rewritten as:

$$\Delta\lambda_B = S_\varepsilon \cdot \Delta\varepsilon + S_T \cdot \Delta T \qquad (4\text{-}6)$$

Where S_ε and S_T are the FBG's strain and temperature sensitivities with typical values of resp. 1.2 pm/μm and 10 pm/°C in the C-band[1] wavelength region (1525 – 1565 nm). As is clear, these sensitivities are actually dependent on the Bragg wavelength λ_B. For wavelength variations within the C-band region, they are usually approximated as being constant, which results in a maximum error of ~2.6% in the wavelength shift[2].

When the fibre is embedded, bonded in a host structure or coated with a different material, the Bragg Equation (4-6) must be modified to account for the thermally induced axial strain (ε_{th}) by the mismatch in expansion and shrinkage of the optical fibre and the surrounding material [7, 8]: $\Delta\varepsilon_{th} = (\alpha_H - \alpha_f)\Delta T$, where α_H is the thermal expansion of the host structure in the longitudinal direction of the optical fibre. This has effect on the strain part of the Bragg equation [9, 10]. A generalised equation can be given, assuming that the strain-transfer of the host structure to the optical fibre is ideal [7, 11]:

$$\Delta\lambda_B = S_\varepsilon \left\{\Delta\varepsilon + \left(\alpha_H - \alpha_f\right)\Delta T\right\} + S_T \Delta T \qquad (4\text{-}7)$$

For example, de Oliveira et al [10] measured the strain coefficients after embedding in an carbon fibre reinforced epoxy composite manufactured on various mould materials. The maximum deviation was 2% for the strain coefficients when compared to that of the bare FBG.

4.2.2 Temperature compensation

Since the wavelength shift of an FBG is sensitive to both strain and temperature, this means that, in order to determine strains in an accurate manner, one must always compensate for the temperature variations. In most publications that studied non-isothermal curing of a polymer with FBGs, this was noted to be of paramount importance for measurement of

[1] The "C-band" wavelength range is most often used in telecommunication applications for its low signal loss.
[2] With 1% strain and a temperature difference of 100°C, $\Delta\lambda$ (λ_B=1525 nm) = 4.34 nm, and $\Delta\lambda$ (λ_B=1565 nm) = 4.45 nm.

shrinkage strains and thermal transitions [11-19]. Two different methods can be used to achieve temperature compensation [4, 11]:

1. Employment of at least two FBGs: one to measure the strains and one to determine the wavelength variations corresponding to temperature changes. This latter must then be free from any external strains. A relative easy and simple method is to use a capillary or ferrule design where the 'temperature'-FBG is kept strain-free [4, 20-22]. The wavelength shifts registered with this grating can be subtracted from those of a similar non-protected FBG (often located in the same optic fibre), to determine the strain ($\Delta\varepsilon$) contribution.
2. Temperature calibration of the FBGs combined with temperature registration during testing [4, 13, 20, 23]. This FBG temperature calibration must be carried out in advance to obtain a relation between the temperature and wavelength. When the temperature of the specimen is measured close to the FBG sensors, with for example a thermocouple, the thermal wavelength shifts can then be calculated and subsequently subtracted from the total wavelength shifts. However, temperature calibration is very time consuming and a hysteresis effect may be present due to annealing of the fibre coating due to high temperature excursions during the test. Therefore, before testing a thermal treatment is recommended to stabilise the optic fibre.

In addition, the use of a thermochromic material is proposed for temperature sensing [24] as well as a method to discriminate between temperature and strain response with only one FBG [25], but these have not yet been applied in a polymer composite environment.
When no temperature compensation is available for the FBG sensor signal, only the wavelength difference at equal temperatures ($\Delta T = 0$) can be determined, from which the strains can be calculated [7].

4.2.3 Peak splitting

Peak splitting of the Bragg wavelength may occur due to non-uniform strain fields around the Bragg grating, see Figure 4.1.

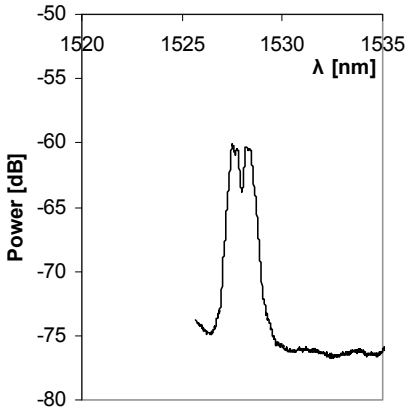

Figure 4.1: Example of peak splitting of a Bragg wavelength.

In the case where a variation in axial strain grating is present along the length of the grating, e.g. due to non-uniform curing around the optic fibre, a double peak is reflected. Some researchers make use of this property by using very long FBG gratings, in the order of centimetres [26, 27]. In this case, the intensity of the peak reflection decreases significantly. One method to distinguish between strain-inhomogeneity along the grating length was presented by Botsis *et al* [28].

Peak splitting can also occur when transversal forces (forces perpendicular to the axial direction of the fibre) are present [23, 29]. This type of peak splitting can be identified by a changing wavelength difference between the split peaks upon temperature variations; usually the difference increases upon cooling. For example when the surrounding material induces transversal strains, such as in a curing polymer, and shrinks further upon cooling, this will induce additional radial forces in the optic fibre.

4.2.4 FBG Hardware

Choice of grating type and characteristic Bragg wavelength is dependent on the data acquisition unit, but even more important are the experiments. The acquisition unit can only register a certain range of wavelengths, which is determined by the optical source of the interrogator. For experiments requiring tensile deformations, it is preferred to have a characteristic wavelength in the lower region of the wavelength bandwidth, whereas for compressive testing (for example shrinkage of polymers) a higher Bragg wavelength is recommended.

Moreover, much effort is ongoing in the world regarding optimisation of the FBG hardware and peak analysis. For example, with a new polarisation filter, it may be possible to quantify strains in three dimensions. For more background regarding the hardware and a more

detailed description of the FBGs and the future capabilities, the reader is referred to the work carried out by the group of Prof. Degriek at Ghent University, Belgium.

Draw Tower Gratings®

The single mode[3] optical fibre that is used for this research, is made of fused silica (SiO_2) with a Germanium (Ge) doped core for high photosensitivity, which is necessary for inducing the periodic refractive index pattern and thus creating the Bragg grating. The 'draw tower' gratings (DTG®s) used for this thesis are inscribed during the manufacturing process of the optic fibre by means of a lithographic process and are coated immediately after the inscription of the Bragg grating [5, 30]. This is different from most other FBGs described in literature, where the fibre is made photo-sensitive by means of a hydrogen environment, usually carried out by stripping the cladding, application of the grating and renewed cladding [10, 31]. This latter type of grating is less stable and requires annealing above the maximum service temperature for several hours [10, 21, 31, 32], whereas the DTG®s can be used immediately. Another disadvantage of 'home-made' gratings is that every grating has its own thermo-optic constant. Therefore, strain and temperature calibrations need to be carried out for every grating whereas with DTG®s, calibration of the batch suffices.

An ORganically MOdified CERamic (Ormocer®) coating was applied, which provides excellent mechanical properties such as an ultimate strain value between 5-6%, good bonding with the optical fibre glass surface, and a comparable CTE as the optic fibre, rendering the effect of $\Delta\varepsilon_{th}$ in Eq. (4-7) negligible.

When using the Draw tower gratings, the following points should be noted:

- Temperatures exceeding 350°C will erase the grating.
- Thermal treatment or temperature variations do not result in significant changes of the strain coefficient (1-P) = 0.78, which is contrary to the commonly used GeO_2 doped silica optic fibres [21, 31].
- Knowledge and experience are prerequisites for splicing and connecting of the optical fibres without extensive signal loss. In this case, the reflected signal is used for data interpretation. This means that at the end of the fibre, a clean cut ("cleave") should be available for a proper signal reflection.
- The minimal bending radius is around 5 mm, therefore acute angles need to be avoided.

Regarding the Ormocer® coating, the following points must be addressed:

- The thermo-optic sensitivity S_T changes from ~10pm/°C to ~12 pm/°C
- During a thermal treatment, especially in the presence of oxygen, the coating shows chemical ageing, resulting in a lower wavelength. Therefore, in the case where a

[3] Single mode fibres are most suitable for transmission of wavelengths over a long distance due to a narrow core through which the rays of light cannot escape [11].

temperature calibration is required, the optic fibre requires a thermal treatment before to stabilise the coating. It is recommended to anneal the optic fibre for at least 15 min to 2 hours at a temperature of 10-20°C above the expected maximum use temperature. This annealing effect of the coating is insignificant below 200°C.

- The coating can absorb moisture from the environment or any other solvent, resulting in an increase of wavelength due to swelling of the coating. Therefore, it is required to dry the optic fibre before testing or to saturate the coating with the solvent that is present in a reactive polymer system. This can be determined by monitoring of the wavelength shift until a constant value is reached due to saturation.

4.3 Experimental procedures

4.3.1 Materials

For the turane polymer two separate components need to be prepared:

- Component A, consisting of the Daron® ZW6154 hybrid system (DSM Composite Resins, Netherlands) mixed with peroxide (Lucidol® CH50X, Akzo Nobel, Netherlands) in a mass ratio of 100:2.
- Component B, consisting of Lupranate® M20R (DSM Composite Resins, Netherlands) mixed with Accelerator (NL64-10P, Akzo Nobel, Netherlands) in a mass ratio of 35:2 (relative to Daron® ZW6154) to form component B.

After mixing the two components, the liquid was degassed for 5 minutes in a vacuum oven.

4.3.2 Test set-up

Glass cylinders (25 ml, outer diameter 21 mm, wall thickness 1.6 mm, height 175 mm) were coated with Renlease® wax (Huntsman, USA). A simple guiding system was placed on top of the cylinder to ensure that the optic fibre was suspended in the centre of the cylinder, see Figure 4.2 The optic fibre and capillary were cleaned with ethanol and connected to an FBGScan 616 (FOS&S, Belgium). A K-type thermocouple was carefully positioned close to the gratings and connected to a Keithley data logging device. Data acquisition frequency was 5 seconds (0.2 Hz). After mixing and degassing, the resin was gently poured into the test tubes and allowed to cure. This test was repeated once.

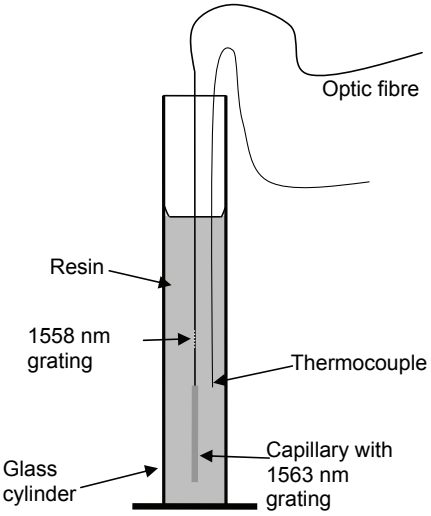

Figure 4.2: Schematic view of matrix shrinkage test set-up.

4.3.3 Optic fibre preparation

The Draw Tower Gratings (DTG®'s) are inscribed in the core of a Single mode optical fibre with core and cladding diameter of 6 and 125 µm resp., as provided by FBGS-Technologies GmbH (Germany). The optic fibres contained two 4 mm long gratings with Bragg wavelengths of 1558 and 1563 nm, and held an Ormocer® coating with outer diameter 195 µm, as supplied by FOS&S, Belgium. Preliminary tests with 4 and 8 mm gratings showed that the 8 mm gratings demonstrated much more splitting of the wavelength peak, which indicates that the strain development is not homogeneous along the length of the optic fibre. To obtain a more stable signal, the smaller grating length of 4 mm was chosen. The disadvantage is that the 4 mm gratings are less reflective.

As noted in Section 4.2.2, strain-free or FBG temperature sensors are required for temperature compensation in the case of strain determination with FBG sensors. For this purpose, the 1563 nm Bragg grating was surrounded by a 40 mm long stainless steel (AISI 304) capillary with inner diameter 0.6 mm and outer diameter 1.0 mm, which was sealed at the extremities with high temperature resistant epoxy glue, Epotek® 353ND (Gentec, Belgium), see Figure 4.3. A tiny polyimide tape was used to seal the gap between the optic fibre and the capillary during gluing. More details on the preparation of these temperature sensors can be found in Appendix B. A metal capillary was chosen for its good thermal conductivity and there is no affinity (static attraction) of the optic fibre towards the metal surface of capillary, unlike a glass ferrule [21].

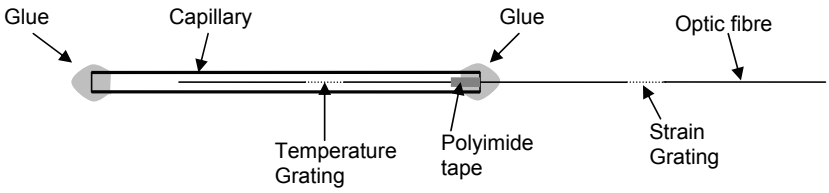

Figure 4.3: Schematic view of Bragg grating temperature sensor.

4.3.4 Calculations

The curing shrinkage of the matrix as experienced by the strain grating, results in a wavelength shift due to strain development in the direction of the optic fibre axis. Since no mechanical strain is applied ($\Delta\varepsilon=0$), it can be said that this strain consists only of the thermally induced axial strain in Eq. (4-7) [7, 8]: $\Delta\varepsilon_{th} = (\alpha_H - \alpha_f)\Delta T$. The linear strain development during cure can then be calculated with Eqs. (4-5) and (4-7), where $\Delta\varepsilon_{lin} = \Delta\varepsilon\ (=0) + \Delta\varepsilon_{th}$:

$$\Delta\lambda_B = \lambda_B(1-P)\cdot\Delta\varepsilon_{lin} + \lambda_B(\alpha_n + \alpha_f)\cdot\Delta T \qquad (4\text{-}8)$$

and

$$\Delta\lambda_B = \lambda_B^i - \lambda_B^0 \qquad (4\text{-}9)$$

λ^0_B and λ^i_B are the initial and the registered wavelengths at points *0* and *i*, resp. The initial Bragg wavelength is determined by averaging a tenfold of wavelength measurements at the reference point.

It must be noted that the Bragg wavelengths λ^0_B for the strain and temperature grating are not equal (1558 and 1563 nm, respectively). Therefore, the wavelength shift of the 'strain-free' grating is used to calculate the temperature dependence $(\alpha_n+\alpha_f).\Delta T$ of the optic fibre. Assumed is that there is no lag in temperature measurement due to the capillary and that the temperature variation between the encapsulated grating and the strain-grating is negligible. This temperature grating experiences a wavelength shift only due to thermal variations: $\Delta\varepsilon_{lin} = 0$. Using this in Eq. (4-8), and a subscript *T* denoting the strain-free grating or temperature grating, gives:

$$\left(\frac{\Delta\lambda_B}{\lambda_B^0}\right)_T = (\alpha_n + \alpha_f)\cdot\Delta T \qquad (4\text{-}10)$$

Combination of Eqs (4-8) and (4-10) then gives:

$$\left(\frac{\Delta\lambda_B}{\lambda_B^0}\right)_S = (1-P)\cdot\Delta\varepsilon_{lin} + \left(\frac{\Delta\lambda_B}{\lambda_B^0}\right)_T \qquad (4\text{-}11)$$

Where subscript *S* represents the strain grating.
The (linear) strain $\Delta\varepsilon_{lin}$ can then be calculated by rearrangement of this equation:

$$\Delta\varepsilon_{lin} = \frac{\left(\frac{\Delta\lambda_B}{\lambda_B^0}\right)_S - \left(\frac{\Delta\lambda_B}{\lambda_B^0}\right)_T}{(1-P)} \qquad (4\text{-}12)$$

The factor (1-P) equals 0.78 for the gratings used here and $(\alpha_n+\alpha_f)$ in Eq. (4-10) is usually 6.27×10^{-6} °C^{-1}.
It must be noted that the wavelength shift value $\Delta\lambda_B$ is dependent on the Bragg wavelength λ_B in Eq. (4-5), and in Eq. (4-12) this is not taken into account. An error analysis in Appendix B showed that this results in a linear strain $\Delta\varepsilon_{lin}$ variation of 0.03%, which can be neglected.
To determine the CTE of the polymer with FBGs for comparison with TMA results, the results for $\Delta\varepsilon_{lin}$ can be used, because there is no externally applied strain: $\Delta\varepsilon = 0$, and therefore $\Delta\varepsilon_{lin}$ equals $\Delta\varepsilon_{th} = (\alpha_H - \alpha_f)\Delta T$. From the slope in a $\Delta\varepsilon_{lin}$ versus temperature graph, $(\alpha_H - \alpha_f)$ can be determined. Since α_f is known, the matrix coefficient of thermal expansion α_H, can be calculated.

4.4 Polymer shrinkage results and discussion

During the matrix shrinkage test the wavelength shifts of the two gratings were recorded as well as the temperature with a thermocouple. The strain was calculated from the FBG wavelength variations with Eq. (4-12). During the first test, the thermocouple failed (specimen 1), but the encapsulated FBG can still be used as temperature sensor. The temperatures that were recorded by the thermocouple before it failed, are used for temperature calibration, i.e. the Bragg wavelengths are fitted to the temperature data. This resulted in a linear equation by which the temperatures can be calculated from the wavelength values.

In the following figure, the time-dependent strain and temperature profiles are shown for the two specimens. At time = 0 minutes, the components were mixed.

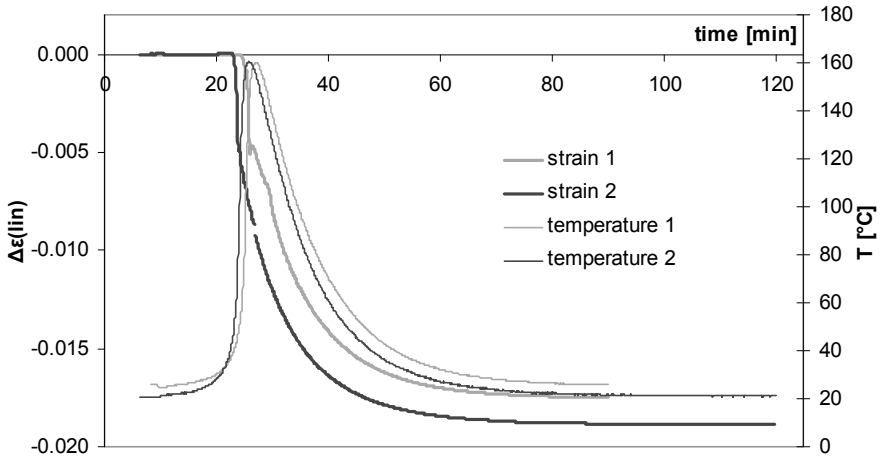

Figure 4.4: Curing strain and temperature of two different turane specimens 1 and 2.

The temperature curves show that the resin temperatures start to rise almost immediately when the measurements were started, indicating that the exothermal polymerisation reaction has already started. After almost 20 minutes, the temperature starts to rise rapidly and very high peak temperatures are reached: the average peak temperature was 160.5°C with standard deviation 0.2°C, which compares well with the peak temperatures of 150-180°C mentioned in the manufacturer's datasheet [33]. The strain curves show that shortly after the temperature rise, the strain gratings register the build-up of compressive strains. This indicates that from that point onwards, the curing polymer has sufficient strength to transfer the shrinkage strains to the optic fibre. This can therefore be identified as the gel point. Gelation at this point was also observed for the remaining resin in the mixing pot. The gel point is reached after 23 and 24.5 minutes for specimen 1 and 2, respectively, which correlates well with the gel time of 20-25 minutes mentioned in the manufacturer's datasheet. From the gel point onward several anomalies can be seen in the curves and therefore in Figure 4.5 this part has been magnified.

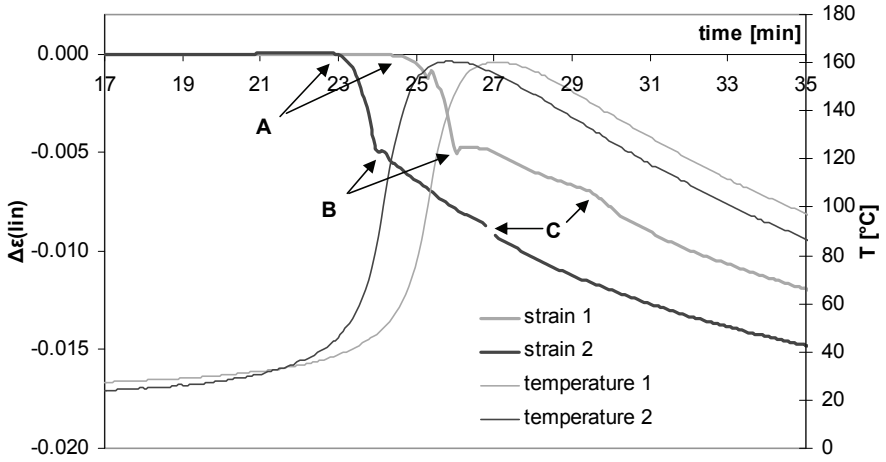

Figure 4.5: Magnification of Fig. 4.4.

The gel point occurs at Point A. It seems that at point B a major event occurs, especially since the slope of the strain-time curve changes. However this cannot be the vitrification point, since the temperature still increases due to the reaction exotherm, meaning that the curing reaction is still taking place. If it had been the vitrification point, the grating would start to register thermal expansion behaviour of the surrounding glassy polymer due to the temperature variation, as seen by Harsch *et al* [19], which is not the case. What is striking, is that this point occurs at equal strain values for both specimens, and not at similar temperatures. This indicates a mechanical effect, such as detachment of the resin from the glass cylinder surface, which was indeed observed to occur quite instantaneous despite the release agent. Unfortunately, the cured polymer could not be released from the glass cylinder to study this tool-part interaction further. Another possible explanation is that moisture absorbed by the Ormocer® coating results in poor bonding between the turane and the optic fibre [34], causing the shrinking turane to debond slightly from the optic fibre with 'stick-slip' behaviour, which would explain the suddenness of the point as well as the change of slope.

At point C the transition from gel to the glassy state occurs, which was also observed in the remaining resin in the mixing pot. Usually this rubber-to-glass transition is accompanied by an exothermic heat release (causing thermal expansion) and a change in slope of the graph, as visible in Fig. 4.4. For both specimens this transition occurs below the peak temperature, i.e. ~140°C for specimen 1 and ~157°C for specimen 2. The gap in the strain curve of specimen 2 around 27 minutes can be explained by temporary peak splitting due to local strain variations around the grating.

The glass transition is also clearly displayed in Figure 4.6, where the strain development with temperature[4] is given for both specimens, and points A, B, and C are the same as indicated in Fig. 4.5.

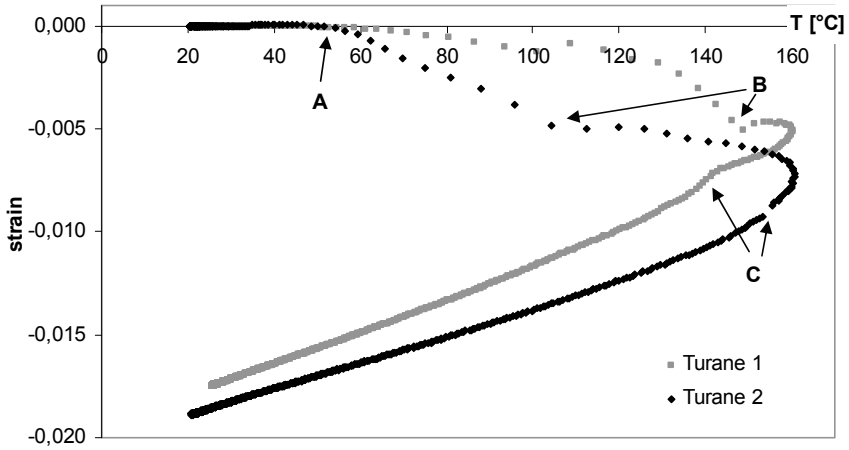

Figure 4.6: Strain development with temperature during cure of turane.

From this figure it is clear that strains start building up when the polymer has a temperature of ~40°C (gel point), which compares reasonably with the ~35°C noted in the manufacturer's datasheet. The results show that almost half of the total shrinkage that contributes to strain build-up is due to chemical shrinkage, whereas the other half comprises thermal shrinkage during cooling from the vitrification point (C).

The slope of the linear portion of the curve below point C can be used for determination of the coefficient of thermal expansion (CTE) of the glassy polymer. Between 100°C and 25°C the CTEs were $76.7 \cdot 10^{-6}$ °C^{-1} and $63.0 \cdot 10^{-6}$ °C^{-1} for specimen 1 and 2, resp. The average linear compressive strain after curing is 1.82% with a standard deviation of 0.10%.

4.5 Postcuring and thermal cycling

4.5.1 Experimental procedures

Specimen preparation

The cured turane specimens with embedded FBG sensors and thermocouples were prepared as described in Section 4.3. For the DSC tests, thin specimens were sliced from the cured resin that was left in the mixing cup. This resin was also used for preparation of the

[4] Please note that the temperature variation is a result of the intrinsic heat release during curing of the polymer and was not induced by external factors.

specimens for TMA/ dilatometry. Rectangular bars with dimensions 60 x 4 x 4 mm were cut with a Struers Unitom® liquid cooled cutting machine. These were then milled and cut to specimens of 10 x 3 x 3 mm. All DSC and TMA specimens were degreased with ethanol and dried overnight in a vacuum drying oven at 60°C prior to testing. To compare the expansion and shrinkage behaviour between the cured and postcured polymer, two out of four TMA specimens were thermally treated (postcured) by placing them in a glass tube that was suspended in the oil bath undergoing the postcure cycle for the FBG specimens, see below.

Test set-up

According to the manufacturer's recommended processing cycle, a postcure cycle of 4 hours at 200°C is required for this type of turane. The glass cylinders with the cured turane were placed in a 2500 ml glass beaker filled with thermally conductive silicone oil, and the beaker was wrapped with silicate wool and aluminium for thermal insulation. The beaker was placed on top of an electrically heated plate (Ikatherm® HCT, from IKA Labortechnik, Germany) with a temperature controller (Yellowline TC1, from IKA Labortechnik, Germany). The optic fibres and thermocouples that were co-cured with the turane were connected to the FBGScan 616 and Keithley data logging device, resp. Another thermocouple was used to monitor the oil temperature.

The oil was heated to 200°C, maintained at that temperature for 4 hours and cooled to room temperature. A second thermal cycle included heating to 150°C[5] and cooling back to room temperature. The temperature was raised and lowered in steps of ~50-80°C, and after each step the oil temperature was kept constant to reach thermal equilibrium in the polymer specimen to obtain isothermal wavelength readings of the FBGs.

The specimens for differential scanning calorimetry were contained in aluminium pans with lids and placed in the DSC apparatus (Perkin Elmer DSC7). The test cycle consisted of heating from 25°C to 225°C, cooling to room temperature followed by a similar second heating cycle, using a heating and cooling rate of 10°C/min. For a temperature-dependent specific heat curve, the test runs were first carried out with the empty sample pan and calibrated with a sapphire sample. In total three test runs were performed. The sample mass was determined with a Mettler AE240 balance with an accuracy of 0.01 mg.

The linear thermal expansion and contraction of the specimens during heating and cooling, resp., was monitored using a Perkin Elmer DMA7e Thermal Mechanical Analyser (TMA) with a push-rod dilatometer apparatus. The displacement sensor and the specimen holder were

[5] During the second heating cycle the temperature was raised only to 150°C and not 200°C, since at that temperature no more strain variations were detected. This will be explained in further detail in the experimental results.

made of quartz and surrounded by an oven. A normal load of 100 mN was applied and the push rod had a diameter of 3 mm. A thermocouple was placed next to the sample for temperature control. The thermal cycle consisted of heating from 30°C to 205°C with 10°C/min, hold at 205°C for 2 minutes and cooling from 205°C to 55°C with 10°C/min. During testing an inert atmosphere was created with nitrogen gas. One heating and cooling cycle was carried out with aluminium (99.5%) for reference purposes. Two cured and two postcured specimens were tested.

Calculations

During postcuring and thermal cycling the thermal expansion and contraction of the polymer with embedded FBGs and thermocouple can be calculated with Eq. (4-12). The initial Bragg wavelength λ^0_B is the same as used for the cure shrinkage test, unless indicated otherwise. For the dilatometry test the following equation can be used:

$$\Delta\varepsilon_{lin} = \frac{l_i - l_0}{l_0} = \frac{\Delta l}{l_0} \tag{4-13}$$

Where l_0 and l_i are the specimen length at the start of the thermal cycle and at any given time *i* during the cycle, respectively.

An effort was made to determine the coefficient of thermal expansion (CTE) by fitting the slope of the strain-temperature graphs that were the result of the dilatometry and FBG tests. Any transition points were identified by the intersection of two tangent lines.

4.5.2 Results and discussion

FBGs

In the following two figures the strains are depicted as determined with FBGs for the two turane specimens during the postcure and second thermal cycle. For this second cycle the maximum temperature was ~150°C, because the strain-free point was already observed below this temperature, and increasing the temperature further to 200°C was therefore deemed unnecessary. The polymerisation shrinkage is also shown for comparison.

As mentioned earlier, the temperature was varied in steps and after each step the temperature was kept constant. Due to the control of the oil bath, small temperature fluctuations still occurred around the set temperature, causing strain variations. This is visible in Figures 4.7 and 4.8 as pigtail-like loops. When during the postcure or thermal cycle the strain was observed to develop differently than could be expected from simple thermal expansion or contraction, for example due to strain relaxation, the temperature was kept

constant at that point to allow full recovery. This was observed to occur at different temperatures for both specimens.

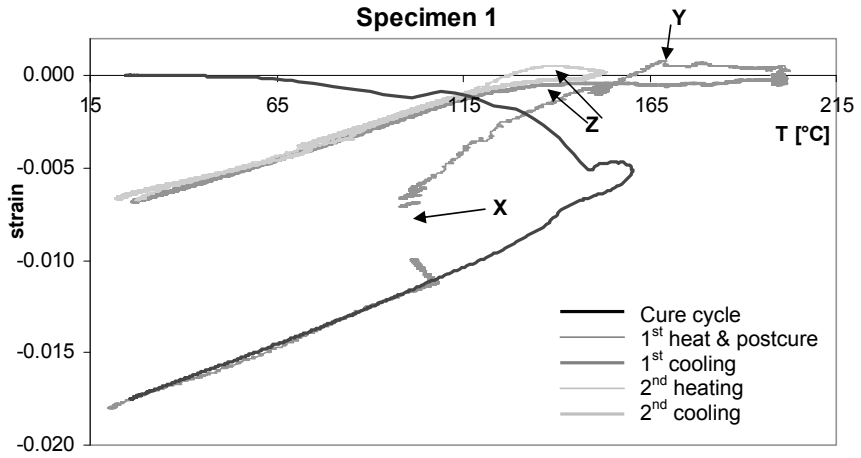

Figure 4.7: Curing strain, postcure and thermal cycling of turane specimen 1.

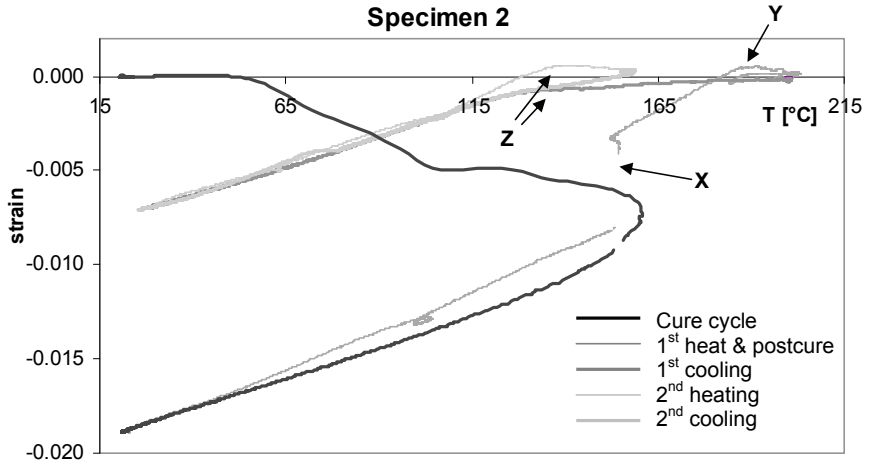

Figure 4.8: Curing strain, postcure and thermal cycling of 2nd turane specimen.

During heating towards the postcure temperature of 200°C, strain development of Specimen 1 closely follows the curing profile during cooling. For specimen 2 this is only the case at lower temperatures. At points X the strain curve shows significant strain relaxation (especially when the temperature was maintained around a set temperature), visible as a significant jump in strain of ~0.005. This temperature was then held until no more relaxation

took place. The gap in the curves can be explained by peak splitting of the FBG signal, which was caused by non-uniform strain relaxation along the axis of the grating. For specimen 1 relaxation occurred at ~105°C over a period of 45-50 minutes, whereas for specimen 2 this was at ~150°C during ~13 minutes. This is consistent with the theory that relaxation takes place faster at higher temperatures. The difference in relaxation temperatures can be explained by the difference in T_g, observed as points C in the previous section, resulting from small differences in resin mixture [35].

Upon further heating to the postcure temperature of 200°C, at points Y the strain-free temperature is reached, where the strain diminishes close to 0. For specimen 1 this is at ~169°C, and for specimen 2 ~188°C. This is in line with observations in literature [36, 37], where a strain-free temperature in the vicinity or slightly above the maximum cure temperature (average 160.5°C) was reported. A small overshoot is visible above $\Delta\varepsilon = 0$, which is possibly caused by a thermal 'lag' in expansion of the specimen, followed by strain relaxation. However, it can also be caused by relaxation of the optic fibre itself, since due to the weight of the temperature sensor it was pre-tensioned before the cure cycle took place [38]. The lower strain-free temperature for specimen 1 can be the consequence of the lower relaxation temperature at X. The strain is close to 0 during the postcure cycle, since postcuring occurs above the strain-free temperature, and therefore does not induce additional strains due to chemical shrinkage.

Upon cooling after the postcure treatment, strain development is relatively insignificant at temperatures above 135°C for both specimens. From points Z, linear thermal contraction is observed during cooling. This behaviour indicates a thermal transition temperature (above which the polymer has insufficient strength to transfer strains to the optic fibre), but according to the manufacturer the T_g is above 200°C after the postcure cycle. This transition might be related to the reversible dissociation of the urethane bonds above 140°C [34], but this is not likely to have such an effect on the mechanical properties of the polymer. Another possibility presents the chemical ageing of the components, resulting in another chemical structure of the polymer with different than usual transition points. The effects of ageing are currently studied by the manufacturer. However, points Z are not far from points C in the curing cycle, which leads to believe that indeed a rubber-to-glass transition is observed.

The final residual compressive strain after the postcure cycle is significantly less than after curing for both specimens: $\Delta\varepsilon$ = -0.007, opposed to -0.018; a reduction of 61%. This can be explained by:

- the amount of relaxation at point X;
- a lower strain-free temperature of ~135°C (points Z) than before postcuring (points Y); and

- lower thermal contraction coefficients from points Z due to the higher degree of cure resulting from the postcure cycle: the CTE's for specimens 1 and 2 are 63 and 62 µm/m°C, resp., compared to 77 and 63 µm/m°C before postcure.

Upon the second heating and cooling cycle the strain closely follows the cooling curve of the postcure cycle for both specimens, indicating no additional chemical changes or relaxation points. This time the strain-free temperature is reached around point *Z* (135°C), which supports the hypothesis of a T_g presence at this temperature. Again a small strain overshoot is found, followed by relaxation.

DSC & TMA

The results of a DSC test of one representative specimen are shown in Figure 4.9.

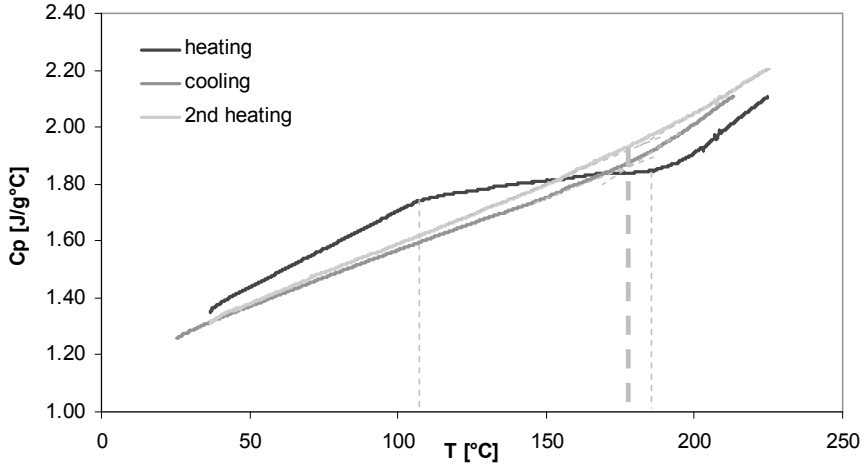

Figure 4.9: DSC curve for cured (not postcured) turane (vertical axis is endothermic energy).

Between 110 and 190°C relaxation behaviour is clearly visible (strain recovery is usually accompanied by exothermic behaviour of the specimen [39]). This is fairly consistent with the relaxation behaviour as observed with the FBGs between points X and Y in the same temperature range. Upon cooling and reheating the curves show no more relaxation, but only a minor deviation from a straight line at temperatures indicated by the fat dotted line around 183°C. The DSC results thus explain the irreversible relaxation behaviour at points X in the previous figures, but not the 'T_g' as found with the FBGs around 135°C (points Z).
Therefore, two cured and two postcured turane specimens were exposed to one heating and cooling cycle in a TMA, of which the results are shown in Figure 4.10.

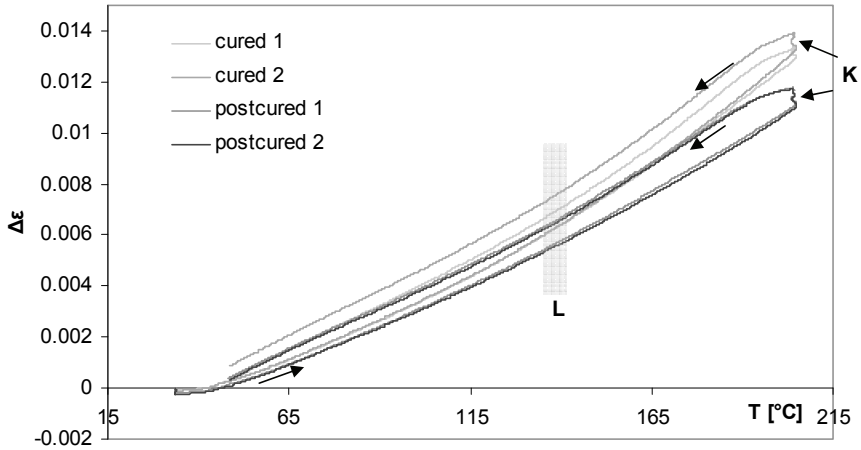

Figure 4.10: Dilatometry results for cured and postcured turane specimens.

During the isothermal step at point K, thermal lag of the test set-up caused additional expansion. This thermal lag is also the cause for the lower slope in the first parts of the heating and cooling curves and can therefore be neglected. The average CTE's and transition temperatures (determined by the intersection of two slopes, area is indicated by L) are given in Figure 4.11 (no CTE value is given by the manufacturer for comparison).

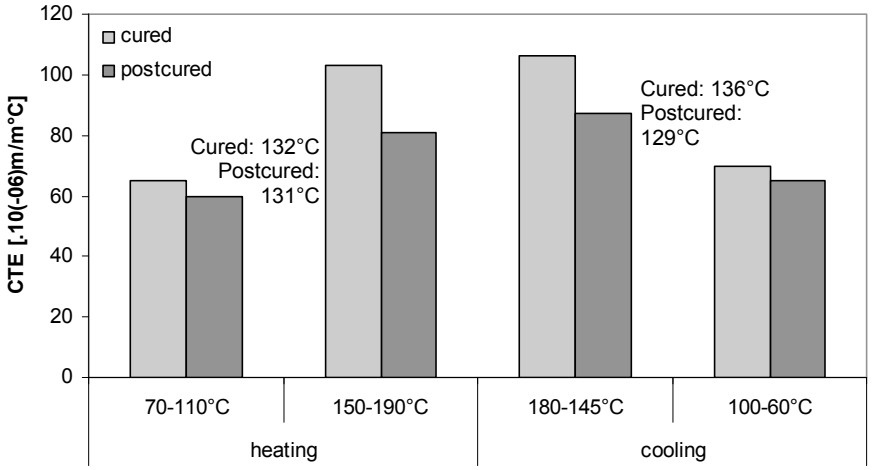

Figure 4.11: CTEs and transition temperatures for cured and postcured turane specimens (TMA).

From Figures 4.10 and 4.11 it is clear that the postcured specimens show lower thermal expansion and contraction upon heating and cooling, resp., than the cured specimens. This

can be attributed to a higher degree of cure after postcuring and was also found with the FBGs. The thermal transition temperatures L are also close to the point Z temperature of 135°C in Figures 4.7 and 4.8. Therefore it is assumed that the same transition is detected, but further research is needed to identify the physical or chemical origins of this transition, which is beyond the scope of this research.

Comparison between FBG and TMA results

A comparison between the FBG and dilatometry data during heating to the postcure temperature is given in Figure 4.12. The FBG results are calculated using the Bragg wavelength at the start of the postcure cycle and the dilatometry curve was shifted over the horizontal axis for comparison.

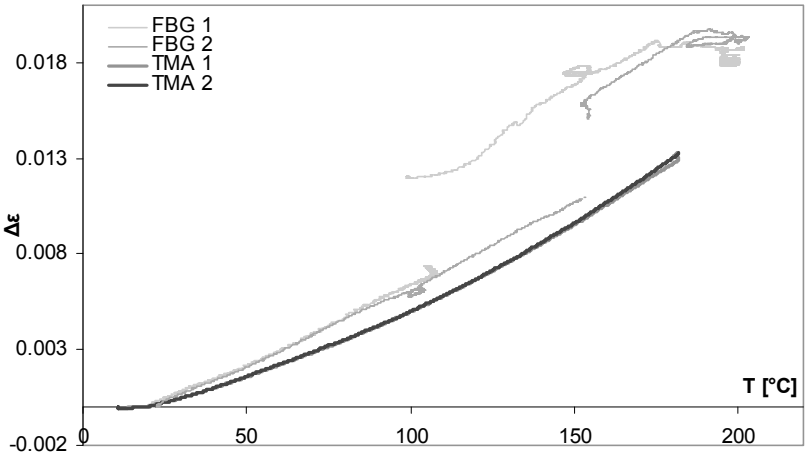

Figure 4.12: Thermal strain upon heating for not-postcured FBG (thin lines) and dilatometry (thick lines) specimens.

The dilatometry results do not match the FBG test results, whereas both FBG specimens show similar behaviour at the lower and higher temperature ranges. Compared to the dilatometry results, the FBG test shows higher thermal expansion as well as relaxation jumps at temperatures above 100°C. The discrepancy in thermal expansion may be caused by a thermal lag in the dilatometry test set-up, however this does not account for the absence of the relaxation jumps.

A similar graph was constructed for the thermal contraction during cooling after postcure in Figure 4.13, even though the dilatometry specimens had not experienced a complete

postcure cycle. The dilatometry and FBG strains are calculated with respect to the specimen length and Bragg wavelength at the isothermal temperature of 205°C, resp. The dilatometry results are shifted over the vertical axis for comparison with the FBG results.

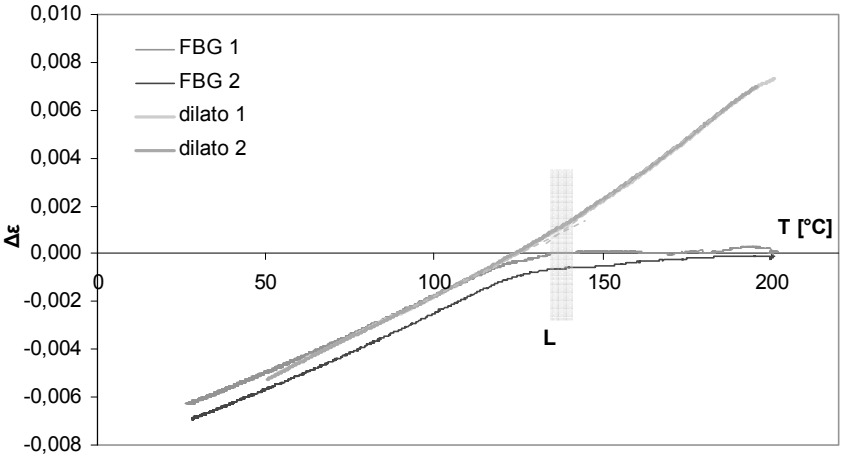

Figure 4.13: Cooling graphs after postcure for FBG specimens (thin lines) and after first heating for dilatometry specimens (thick lines).

The deflection point L in the dilatometry curves lies close to the thermal transition point Z as found with the FBGs. This Figure clearly illustrates the difference in working principle of the two test methods: the FBG method is capable of identifying transitions due to variations in strain transfer to the optic fibre, i.e. due to changing mechanical properties, whereas the dilatometry test monitors volumetric changes that can be related to density.

The FBG and dilatometry results of the second thermal cycle after postcuring are given in Figures 4.14 (heating) and 4.15 (cooling). Reference values for the calculations of strain are taken at the start of the second thermal cycle at room temperature. The dilatometry test results are shifted along the horizontal axis.

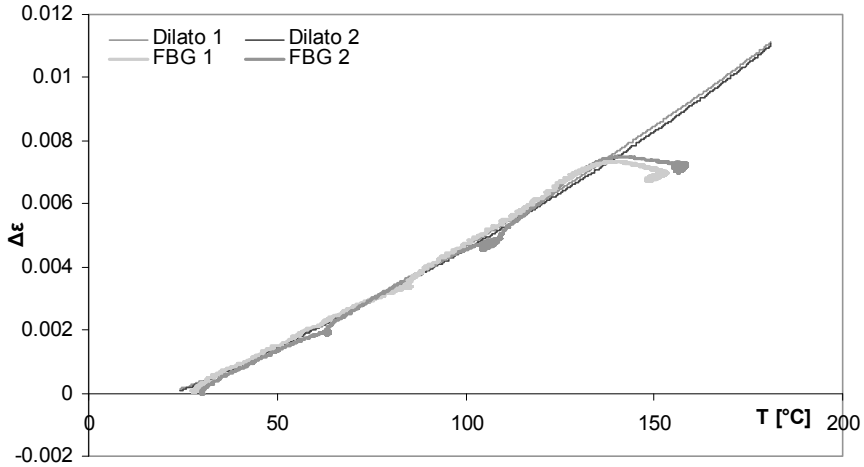

Figure 4.14: Heating of postcured dilatometry (thin lines) and FBG (thick lines) samples.

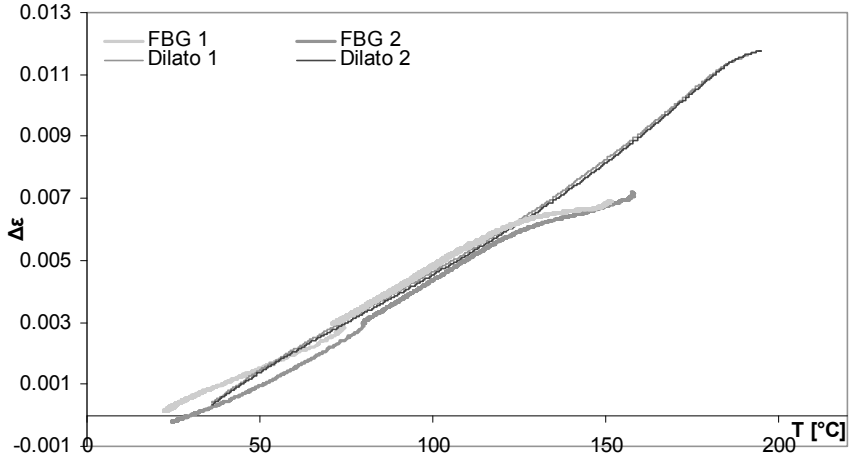

Figure 4.15. 2nd Cooling cycle for FBG (thick lines) and dilatometry (thin lines) specimens.

As is clear from Figures 4.14 and 4.15, the thermal expansion and contraction of the postcured specimens match for both tests below 130°C. The humps in the FBG curves can be attributed to wavelength shifts during isothermal temperatures. The similarity between the dilatometry and FBG curves indicates that the strain transfer between the polymer matrix and the optic fibre is sufficient.

4.6 Conclusions

Attempts to determine the polymer cure shrinkage responsible for residual strain build-up with fibre Bragg gratings were successful, when compensation for the FBGs response to temperature variations was included. This means that one test set-up, namely an optic fibre with separate temperature and strain gratings, can be used to identify a multitude of polymer properties, that could otherwise only be tested with multiple techniques, such as DSC, DMA and TMA. The polymer parameters that could be established during the cure and postcure cycle are the gel point, the vitrification point, contributions of curing shrinkage and thermal contraction to residual strain formation, the thermal response, strain relaxation, the strain-free point, and coefficients of thermal expansion. The point that could not be established with certainty is the glass transition temperature of the (post)cured polymer.
The FBG results for thermal expansion and thermal transitions of the cured polymer were found to agree well with those obtained with dilatometry and DSC tests, leading to believe that the FBG test provides reliable data.

Regarding the cure of the turane polymer itself; the gel point was clearly identified around the onset of the temperature rise due to exothermal polymerisation. The FBG results showed that almost half of the total shrinkage that contributes to residual strain build-up is due to chemical shrinkage, whereas the other half comprises thermal contraction from the vitrification point. Vitrification seems to take place after the exothermic peak temperature is reached.
The postcure treatment was found to relax internal strains significantly and increase the degree of conversion, which resulted in a lower CTE. The strain-free temperature was found below the postcure temperature of 200°C, and therefore the postcure treatment did not induce additional chemical or thermal strains.

References

1. van Rijswijk, K., Thermoplastic Composite Wind Turbine Blades. 2007. PhD thesis Aerospace Engineering, Delft University of Technology, Delft. 249 pages.
2. Bourban, C., Presentation - Introduction Daron Hybrid Technology. 2006, DSM Composite Resins.
3. FOS&S. Fibre Bragg Grating Technology. 2006 [cited. Available from: http://www.fos-s.be/fos%2Ds/.
4. de Waele, W.A.J., Structural monitoring of composite elements using optical fibres with Bragg-sensors. 2002. PhD thesis Faculty of Engineering, Department of Mechanical Construction and Production, Universiteit Gent, Ghent University. 420 pages.
5. De Baere, I., *et al.*, Strain monitoring in thermoplastic composites with optical fiber sensors: Embedding process, visualization with micro-tomography, and fatigue results. Journal of Thermoplastic Composite Materials, 20(5): 453-472, 2007.
6. Hagemann, V.J., Untersuchungen zum dynamischen Einzelpuls-Einschreiben van Faser-Bragg-Gittern un zu deren Anwendung. 2001. PhD thesis.
7. Leng, J.S., Asundi, A., Real-time cure monitoring of smart composite materials using extrinsic Fabry-Perot interferometer and fiber Bragg grating sensors. Smart Materials & Structures, 11(2): 249-255, 2002.
8. Measures, R., Multiplexed fiber optic structural sensing in structural monitoring with fiber optic technology. 2001, USA: Academic Press. 526-594 pages.
9. Betz, D.C., *et al.*, Advanced layout of a fiber Bragg grating strain gauge rosette. Journal of Lightwave Technology, 24(2): 1019-1026, 2006.

10. de Oliveira, R., *et al.*, Influence of the mould thermal expansion on composite stress build-up during cure, in ECCM-12: 12th European Conference on Composite Materials. 2006, ESCM: Biarritz, France.
11. Antonucci, V., *et al.*, Cure-induced residual strain build-up in a thermoset resin. Composites Part A-Applied Science And Manufacturing, 37(4): 592-601, 2006.
12. Antonucci, V., *et al.*, Real time monitoring of cure and gelification of a thermoset matrix. Composites Science and Technology, 66(16): 3273-3280, 2006.
13. Chehura, E., *et al.*, Strain development in curing epoxy resin and glass fibre/epoxy composites monitored by fibre Bragg grating sensors in birefringent optical fibre. Smart Materials & Structures, 14(2): 354-362, 2005.
14. Cusano, A., *et al.*, Chirped fiber-bragg grating as self-temperature referenced strain sensor in nonisothermal thermoset processing. IEEE Sensors Journal, 6(1): 111-117, 2006.
15. Giordano, M., *et al.*, Monitoring by a single fiber Bragg grating of the process induced chemo-physical transformations of a model thermoset. Sensors and Actuators a-Physical, 113(2): 166-173, 2004.
16. Giordano, M., *et al.*, Advanced cure monitoring by optoelectronic multifunction sensing system. Thin Solid Films, 450(1): 191-194, 2004.
17. Giordano, M., *et al.* Non isothermal monitoring of strain build up in thermoset processing by a single chirped fiber Bragg grating. in Proceedings of SPIE - The International Society for Optical Engineering. 2004.
18. Harsch, M., Karger-Kocsis, J., Herzog, F., Influence of cure regime on the strain development in an epoxy resin as monitored by a fiber Bragg grating sensor. Macromolecular Materials and Engineering, 292(4): 474-483, 2007.
19. Harsch, M., Karger-Kocsis, J., Herzog, F., Monitoring of cure-induced strain of an epoxy resin by fiber bragg grating sensor. Journal of Applied Polymer Science, 107(2): 719-725, 2008.
20. Degamber, B., Tetlow, J., Fernando, G.F., Design and development of low-cost optical-fiber sensors for temperature metrology: Process monitoring of an epoxy resin system. Journal of Applied Polymer Science, 94(1): 83-95, 2004.
21. Frövel, M., *et al.*, Performance Evaluation of Fibre Bragg Gratings over a Large Temperature Range, in 5th International Workshop on Structural Health Monitoring. 2005: Stanford.
22. Jung, K., Kang, T.J., Cure monitoring and internal strain measurement of 3-D hybrid braided composites using fiber Bragg grating sensor. Journal of Composite Materials, 41(12): 1499-1519, 2007.
23. Sorensen, L., Gmur, T., Botsis, J., Residual strain development in an AS4/PPS thermoplastic composite measured using fibre Bragg grating sensors. Composites Part A: Applied Science and Manufacturing, 37(2): 270-281, 2006.
24. Fernandez-Valdivielso, C., Matias, I.R., Arregui, F.J., Simultaneous measurement of strain and temperature using a fiber Bragg grating and a thermochromic material. Sensors and Actuators a-Physical, 101(1-2): 107-116, 2002.
25. Oh, S.T., *et al.*, Discrimination of temperature and strain with a single FBG based on the birefringence effect. Optics Express, 12(4): 724-729, 2004.
26. Eum, S., *et al.*, Resin Flow Front Monitoring for VARTM using Fibre Bragg Gratings, in ICCM-16. 2007: Kyoto, Japan.
27. Menendez, Fernandez, Guemes, Sensing with embedded fiber bragg gratings in extreme mechanical conditions, in ICCM-16. 2007: Kyoto.
28. Colpo, F., Humbert, L., Botsis, J., Characterisation of residual stresses in a single fibre composite with FBG sensor. Composites Science and Technology, 67(9): 1830-1841, 2007.
29. Luyckx, G., *et al.*, Three-dimensional strain and temperature monitoring of composite laminates. Insight, 49(1): 10-16, 2007.
30. Chojetzki, C., *et al.*, Large Fibre Bragg Grating Arrays for monitoring applications - Mde by Drawing Tower Inscription. 2005, IPHT & FOS&S: Jena, Germany & Geel, Belgium.
31. O'Dwyer, M.J., *et al.*, Thermal dependence of the strain response of optical fibre Bragg gratings. Measurement Science & Technology, 15(8): 1607-1613, 2004.
32. Frövel, M., *et al.*, Multiplexable fiber Bragg grating temperature sensors embedded in CFRP structures for cryogenic applications, in 3rd European Conference on Structural Health Monitoring. 2006, UPM-Madrid: Granada.
33. DSM_Composite_Resins, Daron XP 45-A-2, ZW 6154, in Product data sheet. 2006.
34. Verleg, R., Chemical reactions and ageing in Daron(R) turane, recipient: Parlevliet, P.P. 21 december 2007. Personal communication.
35. Jansen, K.M.B., Effect of Resin Formulation on Thermoset Viscoelasticity. Journal of Engineering Materials and Technology 128(4): 478, 2006.
36. Crasto, A.S., Kim, R.Y., On the Determination of Residual-Stresses in Fiber-Reinforced Thermoset Composites. Journal of Reinforced Plastics and Composites, 12(5): 545-558, 1993.
37. Gigliotti, M., Wisnom, M.R., Potter, K.D., Development of curvature during the cure of AS4/8552 0/90 unsymmetric composite plates. Composites Science and Technology, 63(2): 187-197, 2003.
38. Reid, R.G., Paskaramoorthy, R., A novel method to measure residual stresses in unidirectional GFRP Composite Structures, 88(4): 388-393, 2008.
39. Kawakami, H., Watanabe, M., Changes in the Thermomechanical Behavior of Epoxy Glasses Under the State of Strain Aging. Journal of applied polymer science, 107(4): 2095-2100, 2008.

Chapter 5: Shrinkage Determination of a Reactive Polymer with a Volumetric Dilatometry Test Set-up

5.1 Introduction

The results presented in the previous chapter show that fibre Bragg gratings (FBGs) can be successfully applied for determination of curing shrinkage responsible for residual strain formation in liquid moulded composites. However, the magnitude of curing shrinkage as detected by the FBGs could not be compared with other data or test results. Therefore another technique needs to be found and used to measure the shrinkage of a curing polymer and compare the results with those of the FBGs.

As explained in Section 3.6.1, several methods exist to determine the matrix volumetric shrinkage due to polymerisation/curing and thermal effects. One of these techniques allows monitoring of volumetric changes during the entire cure cycle as illustrated in Figure 2.6 and is based on the buoyancy principle: the volumetric dilatometry test [1]. When an object or specimen is fully or partially immersed in liquid, buoyancy exerts an upward force on the object produced by the surrounding fluid, which equals the weight of the fluid displaced by the specimen body. When the volume of the immersed object reduces while the mass does not (as is the case for a curing polymer), the amount of displaced fluid will decrease, resulting in a lower upward force. Therefore, this technique has the capability of monitoring the volumetric shrinkage during the entire cure cycle. This mechanism was recently further developed by Li *et al* [1], where a silicone rubber bag was used that closely followed any volumetric change of the curing polymer resulting in detectable buoyancy variations. In addition, the silicone bag does not adhere to the curing polymer and due to its flexibility is assumed to leave the matrix in a strain-free state.

The aim is to try and make this test method suitable for the polymer systems used in this research. For that purpose, experiments have been conducted with the turane resin system and the results are compared to those of the FBG tests from the previous chapter. In addition, the test can provide useful information on the total matrix shrinkage before gelation. This information is valuable for determination of the amount of resin necessary for resin infusion of composite structures and the prevention of shrinkage porosity and pin-holes [2].

5.2 Experimental procedures

5.2.1 Materials

The materials and their preparation are similar to as described in Section 4.3.

5.2.2 Specimen preparation

The silicone bags and their sealing plugs (see Figure 5.1) were prepared by mixing the two Silastic-M® RTV (Dow Corning, USA) components in a mass ratio of 10:1 and subsequent degassing for 2 minutes. This mixture was applied to the outside of a cleaned glass test tube (outer diameter 20 mm) with a brush and left to cure at room temperature for 24 hours, which resulted in a wall thickness of ~0.5 mm. The plugs were prepared by casting the silicone mixture in a cylindrical mould with similar inner dimensions as the silicone bag, with the copper suspension wires, thermocouple, resin inlet and outlet tubes (made from a silicone hose with outer and inner diameters of 3.2 and 1.6 mm, respectively) already put in place. This was also left to cure at room temperature for 24 hours. After demoulding, the bags and plugs were immersed in water for at least 24 hours to remove any volatiles or uncured silicone molecules. The bags and plugs were dried by placing them in a vacuum drying oven for 24 hours at 50°C and subsequently assembled.

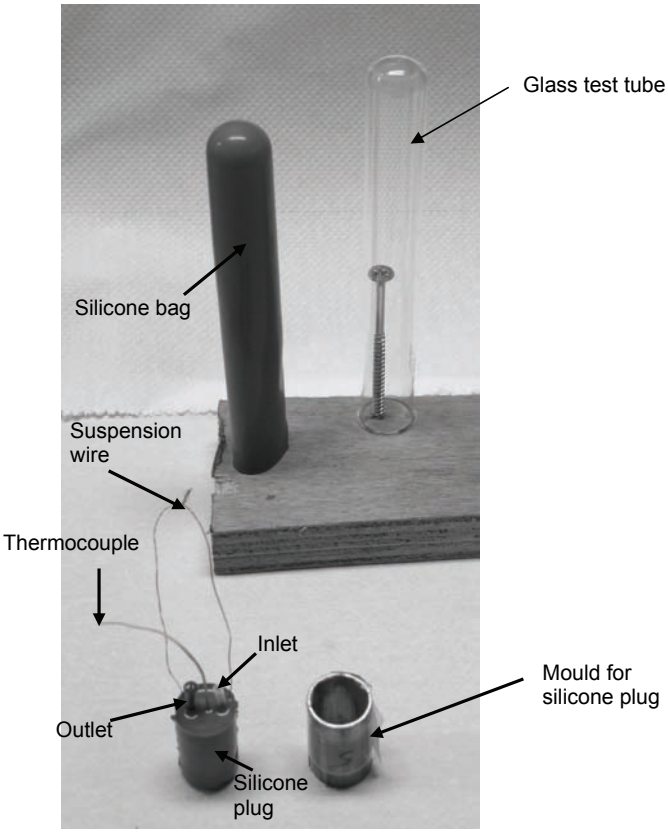

Figure 5.1: Silicone bag and plug for volumetric dilatometry test.

After mixing and degassing of the reactive polymer system in a glass beaker, the mixture was gently poured into a syringe, which was used to fill the silicone bags, see Figure 5.2. The air outlet consisted of a syringe needle, which was retracted after the bag was filled, leaving the silicone rubber to close the puncture to an airtight seal owing to the elasticity of the rubber stopper. Where the thermocouple entered the silicone stopper, a cured epoxy glue (Epotek 353ND, Gentec, Belgium) seal was applied, to prevent oil from seeping into the silicone bag through the braided sleeve surrounding the thermocouple wires. When the silicone bag was filled, the inlet was carefully sealed with a screw.

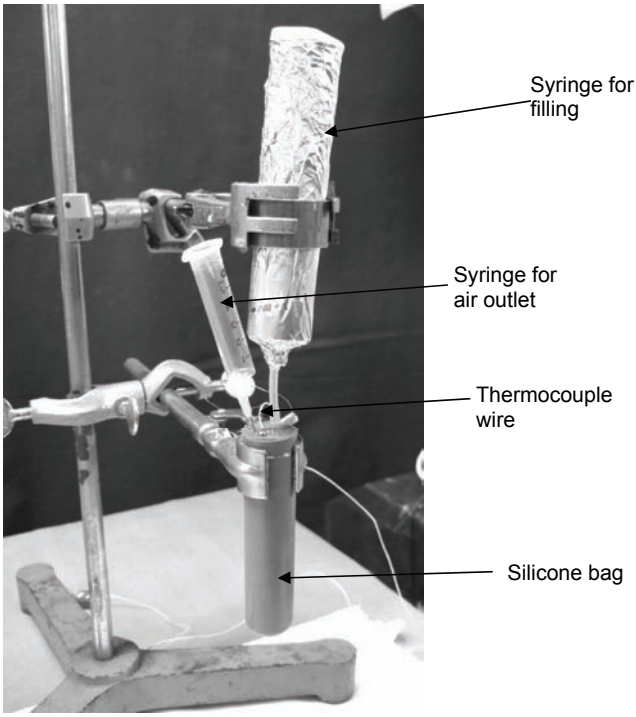

Figure 5.2: Set-up for filling the silicone bag with polymer resin.

5.2.3 Test set-up

A glass beaker (3 litre, Schott Duran) was insulated with silicate wool (RS Components, Netherlands) and aluminium foil. It was filled with Thermia-A® oil (Shell, Netherlands), which is suitable for heat transfer purposes and resistant to temperatures up to 280°C, and placed on a temperature controlled heated plate (Ikatherm® HCT with a Yellowline ETS-D-4 controller, both from IKA Labortechnik, Germany). A resin-filled silicone bag was suspended in the oil below a Mettler Toledo AG204 balance, which was connected to a PC with a data acquisition unit and using Mettler software. This balance was placed on top of a purpose-built

wooden frame, see Figure 5.3. After installation of the silicone bag, an insulated 0.8 mm thin aluminium lid was used to cover the oil-filled beaker and data acquisition was started immediately. A K-type thermocouple was located inside the resin to monitor the temperature during cure and another was positioned in the oil bath to check for isothermal conditions. The thermocouples were connected to a Keithley data acquisition unit connected to a PC. The test was stopped after ~10,000 seconds and the cured polymer released from the bag by careful cutting. The test was performed five times.

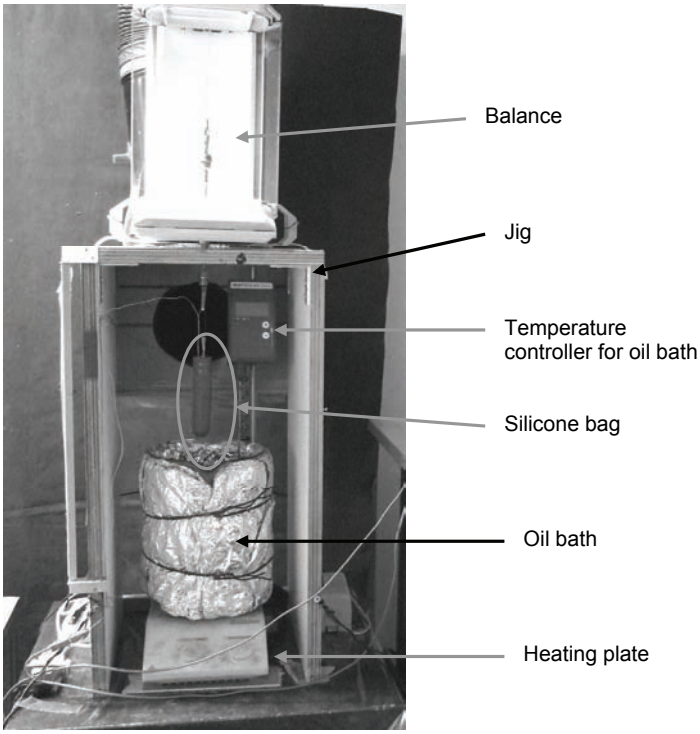

Figure 5.3: Test set-up for volumetric shrinkage detection.

5.2.4 Calculations

The equations to calculate the volumetric shrinkage $\Delta\varepsilon_{vol}$ are derived in Appendix C. For this test, the assumptions of constant polymer mass and constant fluid temperature are valid and, therefore, equation (C-11) can be used:

$$\Delta\varepsilon_{vol} = \frac{m_{tot}^{bal,0} - m_{tot}^{bal,1}}{m_{pol}^{0} - m_{tot}^{bal,0} + m_{bag}^{bal,0}} \qquad \text{(C-11)}$$

Here, m_{tot}^{bal} is the output given by the balance that registers the submersed mass (start value: 20-25 grams), and superscripts *0* and *1* denote the parameters at the reference point and any given time *1* of the test, respectively. The mass of the polymer sample (m^0_{pol}, typical value: 50-60 grams) is determined in air with a similar balance and the empty bag is replaced in the fluid, to determine the mass of the submersed bag $m_{bag}^{bal,0}$ (typical value 11-13 grams).

Possible sources for error are the following:

- When the first values for $m_{tot}^{bal,0}$ are registered, already some time (maximum 5 minutes) has elapsed since the mixing of the resin and a small curing shrinkage may have taken place. This effect is assumed to be negligible compared to the total volume shrinkage.
- During testing, the temperature of the fluid bath may fluctuate due to, for example, heat dissipation of the resin during the exothermic reaction. For the entire duration of a test, a maximum oil temperature variation of 2°C was observed. With Eq. (C-9) and the values mentioned above, this results in an absolute variation in $\Delta\varepsilon_{vol}$ of 0.13%.
- The mass m_{tot}^{bal} recorded during the test, the polymer mass m_{pol}^{0}, and the immersed bag mass $m_{bag}^{bal,0}$ can be determined by the balance with an accuracy of ±10 mg, which results in a variation of ~0.04% in $\Delta\varepsilon_{vol}$.
- When air is entrapped in the silicone bag, this will expand and contract during heating and cooling, resp., resulting in a lower detected volumetric curing shrinkage.

For comparison between the volumetric shrinkage and linear shrinkage, equations have been derived in Appendix A for a few geometrical cases. The equation that is required here is:

$$\Delta\varepsilon_{vol} = (\Delta\varepsilon_{lin} + 1)^3 - 1 \qquad \text{(A-7)}$$

$\Delta\varepsilon_{lin}$ is the linear shrinkage (δ_l in Appendix A) and $\Delta\varepsilon_{vol}$ is the volumetric shrinkage fraction (υ in Appendix A). Rearranging to the linear shrinkage gives:

$$\Delta\varepsilon_{lin} = (\Delta\varepsilon_{vol} + 1)^{1/3} - 1 \qquad \text{(5-1)}$$

5.3 Experimental results and discussion

The volumetric shrinkage results for one specimen are shown in Figure 5.4. At time = 0 minutes the components were mixed. For comparison with the cure shrinkage as measured with the Bragg gratings, the gel point as determined with the FBG test is chosen as reference point (0) in Eq. (C-11), which is when the polymer temperature reached ~40°C.

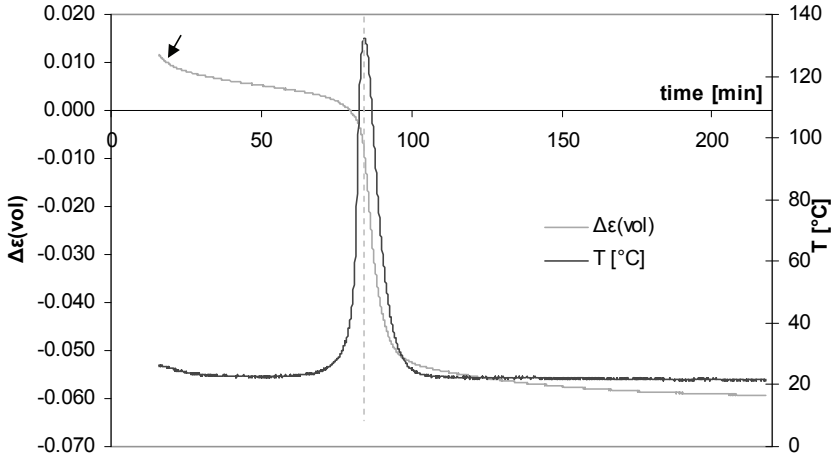

Figure 5.4: Volumetric shrinkage data and temperature profile.

It is clear from the figure that cure shrinkage already occurs immediately after the test has started. On average ~1% volumetric shrinkage has occurred during the test before the gel point is reached. Unfortunately, due to preparation time of the test set-up, it is not possible to determine the polymerisation shrinkage immediately after mixing and degassing, even though the effort was made to prepare the set-up and start the measurements as quickly as possible. Also, the oil bath was somewhat lower in temperature than the resin itself, causing the resin mixture to cool a little, resulting in thermal contraction, which is visible as a somewhat steeper slope in the beginning of the graph (indicated by the arrow). This ongoing reaction is also shown by the rheometric results given by the manufacturer in Figure 5.5; the viscosity starts to increase immediately and proceeds gradually due to curing until after ~66 minutes a steep increase is observed, which should correspond to the gel-point.

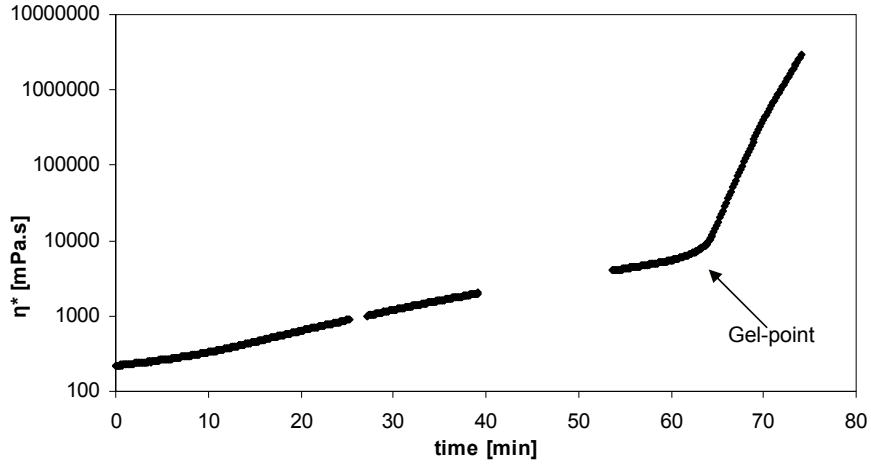

Figure 5.5: Viscosity development with time for Daron® ZW6154.

Also in the volumetric shrinkage test in Figure 5.4, initially the polymerisation shrinkage rate is relatively low, whereas after ~80 minutes a rapid increase can be observed, which is accompanied by a significant exothermal heat release. The time difference may be attributed to the time between mixing and the start of the measurement in Figure 5.5. The average peak temperature was 130°C with a standard deviation of 11°C. It seems that the peak temperature is reached when the shrinkage is fastest, that is where the curing rate is highest (see dotted line in Figure 5.4). The peak temperatures for the five specimens are reached after 75-84 minutes in contrast with 26-27 minutes for the FBG specimens and mentioned in the datasheet. An explanation is that these tests have been carried out 1-2 months earlier than the FBG test and, therefore, the material system was relatively fresh (less aged). At the time of the FBG tests, the A and B components were close to the end of their expiry date and, according to the manufacturer, ageing reduces the gel time significantly [3]. Therefore, the storage time is recommended to not exceed 3 months [4], but ageing is said to not affect the properties of the polymer significantly [3]. The average volumetric shrinkage between the gel point and end of cure is 5.95% with standard deviation 0.07%. This coincides with the 6% volumetric shrinkage mentioned in the manufacturer's datasheet [4].

Regarding the test method itself, it is somewhat worrying that shrinkage is still detected when the polymer temperature has returned to the oil bath temperature, with the polymer assumed to be fully cured. This behaviour was also observed for other polymers, including specimens cured at increased temperatures [5]. One possible explanation can be that volatiles in the silicone bag are still present and are leaching out of the bag. This may even be the cause for the delay in reaction time. The two day soak in water was believed to prevent this, but it may

not have been sufficient. In future tests, this significant source of error (10% of the average volumetric shrinkage from the gel point) will be addressed. It may, therefore, be concluded that this method provides only a qualitative estimate for the volumetric shrinkage development during cure and not an accurate quantitative value.

5.3.1 Comparison with FBG results

The temperature development of the curing resins during both the volumetric shrinkage and FBG tests are shown in Figure 5.6 for one representative specimen per test. The FBG curve is shifted over the time axis, for comparison with the volumetric test results.

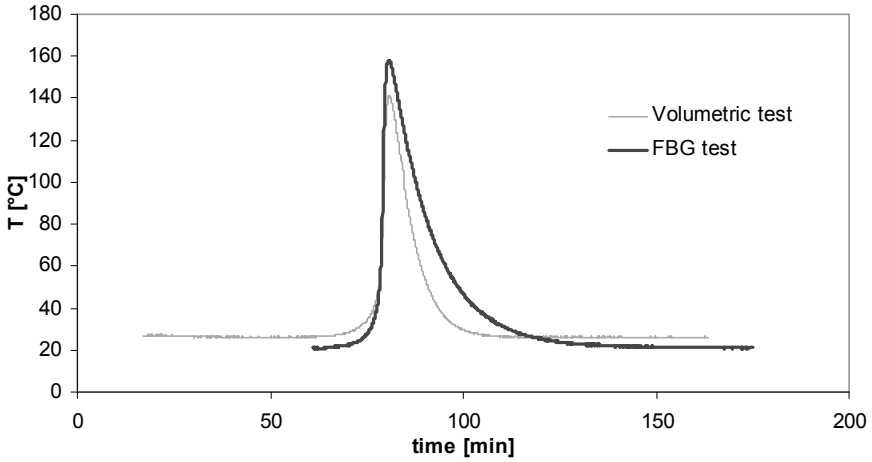

Figure 5.6: Temperature profiles for the volumetric shrinkage and FBG test methods.

In Figure 5.6 it is clear that the curing polymer in the volumetric shrinkage test reaches a lower peak temperature (average 130°C compared to 160.5°C) and cools faster from the peak temperature compared to the FBG test. This can be attributed to the different heat transfer properties of the test set-ups, more specifically of the materials that enclose the curing polymer. The heat generated by the chemical reaction is essentially contained in the relatively thick glass cylinder surrounded by heat-insulating air during the FBG test, whereas the heat in the volumetric test can be more easily distributed through the thin silicone bag to the heat-dissipating oil. The rate at which the peak temperature develops is similar for both test methods.

According to the manufacturer, a higher peak temperature results in a higher glass transition temperature due to a higher degree of cure, which usually results in increased shrinkage of the polymer [3]. Therefore, the FBG test is expected to show more shrinkage. For comparison, both the volumetric shrinkage and FBG results are given for all tested

specimens in Figure 5.7, where the volumetric shrinkage is converted to linear shrinkage with Eq. (5-1) and the FBG results are shifted over the time axis.

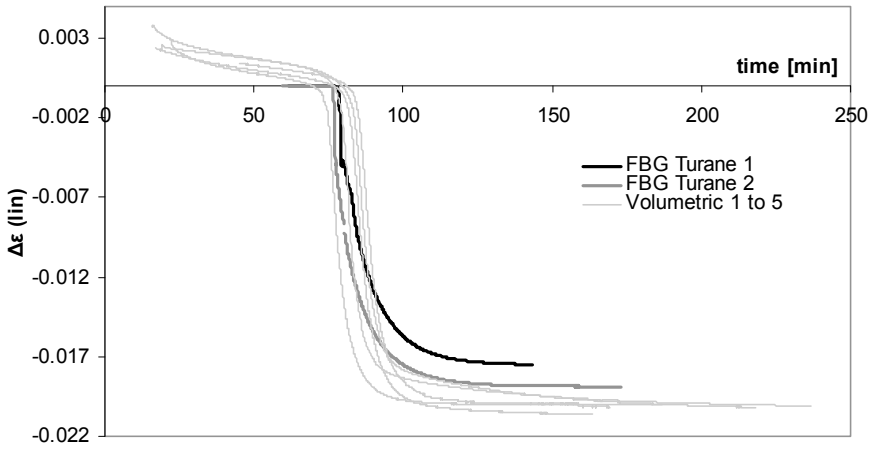

Figure 5.7: Linear shrinkage as determined with the FBG and volumetric tests.

Figure 5.7 shows that the shrinkage strain as determined with the FBGs initially develops faster, but after ~ -0.005 (point B in Figure 4.5) builds up at a lower rate compared to the volumetric shrinkage test. The average linear shrinkage of the volumetric test is 2.02 ± 0.02% compared to 1.82 ± 0.10% for the FBG test. This difference may be attributed to additional chemical shrinkage that could not be detected with the FBG sensors, imperfect bonding between the optic fibre and the matrix, or the gel-point for the volumetric shrinkage test was not chosen correctly. Another explanation may be that the lower cooling rate found during the FBG test caused additional relaxation of the measured strains, which is expressed by a lower compressive strain. However, the most likely cause is the additional shrinkage that is visible in the volumetric shrinkage test after curing, see the explanation given for Figure 5.4.

When the linear shrinkage strain is plotted with respect to temperature, see Figure 5.8, a clear difference in polymer shrinkage behaviour is visible for the two test methods.

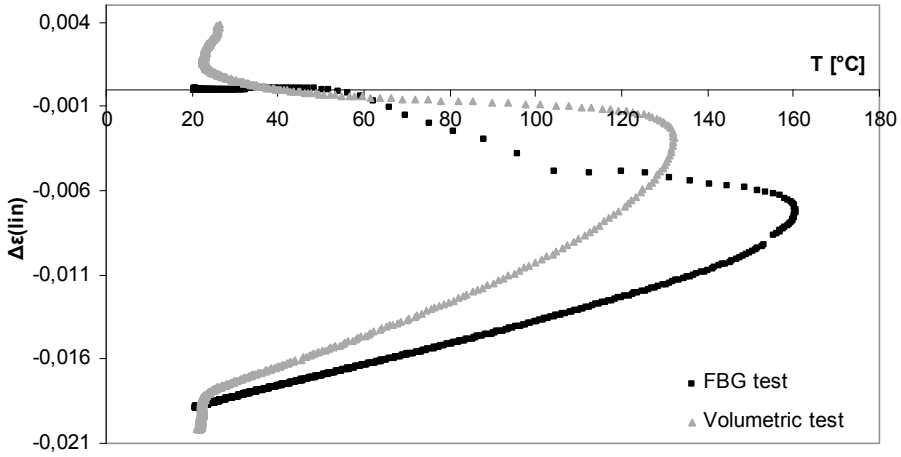

Figure 5.8: Linear shrinkage development with temperature for the FBG and volumetric shrinkage test.

The total linear shrinkage is very similar for both tests at the point where the polymer reaches room temperature again. No transitions can be identified within the volumetric shrinkage test such as points B and C in the FBG profile of Figure 4.6. The curing shrinkage in the volumetric test method is relatively small between the starting (room) temperature and the peak temperature, in comparison with the FBG test. This may be attributed to a small thermal expansion of the silicone bag due to a temperature rise caused by the exothermal curing reaction. When the silicone bag expands, the balance registers a lower mass m_{tot}^{bal}, resulting in a lower shrinkage. However, it also seems that the thermal expansion and contraction of the curing polymer over the temperature profile in the volumetric test is dominating over the chemical shrinkage. Thermal expansion during heating to the peak temperature is visible as less chemical shrinkage and thermal contraction increases it. This behaviour may be caused by a lower degree of conversion resulting from a lower peak temperature.

5.4 Conclusions

The FBG results from the previous chapter were compared with those from a further-developed volumetric shrinkage test based on the buoyancy principle. The advantage of this technique is that it provides an estimate of the total curing shrinkage and not just from the gel-point. The average volumetric shrinkage with respect to the gel-point was 5.95% with standard deviation 0.07%, which shows that the test is relatively reproducible. This corresponds to a linear shrinkage of 2.02% with standard deviation 0.02%, which is close to the FBG results of 1.82% with standard deviation 0.10%. However, no clear transitions such as with the FBG sensors could be identified and it seems that some error was introduced by

the volumetric test method itself. Also, the FBG and volumetric test set-ups resulted in different curing behaviour (different peak temperatures), even though the final shrinkage values were comparable.

While the FBG technique provides a direct measurement of the developed strain sensed by the grating, the test set-up for the volumetric shrinkage test requires assumptions and measurement of certain test parameters before calculation of the volumetric shrinkage is possible. These may introduce significant sources for error, with variations in oil temperature being the most significant one.

References

1. Li, C., *et al.*, In-situ measurement of chemical shrinkage of MY750 epoxy resin by a novel gravimetric method. Composites Science and Technology, 64(1): 55-64, 2004.
2. van Rijswijk, K., Thermoplastic Composite Wind Turbine Blades. 2007. PhD thesis Aerospace Engineering, Delft University of Technology, Delft. 249 pages.
3. Verleg, R., Chemical reactions and ageing in Daron(R) turane, recipient: Parlevliet, P.P. 21 december 2007. Personal communication.
4. DSM_Composite_Resins, Daron XP 45-A-2, ZW 6154, in Product data sheet. 2006.
5. Verburg, P.H., Development of Techniques for Polymer Shrinkage Measurement. 2008. MSc thesis Aerospace Engineering, Delft University of Technology, Delft. 96 pages.

Chapter 6: Residual Strain Determination during Liquid Moulding of Thick Composites with Fibre Bragg Gratings

6.1 Introduction

Monitoring of the curing process during composite manufacturing is very important when it comes to product quality, cure development and residual strains [1]. Usually, techniques to measure this in composites are less straightforward than for pure polymers. One of the technologies that are currently investigated for this purpose are optic fibres with FBGs.
The aim of this chapter is to investigate the suitability of the FBGs to study through-the-thickness residual strain development in thick composite laminates manufactured with liquid resin infusion. For this purpose, a thick glass reinforced laminate was manufactured with the Daron® resin system while FBGs were embedded through the thickness to investigate the development of residual strains due to thermal gradients. Another manufacturing parameter that can be studied with these sensors, namely the flow behaviour, is also addressed. A brief overview of the published literature regarding strain detection in composites with FBGs is given first.

6.2 Residual strain detection in composites with FBGs – a literature survey

Most of the published research on FBGs and composites is dedicated towards structural health monitoring: the optic fibre is glued to the composite surface or embedded within the composite structure and this is subsequently loaded either in service or during mechanical testing to learn the composites' properties [2-5]. In the event of failure or occurring defects such as delaminations, this is captured by the FBG [6, 7]. In addition, multiple gratings positioned through the thickness of the laminates can give an idea about the through-thickness strain distribution during loading [8].
Embedding an optic fibre in a polymer composite before curing can give information on the processing cycle and the material behaviour during processing. Most of the published research describes process monitoring of thermoset laminates, and only few deal with thermoplastic laminates [2, 6]. Studies on strain development during the cure cycle of thermoset prepregs were most often reported [8-12]. For these materials, the FBGs are said to sense strains caused by pressurisation, which upon subsequent heating were found to relax a bit [8]. Chemical shrinkage of the matrix was causing the FBGs to detect a slight contraction of the laminate during the cure dwell [8]. It proved however difficult to establish a gel-point during composites cure [13].

The FBGs were also able to detect the significant influence of the tooling on the strain development through the cure cycle, due to the mismatch in thermal expansion and contraction between the tool and the composite [11, 13]. Even before gelation of the matrix, strain development was caused by this effect [13]. During cooling the FBGs showed jumps in the strain profile caused by 'stick-slip' behaviour between the mould and the prepregs [8]. The release of pressure at the end of the cure cycle was shown to have a dramatic effect on the strain values [8, 13].

The thermal expansion and contraction behaviour of cured composites could be determined with embedded or glued FBGs to establish the coefficient of thermal expansion. But the first results showed that the accuracy of the measurements needs to be increased [10, 14, 15].

Only few studies have been published where FBG sensors were used to monitor the liquid composite moulding process [3, 16-18], such as vacuum assisted resin infusion. These studies showed that one important parameter for this process, the passing of the flow front, could be well observed with the FBG sensors [3, 19, 20]. Eum *et al* reported a significant drop in strain due to resin flow. When the flow front passed the grating, this corresponded to the lowest point in the strain-time curve [19]. They also used a very long strain grating (100 mm), to precisely determine the flow front progression along the FBG length.

The tooling effect on the strain development was also reported for the LCM process [16]. And similar as with prepreg processing, the FBGs detected (vacuum) pressurisation of the dry fabric. Pressurisation was reported to cause more compressive deformation at the flexible vacuum bag side compared to the rigid tool side when FBGs were placed through the thickness in the dry perform [19].

FBGs were also used to monitor strain development during the filament winding process [8]. No residual strains were observed to develop during the winding process itself, since the resin was still liquid. But residual strains during the curing process and effects of the tool were indeed found.

Chehura *et al* [10] and Sorensen *et al* [6] found that the strain state around an optic fibre in a curing composite is rather complex and therefore difficult to predict. Since this is what is measured by the gratings, it is very important to understand the strain state and its separate contributions. Especially in a woven fabric reinforced laminate, the strain field around the gratings can be very complex and therefore it is useful to know the exact positioning of the gratings with respect to the reinforcing fibres [17]. Microbending of the optic fibre, caused by the wavy surface of a fabric, may give significant peak splitting and attenuation of the optical signal intensity [15, 20]. One successful method to study the optic fibre position in carbon fabric composites is microCT scanning [2], though the exact grating position remains invisible.

6.3 Experimental procedures

6.3.1 Materials

1 kg of Daron® ZW6154 hybrid system (DSM Composite Resins, Netherlands) was mixed with 20 g of peroxide (Lucidol® CH50X, Akzo Nobel, Netherlands) to form component A. 350 g of Lupranate® M20R (DSM Composite Resins) was mixed with 20 g Accelerator (NL64-10P, Akzo Nobel) to form component B. The two components were first degassed separately for 5 minutes, after which they were mixed and degassed for 2 more minutes in a vacuum oven. As reinforcement, 21 layers of 20 x 20 cm glass non-crimp fabric with flow mat were used (Unifilo® 1300-935-450, Saint Gobain Vetrotex).

6.3.2 Specimen preparation

A 1.5 mm thick aluminium plate was coated with release agent (Waterworks Departure® from Zyvax Inc., USA) on which the reinforcement plies were laid-up. The fibre optic sensors were cleaned with an ethanol drenched cloth and positioned according to the lay-out in Figure 6.1 with the aid of Flashtape-2 (Aerovac). The dotted sensor parts depict the strain gratings and the thicker grey parts represent the encapsulated temperature-sensing gratings. The distance between the gratings is 40 mm.

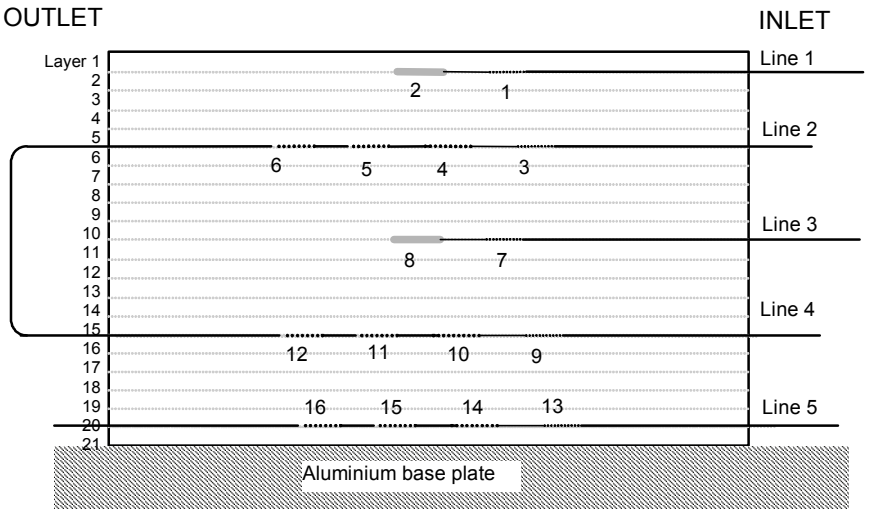

Figure 6.1: Schematic lay-out of the FBG sensors placed in the laminate cross section.

This system was vacuum-bagged with tacky tape and polyamide bagging foil. At the inlet side of the laminate additional flow mesh was added to enhance the infusion through the thickness, see Figure 6.2. The vacuum pressure during infusion was 20 mbar and after

infusion this was decreased to 200 mbar. This resulted in a laminate of approx. 30 mm thickness. A second laminate was made in which K-type thermocouples instead of optic fibres were placed to monitor the exothermal temperature profile. The optic fibres were connected to the FBGScan 616 unit (FOS&S, Geel, Belgium) with pigtail connectors and the K-type thermocouples to a Keithley data logging device. After degassing of the Daron® mixture, the laminate was infused, see Figure 6.2.

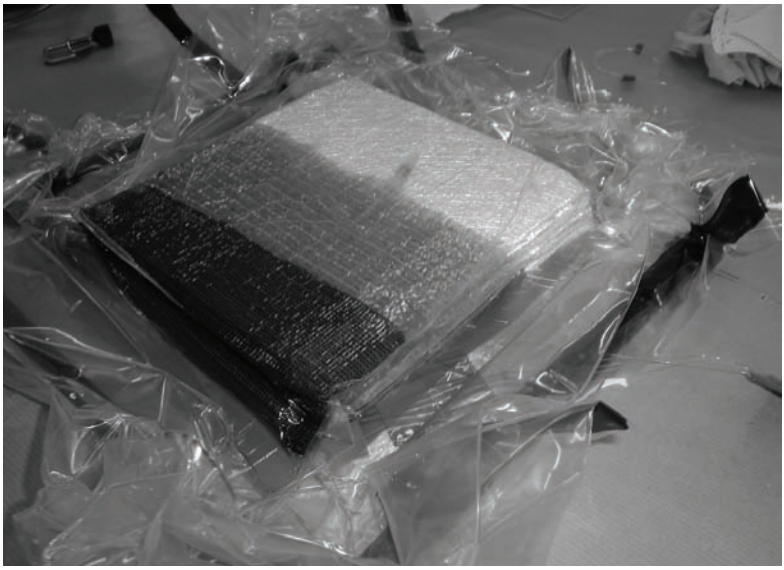

Figure 6.2: Infusion of a thick glass laminate with optic fibres.

6.3.3 Test set-up

8 mm long draw tower gratings® were used with Bragg wavelengths in the entire available range (1530-1563 nm). A polyimide-coated flexible silica capillary (ID 0.25 and OD 0.36 mm) was used for the temperature sensors, since the metal capillaries were not yet available at the time of the experiment. It was observed that these capillaries did not result in strain-free wavelength shifts and therefore the readings of these gratings were not used. Consequently, it was not possible to establish an analysis of the strain development during the manufacturing process of the laminate. Quantitative strain values can in this case only be determined at equal temperatures with Eq. (4-6) and $\Delta T = 0$. The reference Bragg wavelengths were determined after infusion (when the optic fibre was assumed to be in a relaxed state) and compared to the wavelengths measured at the end of the day when the laminate was cooled to 28°C and only a small temperature gradient through the thickness remained (1.2°C difference between the surface and the centre respectively). The resin temperature during infusion was 24°C, so there still is a small difference in wavelength due to

the 4°C temperature difference (1°C results in a wavelength shift of ~12 pm, which compares to a strain $\Delta\varepsilon = 0.1 \cdot 10^{-4}$), but this is not expected to affect the values of the calculated residual strains significantly.
In addition, the FBG readings were used to identify the flow of resin inside the laminate.
It must be noted that the work described here was part of preliminary investigations into the use of FBG sensors in thick laminates. Due to the high cost of the gratings, this test could therefore only be performed once.

6.4 Results and discussion

An example of the wavelength shifts during the processing cycle is given for the gratings between layers 5 and 6 in Figure 6.3. Similar behaviour for the other gratings in the different layers was observed. The wavelength shifts $\Delta\lambda$ are presented here, because the strains could not be calculated due to the absence of temperature compensation. These shifts depend on strain as well as temperature variations.
At the start of the measurement the vacuum pressure was already applied and the components were mixed at time = 0 min and after ~4 minutes the infusion started.

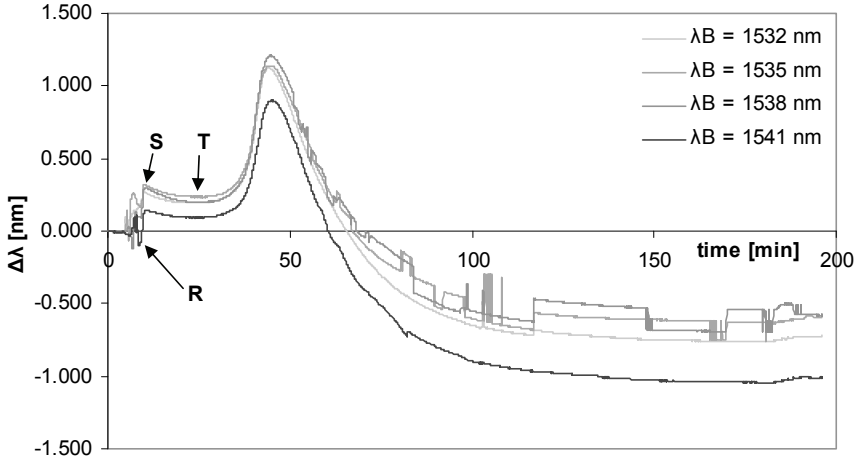

Figure 6.3: Wavelength shifts for the gratings between layers 5 and 6. The 1532 nm grating is closest to the inlet.

In the first few minutes, the wavelength shifts show many sudden jumps during infusion due to the pressure variations. No significant difference in behaviour between inlet and outlet was observed, but when the resin flow front passed a grating, this was immediately reflected by a sudden wavelength shift, see for example point *R*. This allows monitoring of the resin flow

inside the laminate or mould. Moreover, when the inlet is closed, this is reflected by the gratings with a sharp bent in the curve, point *S*. After this point, the gratings seem to 'settle' themselves and the wavelength shift stabilises at point *T*, which is where the reference Bragg wavelength is taken for the residual strain calculations after cure. The variation in $\Delta\lambda$ response between the four gratings seems to originate mainly from the variation in response to pressure and flow variations.

After approx. 30 minutes, the wavelength shift starts to increase as a result of the temperature rise due to the exothermic curing reaction and the peak temperature is reached in 45-48 minutes. This is between the times measured in the FBG and volumetric dilatometry test in Chapters 4 and 5, resp. After the peak temperature was reached, the 1535 and 1538 nm gratings show many sudden jumps in wavelength shift. This may be related to peak splitting due to non-uniform strain fields around the grating. This will result in an error of approximately $1 \cdot 10^{-4}$ in the final strain values.

In Figure 6.3 no clear matrix transitions could be identified, such as in the matrix shrinkage test. Probably a strain-free or temperature-calibrated grating is needed for this, to correct for the overriding thermal effects.

The residual strain after cure was determined for every grating in the laminate, and they are displayed for every 'line' in Figure 6.4 with respect to the distance from the inlet of the laminate. It must be noted that it was difficult to identify the exact location of the gratings in the laminate and therefore an estimate was made based on the flow readings and visual inspection. The grating location with respect to the thickness (*z*) was estimated with the consolidated ply thickness of 1.43 mm, and *z = 0* located at the tool surface.

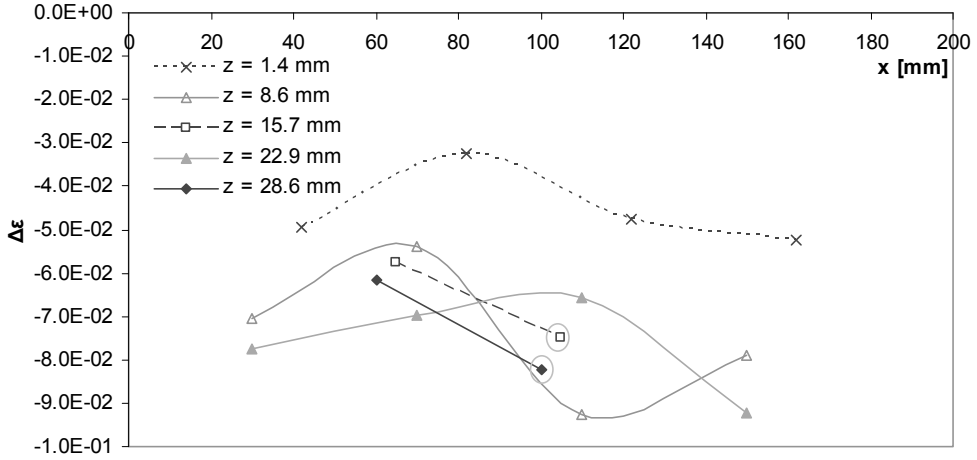

Figure 6.4: Residual strain after cure for FBGs in every ply; encircled points are non-functional temperature sensors (inlet: *x* = 0 mm, outlet *x* = 200 mm).

Figure 6.4 shows that the strain variation is enormous: $\Delta\varepsilon$ ranges from $-3.3\cdot10^{-4}$ to $-9.3\cdot10^{-4}$ and within one line (z = 8.6 mm for example), the strain can vary from $-5.4\cdot10^{-4}$ to $-9.3\cdot10^{-4}$. This large variation in strain values is similar to the results obtained by Jung & Kang [17], who detected curing strains through the thickness in a braided structure during resin infusion. One explanation for this scatter is that due to the coarse fabric, many local variations may exist in matrix density and some voids may have appeared that disturb the strain measurement. In addition, the significant amount of peak splitting causes erroneous results, which is by the way absent for the gratings positioned close to the inlet. This may lead to believe that the voids are concentrated at the outlet, which was confirmed by the visual observation of a higher concentration of pinholes and voids at the laminate surface closer to the outlet. The residual strains are lowest for the gratings that are located closest to the aluminium base plate (z = 1.43 mm).

At this point it is impossible to say much about a strain distribution through the thickness. When the strain values are averaged per depth location and compared to the peak temperatures sensed by the thermocouples in the second laminate, the following Figure is obtained, where the error bars represent the standard deviation of the average strain value. Please note that for the centre and upper surface only one strain value was considered. Second order polynomial fits are depicted by the dotted lines.

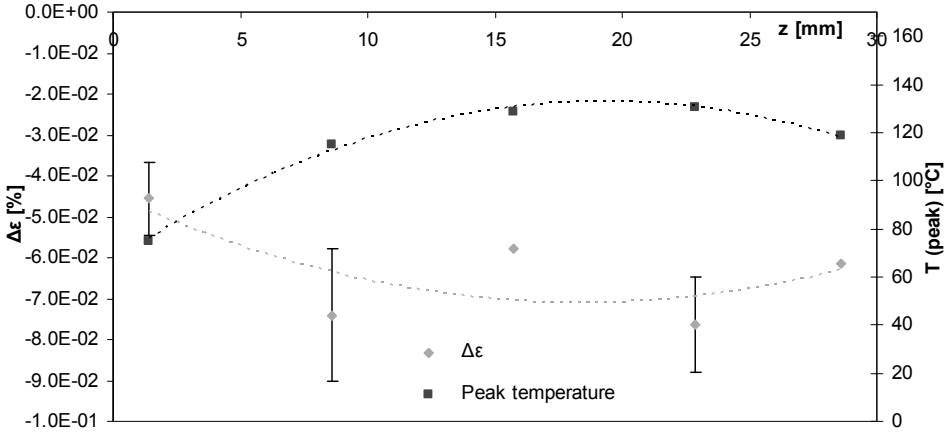

Figure 6.5: Peak temperature and average residual strain distribution through the thickness of a 30 mm glass fibre reinforced turane laminate.

From Figure 6.5 it can be deduced that an increase in peak temperature results in a higher compressive residual strain. This can be explained with the temperature development through the thickness as shown in the following Figure.

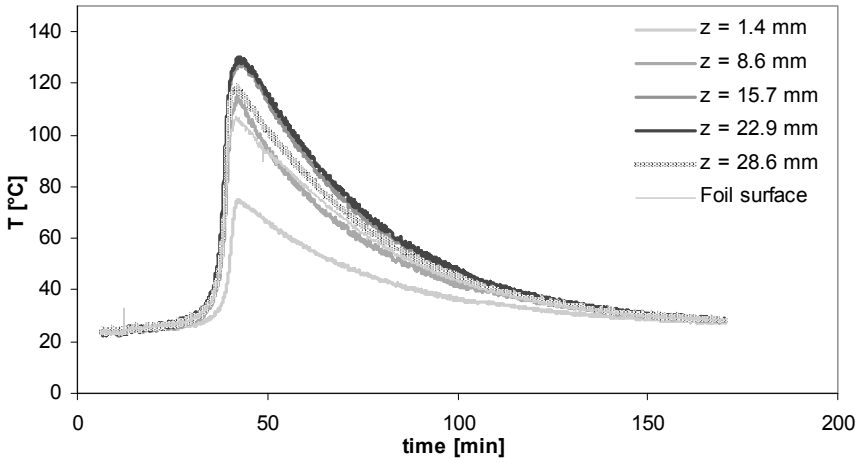

Figure 6.6: Temperature development through the thickness during processing.

It is clear that in the laminate a temperature variation through the thickness exists during cure. After a certain time the reaction rate and generated exothermal heat increases. Depending on the position, this heat is partially contained in the composite due to the thermal insulation of the composite material, resulting in a temperature variation through the thickness. The top surface of the laminate is more or less insulated due to the foil surrounded by air, whereas the heat-conducting aluminium plate acts as a heat sink at the bottom [21], causing an unsymmetrical temperature profile. The time to reach the peak temperatures is the same as for the laminate with FBGs. The peak temperatures are lower than found for the pure polymer shrinkage tests due to the presence of the glass reinforcement that absorbs part of the generated heat and the lower fraction of resin polymerising exothermally.
A higher peak temperature usually means a higher vitrification temperature, corresponding to a higher degree of cure and hence more chemical shrinkage of the matrix. In addition, the higher vitrification temperature exposes the composite to a larger temperature difference upon cooling from this point, resulting in more thermal contraction.
However, the contribution of the matrix chemical shrinkage to the total residual strain of the composite remains unknown. Since the residual strain magnitude of $-3.3 \cdot 10^{-4}$ – $-9.3 \cdot 10^{-4}$ is significantly less than the matrix shrinkage values ($\sim 182 \cdot 10^{-4}$), it can be assumed that the reinforcing glass fibres play a dominating role in residual strain formation.

6.4.1 Comparison with theoretical prediction

When it is assumed that thermal contraction of the composite from the vitrification point onwards is responsible for the majority of the thermal residual strains, an estimation can be made. This can be achieved by taking the temperature difference between the peak temperature and the end temperature (ΔT) and multiply that with the difference in coefficient of thermal expansion (CTE) between the laminate α_c and the optical fibre α_{FBG} (see also Section 3.6):

$$\Delta\varepsilon = \left(\alpha_c - \alpha_{FBG}\right) \cdot \Delta T \qquad (6\text{-}1)$$

The CTE of the composite α_C is calculated with rules-of-mixture [22] and the material property values as given in [23], which results in a value of $9.4 \cdot 10^{-6}$ K^{-1}, and for the FBG sensor the CTE α_{FBG} is given as $0.55 \cdot 10^{-6}$ K^{-1} [24]. The peak temperatures and the calculated and experimentally determined residual strains are given in Table 6.1.

Table 6.1: Temperature and strain values

	Peak T [°C]	End T [°C]	Calculated strain [%]	Experimental strain (FBG) [%]
Line 1	118.4	28.4	-0.080	-0.062
Line 2	130.4	28.6	-0.090	-0.076 ± 0.012
Line 3	128.6	28.5	-0.089	-0.058
Line 4	115.1	28.1	-0.077	-0.074 ± 0.016
Line 5	75.0	27.4	-0.042	-0.045 ± 0.008

Compared to the average FBG strain data, the prediction overestimates the residual strain, but compares well to the results of some individual gratings. Therefore, it may be said that thermal contraction of the cured composite laminate from the peak temperature (which is close to the vitrification point as shown by the matrix shrinkage test) to the service temperature is the prime factor for residual strain formation in a composite laminate; hence thermal variations through the thickness will result in residual strain variations. Nevertheless, it must be borne in mind that this result is based on one test only and therefore more tests or simulations need to be carried out in the future. Of most importance then is the incorporation of thermocouples and temperature gratings, such that strain formation can be identified, and possibly other useful parameters.

6.4.2 Flow behaviour

To estimate the flow behaviour through the laminate, the time was identified when the flow front reached the grating (point R in Figure 6.3) for every grating. The results are shown in Figure 6.7.

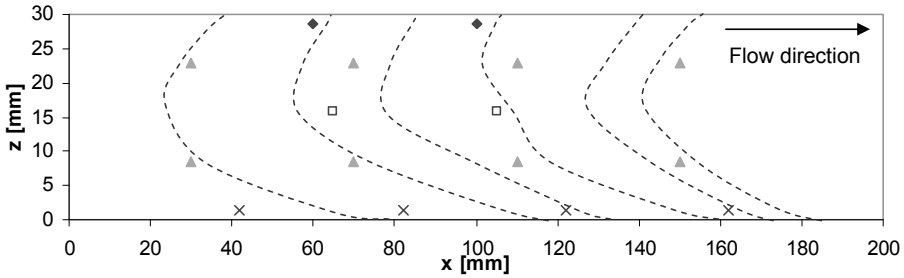

Figure 6.7: Estimation of flow behaviour (lines indicate 30 s intervals and are drawn manually).

Figure 6.7 shows that the flow front proceeded faster along the aluminium base plate and that due to the applied bleeder at the inlet, the top surface was also impregnated somewhat earlier. The centre plies see the flow front pass at a later stage. The consequence is that even though the fibre impregnation looks good at the laminate surface, this is not necessarily the case for the centre plies.

6.5 Conclusions

A successful attempt was made to produce a 30 mm thick glass fibre reinforced hybrid polyurethane/ polyester (turane) laminate with embedded fibre optic sensors (FBGs) through the thickness. Due to the exothermal polymerisation a significant thermal gradient through the thickness was found, which resulted in a variation in peak temperature. This was reflected by a residual strain distribution after manufacturing as determined with the FBGs. Based on an estimation of the thermal contraction of the cured composite from the peak temperature, it seems that this is the prime factor for residual strain formation in a composite laminate and not the chemical shrinkage of the matrix. Hence, thermal variations through the thickness are important factors for causing residual strain variations. The FBG sensors were also found useful to monitor the resin flow behaviour during infusion of the laminate.

References

1. Degamber, B., Fernando, G.F., Process Monitoring of Fiber-reinforced Polymer Composites. MRS Bulletin, (May 2002): 370-380, 2002.

2. De Baere, I., Voet, E., Van Paepegem, W., Vlekken, J., Cnudde, V., Masschaele, B.Degrieck, J., Strain monitoring in thermoplastic composites with optical fiber sensors: Embedding process, visualization with micro-tomography, and fatigue results. Journal of Thermoplastic Composite Materials, 20(5): 453-472, 2007.
3. Calabro, A.M., Mazzola, L., Caneva, C., Integrated sensor system for Smart Materials: Multidisciplinary approach using COTS optic fiber sensors. Design, Validation and calibration in aeronautical components area Proceedings of SPIE - The International Society for Optical Engineering , , 6530: art. no. 65301U 0 2007.
4. Mostafa, M.A., Gmur, T., Botsis, J., Experimental study on the effects of the boundary conditions on the deformations of composite plates. Composites Science and Technology, 66(11-12): 1756-1765, 2006.
5. Menendez, Fernandez, Guemes. Sensing with embedded fiber bragg gratings in extreme mechanical conditions. in ICCM-16, Kyoto, 2007.
6. Sorensen, L., Gmur, T., Botsis, J., Residual strain development in an AS4/PPS thermoplastic composite measured using fibre Bragg grating sensors. Composites Part A: Applied Science and Manufacturing, 37(2): 270-281, 2006.
7. Zhou, G., Sim, L.M., Damage detection and assessment in fibre-reinforced composite structures with embedded fibre optic sensors - review. Smart Materials & Structures, 11(6): 925-939, 2002.
8. Collombet, F., Mulle, M., Hernandez-M, H., Douchin, B., Zitoune, R., Olivier, P.Grunevald, Y.H. On the use of optical fibres with bragg gratings for the identification of process-properties relations of composite structures. in ICCM-16, Kyoto, Japan, 2007.
9. Guo, Z.S., Zhang, B., Du, S.Y., Theoretical and experimental studies on residual stresses of advanced polymer composites. Key Engineering Materials, 334-335 I: 37-40, 2007.
10. Chehura, E., Skordos, A.A., Ye, C.C., James, S.W., Partridge, I.K.Tatam, R.P., Strain development in curing epoxy resin and glass fibre/epoxy composites monitored by fibre Bragg grating sensors in birefringent optical fibre. Smart Materials & Structures, 14(2): 354-362, 2005.
11. Mulle, M., Collombet, F., Olivier, P., Grunevald, Y.H., Assessment of cure residual strains through the thickness of carbon-epoxy laminates using FBGs, Part I: Elementary specimen. Composites Part A: Applied Science and Manufacturing, 40(1): 94-104, 2009.
12. Leng, J.S., Asundi, A., Real-time cure monitoring of smart composite materials using extrinsic Fabry-Perot interferometer and fiber Bragg grating sensors. Smart Materials & Structures, 11(2): 249-255, 2002.
13. de Oliveira, R., Lavanchy, S., Chatton, R., Constantini, D., Michaud, V., Salethé, R.Manson, J.A., Experimental investigation of the effect of the mould thermal expansion on the development of internal stresses during carbon fibre composite processing. Composites Part A: Applied Science and Manufacturing, 39(4): 1083-1090, 2008.
14. Fernandez-Lopez, A., Guemes, A., Menendez, J.M. Measuring the thermal expansion coefficient of composite laminates by fiber optic sensors. in SAMPE Europe International Conference 2007. 2007. Paris.
15. Mulle, M., Zitoune, R., Collombet, F., Olivier, P.Grunevald, Y.H., Thermal expansion of carbon-epoxy laminates measured with embedded FBGS - Comparison with other experimental techniques and numerical simulation. Composites Part a-Applied Science and Manufacturing, 38(5): 1414-1424, 2007.
16. Kosaka, T., Osaka, K., Nakakita, S., Fukuda, T., Fiber optic strain monitoring of textile GFRP during RTM molding and fatigue tests by using embedded FBG sensors Proceedings of SPIE - The International Society for Optical Engineering, (5056): 73-80, 2003.
17. Jung, K., Kang, T.J., Cure monitoring and internal strain measurement of 3-D hybrid braided composites using fiber Bragg grating sensor. Journal of Composite Materials, 41(12): 1499-1519, 2007.
18. Slattery, K.T., Corona-Bittick, K., Dorr, D.J. Composite cure monitoring with Bragg grating sensors. in Proceedings of SPIE - The International Society for Optical Engineering. 1998.
19. Eum, S., Kageyama, K., Murayama, H., Uzawa, K., Ohsawa, I., Kanai, M.Igawa, H. Resin Flow Front Monitoring for VARTM using Fibre Bragg Gratings. in ICCM-16, Kyoto, Japan, 2007.
20. Ferdinand, P., Magne, S., Dewynter-Marty, V., Rougeault, S.Maurin, L., Applications of fiber Bragg grating sensors in the composite industry. MRS Bulletin, 27(5): 400-407, 2002.
21. Guo, Z.S., Du, S.Y., Zhang, B.M., Temperature field of thick thermoset composite laminates during cure process. Composites Science And Technology, 65(3-4): 517-523, 2005.
22. Cowley, K.D., Beaumont, P.W.R., The measurement and prediction of residual stresses in carbon-fibre/polymer composites. Composites Science and Technology, 57(11): 1445-1455, 1997.
23. Andersson, B., Sjogren, A., Berglund, L., Micro- and meso-level residual stresses in glass-fiber/vinyl-ester composites. Composites Science and Technology, 60(10): 2011-2028, 2000.
24. Hagemann, V.J., Untersuchungen zum dynamischen Einzelpuls-Einschreiben van Faser-Bragg-Gittern un zu deren Anwendung. 2001. PhD thesis.

Chapter 7: Thermal Effects on Polymer Property Variations in Thick Composites – a Novel Experimental Approach

7.1 Introduction

One of the key issues in manufacturing of thick composite structures is that through-the-thickness thermal gradients can occur resulting in variations in polymer matrix properties, such as degree of cure or crystallinity level. These property variations in turn can provide an additional source to residual strain development as was described in Chapter 2. In addition, it is important for thick composite products to have known homogeneous properties through the thickness [1]. Therefore, it is important that variations in matrix properties through the thickness are determined.

Chapter 3 showed that a limited number of techniques are described in literature for identification of polymer properties through the thickness. One technique that was used most frequently is the Process Simulated Laminate (PSL) technique [2], which was originally designed for the determination of skin-core residual strains in thick laminates. The PSL technique is employed frequently in combination with Differential Scanning Calorimetry (DSC) to determine the crystallinity [3, 4], even though other techniques are available, such as X-ray (micro)diffraction [5, 6]. This technique is rather time-consuming, since the layers need to be separated first, and to obtain statistically reliable values more than one measurement per layer need to be performed. And even though the used separation films were claimed to have no influence on the morphology (crystallinity) or heat transfer properties in CF/PEEK laminates [4], for many other composites this effect is not known.

In the field of materials science, a commonly used and relatively rapid experimental technique is hardness testing. Variations in polymer properties are known to result in hardness variations and the microVickers indentation test was often used to identify these [7, 8]. This technique has however not been used before to identify matrix property variations in composites caused by thermal gradients during processing. Therefore, the goal of this chapter is to investigate if the microVickers hardness test can be used for this purpose.

Two different materials were used: a 30 mm glass fibre reinforced turane laminate similar to the ones in Chapter 6, and 10 and 20 mm carbon fibre reinforced polyphenylenesulfide (CF/PPS) laminates. The thermal gradient present during manufacturing of the first (shown in Chapter 6) was assumed to result in a variation in degree of cure. For the CF/PPS laminates a variation in cooling rate through the thickness is expected to result in different degrees of crystallinity. This was investigated with DSC tests and compared to the hardness results to

identify a possible relation. First the microVickers hardness test is briefly introduced, followed by a small overview of the literature on hardness testing of polymers and composites.

7.2 Microhardness testing

Hardness can be defined as the resistance of a material to plastic deformation. The hardness value represents a complex material characteristic affected by a combination of properties such as elastic modulus, yield strength, and strain hardening capacity [8, 9]. Hardness tests provide a rapid evaluation of variations in mechanical properties affected by changes in processing conditions, heat treatment, microstructure and ageing. Several hardness testing techniques are available [10], of which the microVickers hardness test seems most suitable for this research for its small indentation size.

7.2.1 MicroVickers hardness – working principle

The Vickers hardness test method consists of indenting the material with a diamond indenter utilising a certain load. This indenter has the shape of a pyramid with a square base and an angle of 136 degrees between opposite faces, which results in an indentation depth of about $1/7^{th}$ of the diagonal length [8], see Figure 7.1.

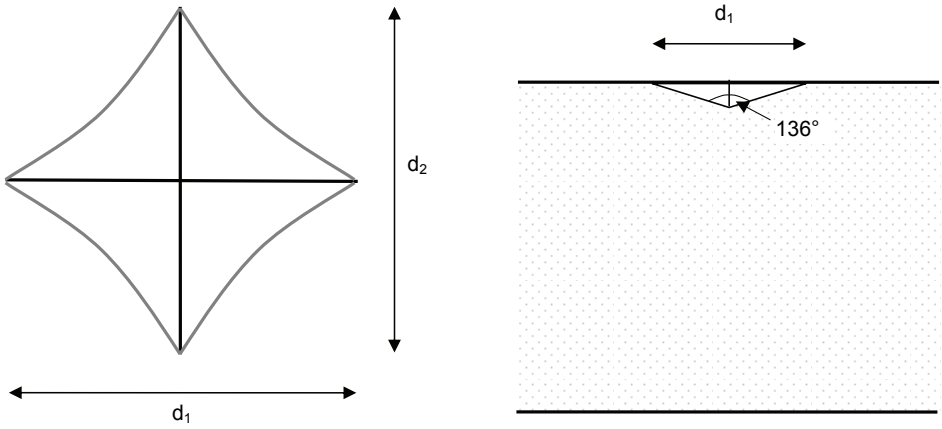

Figure 7.1: Schematic example of microVickers indentation profile in polymers: top view (left) and cross-section (right), after [11] .

The load is normally applied for 10 to 15 seconds. The Vickers hardness is obtained by dividing the load by the area of the sloping surface of the indentation. This value is calculated as

$$HV = 2\sin\left(\frac{136}{2}\right)\frac{P}{d_1 \cdot d_2} \qquad (7\text{-}1)$$

where P is the indentation load in kg and d_1 and d_2 are the lengths of the diagonals in mm [12]. The Vickers hardness is usually reported as a number followed by HV and the indentation load; for example *800 HV10* means that a Vickers hardness of 800 was obtained using a 10 kg load. The term microhardness usually refers to static indentations made with loads lower than 1 kg [10, 13]. There is now a trend towards reporting Vickers hardness in SI units (MPa), particularly in academic papers [10, 14, 15]. Converting HV to MPa is done by multiplying the indentation load in Eq. (7-1) with the gravitational constant g to obtain a force F in Newtons [10].

7.2.2 MicroVickers hardness testing of polymers

A point of concern that is often raised when studying the indentation hardness of polymers is the visco-elastic behaviour, by which the indented area may change in shape over time [11, 16, 17]. It was shown by Low *et al* [11, 16, 18], that the visco-elastic relaxation of the indentation takes place via the sides of the pyramid shaped indentation, and not along the diagonals on which the hardness value is based. Hence, it was concluded that Vickers indentation is a useful tool for evaluating the hardness of polymers, but multiple indentations are always required to obtain reliable average hardness values.

Mechanical properties that can be directly related to microhardness are the yield strength and elastic modulus [19]. Microstructural characteristics of polymers that are dependent on the processing conditions, such as molecular orientation, residual stresses, degree of cure and crystallinity and the crystal structure, can also affect the hardness [20]. Basically, the hardness can be related to the (local) density of the polymer, which depends on these parameters [21, 22]. It is thus essential that the testing environment is kept constant [23], because environmental effects significantly influence the polymer density and hence hardness. Water absorption can cause swelling/ softening of the polymer and a decrease in glass transition temperature (plasticisation) [24] leading to a lower hardness [15, 25]. This renders hardness a reliable index of water diffusion in certain polymers [9]. Higher temperatures decrease the polymer hardness.

The hardness test is a widely accepted tool to test the cure development in thermoset polymers [26, 27]. Lately, it is often used to determine differences in degree of cure in various UV-cured polymer systems [28, 29].

Microhardness in semi-crystalline polymers can be related to the crystalline properties, such as degree of crystallinity and crystal lamellar thickness [30, 31]. The Vickers hardness was

found to increase with increasing crystallinity level [30, 32-35] after for example, annealing [36, 37].

7.2.3 Microhardness of composites

Microhardness testing was also performed on fibre reinforced polymers and not surprisingly, the hardness of a composite is considerably higher than that of a neat resin due to the stiff fibres [8, 37-40]. The fibres can also influence the hardness of the polymer matrix, as they influence for example the level of crystallinity and introduce residual stresses. Experimental results were reported of hardness tests carried out on the outside surface of the composites, as well as on composite cross-sections [8, 39, 40]. The two indentation diagonals showed different lengths, with the diagonal parallel to the fibre direction being shorter than the perpendicular diagonal, which is inherent to the anisotropic nature of fibre reinforced polymers [37, 40]. The scatter in hardness values is quite large compared to neat polymers, due to the presence of resin-rich and resin-poor areas [8, 39, 40]. This was raised as a point of concern. Averaging of the data from multiple indentation profiles on the same sample was proposed as a solution [8]. A standard deviation of 8% of the average hardness in composites was obtained in this manner [8].
An interesting application of the microVickers hardness test was to determine variations in ageing effects of a composite through the thickness [8], which comes close to the application that is intended in this chapter.

7.3 Experimental procedures

It was decided to test the composite hardness with microVickers indentations only in the matrix-rich areas between the fibres in a laminate cross-section. The reasons for this decision are the reported high scatter due to the inhomogeneous material, poor visibility of the indentation [8], and that it is the aim to study the variation in matrix properties caused by temperature variations through the thickness. This proved however only possible for fabric reinforced composites [23] and by using a small indentation load, such as 10 or 25 grams. An example of a matrix indentation in a CF/PPS composite is shown in Figure 7.2.

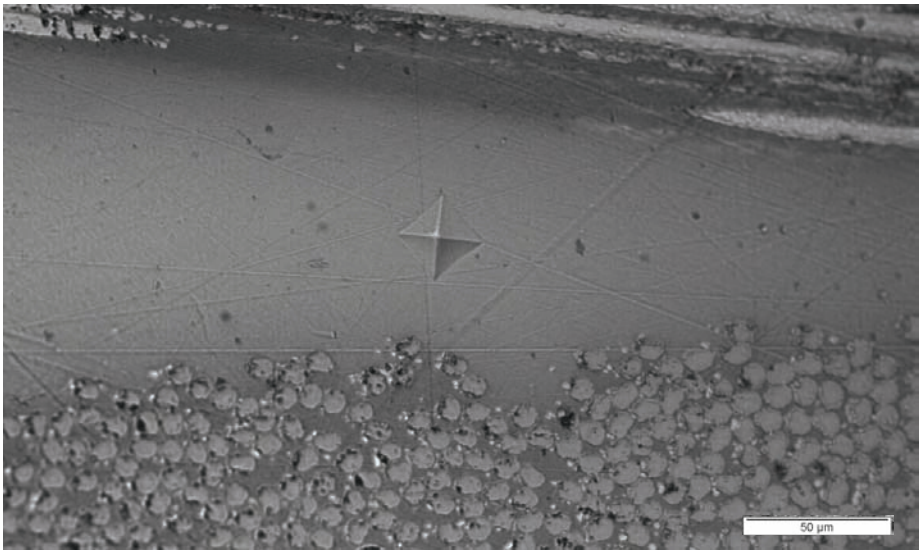

Figure 7.2: Micrograph of a 10 g MicroVickers indentation in a CF/PPS laminate cross-section.

7.3.1 Materials

PPS Cetex® semipregs were obtained from Ten Cate Advanced Composites, (Nijverdal, The Netherlands) and consisted of T300J carbon fibres woven into 5 Harness Satin fabric and a thermoplastic polyphenylenesulfide (PPS) film (Fortron® 0214, Ticona GmbH). In addition, 80 µm thick pure PPS film as well as carbon fabric with PPS-compatible sizing were used. The materials used for the thick glass reinforced turane composite have already been described in Section 6.3.1.

7.3.2 Specimen preparation

A closed aluminium mould as shown in Figure 7.3 was used for the CF/PPS laminates. This tool was designed for the fabrication of 10 and 20 mm thick laminates with length and width 120 and 100 mm, resp. The mould was coated with Semiperm® 4.5GS release agent. 32 semipreg layers with these dimensions were cut for the 10 mm laminate and 66 layers for the 20 mm laminate and subsequently placed in the mould. The layers had been dried overnight in a vacuum drying oven at 80°C. Three to five K-type thermocouples were placed at equidistant positions through the thickness near the middle of the laminate. A Keithley temperature logging system registered the time-temperature profiles of the thermocouples during processing. Cooling rates were determined by calculating the slope of the initial part of the cooling curve.

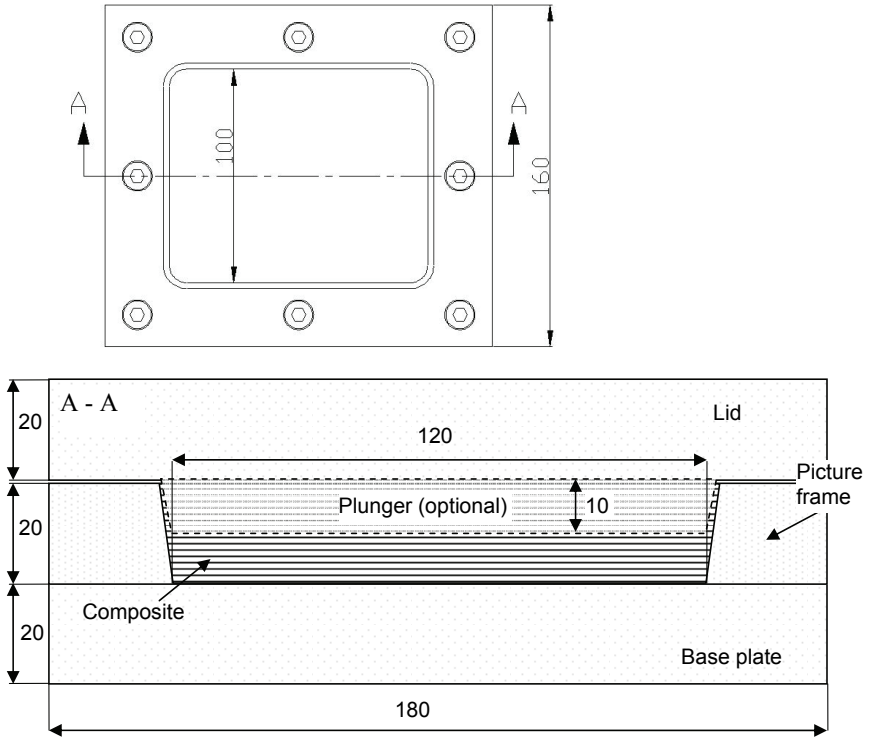

Figure 7.3: Schematic view of the mould used to manufacture the CF/PPS laminates, dimensions are in millimetres.

The thermoplastic laminates were consolidated in a hot platen press (Fontijne, The Netherlands) with the following processing cycle: heating to 320°C at a rate of 10°C/min and with 0.25 MPa pressure; at 320°C the pressure was raised to 1 MPa and maintained for 15 minutes; cooling of the laminate with ~50°C/min or ~35°C/min to room temperature (1 MPa)[1]. This resulted in laminates with 9.8 mm and 20.2 mm thickness, hereafter referred to as the 10 mm and 20 mm laminates, resp.

The 30 mm thick GF/turane laminate was manufactured as described in Section 6.3.2 with thermocouples dispersed through the thickness. One significant difference is that instead of an aluminium tool plate, a glass plate was used resulting in a different (nearly symmetrical) temperature profile through the thickness.

[1] Unfortunately, it was not possible to set the cooling rates of the Fontijne press to a certain value; hence different surface cooling rates were the result.

After release from the mould, the consolidated laminates were cut with a Struers Unitom-5® liquid cooled machine with a corundum blade. Samples with dimensions 10 x 10 x 9.8 mm were cut from the 10 mm CF/PPS laminate and embedded in a 20 mm high and 25 mm diameter wide cup, filled with fast-curing Technovit® 4071 resin (Heraeus Kulzer GmbH&Co KG). From the 20 mm laminate a sample with dimensions 25 x 25 x 20 mm was cut, which was not embedded. A 20 x 20 mm piece with thickness 30 mm was cut from the centre of the cured GF/turane laminate.
These specimens were wet grinded on a Buehler Ecomet machine with SiC sandpaper and polished to 1 µm with SiC paste and ethanol lubricant on a Struers DAP-7 Pedemin machine. The samples were cleaned between all steps by ultrasonication in an ethanol-filled bath and dried with compressed air between the polishing steps. These specimens were used for microVickers testing.

Samples for differential scanning calorimetry (DSC) were prepared by peeling off plies similar to the ones where the thermocouples are located, with the aid of a Stanley knife. These plies were cut into 5 mm diameter discs and dried in a vacuum drying oven at 50°C for 48 hours before testing.

7.3.3 Test set-up

MicroVickers indentation

For determination of the microVickers hardness, a Buehler Omnimet® MHT hardness tester was used with a 10 and 25 gram load. The load was applied for 15 seconds and the test environment consisted of ambient conditions (room temperature ~21°C and relative humidity ~70%). Perrin *et al* [41] observed a decreasing hardness with increasing indentation load when the samples were not fully dried and this effect was absent when testing dry specimens. Therefore, an effort was made during this research to test fully dry specimens, but it was found that the moisture content of the polymer increased during testing, and the hardness values decreased accordingly [23]. Thus, it was made sure that the specimens reached environmental equilibrium before testing, by leaving them for at least 2 weeks at ambient conditions.
The lengths of the diagonals were measured using a CCD camera mounted on the microscope set to magnify 400 times, and the Omnimet® software programme. This was done immediately after load removal to prevent relaxation. The diagonals of each indentation were measured at least three times. The hardness values were calculated using Eq. (7-1) and multiplied with the gravitational constant (9.81) to obtain the values in MPa units.
Two test parameters were varied to establish the most suitable testing method for the CF/PPS composites:

- Two different indentation loads were used: 10 or 25 gram.
- Two procedures were adopted with regard to the pattern in which the indentations are made in the cross-section of the specimen, see Figure 7.4:
    - Procedure 1: Three lines across the thickness of the specimen resulting in a 'scatter plot' of hardness values with location in the laminate (a).
    - Procedure 2: A minimum of 10 indentations were made in five distinct plies, similar to those where the thermocouples were placed. This resulted in average hardness values with a standard deviation for these plies (b).

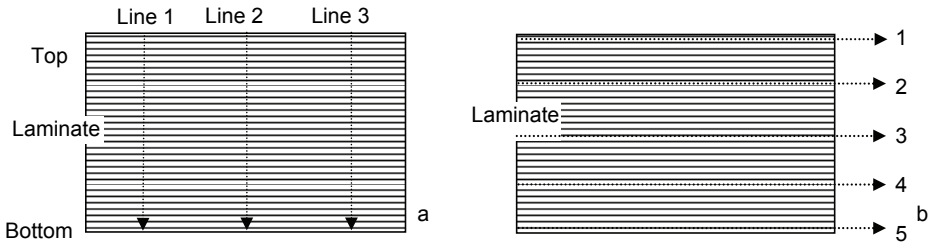

Figure 7.4: MicroVickers indentation profiles according to Procedure 1(a) and Procedure 2(b).

For the GF/turane specimens Procedure 2 with a 25 gram load was applied, because the resin pockets were very large in this material.

One important thing that must be noted regarding microVickers hardness testing is that the measurement of the diagonals is performed by the person operating the machine. The pattern recognition software for automatically establishing the diagonal length is not capable to detect the indent diagonal lengths in polymers due to the low contrast and light reflection. Every person was found to assess the diagonals differently, which has a significant effect on the hardness values. In addition, for one person this may even differ per day (~20 MPa). Therefore, the microVickers hardness test can be used for qualitative assessment only.

Differential Scanning Calorimetry (DSC)

To establish the level of crystallinity in the CF/PPS composites after processing, Differential Scanning Calorimetry experiments were carried out on a Perkin Elmer DSC7. The samples were heated from 25°C to 340°C with 10°C/min, contained in aluminium pans with lids. For the specific heat versus temperature graph, the test runs were first carried out with the empty sample pan and calibrated with a sapphire sample. The area under the melting peak (ΔH_c) in the specific heat graph was determined for calculation of the crystallinity level, with an accuracy of ±1 J/g. If present, the area under the recrystallisation peak was subtracted. The

crystallinity level (X_c) was calculated with Eq. (7-2), where w_m is the matrix weight fraction of the composite, which was determined with thermal gravimetric analysis (TGA). For 100% crystalline PPS a fusion enthalpy (ΔH_0) of 112 J/g was used [42].

$$X_c = \frac{1}{w_m}\left(\frac{\Delta H_c}{\Delta H_0}\right) \qquad (7\text{-}2)$$

Three to five runs for every material (ply) were carried out to obtain average crystallinity values with a standard deviation. The sample mass was determined with a Mettler AE240 balance with an accuracy of 0.01 mg.

DSC tests have been carried out on the GF/turane specimens taken through the thickness to check for the T_g as a measure for degree of cure. The tests were carried out on a Mettler Toledo DSC machine at DSM Composite Resins in Zwolle.

Thermal Gravimetric Analysis (TGA)

Thermal gravimetric analysis on a Perkin Elmer TGA7 machine was performed on the DSC samples to establish the matrix weight fraction w_m, because this can vary from location to location in fabric reinforced composites. The method devised by Kim *et al* [5] was used, since carbon fibres degrade at the evaporation temperatures of PPS. This method uses equal TGA temperature profiles for the pure PPS film, the bare carbon fibres and the PPS/carbon samples used in the DSC measurements. This TGA temperature profile consists of heating from room temperature to 500°C at 40°C/min and maintain that temperature for another 50 minutes. At a certain time the remaining weights of the materials are approximately constant, which in this case was found to be around 40 min. For the fibres and the pure matrix, five test runs per material were carried out to establish an average mass fraction after 40 minutes. By comparing the TGA curves for the carbon fibres, the pure PPS and the composite as shown in Figure 7.5, the matrix weight fractions w_m can be calculated by means of Eq. (7-3):

$$w_m = \frac{m_c - m_f}{m_p - m_f} \qquad (7\text{-}3)$$

where m_c, m_f and m_p denote the remaining composite, fibre and polymer mass fractions after 40 min residence in the TGA, resp. The average fibre and polymer weight fractions, m_f and m_p in Eq. (7-3) were found to be 99.2% and 65.2% with standard deviations 0.2% and 0.8%, respectively. The average matrix weight fraction w_m was 0.37 with standard deviation 0.04.

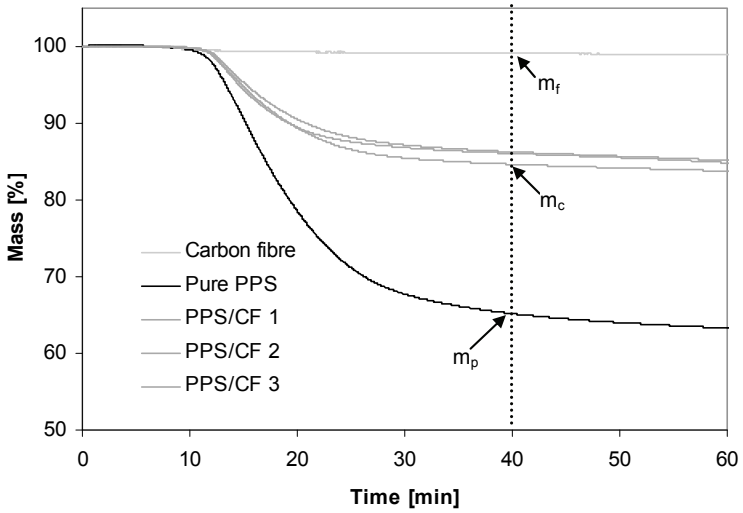

Figure 7.5: Examples of TGA graphs used for determination of the matrix weight fraction.

7.4 Thick glass fibre reinforced turane laminate: results and discussion

The results for the temperature measurements through the thickness during cure of a thick GF/turane laminate are shown in Figure 7.6.

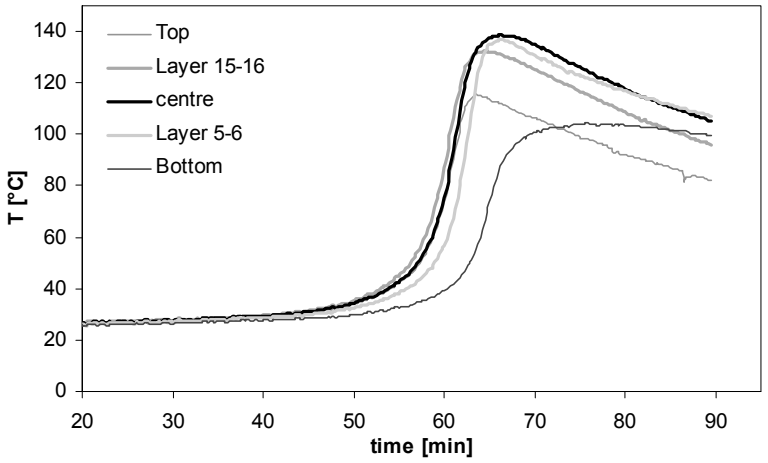

Figure 7.6: Temperature development through the thickness in 30 mm thick GF/turane laminate.

In figure 7.6 it is clear that the glass tool plate has a significant effect: it takes much longer for the bottom plies to reach the peak temperature than the other plies. This can be attributed to the insulating properties of the glass plate: it takes a long time before it heats up by the exothermal reaction, but when it is warm it cools very slowly. The exothermal temperature rise also occurs later, because the colder tool surface decreases the reaction rate and the temperature. The thermocouple at the top was placed directly beneath the vacuum bag where it is easier for the heat to be transferred to the cooler environment; hence the measured peak temperature was lower. The thermal behaviour of the more centred laminate plies was more or less similar. The peak temperatures are similar as those for the laminates described in Chapter 6.

Results of the microhardness test are shown in Figure 7.7 with the corresponding peak temperatures.

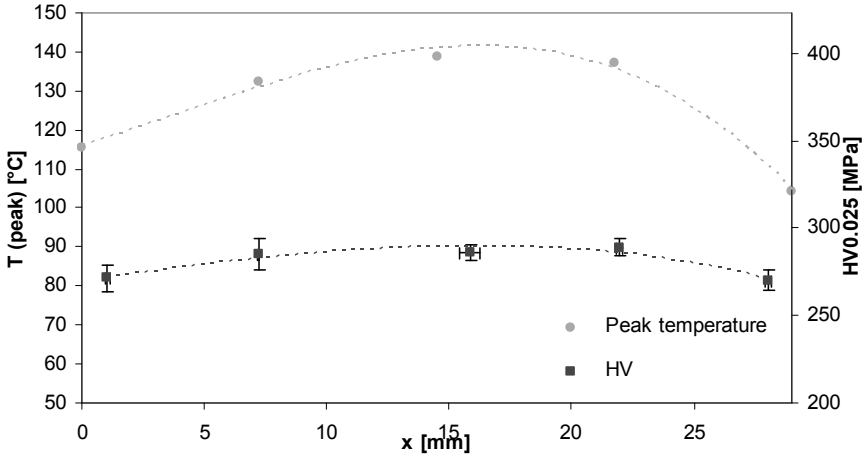

Figure 7.7: Microhardness and peak temperatures (glass base plate was located at x = 30 mm).

The trends for the peak temperatures and microhardness values are very similar. Both the peak temperatures and the hardness are lower at the laminate surfaces. This indicates that a variation in peak temperature through the thickness induces a variation in polymer properties, which is probably related to the degree of cure [27], see Section 7.2.2. So thermal variations through the thickness not only lead to residual strain variations as shown in Chapter 6, but also to variations in polymer properties.

The DSC test was carried out before postcuring to check for thermal effects on the T_g, which is a measure for degree of cure. However, a significant relaxation effect during the DSC test,

similar as in Figure 4.9, obscured the T_g determination. The amount of energy released during postcuring could be a measure for the initial degree of cure, but the variation in results (not shown) was such that no sound relation could be established.

7.5 Thick carbon fibre reinforced PPS laminates: results and discussion

7.5.1 Cooling profiles

The cooling profiles of the 10 and 20 mm laminates are shown in Figures 7.8 and 7.9, resp. The initial cooling rates are given in the figures.

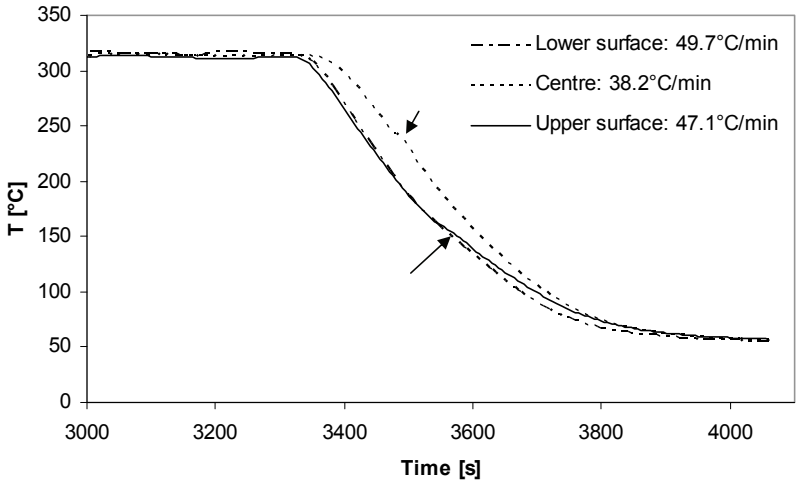

Figure 7.8: Cooling profile of 10 mm thick carbon fibre reinforced PPS laminate.

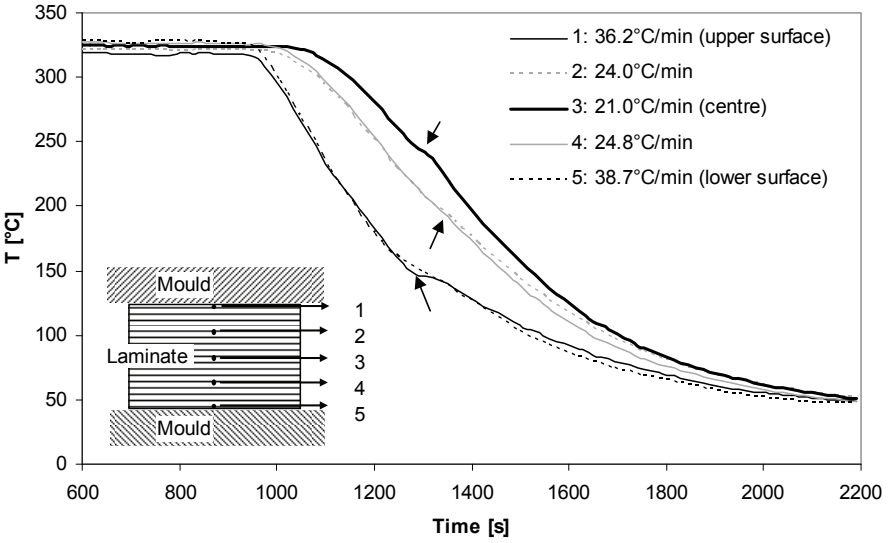

Figure 7.9: Cooling profile of 20 mm thick carbon fibre reinforced PPS laminate.

For both laminates it is clear that the surface plies experienced a higher cooling rate than the centre plies. The 20 mm laminate clearly experienced a parabolic temperature profile through the thickness during cooling.

The arrows in the figures indicate 'humps' in the cooling profile, which can be explained by crystallisation of the PPS matrix. Polymer crystallisation is an exothermal process and therefore the temperature decreases more slowly during the brief crystallisation process. This crystallisation occurs at a higher temperature in the centre plies, which is related to the lower cooling rate: lower cooling rates result in a higher crystallisation temperatures and increased crystallinity, as was explained in Section 2.3.2.

7.5.2 MicroVickers hardness

The MicroVickers hardness results obtained with Procedure 1 are displayed in Figures 7.10 to 7.13. In these Figures a parabolic fit is indicated by the solid line and the broken lines indicate the interval in which 95% of the data points are located. The widths of these intervals with respect to the average values of all data points are given in Table 7.1.

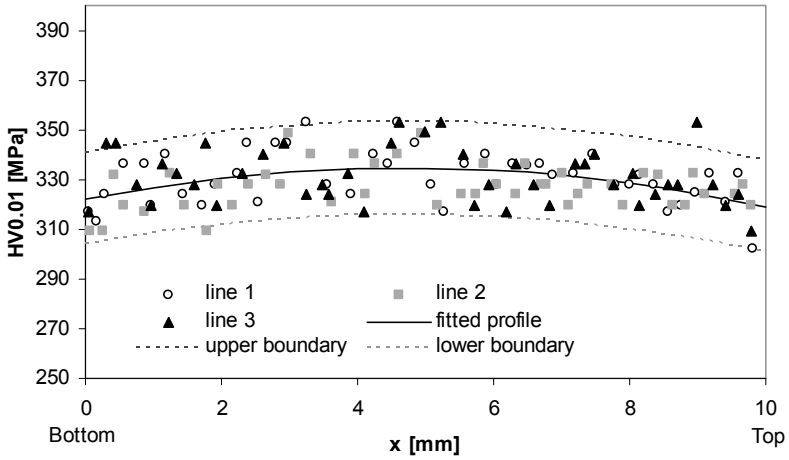

Figure 7.10: MicroVickers hardness for 10 mm CF/PPS laminate (Procedure 1, 10 gram).

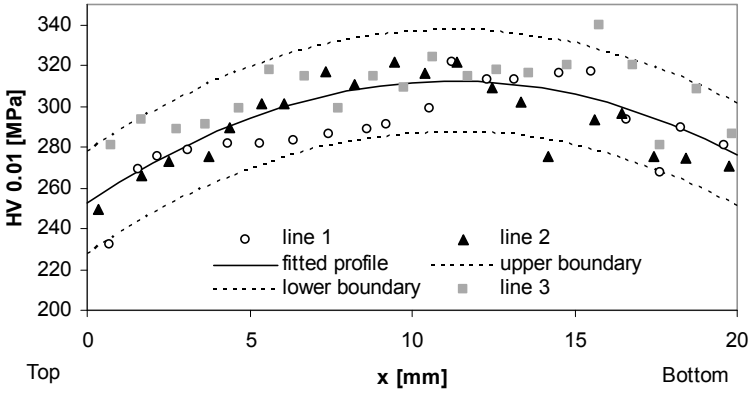

Figure 7.11: MicroVickers hardness for 20 mm CF/PPS laminate (Procedure 1, 10 gram).

Table 7.1: 95% bandwidth of scatter plots (from Figures 7.10 – 7.13).

Load	10 mm laminate	20 mm laminate
10 g	11.2%	16.9%
25 g	9.3%	12.3%

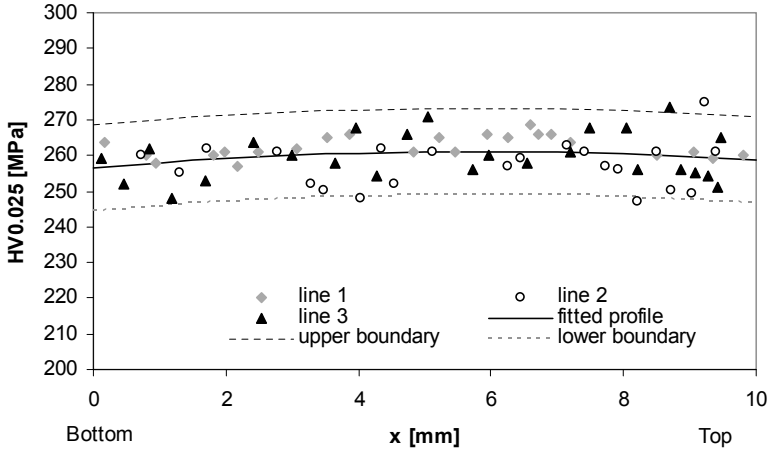

Figure 7.12: MicroVickers hardness for 10 mm CF/PPS laminate (Procedure 1, 25 gram).

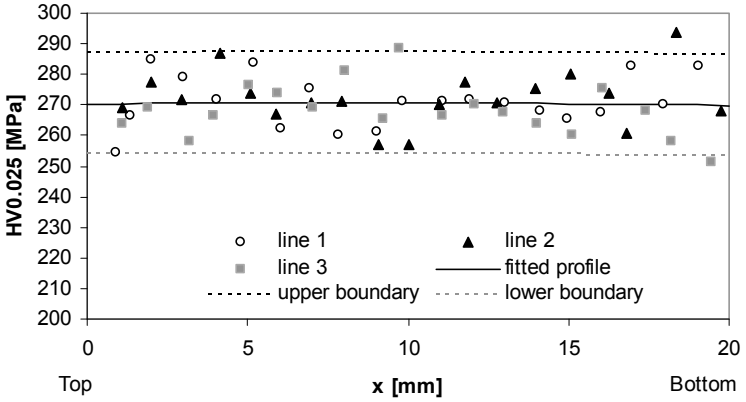

Figure 7.13: MicroVickers hardness for 20 mm CF/PPS laminate (Procedure 1, 25 gram).

It is clear from Figures 7.10 and 7.11 when compared to Figures 7.12 and 7.13, that for the 10 gram load a distinct parabolic shaped trend corresponding to the temperature profile can be found, whereas for the 25 gram load, this trend is less clear[2]. It seems that using the 25 g load makes the measurements less sensitive to microstructural variations. This is not likely related to the presence of the fibres, since even though the indented area with the 25 g load is larger than for 10 grams, it was made sure that the fibres did not disturb the measurement. One explanation may be that the smaller area covered by the 10 gram indentation load is more sensitive to variations in crystalline structure. An example of the crystal structure in pure PPS is shown in Figure 7.14. The spherulites are easily recognised, but there seems to

[2] Though the fit of the scatter plot resulted in higher R^2 values for a parabolic fit than for a fitted line.

be a wide range in their dimensions, i.e. widths and lengths ranging from 5 to 30 μm, with unordered (white) areas randomly distributed.

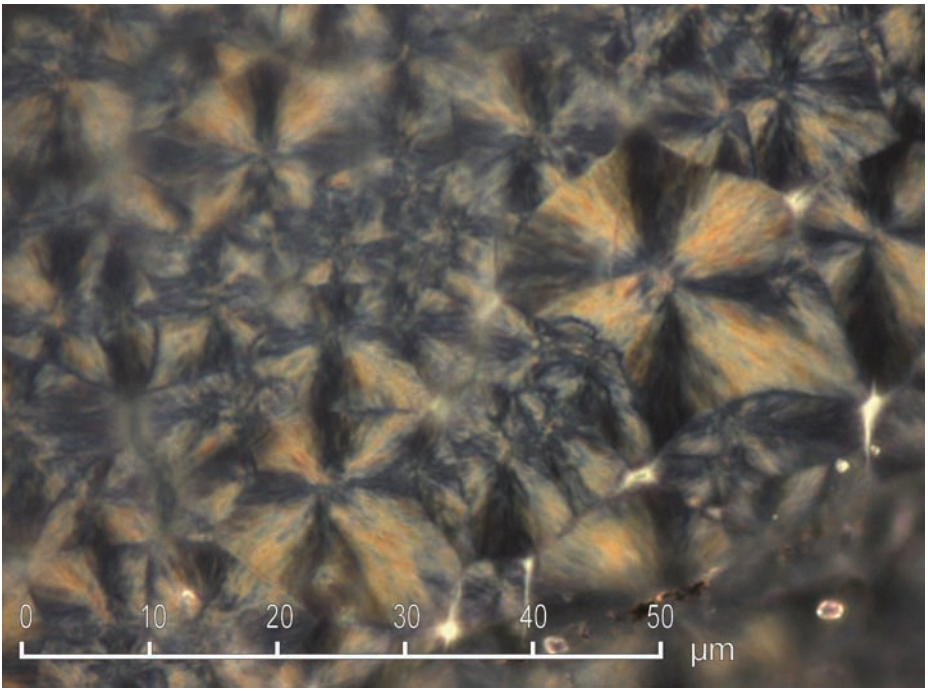

Figure 7.14: Crystalline structure in a hot-pressed PPS foil (polarisation optical microscopy).

With 10 g indentation load, the average indent size (~22 μm) is of the same order as the spherulite sizes, while the 25 gram indents (~41 μm) will always cover multiple spherulites. Usually, a slower cooling rate results in larger spherulites and a single crystal is harder than multiple smaller crystals. In the case that the slower cooling rates in the centre result in larger spherulites, the chances of covering only one spherulite for the 10 gram indentation are higher than at the surface. The 25 g indentations will always cover more spherulites and are therefore less sensitive to variations in crystal structure, while with the 10 g indentation a higher hardness may be found in the centre plies. This also explains the increased scatter as shown in Table 7.1 for the 10 gram load.

With Procedure 2 the 10 gram indentation load also gives a more distinct profile than the 25 gram load as can be seen in Figure 7.15, where the error bars represent the standard deviations of the average hardness values. With Procedure 2 similar trends of hardness variation through the thickness are found as with Procedure 1, but Procedure 2 definitely provides a more elegant display.

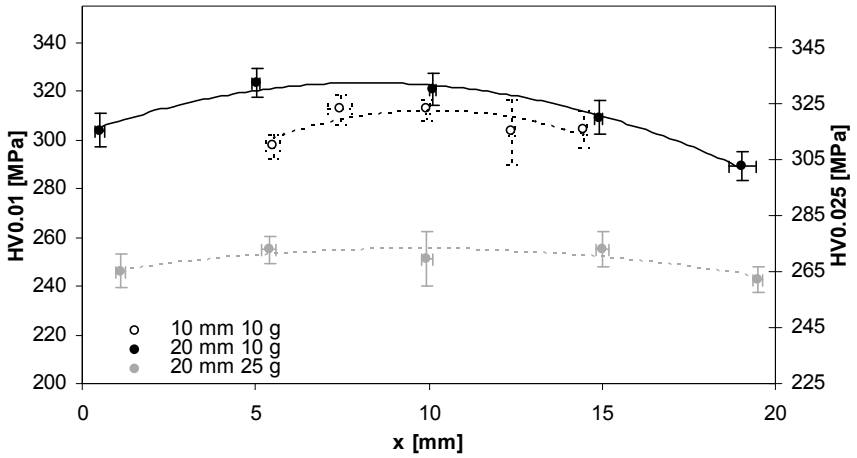

Figure 7.15: MicroVickers hardness for 10 and 20 mm CF/PPS laminates according to Procedure 2 with 10 and 25 gram indentation load.

In Figure 7.15 it is clear that the higher indentation load of 25 grams gives lower hardness values than the 10 grams indentation load, which can also be observed in Figures 7.10 and 7.11 compared to Figures 7.12 and 7.13. This is consistent with several published studies where it was shown that for this low loading range, a higher load gives a lower hardness value [16, 41, 43-45]. Therefore direct comparison between the hardness values determined with these two different small loads is not possible.

Summarising, because the variance (standard deviation divided by the average) in Figure 7.15 is comparable for the 10 and 25 gram loads, and 10 gram indentation load seems to be more sensitive to crystallinity morphology resulting in a more distinct profile, the 10 gram indentation load is preferred for identification of a hardness variation through the thickness of a laminate with a semi-crystalline matrix. When comparing Procedures 1 and 2 as described in Section 7.3.3, it can be said that Procedure 1 provides the researcher with a clear view of the scatter/ variation of hardness values, but for further analysis and correlations with other physical properties (such as degree of crystallinity) Procedure 2 is more suitable, as will be shown in Section 7.5.3.

Further explorations

To check the repeatability of the test, another 20 mm CF/PPS laminate was consolidated and cooled at a rate of 50°C/min in a Joos hot platen press, which resulted in a surface cooling rate of ~37°C/min. Again the cooling profile was parabolic in nature; with the centre plies and the plies at ¼ and ¾ experiencing a cooling rate of ~25°C/min and ~26°C/min, respectively. The corresponding parabolic hardness profiles are shown in Figure 7.16, together with the results for Fig. 7.15. This shows that the 25g load provides a higher repeatability, but the 10g loads indicate a more significant parabolic profile that can be related to microstructural variations. The large difference between the two 10g hardness profiles can be related to the smaller indentation diagonals, providing a larger statistical source for error as in Table 7.1, the operator effects mentioned in Section 7.3.3, or the earlier-mentioned variation in microstructure. These results indicate that the test can be repeated for other specimens and that a (qualitative) relation exists between thermal variations and microVickers hardness through the thickness of a composite.

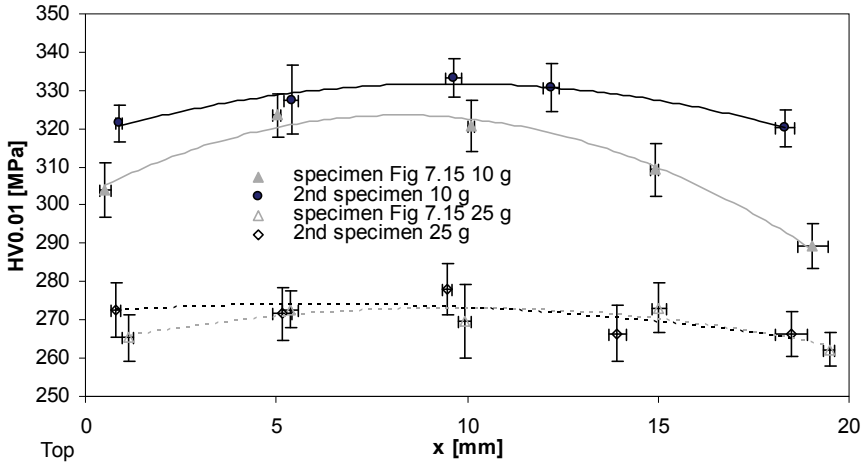

Figure 7.16: Hardness profile of a 20 mm thick CF/PPS laminate exposed to a surface cooling rate of 37°C/min (Procedure 2).

To confirm the relation between cooling rate and microVickers hardness, thin 4-ply carbon fibre fabric reinforced PPS laminates were produced in a Joos hot platen press at cooling rates (measured with thermocouples) similar to those experienced by the plies in the thick laminates. The hardness was tested of specimens taken from the plates' centres. A clear relation between cooling rate and microVickers hardness was found as can be seen in Figure 7.17.

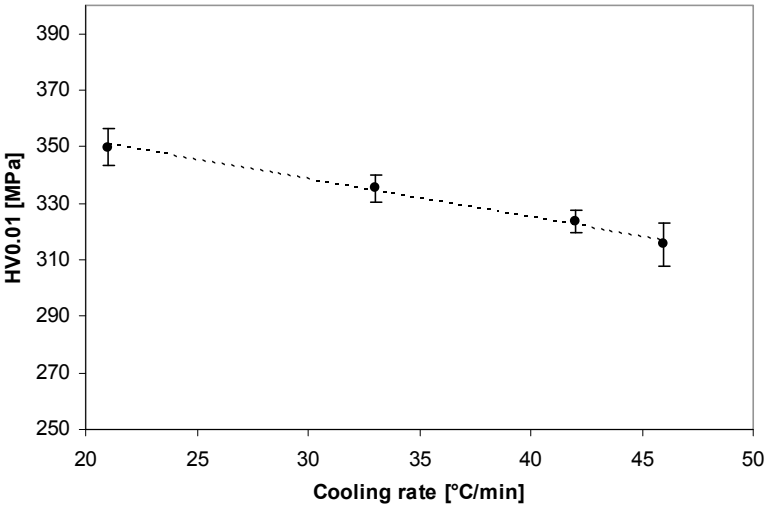

Figure 7.17: Relation between cooling rate and microVickers hardness (10 gram load, procedure 2) for thin hot-platen pressed CF/PPS laminates.

7.5.3 Comparison between degree of crystallinity and microVickers hardness

The question is whether the variation in hardness is related to differences in degree of crystallinity caused by the varying cooling rates. To answer this, the crystallinity profiles as obtained with DSC tests are compared to those of the microVickers test in Figures 7.18 and 7.19 for the 10 and 20 mm laminates, resp. A parabolic fit is indicated by the broken lines and the position numbering is as depicted next to Figure 7.18. In Table 7.2 the average crystallinity and hardness values ± the standard deviation are shown depending on the cooling rate (CR).

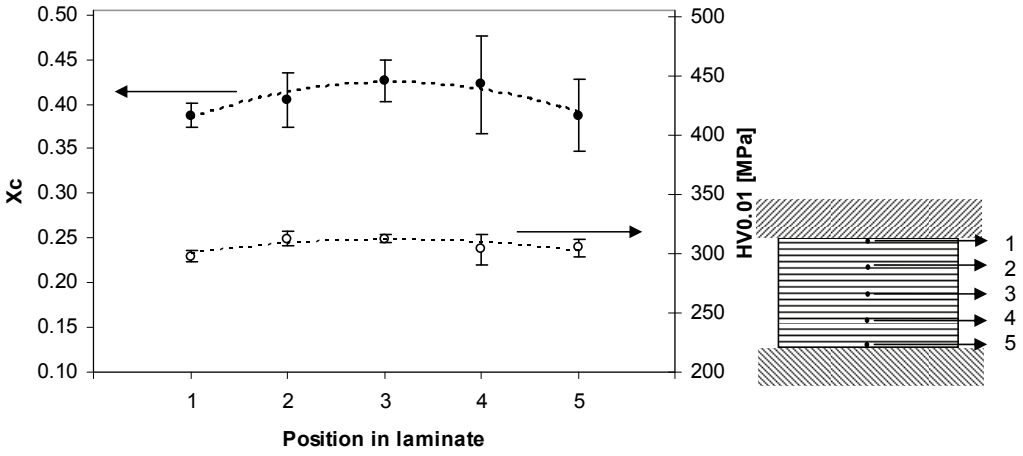

Figure 7.18: Degree of crystallinity (solid points) and hardness (open points) profiles for 10 mm CF/PPS laminate[3].

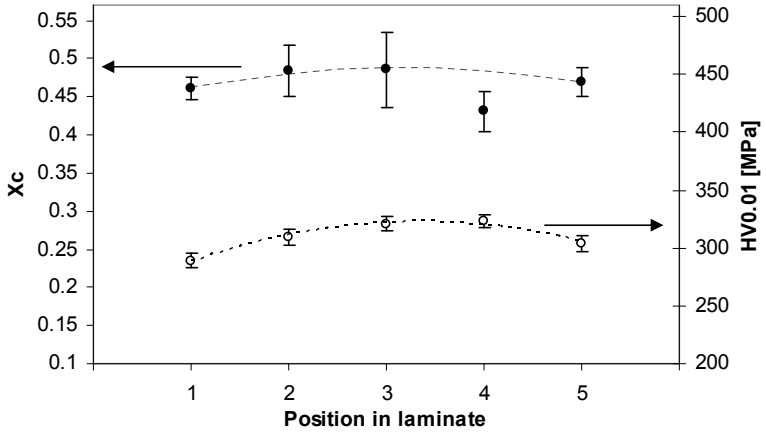

Figure 7.19: Degree of crystallinity (solid points) and hardness (open points) profiles for 20 mm CF/PPS laminate.

[3] The scales are chosen such that the curves can be compared.

Table 7.2: Experimental results of cooling rates and degree of crystallinity for the 10 and 20 mm thick CF/PPS laminates.

	10 mm laminate			20 mm laminate		
Position in laminate	CR [°C/min]	Degree of crystallinity	HV0.01 [MPa]	CR [°C/min]	Degree of crystallinity	HV0.01 [MPa]
1 (top)	47.1	0.39 ± 0.01	298 ± 5	36.2	0.46 ± 0.02	289 ± 6
2	-	0.40 ± 0.03	313 ± 7	24.0	0.48 ± 0.03	309 ± 7
3	38.2	0.43 ± 0.02	313 ± 4	21.0	0.49 ± 0.05	321 ± 7
4	-	0.42 ± 0.05	304 ± 13	24.8	0.43 ± 0.03[4]	323 ± 6
5 (bottom)	49.7	0.39 ± 0.04	305 ± 8	38.7	0.47 ± 0.02	304 ± 7

The crystallinity values for the CF/PPS laminates seem consistent with values found in literature [6]. This indicates that the TGA + DSC method as described in Section 7.3.3 provides reasonable crystallinity values.

In the Figures it seems that even for the low cooling rates present during manufacturing of these laminates, the parabolic variation of cooling rate through the thickness seems to result in a parabolic variation of degree of crystallinity: upon higher cooling rate (as in the surface plies), the level of crystallinity decreases.

However, the variation in crystallinity through the thickness is rather small: only 4% difference between the surface and centre plies for the 10 mm laminate, and 3% for the 20 mm laminate. This small variation is similar to that found by Lawrence et al. [4], who subjected a 20-ply CF/PEEK laminate to a higher cooling rate than applied in this work, resulting in crystallinity levels of 14 and 18 vol% at the surface and centre, respectively. Moreover the standard deviations mostly overlap, due to which the observed trend cannot be considered significant. The large variance (i.e. standard deviation divided by average) may be attributed to the multiple addition of experimental errors, such as in the determination of the area under the melting peak and polymer weight fraction. The accuracy in determination of the area under the melting peak is ~1 J/g, which results in an accuracy of ~3% in degree of crystallinity. In addition, a variation of 0.5% in the polymer matrix mass fraction m_c as determined with TGA, results in a crystallinity difference of 1.5%. The maximum variation in degree of crystallinity as found here (~4% for the 10 mm laminate), falls within the sum of these variations, and therefore no conclusions can be drawn based on these results. For future research, it is recommended to investigate if other experimental techniques, such as Fourier transformed infrared spectroscopy or X-Ray diffraction, are capable of generating more discriminative crystallinity values.

[4] The lower value for Position number 4 in Figure 7.19 and Table 7.2, may be attributed to the circumstance that the layer fractured during splitting and only two suitable specimens for DSC testing could be obtained. Therefore, it could not be verified whether the lower value was consistent or not.

However, it seems that the hardness variation through the thickness of the laminate corresponds with the crystallinity variation: the higher crystallinity values found in the centre of the laminate result in higher hardness values. In addition, where the crystallinity variation falls more or less within the margins of experimental error, the hardness variation gives a clearer trend of higher values in the centre and lower hardness in the surface plies, which is especially clear for the 20 mm laminate. Therefore, it may be concluded that the hardness variations can be attributed to variations in crystallinity properties caused by a varying cooling rate through the thickness.

7.6 Concluding remarks

This chapter showed the efforts to investigate whether the microVickers hardness test can be used to identify variations in polymer properties in composites caused by temperature variations through the thickness during processing.

In a 30 mm thick glass fibre reinforced turane laminate the temperature variation through the thickness during cure resulted indeed in a variation in matrix hardness.

In hot pressed carbon fabric reinforced polyphenylenesulfide (CF/PPS) laminates with 10 and 20 mm thickness, a parabolic gradient in cooling rate was found through the thickness. This was reflected by a parabolic hardness profile and the appearance of a similar crystallinity profile. However, the experimental method to determine the crystallinity of the composite as proposed in this paper, based on DSC and TGA, proved unable to distinguish between the small crystallinity variations (4%) as found in CF/PPS cooled at rates between 20 and 50°C/min.

For the CF/PPS composites the most detailed hardness results were obtained with averaging 10 to 15 indentations made with the smallest load of 10 g. The indentations were made on the laminate's cross-section in the matrix-rich areas in the layer of interest.

It may therefore be concluded that the microVickers indentation technique is a useful tool for obtaining fast and qualitative results on polymer property variations through the thickness in composite structures.

References

1. Parlevliet, P.P., Bersee, H.E.N., Beukers, A., Residual Stresses in Thermoplastic Composites - A Study of the Literature - Part I: Formation of Residual Stresses. Composites Part A-Applied Science and Manufacturing, , 37(11): 1847-1857, 2006.
2. Manson, J.A.E., Seferis, J.C., Process Simulated Laminate (Psl) - a Methodology to Internal-Stress Characterization in Advanced Composite-Materials. Journal of Composite Materials, 26(3): 405-431, 1992.
3. Deshpande, A.P., Seferis, J.C., Processing characteristics in different semi-crystalline thermoplastic composites using process simulated laminate (PSL) methodology. Journal of Thermoplastic Composite Materials, 9(2): 183-198, 1996.

4. Lawrence, W.E., Manson, J.A.E., Seferis, J.C., Thermal and Morphological Skin Core Effects in Processing of Thermoplastic Composites. Composites, 21(6): 475-480, 1990.
5. Gutierrez, M.C.G., *et al.*, Spatially resolved flow-induced crystallization precursors in isotactic polystyrene by simultaneous small- and wide-angle X-ray microdiffraction. Macromolecules, 37(2): 478-485, 2004.
6. Spruiell, J., Janke, C., A review of the measurement and development of crystallinity and its relations to properties in neat poly(phenylene sulfide) and its fiber reinforced composites. 2004, Oak Ridge National Laboratory: Oak Ridge. p. 80.
7. Baltá Calleja, F.J., Fakirov, S., Effect of Crystallinity on hardness, in Microhardness of Polymers, Clarke, D.R., Suresh, S., and Ward, I.M., Editors. 2000, Cambridge University Press: Cambridge. p.90-94.
8. Parvatareddy, H., *et al.*, An evaluation of chemical aging/oxidation in high performance composites using the vickers micro-indentation technique. Journal of Composite Materials, 30(2): 210-230, 1996.
9. Baltá Calleja, F.J., Martinez-Salazar, J., Rueda, D.R., Hardness, in Concise Encyclopedia of Polymer Science and Engineering, Kroschwitz, J.I., Editor. 1990, John Wiley & Sons, Inc.: New York. p.441-442.
10. England, G., Hardness testing, http://gordonengland.co.uk/hardness/microhardness.htm. 2006.
11. Low, I.M., Paglia, G., Shi, C., Indentation responses of viscoelastic materials. Journal of Applied Polymer Science, 70(12): 2349-2352, 1998.
12. Callister, W.D.J., Hardness, in Materials Science and Engineering - An Introduction. 1994, John Wiley & Sons, Inc.: New York. p.128-132.
13. ASTM_International, ASTM E384-05a: Standard Test Method for Microindentation Hardness of Materials. 2005. p. 24.
14. Baltá Calleja, F.J., Fakirov, S., Recent advances in the study and characterization of polymers by microhardness. Trends in Polymer Science, 5(8): 246-249, 1997.
15. Calleja, F.J.B., Sanditov, D.S., Privalko, V.P., Review: the microhardness of non-crystalline materials. Journal of Materials Science, 37(21): 4507-4516, 2002.
16. Baltá Calleja, F.J., Fakirov, S., Time dependence, in Microhardness of Polymers, Clarke, D.R., Suresh, S., and Ward, I.M., Editors. 2000, Cambridge University Press: Cambridge. p.15-16.
17. Low, I.M., Effects of load and time on the hardness of a viscoelastic polymer. Materials Research Bulletin, 33(12): 1753-1758, 1998.
18. Eyerer, P., Lang, G., Kunststoffe, 62: 322, 1972.
19. Baltá Calleja, F.J., Fakirov, S., Tabor's relation, in Microhardness of Polymers, Clarke, D.R., Suresh, S., and Ward, I.M., Editors. 2000, Cambridge University Press: Cambridge. p.6-8.
20. Baltá Calleja, F.J., Fakirov, S., Microhardness determination in polymeric materials, in Microhardness of Polymers, Clarke, D.R., Suresh, S., and Ward, I.M., Editors. 2000, Cambridge University Press: Cambridge. p.11-45.
21. Baltá Calleja, F.J., *et al.*, Correlation of hardness and microstructure in unoriented lamellar polyethylene. Journal of Materials Science, 16(3): 739-751, 1981.
22. Bai, S.L., Indentation properties of the filler and matrix in polymer composites. Journal of Materials Science Letters, 21(1): 85-88, 2002.
23. van der Werf, A.W., MicroVickers indentation as an analysis tool for matrix properties in thermoplastic composites. 2006 Aerospace Engineering, Delft University of Technology, Delft.
24. Favre, J.P., Residual thermal stresses in fibre reinforced composite materials - A review. Journal of the Mechanical Behavior of Materials, 1(1-4): 37-53, 1988.
25. Fakirov, S., Baltá Calleja, F.J., Krumova, M., On the relationship between microhardness and glass transition temperature of some amorphous polymers. Journal of Polymer Science Part B: Polymer Physics, 37(13): 1413-1419, 1999.
26. Strong, A.B., Curing tests, in Fundamentals of Composites Manufacturing: Materials, Methods and Applications. 2008, SME. p.274-275.
27. Compston, P., Dexter, D., The effect of ultraviolet (UV) light postcuring on resin hardness and interlaminar shear strength of a glass-fibre/vinylester composite. Journal of Materials Science, 43: 5017–5019, 2008.
28. Colton, J., Blair, B., Experimental study of post-build cure of stereolithography polymers for injection molds. Rapid Prototyping Journal, 5(2): 75-81, 1999.
29. Yin, Y., *et al.*, Preparation and properties of UV-curable polymer/nanosized indium-doped tin oxide (ITO) nanocomposite coatings. Journal of Materials Science, 42(15): 5959-5963, 2007.
30. Suwanprateeb, J., Rapid examination of annealing conditions for HDPE using indentation microhardness test. Polymer Testing, 23(2): 157-161, 2004.
31. Rueda, D.R., Martinez-Salazar, J., Baltá-Calleja, F.J., Annealing effects in lamellar linear polyethylene as revealed by microhardness. 20(3): 834-838 1985.
32. Stuart, B.H., Briscoe, B.J., Scratch hardness studies of poly(ether ether ketone). Polymer, 37(17): 3819-3824, 1996.
33. Krumova, M., *et al.*, Elastic Properties of Oriented Polymers, Blends and Reinforced Composites Using the Microindentaion Technique. Colloid & Polymer Science, 280(7): 591-598, 2002.
34. Minkova, L., Peneva, Y., Microhardness of PET-based liquid crystalline copolyesters: influence of the microstructure. Polymer, 44(21): 6483-6488, 2003.
35. Miyazaki, N., Effect of crystallization of thermoplastic polyimide resin on erosion rate. Journal of Materials Science Letters, 15(16): 1422-1423, 1996.
36. Gonzalez, A., *et al.*, A microhardness test to detect crystallinity changes in stabilized rigid PVC. Polymer Testing, 6(5): 361-367, 1986.
37. Ramanathan, T., Schulz, E., Subramanian, K., Determination of micro-hardness and elastic modulus in the transcrystalline zone of carbon fibre/PPS composites using a knife edge indentor. Composites Science and Technology, 65(1): 1-7, 2005.
38. Dubey, V., *et al.*, Studies on the Microhardness of Glass-Fiber Reinforced Polymer (Gfrp). Polymer Testing, 11(3): 225-231, 1992.
39. Kucner, L.K., McManus, H.L., Experimental Studies of Composite Laminates Danaged by Fire, in International SAMPE Technical Conference. 1994, SAMPE. p. 341-353.
40. Paplham, W.P., *et al.*, Microhardness of Carbon-Fiber-Reinforced Epoxy and Thermoplastic Polyimide Composites. Polymer Composites, 16(5): 424-428, 1995.
41. Perrin, F.X., Nguyen, V., Vernet, J.L., Mechanical properties of polyacrylic-titania hybrids--microhardness studies. Polymer, 43(23): 6159-6167, 2002.

42. Cebe, P., Review of Recent Developments in Poly(Phenylene Sulfide). Polymers & Polymer Composites, 3(4): 239-266, 1995.
43. Amitay-Sadovsky, E., Wagner, H.D., Evaluation of Young's modulus of polymers from Knoop microindentation tests. Polymer, 39(11): 2387-2390, 1998.
44. Chen, X., Yan, J., Karlsson, A.M., On the determination of residual stress and mechanical properties by indentation. Materials Science and Engineering a-Structural Materials Properties Microstructure and Processing, 416(1-2): 139-149, 2006.
45. Swaddiwudhipong, S., *et al.*, Modeling nano-indentation tests of glassy polymers using finite elements with strain gradient plasticity. Materials Science and Engineering: A, 404(1-2): 179-187, 2005.

Chapter 8: Shrinkage of Anionic Polyamide-6

8.1 Introduction

This chapter is the first where the aim is to identify the parameters responsible for residual strains in thick APA-6 composites, by using the previously described experimental techniques. The most important matrix properties responsible for process-induced residual strains were identified in Chapter 2 as shrinkage and the temperature range over which strain development occurs, while Chapter 4 showed that this can be detected with the fibre Bragg grating (FBG) technology.

Therefore, this chapter shows an effort into identifying these parameters in the virgin APA-6 system with FBGs. The efficiency of strain transfer of the shrinking APA-6 to the optic fibres was investigated by inspection of the interface between the two. In order to verify the FBG results, volumetric dilatometry tests as described in Chapter 5 were conducted to determine the volumetric shrinkage of APA-6 during the entire processing cycle. First, the background on the APA-6 system and the relations between processing, microstructure and properties are discussed.

8.2 Processing, microstructure and property relations in anionic polyamide-6

The APA-6 material system used for this thesis contains the following components: a caprolactam monomer (*a* in Figure 8.1) that can be transformed with the bromomagnesiumcaprolactamate initiator (*b*) and carbamoylcaprolactam activator (*c*) into the APA-6 polymer by means of a chemical reaction, see Figure 8.2.

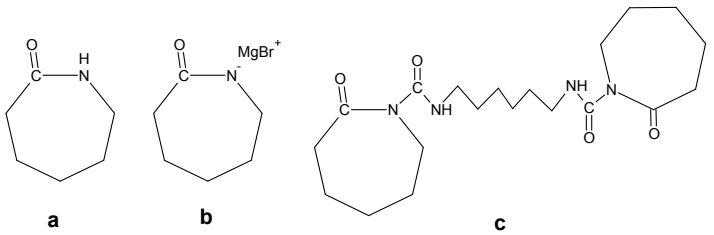

Figure 8.1: Chemical structure of (*a*) caprolactam; (*b*) caprolactam magnesiumbromide; and (*c*) hexamethylene-1,6-dicarbamoylcaprolactam, from [1].

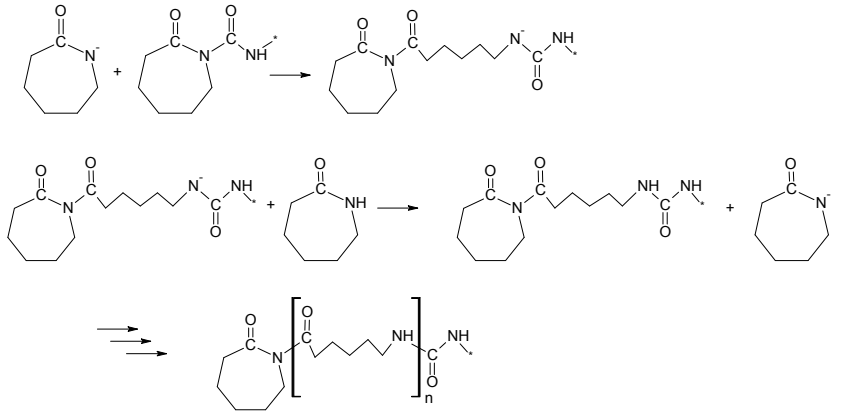

Figure 8.2:. Anionic polymerisation process of caprolactam into polyamide-6, from [1].

The three chemical ingredients are available as solid flakes or powder at room temperature. To enable proper mixture these components need to be molten first by heating them above the melting temperature of caprolactam, which is 70°C. It was found that at 110°C the above-mentioned combination of activator and initiator allows a useful processing window for infusion of a laminate, and reproducible GF/APA-6 laminates with good properties could be obtained [1]. Even though other fibre sizings and activator/ initiator combinations are being investigated, the results from these studies proved less reproducible and had not yet reached maturity during this investigation. Therefore, this 'basic' system was chosen for further study, not in the least because relatively much knowledge is available regarding this system.

8.2.1 Relations between processing temperature and thermal behaviour for APA-6

Anionic polymerisation of polyamide-6 can be achieved at temperatures between 120°C and 200°C [2]. A higher polymerisation temperature results in an increased reaction rate [3] and decreased initiation time: at 160°C, the reaction starts after ~6 minutes, whereas at 180°C this time has shortened to 3 minutes. This is shown in Figure 8.3 where the viscosity development is representative for the degree of polymerisation.

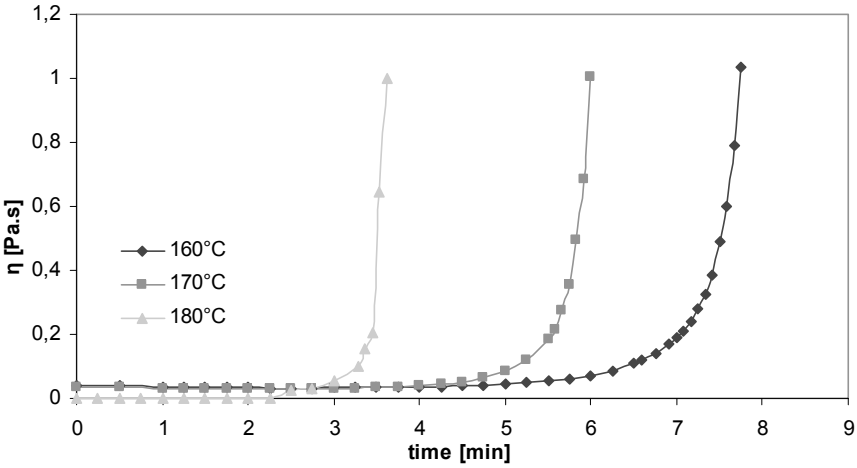

Figure 8.3: Effect of mould temperature on viscosity development for cast APA-6, from [1].

Polymerisation of ε-caprolactam is an exothermic process and therefore the temperature is not constant during polymerisation, i.e. there is a significant temperature rise as can be seen in Figure 8.4, due to which the polymerisation rate will also increase. This self-accelerating effect is also known as the thermally induced auto-catalytic effect. This process slows down as the monomer concentration reaches depletion.

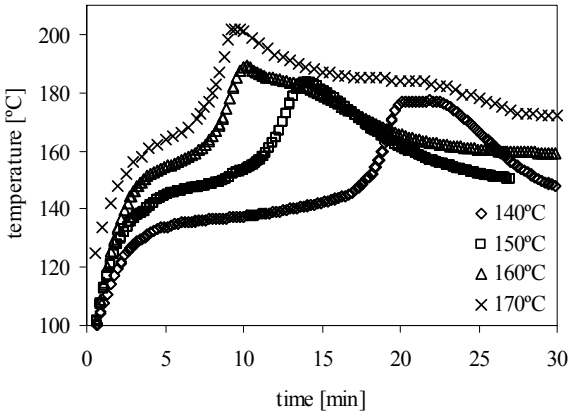

Figure 8.4: Temperature development of cast APA-6 at different mould temperatures, from [1] for a similar material system with less initiator.

Another thermal effect is presented by the crystallisation of the polymer chains, which is also an exothermic process. Crystallisation in a semi-crystalline polymer occurs when the temperature is below the melt crystallisation temperature (~220°C for common PA-6).

Therefore, polymerisation and crystallisation can take place simultaneously at the lower polymerisation temperatures, causing an enhanced exothermic temperature increase. While a rising process temperature increases the rate of polymerisation, it decreases the rate of crystallisation due to a smaller driving force for crystal formation (the temperature difference between the actual temperature and the melt crystallisation temperature). The exothermal temperature rise due to polymerisation + crystallisation may be sufficient in itself to partially melt the already-formed crystals. In that case energy in the form of heat is consumed because melting of crystals is an endothermic process. This self-regulating mechanism prevents overshooting of temperatures in the centre of thick products, where due to the polymer's insulating properties otherwise the temperature may reach the degradation temperature.

8.2.2 Relations between processing temperature, microstructure and properties

Since an equilibrium exists between the polymer and monomer content, it is not possible to obtain a 100% degree of monomer conversion into polymer. With increasing temperature this equilibrium shifts to the monomer side in Figure 8.2. Unreacted caprolactam acts as a plasticising agent, resulting in a lower glass transition temperature, lower melting peak temperature, and decreased mechanical properties [1, 4].

The viscosity[1] was observed to increase rapidly for APA-6 polymerised at temperatures above 150°C [1]. This was explained with the formation of side-reactions: the iso-cyanate groups in the carbamoyl activator will start de-blocking at temperatures above 160°C. This results in branching of the polymer chains, or even cross-linking at higher temperatures (>180°C), see Figure 8.5.

A depletion of activator is the result and it slows down the reaction, causing a reduction in the final degree of conversion. In addition, branching hinders the formation of crystals and therefore a lower final degree of crystallinity is obtained, including a lower melting temperature. In thick APA-6 products the maximum temperature in the centre is higher, resulting in more branching reactions. This causes a reduction in catalytic activity due to which the degree of conversion decreases and a higher concentration of caprolactam monomer is found in the centre.

[1] as measured by dilute solution viscosimetry

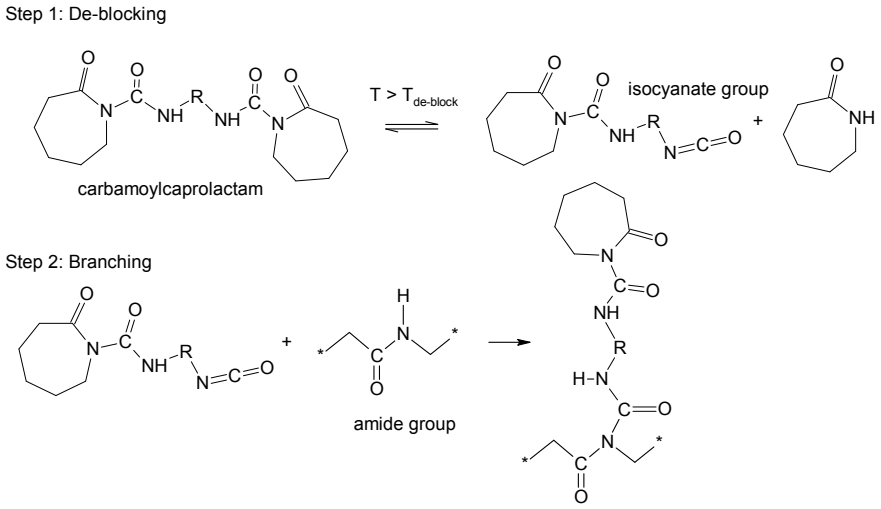

Figure 8.5: Chemical reaction during branching, from [1].

Another effect on degree of conversion is related to the degree of crystallinity: it is assumed that the conversion within a crystal is 100% and therefore, with higher degrees of crystallinity, higher degrees of conversion can be reached [1]. Van Rijswijk found that the degree of conversion of APA-6 only slowly decreases from ~98% to ~96.5% between polymerisation temperatures 150 and 180°C [1]. At temperatures above 180°C however, the degree of conversion drops significantly due to branching and a lower degree of crystallinity. At 140°C, crystallisation is so fast that it possibly traps caprolactam inside growing crystals before it can react with the other components. This not only lowers the degree of conversion significantly, but also gives white colouration of the crystals. The fast crystallisation shrinkage was found to cause internal void formation, because the liquid caprolactam flow cannot replenish the local volume decrease.

The melting temperature and degree of crystallinity decreased with increasing process temperature from 220°C and 47% for 140°C, resp., to 209°C and 33% for a processing temperature of 190°C. At higher temperatures, the driving force for crystal formation is smaller due to the increased mobility of the molecular chains. In addition, the time to form crystals is longer, leaving more time for possible side reactions that hinder the crystal formation. Residual caprolactam, crystal imperfections and branching/ side-reactions reduce the melting temperature.
DSC measurements showed two overlapping melting points in polymer samples that were processed at temperatures of 160°C and higher, indicating two types of crystals. Van Rijswijk concluded that both were alpha crystals, only with different levels of perfection [1]. Based on

this observation two stages of crystallisation were identified - primary and secondary crystallisation. Primary crystallisation occurs at the beginning of the reaction when a driving force for crystallisation exists during polymerisation, i.e. the temperature is sufficiently low. Typically, polyamide begins to crystallise during cooling at temperatures 20 to 30°C below the melting temperature [5]. Primary crystallisation will slow down when the temperature increases due to the exothermal heat, and the process may end or reverse. Secondary crystallisation occurs during cooling between the exothermic peak temperature and mould temperature during the dwell time, and during subsequent cooling to room temperature. The finally obtained degree of crystallinity is fixed when the temperature drops below the glass transition temperature of ~70°C.

Secondary crystallisation encounters more resistance, because during the hold time the temperature is higher, the molecular weight is higher and more side-reactions have taken place, which introduce a larger number of imperfections. This decreases the final degree of crystallinity and melting point. At low processing temperatures, the contribution of secondary crystallisation is much less than at higher temperatures and therefore more perfect crystals are obtained.

8.3 Detection of APA-6 shrinkage strains with fibre Bragg gratings

The thermal behaviour as shown in Figure 8.4 indicates that crystallisation proceeds differently at varying processing temperatures, which may have an effect on the total matrix shrinkage during polymerisation and crystallisation. Moreover, a variation in thermal contraction during cooling from the process temperature may be found due to differences in crystallinity level and/or degree of conversion. Hence, an effort was made to monitor the shrinkage induced by polymerisation and crystallisation as well as thermal contraction during cooling of APA-6 by means of the fibre Bragg grating technology. As was shown in Chapter 4, the FBG technology also allows the identification of the point where the resin is capable of strain-transfer to the optic fibre, i.e. ‘gel-point’. Thus far, it is unknown when this occurs during the polymerisation of APA-6 and which mechanism causes it.

8.3.1 Experimental procedures

Based on the results of van Rijswijk *et al* and Teuwen *et al* as described in the previous Section, FBG shrinkage tests were carried out in the temperature range of 160-180°C with the basic carbamoylcaprolactam activator and a holding time of 45 minutes, because these polymerisation temperatures and holding time resulted in optimum properties [1]. Initially the aim was to perform two tests at 160°C, 170°C and 180°C, resulting in six tests in total, because due to the high costs only a limited number of FBGs was available. However, the

first tests at ~180°C and ~160°C showed unreliable results and therefore it was decided to use the remaining optic fibres for tests at 165°C and 175°C, such that still some useful information could be obtained in this temperature range. Where possible, useful data were extracted from these first tests and used to explain observed trends in the results. The thermal and shrinkage behaviour were monitored with thermocouples and FBGs, resp.

Materials

The anionic polyamide-6 matrix was obtained by anionic polymerisation of ε-caprolactam, using 1.2mol% caprolactam magnesium bromide (Brüggolen C1) as initiator and 1.2mol% hexamethylene-1,6-dicarbamoylcaprolactam as activator (Brüggolen C20), see Figure 8.2. All chemicals were supplied by Brüggemann Chemical, Germany.

A mini mixing unit (MMU) was designed and manufactured by Bronk Industrial BV in the Netherlands to melt and mix the ingredients. In tank 'A' a monomer-activator solution was mixed and in the second tank 'B' a monomer-initiator solution, both surrounded by a nitrogen environment at 110°C. When the two solutions were ready, they were mixed through a heated static mixer.

Specimen preparation and test set-up

For every test, three glass test tubes were filled with the reactive mixture and these were placed in an oil bath that was set to the required polymerisation temperature. After 45 minutes the test tubes were taken from the oil bath and allowed to cool down to an ambient environment (~21°C).

The test set-up is schematically shown in Figure 8.6: a large (2500 ml) glass beaker was filled with thermally conductive silicone oil (Dow Corning 550 Fluid from Mavom B.V., Netherlands), and wrapped with silicate wool (RS Components, Netherlands) and aluminium foil for thermal insulation. The beaker was placed on top of an electrically heated plate (Ikatherm® HCT, from IKA Labortechnik, Germany) with a temperature controller (Yellowline TC1, from IKA Labortechnik, Germany) and the oil was heated to the desired polymerisation temperature with an accuracy of 1-3°C around the set temperature. An aluminium lid with holes equal to the size of the test tube outer diameter (20 mm) was placed on top of the beaker, such that the test tubes could be suspended in the oil bath.

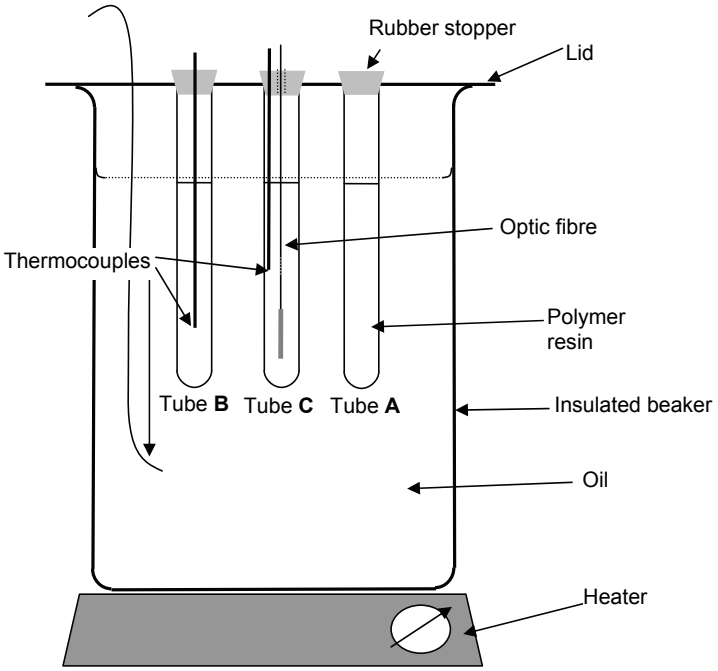

Figure 8.6: Schematic view of test set-up.

For every test, three Schott Fiolax® glass test tubes (Duran GmbH, Germany) were used with diameter and length of 20 and 150 mm, respectively. After thorough cleaning, the test tubes were coated with Nyrim® Mould Sealer (Brüggemann, Germany) for easy release and to allow free expansion and contraction of the polymer, because additional strain build-up due to interaction of the APA-6 with the untreated inner glass surface can affect the results significantly[2]. The three test tubes and their purpose are described below:

- Test tube 'A' was filled with the mixed resin directly from the MMU and placed in the oil bath. A rubber stopper was placed on top immediately to prevent any environmental moisture to react with the APA-6. The polymer from this tube was used for further property analysis.
- Test tube 'B' held a rubber stopper where a metal tube with 1.5 mm diameter was inserted. This tube contained a K-type thermocouple and ensured that the thermocouple was located exactly in the centre of the test tube. In addition, a 3 mm diameter metal resin inlet and air outlet tube were inserted in the rubber stopper. The resin inlet tube was connected to a syringe with a silicone hose, see Figure 8.7. The test tube with

[2] The adhesion between APA-6 and the glass surface is very good, and polymerisation shrinkage is therefore constrained at the inner surface of the glass tube. This results in a significant compressive strain in the circumferential direction, due to which spontaneous fracture of the glass tube was observed to occur.

attached syringe was already placed in the hot oil bath. Another test tube was filled with the liquid mixture directly from the MMU and was used to slowly pour the resin into the syringe after which the syringe was sealed with a rubber stopper.

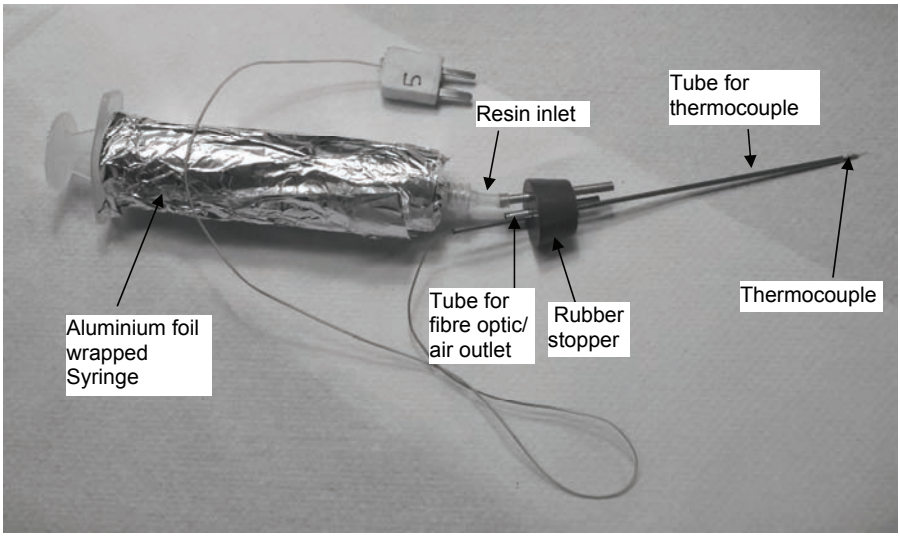

Figure 8.7: Syringe and rubber stopper for APA-6 test tubes.

- Test tube 'C' is similar to test tube 'B', besides the presence of a central guidance tube (outer diameter 3.0 mm) for the optic fibre with the two gratings. The metal capillary of the FBG temperature sensor possessed sufficient mass to ensure that the fibre optic sensor was suspended straight in the centre of the test tube. An inlet tube and thermocouple guidance were also present. The thermocouple was not located in the centre of the test tube, since it would interfere with the optic fibre.

Fibre Bragg Gratings

Similar optic fibres as described in Section 4.3.3 were used for determination of strain build-up during the anionic reaction of APA-6: two 4 mm gratings with Bragg wavelengths of 1558 nm and 1563 nm for the strain grating and temperature grating, resp. The FBG temperature sensors were prepared as described in Section 4.3.3 and Appendix B.

However, the Epotek® glue proved to be chemically affected by the caprolactam and sometimes the caprolactam mixture would find its way into the capillary and affect the FBG T-sensor measurements, which occurred for example with the specimen polymerised at 174.6°C. After cooling and solidification of the caprolactam around the grating, a residual (compressive) strain was then observed. The temperature readings of the thermocouple

during heating to the processing temperatures (before the glass tube was filled with APA-6 mixture) were used for temperature calibration of the grating by fitting the wavelengths of the strain FBG to the temperatures. The temperatures registered by the thermocouples during the polymerisation cycle were used next in the obtained fitted equation to calculate the wavelength shifts due to thermal variations, i.e. $(\Delta\lambda_B/\lambda^0_B)_T$ in Eq. (4-10). This is however not ideal, because the thermocouples are not located in the centre of the test tube, close to the strain grating.

The optic fibres and strain-free sensors were cleaned with ethanol and connected to an FBG-Scan616 interrogator (FOS&S, Belgium). Reference wavelengths were recorded at room temperature to determine the initial Bragg wavelengths of the gratings λ^0_B. K-type thermocouples (two for the test tubes and one for the oil bath) were also cleaned and connected to a Keithley data logging device. The data acquisition frequency was 5 seconds (0.2 Hz). Eq. (4-12) is used for calculation of the linear strain development $\Delta\varepsilon_{lin}$ as detected by the strain grating.

8.3.2 Results and discussion

Strain development during processing

Strain development as registered by the FBGs during polymerisation, crystallisation and subsequent cooling is first discussed for one representative test. The average oil bath temperature during polymerisation of this particular specimen was 166.5°C. The results for temperature and strain development are shown in Figure 8.8. The curve for the temperature grating (FBG T-sensor) was determined with the factor $(\Delta\lambda/\lambda^0_B)_T$.

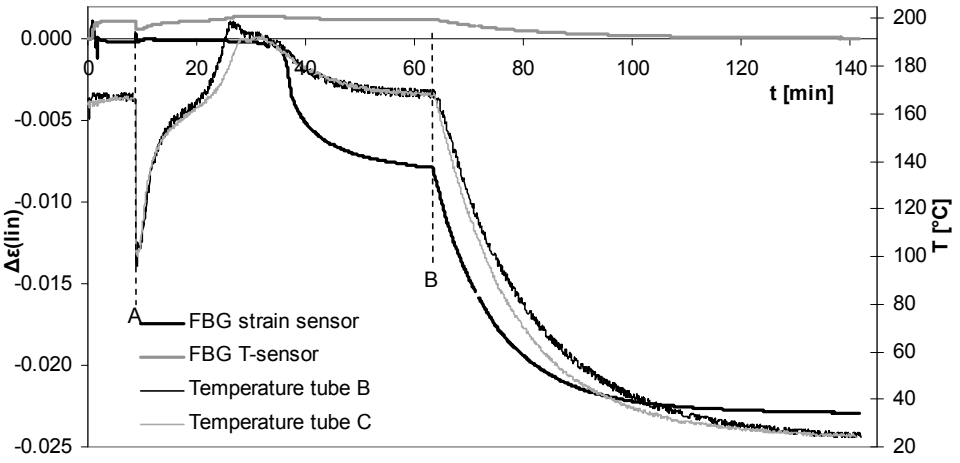

Figure 8.8: Strain and temperature development with time during polymerisation of APA-6 at 166°C.

Point *A* represents the time when the liquid mixture of ~110°C was poured into the test tubes and point B corresponds to the time when the test tubes were removed from the oil bath and allowed to cool down to the environment. The curve representing the FBG T-sensor returns to zero when cooling to room temperature, which confirms that the wavelength shifts between the reference measurement and the end of the cure cycle were caused only by temperature variations. The enlarged curves between points A and B are shown below. The measured wavelength differences *Δλ* of the FBGs are shown to clarify the difference in response between the temperature grating and the strain grating[3], for which the wavelength difference is the sum of thermal and strain effects. A wavelength shift of 1 nm corresponds roughly to a temperature difference of 80°C in the absence of external strains.

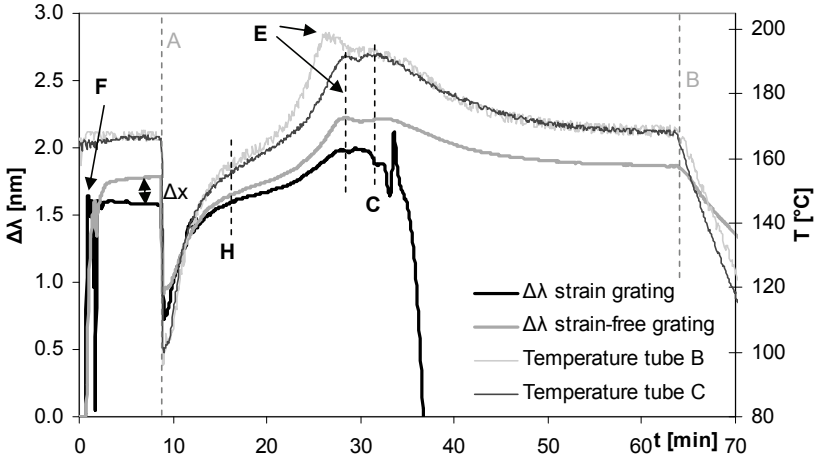

Figure 8.9: Wavelength shifts and temperature variations during polymerisation of APA-6.

Several points are highlighted, which will be discussed in chronological order:
Point F corresponds to the suspension of the optic fibre inside the empty test tube that was already placed in the hot bath. The strain grating instantly shows a wavelength shift due to the temperature difference, whereas the encapsulated temperature grating shows a more gradual development towards the final wavelength difference: thermal lag. The difference in wavelength shift *Δx* between the two gratings is probably not caused by a temperature difference within the test tube, but it was frequently observed that gratings within the same fibre show different wavelength shifts when exposed to equal temperature differences [6]. The exact nature of this remains to be clarified. On a total wavelength shift of -28 nm

[3] Plotting of the strains with time would provide a less clear picture.

corresponding to -2.3 % compressive strain after production, this 0.2 nm difference results in a final strain variation of 0.02 % (1 % of the total value), which falls inside the variation of the results and is therefore not considered significant.

At **point A** (t = 9 min), the thermocouples and FBGs clearly sense the relatively cold liquid when this is poured inside the test tubes. The liquid starts to heat up immediately due to the hot environment of the oil bath.

At **point H** a deflection point is visible that indicates that polymerisation of APA-6 has started and exothermal heat is generated that increases the heating rate (auto-catalytic effect). At this point the mixture has reached a temperature of ~160°C, which is ~9 minutes after the mixture was poured in the test tubes. Unfortunately, no thermal data for the viscosimetry tests in Figure 8.3 (Section 8.2) are available for comparison, while the polymerisation seems to start a few minutes later compared to the onset of viscosity increase in Figure 8.9, but this can also be attributed to a difference in test set-up.

After H a difference in heating rate can be noted between the two test tubes, with a different peak temperature (**point E**) as a result. The peak temperature in test tube B (199°C) is higher than in test tube C (192°C) and this temperature is also reached sooner (t = 26.5 min, compared to t = 28 min, resp.) This difference can be attributed to the central location of the thermocouple in test tube B, while in test tube C the thermocouple position is closer to the side of the test tube.

After the exothermic peak, another hump in the temperature profile can be seen at **Point C**, which is attributed to the exothermal crystallisation of the polymer chains. The polymer temperature is then around 191°C at ~32 minutes. Surprisingly, these points coincide for both thermocouples, whereas for the FBG temperature sensor this effect seems somewhat delayed, which may be explained by the thermal lag as mentioned earlier. This is also the point where the strain-grating curve starts to deviate significantly from the temperature-related curves, indicating the onset of strain build-up around the optic fibre. This strain build-up does not occur smoothly, as is shown by the erratic peaks in the curve. In Figure 8.10, where the strain development $\Delta\varepsilon_{lin}$ is shown together with the thermal response of the FBG T-sensor, it is clear that the strain grating experiences a significant strain from point C onwards, which can be related to the crystallisation of the APA-6 polymer.

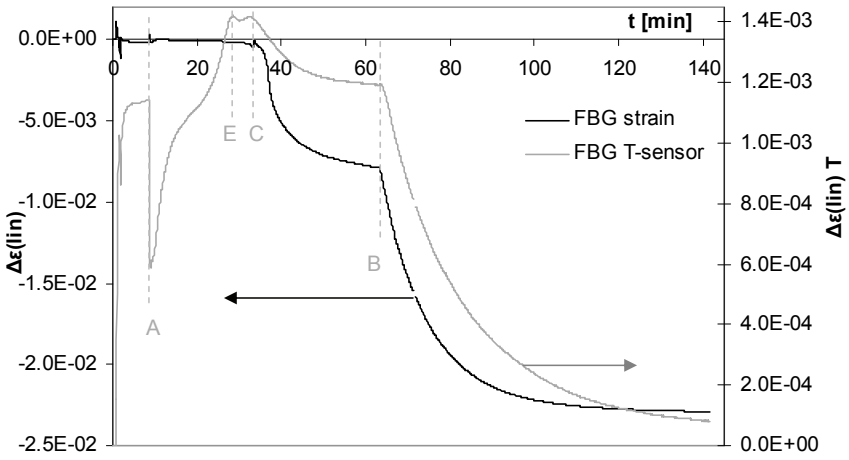

Figure 8.10: Strain development and thermal wavelength shifts of an FBG during cure of APA-6.

A polymerisation shrinkage effect that might be expected to occur around point E is hardly registered by the FBG. It is assumed that before point C the formed polymer chains are in the amorphous state (consisting of a mixture of APA-6 polymer chains and caprolactam [7]), since the temperature is still too high (~192°C) to induce significant or detectable crystallisation. It is also far above the glass transition temperature of the polymer (70°C), which renders the rubbery amorphous phase unable to transfer strains.
The strain profile between points C and B resembles the temperature profile, which suggests that thermal contraction during cooling from the exothermal peak temperature, possibly in combination with additional crystallisation shrinkage, causes the compressive strain of -0.008 at point B.

Comparison of thermal behaviour at different processing temperatures
The temperature readings of all test tubes 'B' are displayed in Figure 8.11. The mentioned temperatures are the average oil bath temperatures during polymerisation. The curves are shifted over the time axis, such that the times of injection at t = 0 min coincide for all specimens.

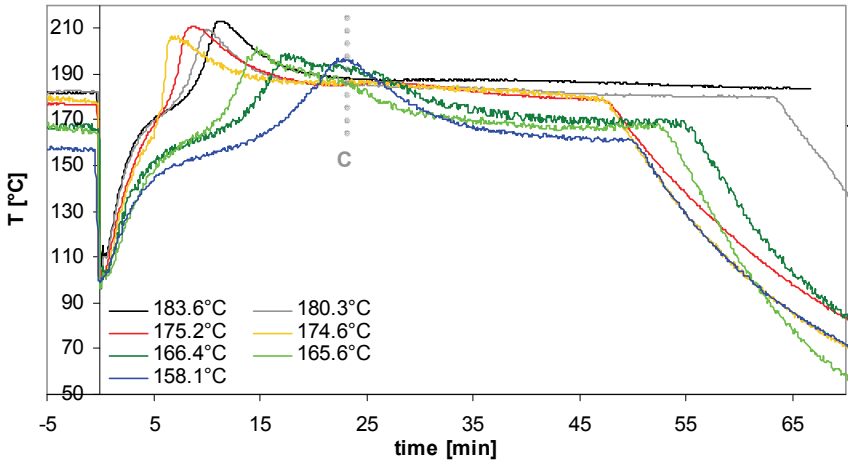

Figure 8.11: Temperature development in test tubes B with centred thermocouple for various polymerisation temperatures.

It is clear from this Figure that the polymerisation reaction starts earlier for higher processing temperatures. The exothermal polymerisation peaks become higher and narrower for temperatures of 175°C and higher, which indicate higher polymerisation rates. The crystallisation peaks on the other hand, are extended to broad humps at these temperatures, indicating that crystallisation goes very slowly due to less super-cooling. Distinct crystallisation peaks are visible for the polymerisation temperatures around 166°C, and only one peak is found for 158°C, which is explained by simultaneous crystallisation and polymerisation and is therefore visible as one large peak. This is consistent with the studies described in Section 8.2.

The specimens processed at 180-183°C show a lower exothermal development rate than the 175°C specimens, which may be attributed to the absence of a crystallisation exotherm due to the high temperatures.

The temperature readings from test tubes ‘C’ are displayed in the following Figure:

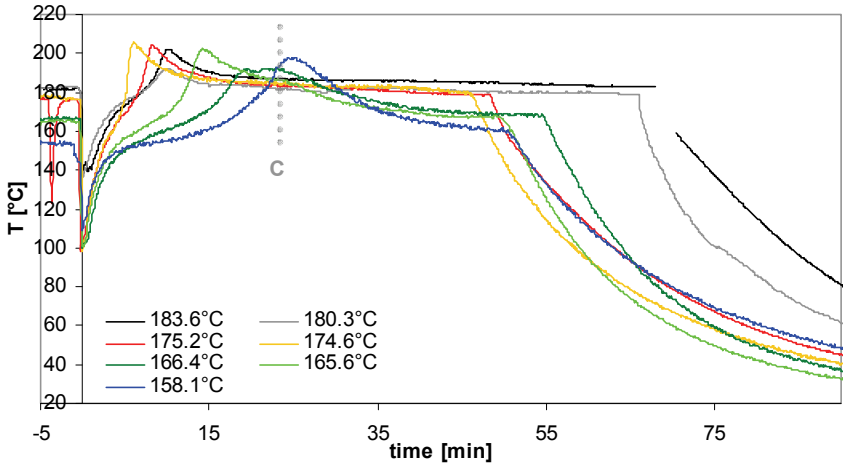

Figure 8.12: Temperature development in test tubes C for various polymerisation temperatures.

In general, the exothermal peak temperatures for these tubes are lower and the widths smaller than in test tubes B. This can be explained by the position of the thermocouple closer to the glass surface where the exothermal heat can be transferred better to the surroundings. The wavelength shifts of the temperature gratings are shown in the following figure. An almost linear relation exists between wavelength and temperature (1°C = ~0.012nm or 1nm = ~83°C). Similar trends as for the thermocouples can be observed.

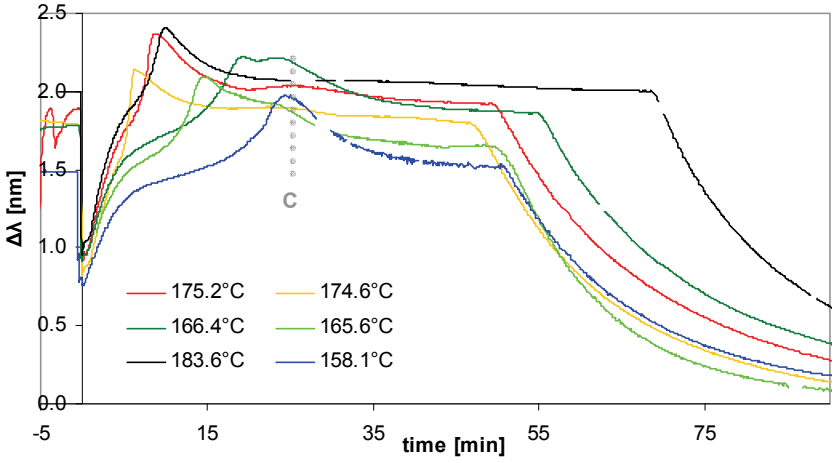

Figure 8.13: Thermal effects during polymerisation of FBG T-sensors.

The crystallisation peak temperatures for the 175°C specimens are more clear than for the thermocouples in Figure 8.11, which can be explained by the higher sensitivity of the

temperature grating. The thermocouples show significant scatter within 1°C, whereas for the FBG this is maximal 0.010 nm, corresponding to 0.83°C. The wavelength shift due to the thermal crystallisation peak is for example 0.020 nm in the 175.2°C specimen, corresponding to a temperature variation of 1.7°C, which is barely noticeable with the thermocouples.

Except for 183°C, since at this temperature crystallisation is significantly delayed, all temperature curves show a peak crystallisation exotherm (Point **C**) around 24 minutes after infusion. The corresponding temperature is 185°C ± 3°C, which can be regarded as the crystallisation temperature.

Strain development at different processing temperatures

Around the crystallisation time (Point C, 20-25 minutes), the FBG sensors start to detect strain formation, see Figure 8.14.

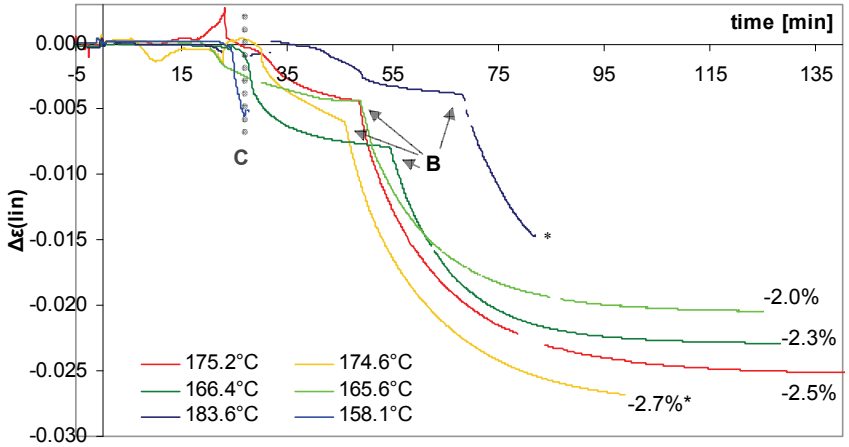

Figure 8.14: Strain development with time, the final strain values are depicted in the graph.
*: The Bragg wavelength of the strain grating went below the lower detectable range, and therefore no strain values could be calculated for temperatures below this point.

The majority of the strain clearly develops after the test tubes were taken from the oil bath (points **B**), i.e. during cooling from the processing temperature to room temperature. This is reflected by the higher strains in the specimens produced at a higher temperatures. The detected polymerisation + crystallisation shrinkage until this point B varies significantly and no trend can be observed for the different temperatures.

The strain curves for the 175°C temperatures and higher show much variation and sudden jumps before final shrinkage is detected. This can be attributed to the inhomogeneity in the crystallisation process, because at high temperatures many competing mechanisms play a

role, such as fast polymerisation, melting of the primary crystals, branching and recrystallisation, as mentioned in Section 8.2.
In Figure 8.15 the strains with temperature development are displayed:

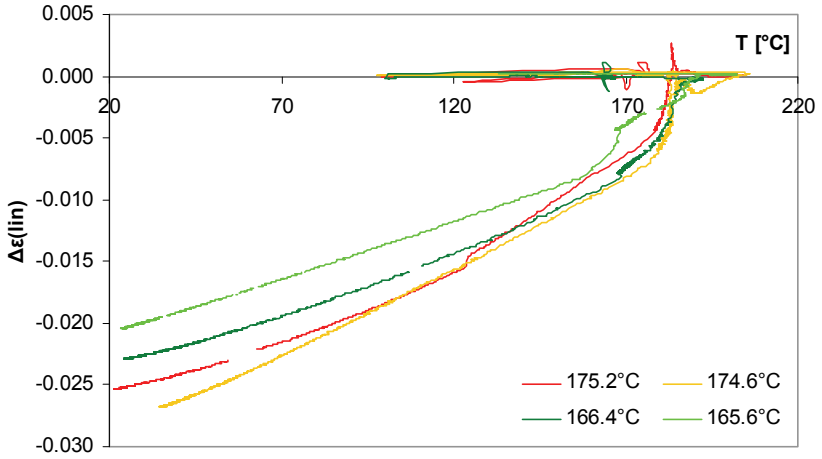

Figure 8.16: Development of strain with temperature.

Strain development for all specimens starts between 187 and 183°C, which coincides with the crystallisation temperature (Points C in Figures 8.11 and 8.12). From this figure it is clear that a higher processing temperature generates a higher residual compressive strain in the optic fibre. The non-linearity of the curves shows that this is a semi-crystalline polymer: upon cooling the degree of crystallinity increases until the glass transition temperature is reached.

8.4 Optic fibre - matrix interaction

To assess the reliability of the measured strains, it is necessary to investigate the efficiency of strain transfer from the APA-6 matrix to the optic fibre, since no shrinkage data are available for comparison. Specimens were therefore prepared for examination with Scanning Electron Microscopy and optical microscopy to investigate the fibre-matrix interface.
In addition, an effort was made to study possible debonding and the presence of voids around the optic fibre by means of micro-Computed Tomography (MicroCT) scanning.

8.4.1 Experimental procedures

MicroCT scan

The specimens for microCT scanning were prepared similarly to test Tube ‘A’, with the difference that an optic fibre without any grating was suspended in the mixture. To ensure

that the fibre was suspended straight inside the test tube, a metal capillary was glued at the fibre extremity. The processing temperature was 175°C. After cooling to room temperature, the reacted polymer was cut with a liquid cooled cutting machine in sections of ~4 cm length for the central parts and ~2 cm for the extremities. A SkyScan 1174 compact micro-CT (SkyScan, Belgium) scanner, located at the University of Warsaw, was used to study the 3-dimensional positioning of the optic fibre in the polymerised APA-6.

Microscopy

Cross-sections of the MicroCT Scan specimens were used for microscopic examinations and these were grinded and polished according to the recommended preparation cycle for polyamides by Struers GmbH [8]. The specimens were gold coated with a Balzers Union SCD040 gold sputter coater. The cross-sections were studied with a Jeol JSM-840 Scanning Electron Microscope (SEM), a Jeol JSM-7500F Field Emission SEM and a Zeiss Axiovert 40MAT inverted microscope.

8.4.2 Results and discussion

A scanning electron micrograph below shows the area of the interface between the optic fibre and the surrounding APA-6, where it is clear that at this stage no adhesion between the Ormocer® coating and the APA-6 polymer is present.

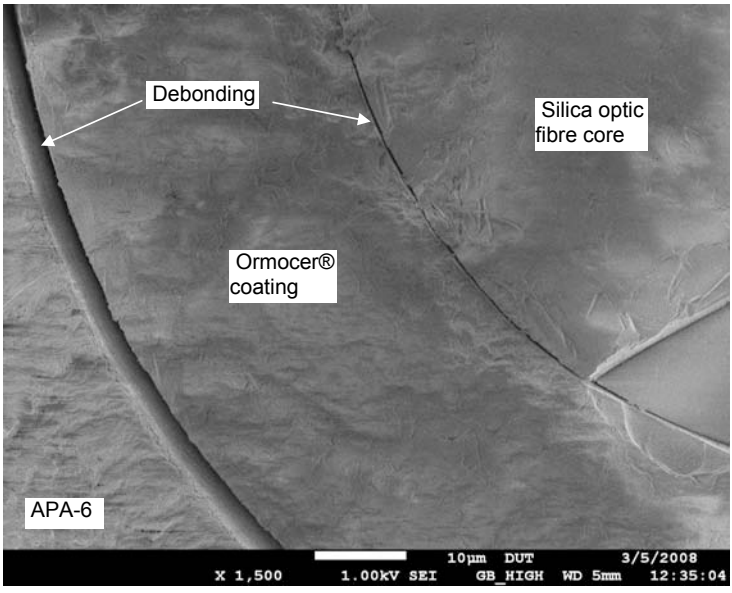

Figure 8.16: SEM picture of Ormocer® coated optic fibre embedded within APA-6.

The question remains though what caused this lack of adhesion. Bonding can be achieved by two mechanisms (see Chapter 2): chemical bonding and mechanical locking. In the case that chemical bonding was present between APA-6 and the Ormocer® coating, it can be that the grinding and polishing steps caused debonding, since water was used as a lubricant and it is known that this can disrupt the bond between polyamide and the fibre [9]. When no chemical bonding exists between the fibre coating and the polymer and strain transfer occurs only via mechanical locking, debonding in longitudinal direction may have occurred due to the high shrinkage of the APA-6 matrix compared to the optic fibre. In addition, the mechanical locking caused by radial shrinkage strains around the optic fibre can be relaxed by moisture absorption from the environment or during grinding. Since a smooth shrinkage curve is obtained (no stick-slip behaviour characteristic for longitudinal debonding) and the shrinkage values are relatively high, it is assumed that the most significant debonding occurred after the production cycle. One solution to prevent debonding is the use of a different optic fibre coating that is known to bond well with APA-6, such as the silane-based sizing used on the glass reinforcement used by van Rijswijk [1]. However, at the time of this research this coating was not yet available for the optic fibres.

Figure 8.16 also shows poor bonding between the optic fibre core and the Ormocer coating, which could also have been caused by grinding and polishing. A more plausible explanation however is that during chemical resistance tests, caprolactam was seen to produce significant swelling of the coating (detected as tensile strain by the grating), which may result in a decreased level of adhesion between the Ormocer® coating and the optic fibre core. In this case, the strain transfer by the Ormocer coating to the grating in the optic fibre core is not optimal. The observed debonding implies that the residual strains as detected by the optic fibre with Ormocer® coating are lower than the actual shrinkage contribution. Therefore, an optic fibre with another coating based on polyimide was examined as is illustrated in the Figure below.

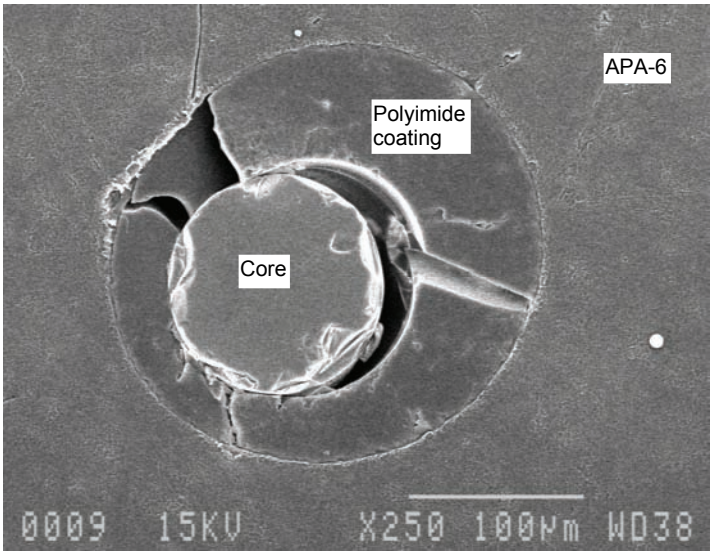

Figure 8.17: SEM picture of optic fibre embedded in APA-6 with a Polyimide coating.

This figure clearly shows that the polyimide (PI) coating was not applied homogeneously around the optic fibre. And even though no significant debonding is visible between the APA-6 and the PI coating, the debonding between the glass core and the PI coating is evident. One explanation can be that the caprolactam environment disrupts any bonds between the glass core and the PI. After exposure to CL at higher temperatures, the PI coating of optic fibres and capillaries was freed from its glass substrate and could be easily removed by hand. In addition, the glue for the capillary of the temperature grating did not adhere well to the PI coating.

The final choice for Ormocer® was based on a test with optic fibres coated with both PI and Ormocer® including 8 mm gratings. During polymerisation of APA-6, the results of both optic fibres were compared and it was found that the optic fibre with Ormocer® coating showed extensive peak splitting, whereas the one with PI did not. This implies that there is significant strain transfer between the APA-6 and Ormocer and much less with the PI coated fibre. The peak splitting may be related to crystallisation nucleation at the Ormocer® surface, see Figures 8.18 and 8.19, which was not visible for the specimen with the PI coated optic fibre in Figure 8.17.

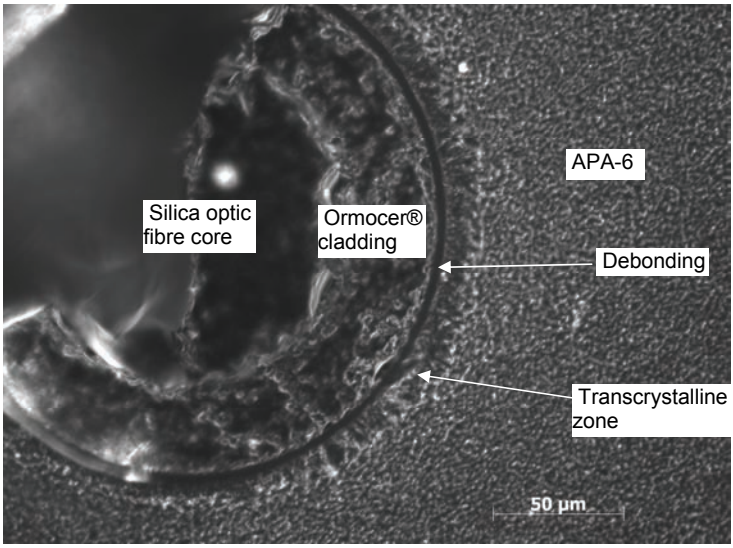

Figure 8.18: Micrograph of Ormocer® coated optic fibre embedded in APA-6 (Darkfield image).

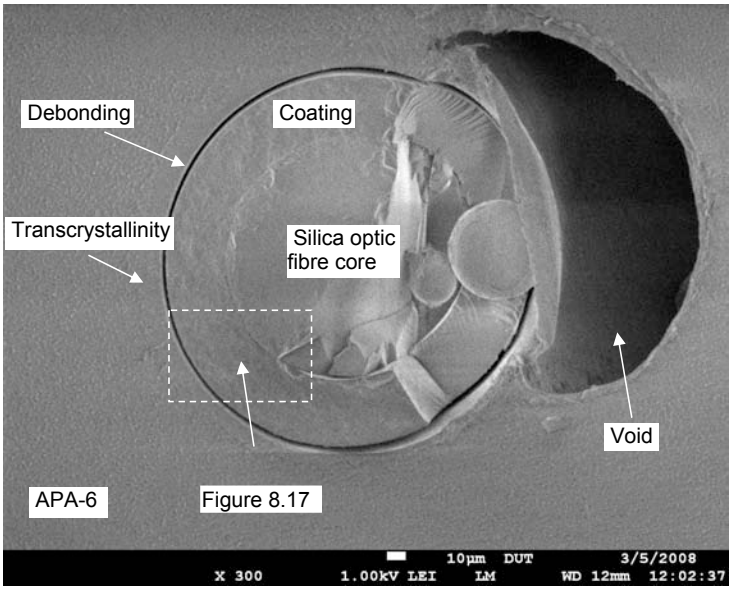

Figure 8.19: Overview of an Ormocer® coated optic fibre embedded in APA-6 (SEM).

Micrographs 8.18 and 8.19 present an overview of the optic fibre embedded in APA-6. Besides debonding, it is clear that a transcrystalline region has formed around the optic fibre, indicating crystal nucleation at the fibre surface [10], see also Figure 2.7 in Chapter 2, where this region was related to the formation of local residual strains. One of many factors that play a role in crystallisation nucleation and that could explain the different behaviour for the

PI and Ormocer® coating is the chemistry of the fibre surface [11]. The (partial) dissolution of the polyimide coating in the caprolactam may hinder crystal nucleation, but this falls outside the scope of this thesis.

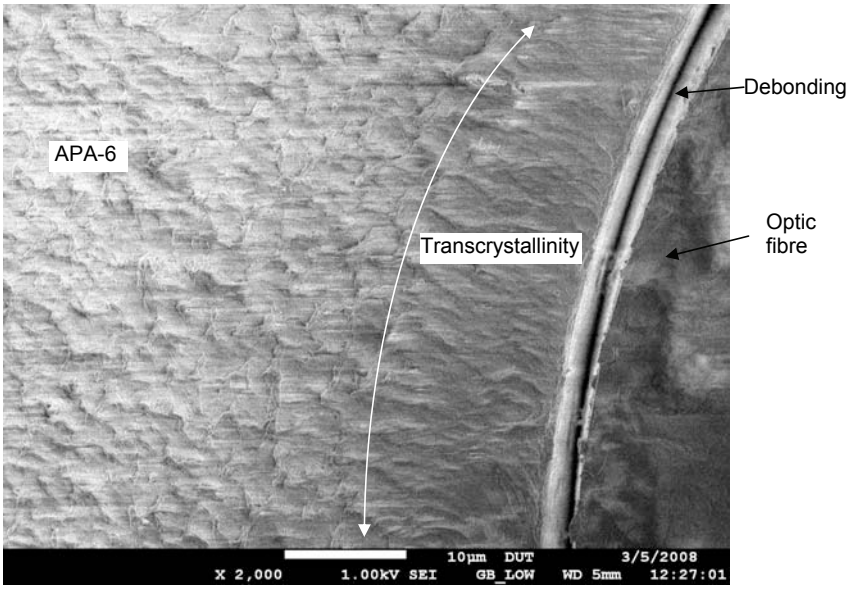

Figure 8.20: SEM picture of interface between the optic fibre and APA-6.

Apparently the Ormocer® surface provides nucleation sites for crystal formation, which results in epitaxial spherulite growth giving a transcrystalline layer. This explains why strain formation with the FBGs is detected at the onset of crystallisation, since the higher stiffness of the crystalline layer enables strain transfer to the optic fibre.
For HPA-6 and glass fibres, it was reported that slow cooling was the prime governing factor for formation of such a columnar crystal structure around the fibre [10, 12]. For this particular sample, the temperature was 175°C, which is close to the crystallisation temperature of 185°C. This results in a relatively low number of nuclei in the bulk polymer and hence crystallisation favourably nucleates at a solid surface, such as the optic fibre. This high mould temperature then results in slow crystallisation, as can be seen in the temperature curves in Figures 8.11 to 8.13.

In Figure 8.19 a large void can be seen next to the optic fibre. Now the question is, whether it is just poor chance that at this particular cross-section a void appeared, or is void formation around the optic fibre common. As an answer to this question, microCT images of lengthwise cross-sections of the middle section of the specimen are shown below.

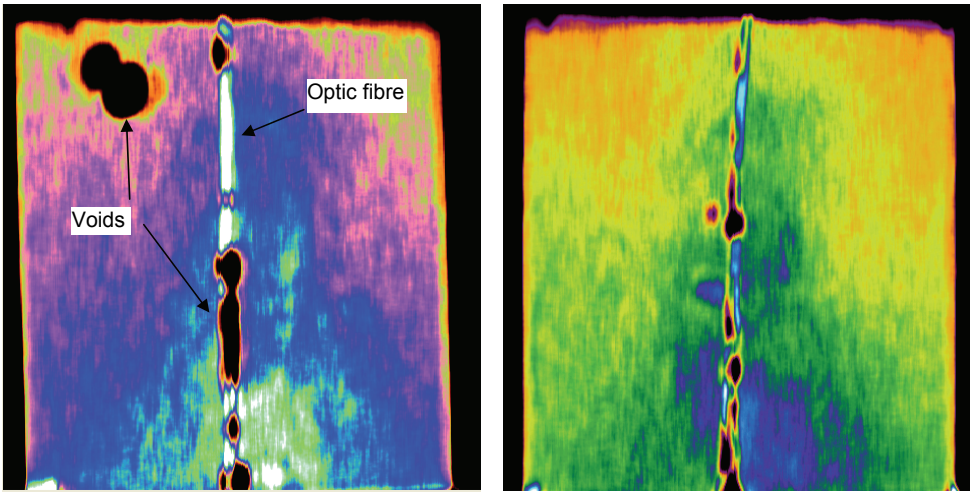

Figure 8.21: MicroCT Scan images from specimen centre, specimen diameter is ~18 mm, polymerisation temperature 175°C.

The microCT results show that many voids reside around the optic fibre, but are present in other locations in the polymer specimen as well. If voids appear around the grating[4], the local strain-transfer between the polymer and grating is hindered. This may cause a lower measured strain and mostly temperature variations will be detected. Strains generated in the bulk of the polymer may however still be detected, since the optic fibre will be bonded to the polymer at other locations and strains can be transferred over the entire optic fibre length. Several explanations for void formation can be put forward:

- Voids may be caused by the little *moisture* that is absorbed by the Ormocer® coating and this can interfere with the APA-6 polymerisation. However, since the optic fibre was placed in the hot test tube long before filling with APA-6, it is assumed that any remaining moisture has evaporated.
- *Nitrogen* is used as a storage environment for the molten initiator and activator mixtures to prevent oxygen and moisture from reacting with caprolactam, which renders the caprolactam unsuitable for further polymerisation. Nitrogen is soluble in caprolactam, but not in polyamide and therefore during polymerisation nitrogen gas is released. In the case that polymerisation occurs too fast, nitrogen gas has little time to escape and voids can occur. One method to overcome this, is by degassing of the resin at low pressure [1].

[4] If a void appears around the encapsulated temperature sensor (which could not be detected with microCT scan due to scattering effects of the metal), an insulating effect will cause a slower registration of the temperature variations, resulting in larger strain variations.

- *Air* from the surroundings can become entrapped during casting of the liquid mixture, which can be released over time. When polymerisation occurs too fast, this air becomes entrapped in the form of voids. A slow filling process can prevent air entrapment.

For this particular specimen, the liquid was degassed nor slowly poured[5], rendering it likely that entrapped gasses were present. Since polymerisation occurs very fast at a polymerisation temperature of 175°C, the gases have had little time to escape, which is validated by the regular observations that specimens manufactured at high temperatures have more voids [13]. The congregation of voids around the optic fibre can be explained by the phenomenon that voids tend to nucleate at solid surfaces.

8.5 Volumetric shrinkage of APA-6 during processing

With the volumetric dilatometry test as described in Chapter 5, the APA-6 properties that provide a source for residual strain formation as detected with FBGs and the effect of the poor fibre-matrix bond can be validated. In addition, the test can provide useful information on the total matrix shrinkage before gelation.

8.5.1 Experimental procedures

The APA-6 material and its preparation were described in Section 8.3.1 and the test set-up is similar to the one described in Section 5.2.3. For APA-6 the silicone bags were first preheated to 110°C in an oven. A glass beaker was filled with the reactive APA-6 mixture directly from the Mini-Mixing Unit (MMU) and this was used to fill the silicone bags through the syringe. The oil bath was heated to the desired polymerisation temperature (160, 170 and 180°C) and the filled silicone bag was carefully suspended in the oil bath and attached to the balance. After ~60 minutes[6], the heater plate below the oil bath was switched off and the polymer was allowed to cool to room temperature. For every polymerisation temperature, at least two experiments were carried out.

The assumptions of equal oil temperature and silicone bag mass do not apply as in Chapter 5: the oil temperature was found to vary around the set temperature and the silicone bags appeared to absorb the heating fluid at these high temperatures. Fortunately, the oil permeation nor the silicone bag itself affected the polymerisation of the APA-6 resin. Therefore, this test was continued, taking into account these effects by modifying the equations.

[5] For the FBG specimens in Section 8.3 both degassing and slow pouring was performed.
[6] In comparison with the FBG specimens, the volumetric shrinkage specimens were kept longer in the oil bath before cooling, because in the first tests it was observed that still changes occurred in the measurement, not realising this was oil absorption of the silicone bag. No major differences are expected because of this.

The polymer volumetric shrinkage is given by Equation (C-7) from Appendix C, where the *0* and *1* represent the test reference time and any time during the test, respectively:

$$\Delta\varepsilon_{pol} = \frac{\Delta V_{pol}}{V_{pol}^{0}} = \frac{V_{pol}^{1} - V_{pol}^{0}}{V_{pol}^{0}} \qquad \text{(C-7)}$$

The theoretical volume of the liquid APA-6 mixture at room temperature is chosen for the reference point V^{0}_{pol}, since this point can be established for all specimens and enables comparison of the volumetric behaviour during the entire cure cycle for specimens polymerised at different temperatures. It can be assumed that the volume and density of the pristine mixture is similar to that of pure caprolactam, because the caprolactam (CL) monomer comprises 86 mass% of the total mixture, and the initiator and activator are both caprolactam-based as well [14]. V^{0}_{pol} is therefore taken as the theoretical[7] liquid caprolactam volume determined from the measured polymer mass divided by the theoretical liquid density of caprolactam at room temperature (20°C = 293.15K) [16]:

$$\rho_{CL} = -4.3586 \cdot 10^{-4} T^{2} - 0.67540T + 1074.3 \qquad \text{(8-1)}$$

V^{1}_{pol} equals:

$$V_{pol}^{1} = \frac{m_{pol} - m_{pol}^{bal}}{\rho_{fl}} = \frac{m_{pol} - m_{tot}^{bal} + m_{bag}^{bal}}{\rho_{fl}} \qquad \text{(C-5)}$$

The polymer mass m_{pol} can be assumed to remain constant during the reaction, and is determined with a balance after the test was performed (see Section 5.2.4). However, it was clearly visible that oil had permeated through the silicone bag, causing a visible colour change of the surface layer (~100 µm thick) of the reacted polymer. Yet this effect was only observed at the surface and since this represents a small volume fraction of the entire polymer specimen (~2%), this effect is neglected.

The mass of the submersed assembly m^{bal}_{tot} (silicone bag with polymer) is registered by the balance during the test.

The buoyancy fluid density ρ_{fl} varies with temperature. The heat controller modulates the temperature around the set temperature (± 1.5°C) and therefore the oil temperature fluctuates during testing. This has a significant effect on the fluid density and therefore this

[7] Theoretical, because the caprolactam-based components are solid at room temperature and upon heating from room temperature (*a'*) start to melt at 69.2°C [15]. For simplicity, this is not taken into account.

parameter needs to be established for every data point. This can be accomplished by measuring the oil temperature with a thermocouple and calculating the fluid density with [17]:

$$\rho_{fl} = -0.6507.T + 902.95 \qquad (8\text{-}2)$$

The most problematic parameter is the contribution of the silicone bag to the total submersed mass as registered by the balance during the test, $m^{bal}{}_{bag}$. Two effects play a significant role: thermal expansion and shrinkage of the silicone rubber with temperature variations, and oil absorption. To gain insight in the development of $m^{bal}{}_{bag}$ during the test, a clean empty silicone bag was suspended below the balance in the oil and exposed to a similar thermal cycle as during the APA-6 polymerisation tests, where the temperature increase due to the polymer's exothermal reaction is neglected. The results can be found in Figure 8.22.

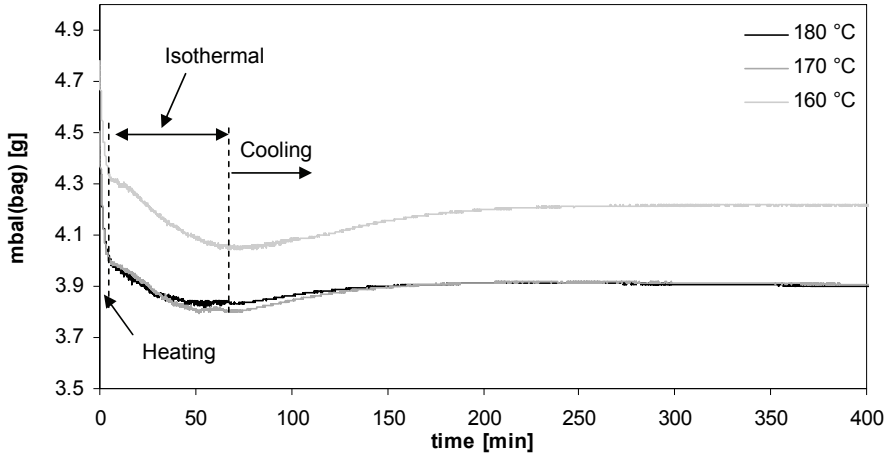

Figure 8.22: Mass development of silicone bag during APA-6 thermal cycle.

During the heating stage the silicone bags respond simply by thermal volumetric expansion[8], while during the isothermal hold at the polymerisation temperature oil absorption takes place. During cooling the silicone bag contracts and possibly excretes oil due to a lower saturation concentration.

For every test a new silicone bag was used. Since the bags were made by hand and can therefore differ in weight and local thickness, this can result in significant differences in $m^{bal}{}_{bag}$ values between each test, as shown by the 160°C specimen in Figure 8.22. Therefore, with

[8] It must be noted that due to thermal volumetric expansion of the silicone bag, the buoyancy force increases; hence the mass as detected by the balance decreases.

data regression and analysis of these measurements, fractional mass changes were used to derive values for $m^{bal}{}_{bag}$ during the test cycle. However, thermal fluctuations and time steps slightly differed for each test rendering the $m^{bal}{}_{bag}$ values not very reliable.
Unfortunately, these values have a paramount effect on the calculated volumetric shrinkage during the test. For example when comparing the determined polymer volume with the theoretical caprolactam volume at the polymerisation temperature at the end of the heating stage (after ~250 seconds), this effect can already result in an absolute polymer volume difference of 2%, corresponding to >10% error. This leads to the conclusion that this test cannot be used for determination of quantitative shrinkage values of APA-6. However, currently there is no information available at all on the shrinkage development of APA-6 during polymerisation and crystallisation. And with this test at least some qualitative insight into the APA-6 shrinkage behaviour might be obtained. Therefore, despite all the shortcomings, the tests were continued.

8.5.2 Results and discussion

For each polymerisation temperature two tests were carried out, and in Figures 8.23 to 8.25 the temperature and shrinkage profiles for the APA-6 specimens produced at 162°C, 172°C and 181°C are shown. Just the first 90 minutes are displayed here, because the cooling phase was extremely slow and would compromise details in the graph. For clarity the curves are shifted on the y-axis such that the maximum volume corresponds to $\Delta\varepsilon_{vol} = 0$ (see left dotted lines in Figures 8.23 and 8.24).

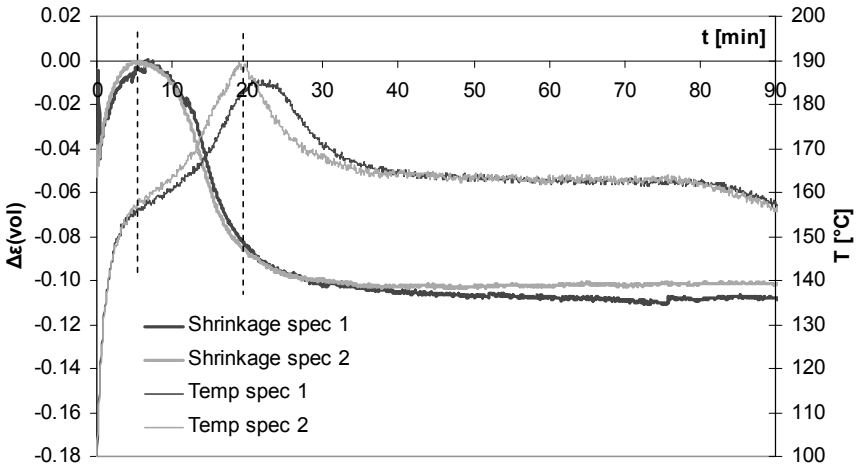

Figure 8.23: Temperature and volumetric shrinkage profiles of two APA-6 specimens (162°C).

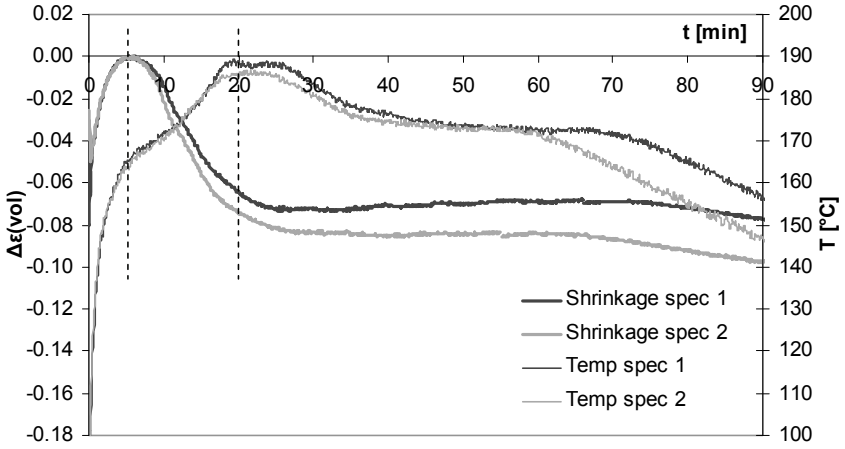

Figure 8.24: Temperature and shrinkage profiles of two specimens produced at 172°C.

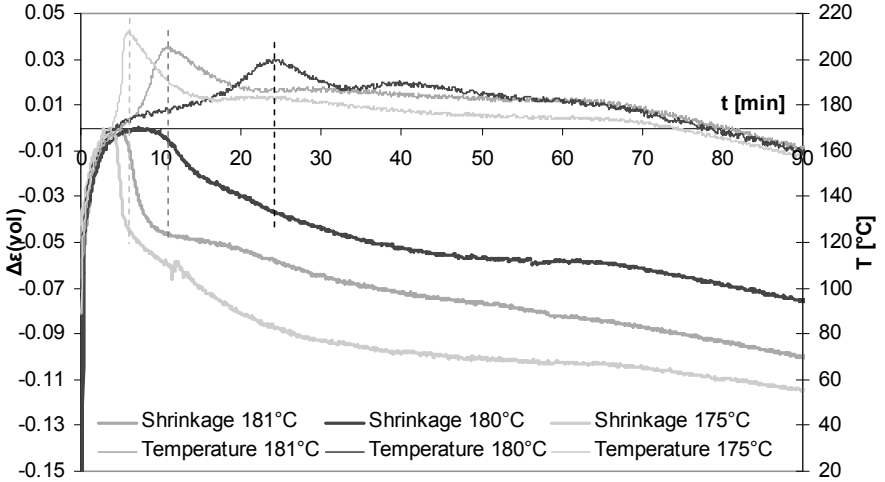

Figure 8.25: Three APA-6 specimens produced at ~180°C and 175°C.

For 162 and 172°C reproducible graphs were found, while the tests at 180°C showed a wide variation. For comparison with FBG results, one additional test was performed at 175°C.
In Figures 8.24 and 8.25 it is clear that the onset of exothermal temperature rise (see left-hand dotted line) coincides with the onset of volumetric shrinkage, which is largely caused by the difference in number of molecules due to polymerisation: ~8850 mmol to 10–50 mmol/kg [18]. This starts already before the set temperature is reached (5-10°C below). The majority of the polymerisation shrinkage has taken place when the exothermal peak temperature is reached (right-hand dotted line). In the 162°C polymerised specimens polymerisation and

crystallisation occur simultaneously, which results in a somewhat steeper shrinkage slope including more shrinkage: 9 – 10% for 162°C compared to 7 – 8% for 172°C. This indicates a higher level of crystallinity for the 162°C specimens, since due to the higher density of the crystal phases compared to the amorphous polymer phase [2], an increasing level of crystallinity results in an additional volume decrease.
The shape of these shrinkage curves is similar as those found by Zarelli *et al* [19] for reactive polymers cured above room temperature [19].

The specimens cured at 175°C, 180°C and 181°C show different behaviour. It is clear that upon reaching the first peak temperature (see dotted lines), only a part of the total shrinkage during the dwell time has taken place. After this, crystallisation shrinkage presumably continues slowly at these high temperatures and is still ongoing after 60 – 70 minutes when the heater was switched off. It can be observed that increased shrinkage takes place when the crystallisation peaks occur (15-20 minutes after the polymerisation peak). Another observation is the variety in curves with respect to time scale and rate, and temperature and shrinkage profiles. The specimens with slower reactions show a smaller amount of volumetric shrinkage. This variety can be explained by the competing branching and crystallisation kinetics at these high temperatures. First of all, higher manufacturing temperatures delay the crystallisation start and the crystallisation process is slowed down. Second, the high temperature causes the formation of branches and cross-links, see Section 8.2. The longer the polymer mixture resides at high temperatures, the higher the likelihood of branching and cross-link formation. This makes the mixture very viscous causing not only an additional retardation in crystallisation, but also renders the entire crystallisation process to become less ‘neat’. Branching therefore results in a lower degree of crystallinity, as well as a lower degree of conversion, which reduces the shrinkage. It is therefore assumed, that the 180° specimen in Figure 8.25 experienced a significant branching effect. For comparison, at 160°C little to none branching occurs, while crystallisation starts during polymerisation and encounters little resistance, because the mixture is still relatively fluid enabling volumetric shrinkage to take place freely.
The shrinkage is plotted against the temperature for several specimens in Figure 8.26:

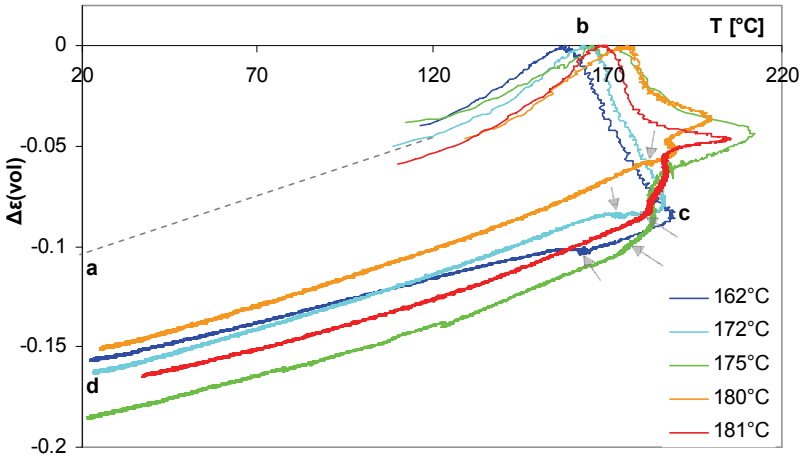

Figure 8.26: Volumetric shrinkage profiles with temperature for APA-6 specimens polymerised at different temperatures.

This graph can be divided in several parts, based on Figure 2.6:
a-b represents the thermal expansion of the unreacted polymer mixture upon heating to the polymerisation temperature. For all specimens this behaviour is similar (i.e. when the curves are shifted over the temperature axis, they will coincide). The non-linearity is attributed to the influence of the silicone bag.
b-c signifies the shrinkage at the curing temperature accompanied by an increase in temperature, caused by the exothermic polymerisation and crystallisation. The total amount of shrinkage before cooling varies significantly (points *c* are indicated by the arrows), similar as the FBG results, and no clear trend with respect to curing temperature can be identified.
c-d represents the thermal shrinkage upon cooling from the polymerisation temperature. Here, a somewhat non-linear behaviour is observed, which corresponds to the FBG results, and can be explained by the slow cooling causing additional crystallisation, since a maximum driving force for crystallisation of APA-6 exists between 160 and 140 °C [14]. The specimen cured at the lowest temperature shows the smallest slope, which can be attributed to a higher level of crystallinity [20, 21]. At this point, no rubber-to-glass transition temperatures T_g can be distinguished for any of the specimens, which was expected at 70°C where the amorphous phases undergo a rubber-to-glass transition temperature (T_g) [22].

The parts that can form a contribution to residual strain formation are *b-c* and *c-d*. In part *b-c* it is very difficult to separate the polymerisation and crystallisation shrinkage contributions;

hence for every specimen, the volumetric shrinkage caused by polymerisation + crystallisation (*b*-*c*) is calculated with

$$\Delta\varepsilon_{vol}^{(b-c)} = \frac{V_{pol}^{c} - V_{pol}^{b}}{V_{pol}^{b}} \tag{8-3}$$

And the thermal contraction upon cooling from the processing temperature (*c*-*d*):

$$\Delta\varepsilon_{vol}^{c-d} = \frac{V_{pol}^{d} - V_{pol}^{c}}{V_{pol}^{c}} \tag{8-4}$$

where the volume at point *d* is taken at 40°C, because for this temperature the data were available for all specimens. The results are shown in Figure 8.27:

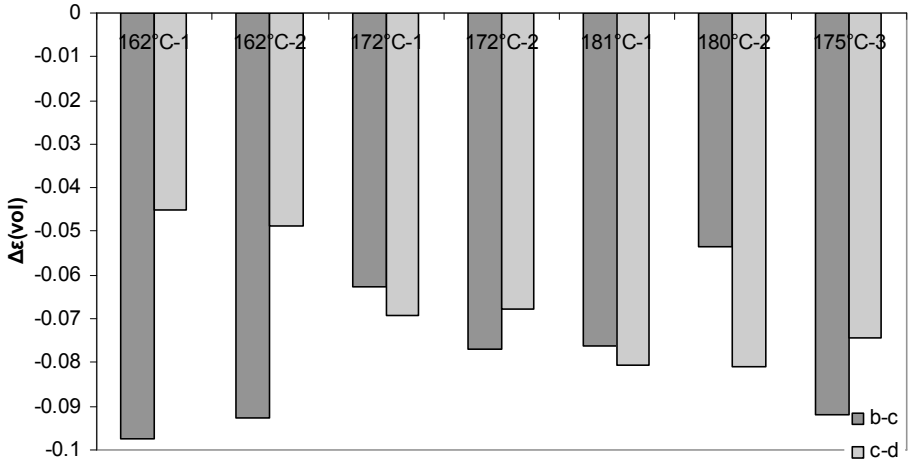

Figure 8.27: Polymerisation + crystallisation shrinkage (*b*-*c*) and thermal contraction upon cooling (*c*-*d*) for APA-6 specimens processed at different temperatures.

It is clear from Figure 8.27 that trajectory *b*-*c* is highest for the 162°C polymerisation temperature, which is caused by the combined polymerisation and 'neat' crystallisation. At higher temperatures, lower degrees of crystallisation and conversion are usually obtained, which is reflected by the lower amount of shrinkage between points *b* and *c*. The significant variation for the last three specimens was explained earlier, see Figure 8.25.
Thermal contraction upon cooling (*c*-*d*) obviously increases with increasing polymerisation temperature, which cannot be solely related to the larger temperature difference, since the

shrinkage per °C ranges from ~4.10^{-4}/°C for the 162°C samples to ~5.10^{-4}/°C for the 172°C specimens and ~6.10^{-4}/°C for the 180°C cured specimens. This can be attributed to the degree of crystallinity as well as branching; usually branched molecular polymers possess a higher thermal expansion coefficient due to weak secondary intermolecular bonds [21]. In addition, the slow cooling process can induce additional (secondary) crystallisation in the high temperature cured specimens [5, 14].

8.6 Comparison between FBG and volumetric dilatometry results

The temperature profiles in Figures 8.23 to 8.25 resemble those for the FBG specimens in Figure 8.11, including higher peak temperatures for higher polymerisation temperatures and similar appearance of crystallisation exothermal temperature peaks. While for the 162°C cured specimens a single relatively sharp peak is visible, similar to the 158°C FBG profile, a widened or double peak is evident for the 172°C cured specimens, which resembles the temperature profiles of the 166°C polymerised FBG specimens. In turn, the 180°C curves are similar to the 175°C FBG curves. This similarity is caused by the lower peak temperatures compared to the FBG specimens, because of the better heat-dissipating properties of the test set-up. Similar results were found for turane in Section 5.3.1.

For comparison with the FBG strain data, the volumetric shrinkage results are converted to linear shrinkage with Eq. (5-1):

$$\Delta\varepsilon_{lin} = (\Delta\varepsilon_{vol} + 1)^{1/3} - 1 \qquad (5\text{-}1)$$

In Figures 8.28 to 8.30 the resulting curves have been shifted vertically to $\Delta\varepsilon_{lin} = 0$ at ~185°C, which corresponds to the temperature around which the FBG strains were found to start building up. GI denotes 'Gravimetric Immersion', which are the volumetric shrinkage results and FBG represents the results as detected with fibre Bragg gratings.

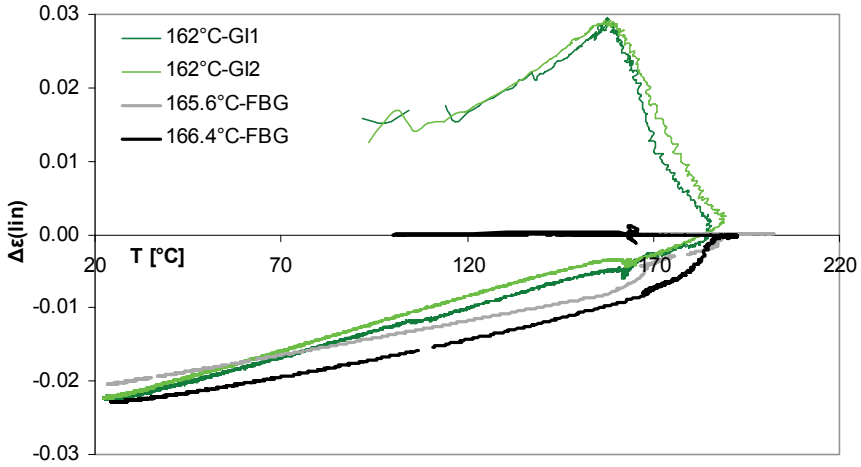

Figure 8.28: Comparison between volumetric shrinkage and FBG results for temperatures 162°C and 165°C, resp.

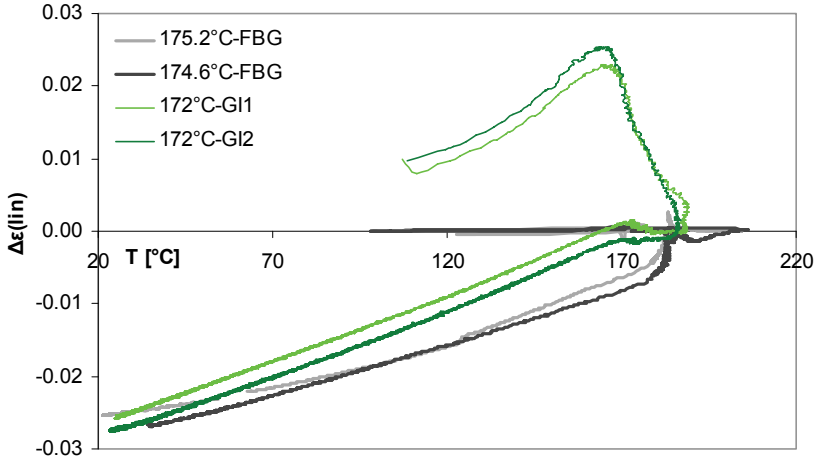

Figure 8.29: Comparison between volumetric shrinkage and FBG results for temperatures 172°C and 175°C, resp.

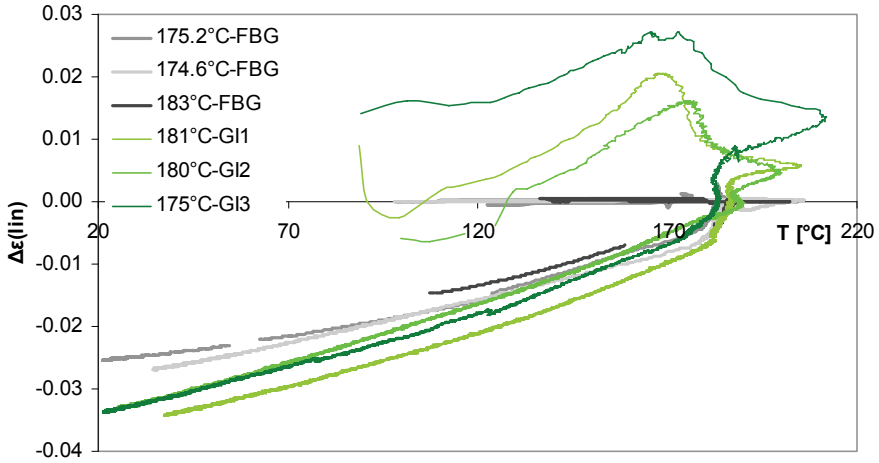

Figure 8.30: Comparison between volumetric shrinkage and FBG results for temperatures of 175°C and higher.

Looking at Figures 8.28 to 8.30 it seems that for all volumetric shrinkage specimens, the cooling slope, or thermal contraction, is steeper in comparison to the FBG results. This can be explained by the poor bonding and hence strain transfer between the optic fibre and the APA-6 polymer as discussed in Section 8.4.

For the temperatures of 175°C and higher in Figure 8.30, the non-linearity of the cooling curve is more evident than in the other Figures. This can be related to the additional secondary crystallisation during the slow cooling process. At lower polymerisation temperatures, the APA-6 specimens apparently already reached optimal crystallinity levels before cooling started.

For higher production temperatures, higher shrinkage values at room temperature are detected with FBGs as well as volumetric shrinkage. This can be related to the thermal contraction upon cooling from the dwell temperature, which for both the FBG as volumetric test is higher for higher processing temperatures.

The comparison in the figures above is based on the result of Section 8.4 that shrinkage seems to be detected by the FBGs from the crystallisation point onwards at ~185°C. The result is that only the curves in Figure 8.30 show resemblance below $\Delta\varepsilon_{lin} = 0$. This may be attributed to the separate crystallisation effect at these high temperatures, which is detected by both tests below this point.

8.7 Conclusions

In this chapter novel experimental techniques were investigated to determine the shrinkage behaviour of anionic polyamide-6 (APA-6) responsible for residual strain formation in structural composites. Linear processing shrinkage strains were studied with fibre Bragg gratings and volumetric shrinkage with volumetric dilatometry. The FBG temperature sensor was successful in determining the thermal behaviour of APA-6 polymerised at different temperatures.

A quantitative analysis of these parameters proved difficult, because several experimental shortcomings were identified in both tests. For the FBGs, the problem was a lack of adhesion between the optic fibre coating and the APA-6. In addition, the Ormocer® coating of the optic fibre was found to induce transcrystallinity, rendering the measurements not representative for the bulk material properties. In the volumetric shrinkage test, the silicone bag showed a significant source of error by unexpected heating fluid absorption, which could not be adequately compensated for.

Both the FBG and volumetric shrinkage techniques identified significant shrinkage for APA-6. For example, back at room temperature the shrinkage estimations are in the order of -2 to -3% linear strain and 15-20 % volumetric shrinkage, with higher processing temperatures resulting in higher values in both tests. This was related to the relatively higher shrinkage upon cooling from the processing temperature to room temperature for specimens manufactured at higher temperatures, which can be attributed to the postponed effect of crystallisation.

The volumetric shrinkage test showed that polymerisation shrinkage as well as the development of a polymerisation exotherm started already during heating from the infusion temperature (110°C) to the polymerisation or mould temperature. Besides, most of the shrinkage for the specimens cured at 172 and 162°C occurs before the peak temperature is reached, while for the specimens produced at higher temperatures, significant (crystallisation) shrinkage was still observed after reaching the peak temperature. At temperatures of 175°C and higher, a large variety of curves was shown, which was related to the competing kinetics of polymerisation, branching, and crystallisation. The onset of strain transfer was detected by FBGs at the peak crystallisation temperature of 185 ± 3°C, which was attributed to crystal nucleation at the optic fibre surface.

Based on these trends both techniques are considered promising for assessment of (APA-6) matrix shrinkage during processing and residual strain formation, provided that further improvements are made, see the recommendations in Chapter 12.

References

1. van Rijswijk, K., Thermoplastic Composite Wind Turbine Blades. 2007. PhD thesis Aerospace Engineering, Delft University of Technology, Delft. 249 pages.
2. Bessell, T.J., Hull, D., Shortall, J.B., The effect of polymerization conditions and crystallinity on the mechanical properties and fracture of spherulitic nylon 6. Journal of Materials Science, 10: 1127-1136, 1975.
3. Sittler, E., Sebenda, J., Alkaline Polymerization of Caprolactam. XXI. Dissociation of Alkali Metal Salts of 6-Caprolactam in the Polymerization of 6-Caprolactam. Journal of Polymer Science: Part C, 16: 67-77, 1967.
4. Young, R.J., Lovell, P.A., Crystallisation and melting, in Introduction to Polymers. 1991, Chapman & Hall: London. p.276-290.
5. Kohan, M.I., Crystallization, in Nylon Plastics Handbook. 1995, Hanser Publishers: Munich. p.120-122.
6. Balvers, J.M., Monitoring the RTM process with FBGs - Progress report. 2008, Delft University of Technology: Delft. p. 61.
7. van Geenen, A.A., Stuk APA-6, recipient: Parlevliet, P.P. 15 August 2008. E-mail correspondence.
8. Struers. e-metalog. 2007. Accessed: September 2007, Available from: www.struers.com.
9. Kim, J.-K., Mai, Y.-W., Engineered interfaces in fiber reinforced composites. First ed. 1998, Oxford: Elsevier Science Ltd. 401 pages.
10. Cartledge, H., Baillie, C.A., Studies of Microstructural and Mechanical Properties of Nylon/Glass Composites. Part I: The Effect of Thermal Processing on Crystallinity, Transcrystallinity and Crystal Phases. Journal of Materials Science, 34(20): 5099-5111, 1999.
11. Quan, H., *et al.*, On transcrystallinity in semi-crystalline polymer composites. Composites Science and Technology, 65(7-8): 999-1021, 2005.
12. Clark, R.L., Influence of the Interphase on the Mechanical Properties of Nylon 66 Composites. 1996. PhD thesis Materials Engineering Science, Virginia Polytechnic Institute and State University, Virginia.
13. Teuwen, J.J.E., deel 2 van dit hoofdstuk, recipient: Parlevliet, P.P. 13 June 2008. E-mail correspondence.
14. van Geenen, A.A., Vragen n.a.v. verklaren resultaten in proefschrift P. Parlevliet, recipient: Parlevliet, P.P. 10 december 2008. Personal correspondence.
15. DSM_Fibre_Intermediates. Product Data Sheet - Caprolactam A.P. Quality (flakes). 2008 July 1998 [cited 2008 15 December 2008]; DFI 7/98.
16. Pure component properties - Caprolactam. 1993, DSM.
17. Shell Thermia A Technical Data Sheet, Shell Lubricants: Pernis, Netherlands.
18. van Geenen, A.A., Opmerkingen n.a.v. afstudeerverslag van Pieter Verburg: "development of techniques for polymer shrinkage measurement", Parlevliet, P.P., Editor. 2008, AvG Consultancy. p. 2.
19. Zarrelli, M., Partridge, I.K., D'Amore, A., Warpage induced in bi-material specimens: Coefficient of thermal expansion, chemical shrinkage and viscoelastic modulus evolution during cure. Composites Part A-Applied Science And Manufacturing, 37(4): 565-570, 2006.
20. Baltá Calleja, F.J., Fakirov, S., Effect of Crystallinity on hardness, in Microhardness of Polymers, Clarke, D.R., Suresh, S., and Ward, I.M., Editors. 2000, Cambridge University Press: Cambridge. p.90-94.
21. Callister, W.D.J., Thermal Expansion, in Materials Science and Engineering - An Introduction. 2000, John Wiley & Sons, Inc.: New York. p.661-664.
22. van Geenen, A.A., Anionic Polyamide - Chemistry and processing. 2007, AvG Consultancy.

Chapter 9: Anionic Polyamide-6 Properties

9.1 Introduction

The goal of this chapter is to investigate whether the experimental techniques from the earlier chapters can be applied to study the properties of anionic Polyamide-6 (APA-6) that can affect the residual strain state. These include the thermal cycling tests as presented in Chapter 4 to investigate annealing effects, and the microVickers hardness test from Chapter 7 to investigate processing temperature effects on material properties, such as crystallinity.

9.2 Thermal cycling of APA-6

After the processing cycle, the APA-6 specimens with FBG sensors were exposed to a thermal treatment to identify possible thermal transitions or annealing effects on the residual strain state, such as found for turane in Chapter 4. Usually, annealing of semi-crystalline thermoplastics such as PA-6 is carried out between the glass transition temperature and melting temperature, for improvement of the degree of crystallinity, crystal perfection and relaxation of internal strains [1, 2]. For APA-6, the optimum recrystallisation temperature is 140-160°C [3]. The results are compared to linear dilatometry test results to assess the effect of the poor optic fibre-matrix adhesion observed in the previous chapter.

9.2.1 Experimental procedures

Fibre Bragg Gratings (FBGs)

For the thermal treatment of FBG specimens polymerised at different temperatures (166°C, 175°C and 183°C), a similar set-up as described in Section 4.5.1 was used. Here also, the thermal cycle was carried out in heating steps of ~50-80°C, maintaining the isothermal temperatures for 15 minutes, to a maximum temperature of 180°C, and allowed to cool down again. This cycle was followed by another heating cycle to ~100°C, which is above the assumed T_g, to confirm possible annealing effects.

Thermal Mechanical Analysis (TMA)

Linear dilatometry specimens were taken from test tubes 'A' as described in Section 8.3, from APA-6 polymer specimens cured at 165.6°C and 183°C. The same test set-up and procedure was used as for the Turane samples in Section 4.5.1, including drying of the specimens overnight at 60°C under vacuum. It must be mentioned that the thermal control of the TMA malfunctioned and an effort was made to correct for this.

9.2.2 Results and discussion

FBGs

In Figures 9.1 and 9.2 representative thermal cycling profiles are shown together with the polymerisation cycle.

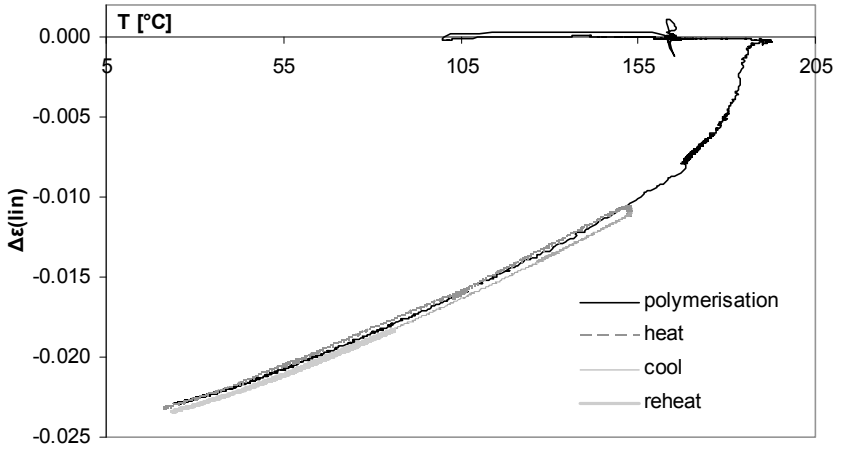

Figure 9.1: Thermal cycling of APA-6 specimen cured at 165.6°C.

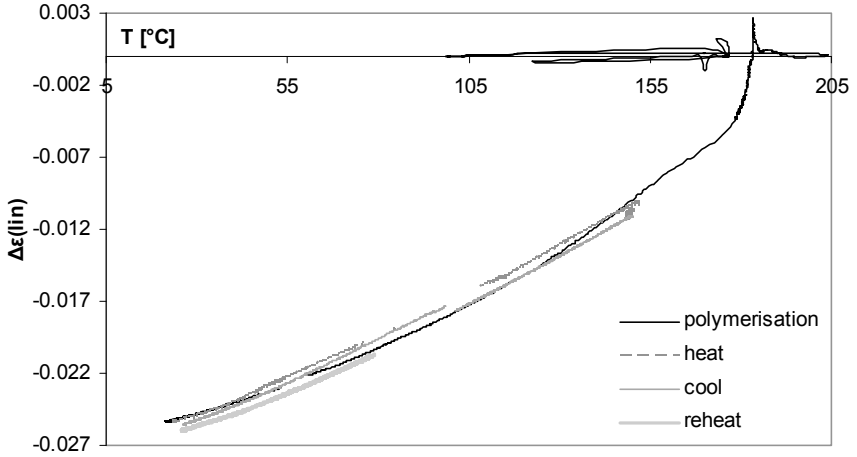

Figure 9.2: Thermal cycling of FBG specimen cured at 175°C.

In general, the heating and cooling cycles follow the polymerisation cycle and no significant thermal transitions, relaxation behaviour or annealing effects could be observed. It can be noted that the second heating cycle lies somewhat below the first heating curve, which can

be caused by minor shrinkage during the first cycle, due to crystallisation or evaporation of moisture.

For some specimens in Chapter 8 the entire shrinkage profile could not be obtained because the wavelength got out of range, such as the 183°C specimen in Figure 8.14. In these specimens the signal reappeared upon heating around the same temperature as where it was lost, see Figure 9.3.

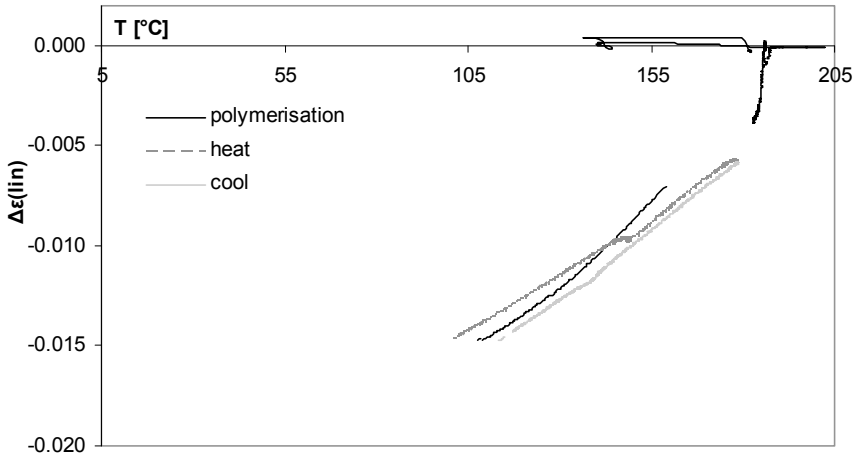

Figure 9.3: Thermal cycling of the FBG specimen produced at 183°C.

The thermal cycling curves of this specimen do not closely follow the polymerisation cycle like the other profiles, which could be caused by recrystallisation resulting in a lower coefficient of thermal expansion and contraction. In Section 8.6, it was assumed that for specimens polymerised at these high temperatures, crystallisation not only occurred in the dwell period, but also during cooling. This may lead to a polymer where still a driving force for recrystallisation exists.

Thermal Mechanical Analysis (Dilatometry)

In the following Figure, two representative curves for the dilatometry results of the 166°C and 183°C polymerised specimens are shown. It must be noted that the temperatures are not completely reliable and therefore only qualitative analyses can be deduced from this graph.

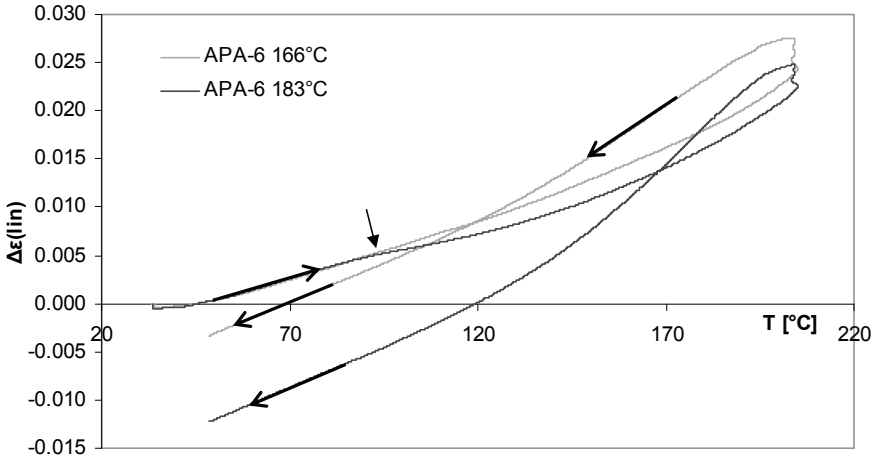

Figure 9.4: Dilatometry results for APA-6 specimens taken from FBG test tubes.

It can be noted in Figure 9.4 that both specimens start with equal linear expansion upon heating, but different from the 166°C specimen is that at ~95°C the expansion for the 183°C specimen decreases, see the small arrow. This point is above the glass transition (70°C) [4], and therefore it is suggested that this behaviour is connected to relaxation or recrystallisation due to the increased molecular mobility of the amorphous phase, see Chapter 2. This behaviour could not be verified with the FBG sample, since the wavelength for this particular specimen was out of range in this region. Annealing is usually carried out above 115°C [3], but it is possible that this process starts already at lower temperatures due to increased mobility of the molecules caused by the presence of unreacted caprolactam. The specimens were taken from the centre of the test tubes, where it is likely that some residual caprolactam still is present (see Section 8.2). Why this behaviour was not observed for the 166°C specimen can be explained by the assumed complete crystallisation of this specimen at the polymerisation temperature based on the results in Chapter 8, while the 183°C specimen showed much secondary crystallisation during cooling, which may not have been completed. Above ~132°C, and ~120°C for the 166°C specimen, the slopes of the curves increase further non-linearly, which is consistent with the notion that thermal expansion is dependent on, i.e. increases with, temperature [1]. Upon reaching the isothermal temperature of 205°C, the thermal expansion continues, which can be related to a thermal lag of the specimen. During cooling between 200°C and 120°C, the 183°C specimen shrinks considerably more than the 166°C specimen, which can be related to a higher amount of monomer present in the 183°C specimen (see the DSC results in Section 9.3.2): this residual monomer decreases the melting point, due to which a fraction of the APA-6 polymer may have molten during the isothermal step. During cooling this results in additional crystallisation shrinkage of

the molten fraction. Both specimens show considerable shrinkage compared to the starting dimensions after cooling to room temperature. This can be related to recrystallisation and relaxation phenomena during heating.

The slopes of the curves represent the coefficients of thermal expansion (CTE's). The CTEs are average 116.10^{-6} °C^{-1} (with standard deviation 6.10^{-6}) and 113.10^{-6} °C^{-1} (3.10^{-6}) in the temperature range of 50-80°C for the 166°C and 183°C specimens, resp. So there is no difference in CTE during the initial heating stage. These values are significantly higher than literature values for PA-6 in this temperature range (85-91.10^{-6} °C^{-1}) [1]. This can be related to a lower degree of crystallinity and a higher residual amount of caprolactam, increasing the mobility of the molecules.
During cooling in the same temperature range, the CTE's are again similar, but significantly higher as during heating: 174.10^{-6} °C^{-1} and 171.10^{-6} °C^{-1} for the 166 and 183°C specimens, respectively. No clear explanation can be given for this, but several effects may play a role: thermal lag of the equipment (~10°C) resulting in a higher actual sample temperature giving a higher CTE, or a lower degree of crystallinity due to partial melting of the crystals at the isothermal temperature (caused by depreciation of melting temperature due to caprolactam presence). That the CTEs are relatively similar for both specimens at lower temperatures implies that a variation in crystallinity has little influence on the CTE below the glass transition temperature.

Residual strains
In this section, relaxation of internal strains is mentioned. What was not discussed until now, is how these internal strains arise in the APA-6 polymer manufactured in the test tube. During processing at 166°C, polymerisation and crystallisation take place more or less simultaneously in a still liquid phase and therefore shrinkage can take place relatively unconstrained without building up significant residual strains. Polymerisation and crystallisation start at the test tube surface since the polymerisation temperature is reached there sooner and the shrinkage can be replenished with still liquid polymer in the centre of the test tube. After cooling, this is visible as a significant meniscus or valley in the centre of the test tube, which is absent for the 180°C specimens. In this case, the internal strains are relatively low. For the specimens manufactured at 183°C only a minor driving force exists for crystallisation at this temperature and the volume will decrease mainly due to polymerisation shrinkage. Upon (relatively fast) cooling from the processing temperature crystallisation can occur, but due to the already fairly high stiffness of the amorphous polymer, crystallisation shrinkage is restrained. This causes high internal strains, which upon reheating of the cooled specimen can be released. It was observed that 180°C cured specimens were more difficult

to remove from the glass test tube (although release agent was applied) than 160°C specimens, indicating less shrinkage in the radial direction.
A density variation from the outside-inwards is made visible with the microCT scan for a specimen processed at 175°C described in Section 8.4, see Figure 9.5 where lighter areas mean lower density. This confirms the hypothesis that polymerisation and crystallisation shrinkage took place from the outer side inwards and explains the concentration of voids in the centre, as in Figure 8.22.

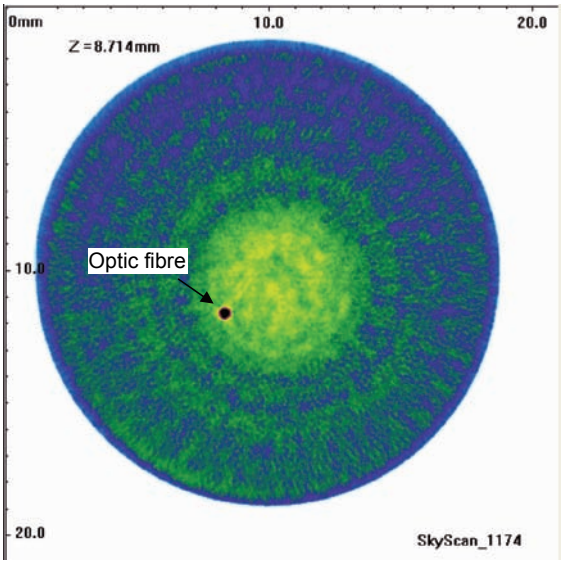

Figure 9.5: MicroCT cross-section of APA-6 specimen with optic fibre.

Comparison of FBG and dilatometry results

The dilatometry specimens were taken from test tube specimens that have undergone the same production cycle as the FBG specimens. One major difference between the two test set-ups are the heating and cooling rates during thermal cycling. For the FOS samples this is significantly lower (~2 °C/min) compared to the dilatometry samples (~8 °C/min) due to the limited heating rate of the oil bath. In addition, for the dilatometry test the specimens have undergone a machining and drying step, while the FBG specimens are the same as after the production cycle.
In Figures 9.6 and 9.7 the heating and cooling steps as measured with Fibre optic sensor (FOS) and dilatometry are compared for the two specimens. For both curves, the linear thermal expansion/ contraction is recalculated such that the reference (wave)length (i.e. $\Delta\varepsilon_{lin} = 0$) is at the same temperature.

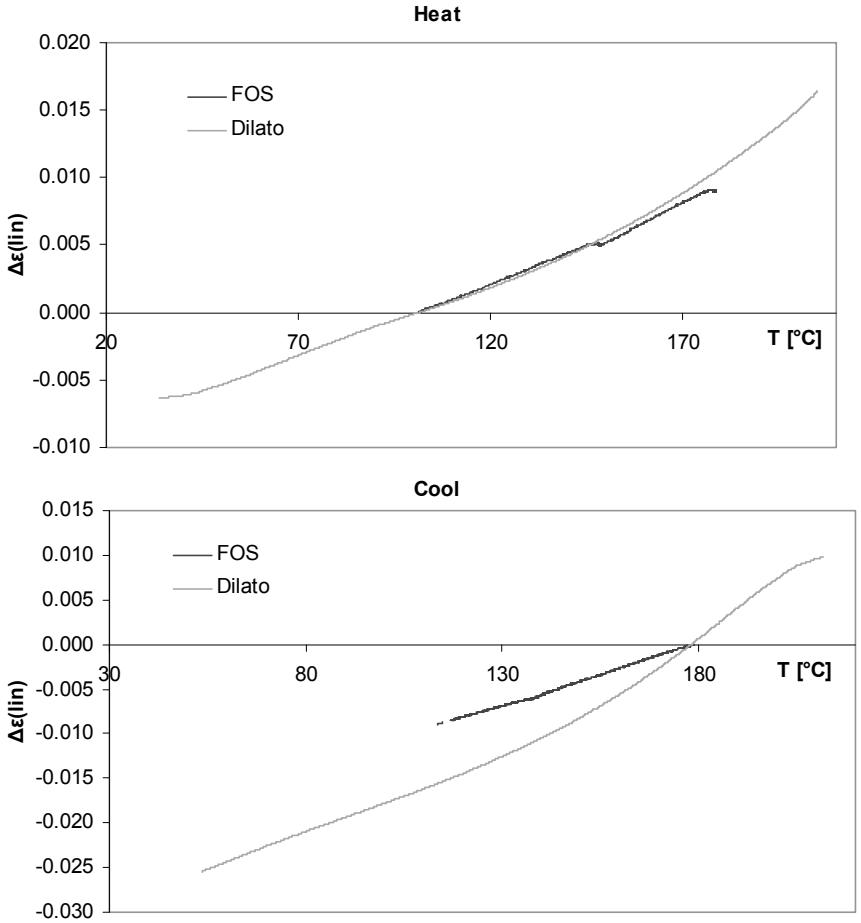

Figure 9.6: Thermal FOS and dilatometry cycles for specimens produced at 183°C.

During heating the two curves follow each other with similar slopes. At higher temperatures, the dilatometry curve shows an increase in expansion/ slope, while the FBG results continue in a more-or-less straight line or even show a small decline, which can be caused by a decrease in stiffness or strain-transfer efficiency of the APA-6 matrix to the optic fibre.
The results at the beginning of this section showed that cooling of the FBG specimens followed the same trend as the heating cycle, while for the dilatometry specimens this certainly was not the case. Therefore, it is expected that the cooling curves as measured with the two techniques are not similar, which is indeed shown in Figures 9.6 and 9.7.

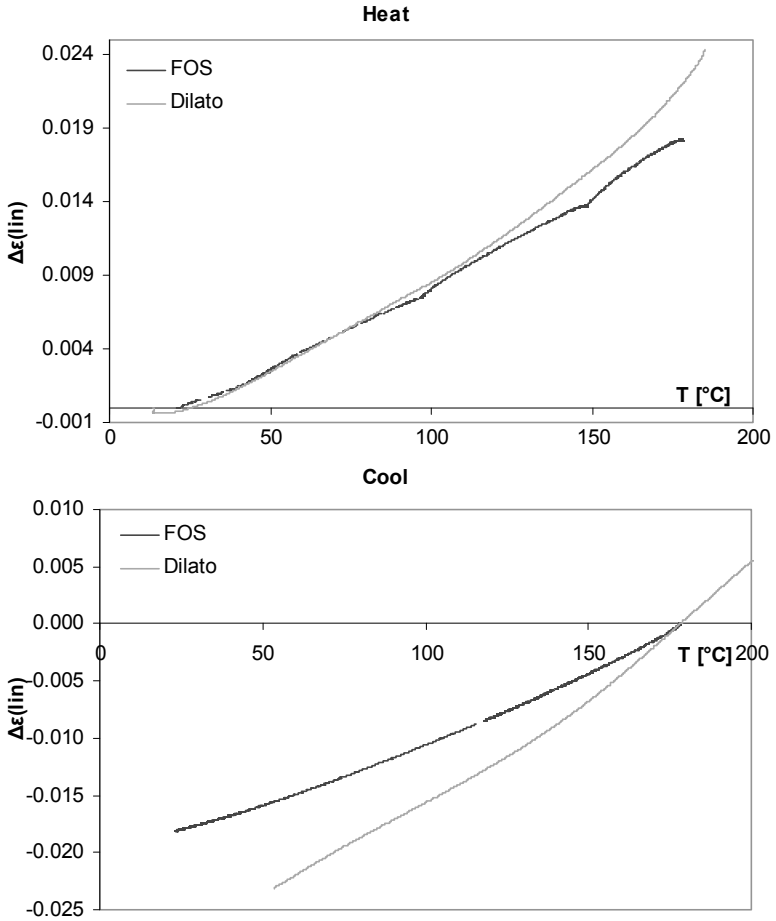

Figure 9.7: Thermal FOS and dilatometry cycles for specimens produced at 166°C.

The coefficients of thermal expansion (CTE's) of both techniques are compared in Table 9.1.

Table 9.1: Calculated CTE's for dilatometry and FBG specimens.

		Dilatometry		FBG	
	Specimen	Temperature range [°C]	CTE [$.10^{-6}$ °C^{-1}]	Temperature range [°C]	CTE [$.10^{-6}$ °C^{-1}]
Heating	183°C	50-80	116 ± 6*	105-145 [1]	113
	166°C	50-80	113 ± 3	50-80	108
Cooling	183°C	80-50	171 ± 2	135-120	122
	166°C	80-50	174 ± 10	80-50	101

*: Standard deviation

[1] For the 183°C specimen no data points are available in the lower temperature range.

For both specimens, the FBG CTE's compare very well with the dilatometry CTE's during heating. As was already clear from the cooling figures, the CTE's during cooling differ considerably. This can be related to the high temperature excursion for the dilatometry samples causing partial melting and the accompanied additional shrinkage after cooling, which was absent for the FBG specimens.
Since the CTE's during heating are similar for the FBG and dilatometry tests, it may be concluded that the strain transfer between the polymer and optic fibre is sufficient. In effect, even though locally the bonding is poor, the FBG can still sense the bulk properties.

9.3 MicroVickers hardness and crystallinity of APA-6

Chapter 7 showed that the microVickers hardness test can be useful in identifying variations in matrix properties caused by temperature variations. Therefore, an effort is made to study this in the APA-6 specimens polymerised at different processing temperatures.

9.3.1 Experimental procedures

Differential Scanning Calorimetry (DSC) was carried out as described in Section 7.3.3, by heating to 240°C with 10°C/min. Three specimens were taken from test tubes 'A' of the FBG polymerisation tests at 158°C, 166°C, 175°C and 184°C. The degree of crystallinity was calculated by measuring the area under the crystallisation melting peak, and dividing that by the theoretical value for a 100% crystalline APA-6 sample: ΔH_0 = 190 J/g [5]. The polymer matrix still contains a fraction of unreacted monomer, which evaporates during DSC testing and does not contribute to the degree of crystallinity. Therefore, the specimen is also weighed after DSC testing, which value is used for the calculation of degree of crystallinity. A rough estimate of the degree of conversion (DoC) can be obtained by dividing the specimen mass after testing by the mass before testing. This method is not as accurate as the extraction test used by van Rijswijk [6], but it provides a good indication of a variation in DoC between the specimens.
Similar equipment and test set-up were used as described in Section 7.3.3 for the microVickers hardness test. The same source materials as for the DSC test were used for the microVickers hardness test. An indentation load of 10 gram was used and at least 10 indentations were made per specimen. The method of specimen preparation was equal to the procedure described in Section 8.4.1 for the microscopy samples.

9.3.2 Results and discussion

Differential Scanning Calorimetry

In Figure 9.8 the DSC results for three materials are displayed.

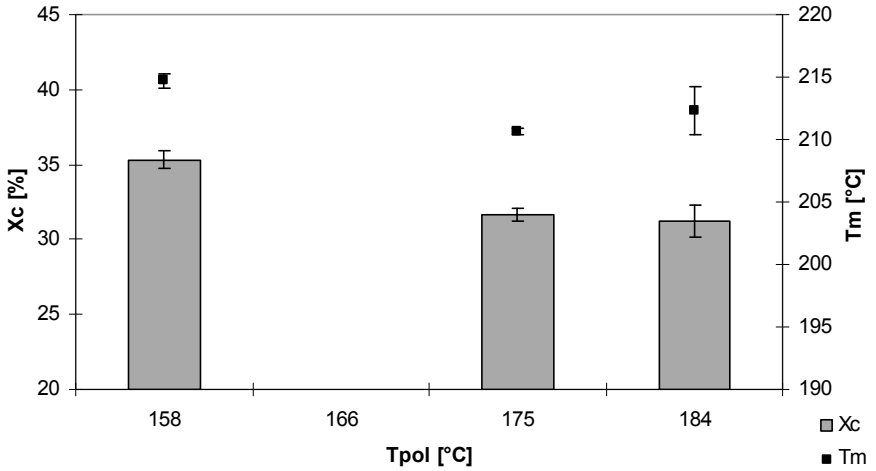

Figure 9.8: Degree of crystallinity (*Xc*) and peak melting temperature (*Tm*) for the FBG samples.

The 158°C cured specimen has a significantly higher degree of crystallinity compared to the other specimens as well as a higher peak melting temperature. The latter indicates that the crystal lamellar thickness is larger and that the crystals are more neatly ordered [6, 7]. With the discussion of the volumetric shrinkage results, it was assumed that the samples manufactured at the lowest temperature (158°C) had the highest degree of crystallisation of all samples, which is proven by the DSC results. The 184°C cured sample shows a significantly higher variation in both melting temperature and degree of crystallinity. The trend in X_c and T_m (lower decrease with increasing polymerisation temperature) is consistent with that found by van Rijswijk [6], although he did not identify any trend in variation. The crystallinity values themselves are somewhat lower compared to those found by van Rijswijk [6], which can be explained by the manufacturing method: he used a metal mould in which the exothermal heat could be better dissipated, causing lower peak temperatures with higher crystallinity levels as a result.

The degree of conversion estimates are 97.2 ± 0.9%, 97.1 ± 0.3% and 96.6 ± 0.5% for the 158°C, 175°C and 184°C specimens, resp., which are consistent with those found by van Rijswijk [6]. This shows that the polymerisation temperature of 184°C results in a lower DoC, which explains the dilatometry results in Figure 9.4.

MicroVickers hardness

The results for the microVickers hardness test are displayed in Figure 9.9.

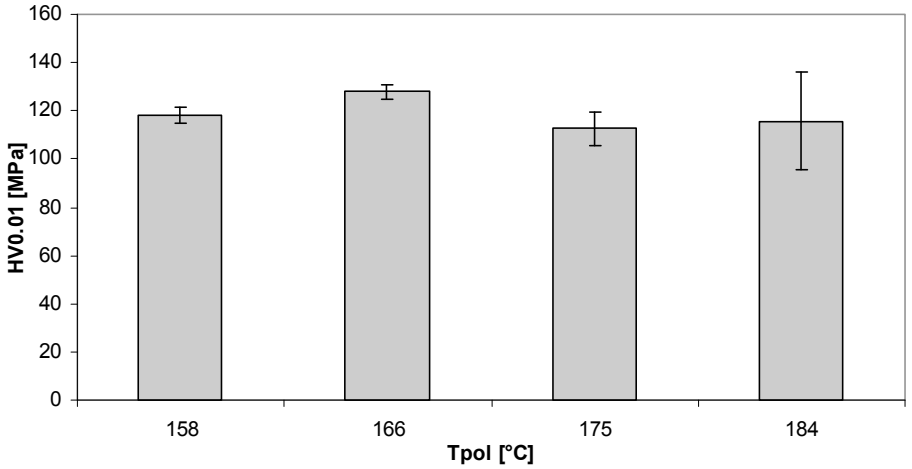

Figure 9.9: MicroVickers hardness for APA-6 specimens polymerised at different temperatures.

The highest hardness values are found for the specimen polymerised at 166°C, but a general trend of polymerisation temperature on the microVickers hardness appears absent, similar to the DSC results for the higher polymerisation temperatures. This might be explained by the relation between microVickers hardness and yield stress (see Section 7.2): Bessell *et al* [8] showed that the yield stress is mainly dependent on the degree of crystallinity of APA-6, but they found that the degree of crystallinity nor the yield stress changes much within the polymerisation temperature range used here (158 – 183°C).

One observation is that the variation of the average hardness value increases with increasing polymerisation temperature, which is also visible for the DSC results. This indicates that for higher polymerisation temperatures, a significant heterogeneity in microstructure exists, see Section 7.5.2. This is confirmed by Bessell *et al* [8], who found that the spherulitic diameter increases as well as the standard deviation therein for APA-6 polymerised at increasing temperatures. Crystal or spherulite sizes of 46 to 63 ± 12 µm were reported, which is relatively large in comparison to the indented dimensions (diagonal length is 30 - 35 µm). Another effect can be that at higher temperatures the effect of secondary crystallisation is enhanced, creating a larger number of imperfections, which is reflected by the large variance found for the hardness values, crystallinity and melting points [3], and lower degree of conversion.

9.4 Concluding remarks

During thermal cycling of the APA-6 specimens with FBGs, the strain curve mainly followed the polymerisation curve and no thermal transitions, strain-free temperatures or strain relaxation could be identified, such as with the turane samples in a previous chapter.
The dilatometry test on the other hand showed a significant amount of recrystallisation or relaxation shrinkage above T_g for the 183°C specimen, which was absent in the 166°C specimen. The difference in behaviour was related to secondary crystallisation behaviour of the 183°C specimen and the lower degree of conversion. Back at room temperature, both dilatometry specimens showed additional shrinkage compared to the initial dimensions.
During heating, the FBG and dilatometry curves compare well, from which the conclusion can be drawn, that despite suboptimal bonding between the optic fibre and the polymer, the (bulk) thermal expansion is measured correctly by the FBGs.
It proved not possible to establish a clear relation between microVickers hardness and degree of crystallinity or peak melting temperature in the APA-6 FBG specimens. There seems however to be a relation between processing temperature and variance of the hardness data, which was related to microstructural heterogeneity caused by secondary crystallisation at higher polymerisation temperatures.

References

1. Kohan, M.I., Dimensional Stability, in Nylon Plastics Handbook. 1995, Hanser Publishers: Munich. p.326-333.
2. Kohan, M.I., Crystallization, in Nylon Plastics Handbook. 1995, Hanser Publishers: Munich. p.120-122.
3. van Geenen, A.A., Vragen n.a.v. verklaren resultaten in proefschrift P. Parlevliet, recipient: Parlevliet, P.P. 10 december 2008. Personal correspondence.
4. van Geenen, A.A., Anionic Polyamide - Chemistry and processing. 2007, AvG Consultancy.
5. Cartledge, H., Baillie, C.A., Studies of Microstructural and Mechanical Properties of Nylon/Glass Composites. Part I: The Effect of Thermal Processing on Crystallinity, Transcrystallinity and Crystal Phases. Journal of Materials Science, 34(20): 5099-5111, 1999.
6. van Rijswijk, K., Thermoplastic Composite Wind Turbine Blades. 2007. PhD thesis Aerospace Engineering, Delft University of Technology, Delft. 249 pages.
7. Baltá Calleja, F.J., Fakirov, S., Effect of Crystallinity on hardness, in Microhardness of Polymers, Clarke, D.R., Suresh, S., and Ward, I.M., Editors. 2000, Cambridge University Press: Cambridge. p.90-94.
8. Bessell, T.J., Hull, D., Shortall, J.B., The effect of polymerization conditions and crystallinity on the mechanical properties and fracture of spherulitic nylon 6. Journal of Materials Science, 10: 1127-1136, 1975.

Chapter 10: Resin Infused Glass Fibre Reinforced Anionic Polyamide-6

10.1 Introduction

The previous two Chapters described investigations into the APA-6 matrix parameters governing residual strain formation with the experimental techniques presented earlier in this thesis. The next step is to apply these techniques to glass fibre reinforced anionic polyamide-6 (GF/APA-6) composites manufactured with resin infusion. In this chapter, the response of fibre Bragg gratings (FBGs) is studied during GF/APA-6 processing and thermal cycling. In addition, the microVickers hardness of the APA-6 matrix is tested in composites manufactured at different polymerisation temperatures. The results are compared with those obtained with Differential Scanning Calorimetry.

First, the behaviour in two dimensions is studied in thin (2 mm) laminates, before the extra dimension through the thickness of thick laminates is considered in the next Chapter. The state-of-art on manufacturing of the thin GF/APA-6 composites is briefly described below.

10.2 Processing of GF/APA-6 composites

Van Rijswijk developed a process for the manufacturing of a flat 2 mm glass fibre fabric reinforced APA-6 composite plate based on a standard vacuum infusion set-up [1]. The dry glass fabric is positioned on a mould and is covered with a vacuum bag. The inlet is connected to the liquid resin while a vacuum pressure is present at the outlet, see Figure 10.1.

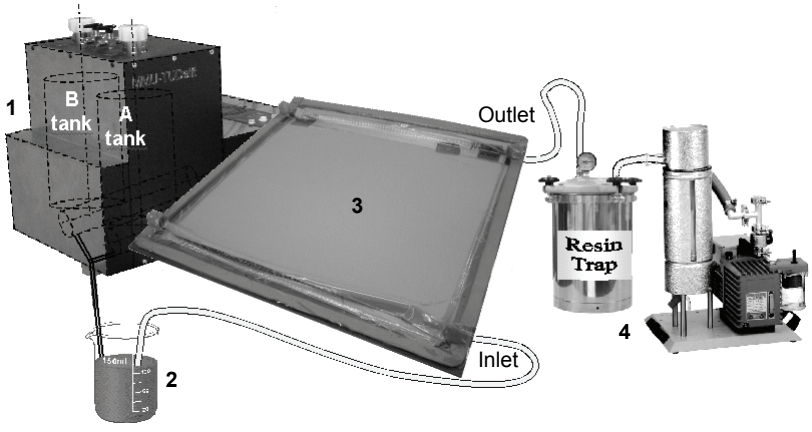

Figure 10.1: Schematic representation of the processing equipment: (1) mixing/dispensing machine, (2) resin buffer, (3) mould and vacuum bag system, and (4) pressure control system, from [1].

As mentioned in Chapter 8, the monomer-initiator-activator mixture is liquid at temperatures above 70°C. For a sufficiently large processing window and to shorten the heating time to the polymerisation temperature, the liquid is heated in the mixing & dispensing unit to 110°C and kept at that temperature in the buffer vessel before infusion. This mixture is then degassed at vacuum pressure to release entrapped air and dissolved nitrogen gas avoiding formation of voids in the laminates. Fibre compaction and resin injection are performed under vacuum pressure. When the resin has fully impregnated the dry fibres by line infusion and reached the outlet, the resin inlet is closed and the composite is allowed to cure at the APA-6 polymerisation temperature for one hour under vacuum pressure.

In the original set-up the dry fibres were already preheated to the polymerisation temperature (150-190°C), while the resin mixture had a temperature of 110°C. This resulted in a significant temperature gradient in flow direction [1, 2], causing a variation in composite properties. This included differences in void concentrations, in polymerisation rates, degrees of crystallinity and conversion, and mechanical properties.
Isothermal infusion was presented as a way to overcome the thermal gradient [3, 4]. This means that the glass fibres are at equal temperature as the resin during infusion and after full impregnation the entire assembly is heated to the desired polymerisation temperature. A significant advantage, especially for thick composites, is that the processing window for infusion can be increased tremendously, because the gel time at these infusion temperature (110-130°C) is almost infinite [4].
Even though better polymer properties were found at lower mould temperatures (~160°C), higher temperatures (~180°C) were observed to provide an optimal fibre-matrix bond strength, due to the reaction of the de-blocked activator with the glass fibre, resulting in better mechanical (interlaminar shear) properties [1]. Therefore, the isothermal process requires fast heating rates for sufficient mechanical properties, since polymerisation may already start before the de-blocking temperature of the activator is reached and most of the activator will then react with the monomer instead of the glass fibre. Sufficiently fast heating rates for thin composite laminates were achieved with infrared panels [3].
Summarising, isothermal infusion at 110-130°C and subsequent heating to 180°C with infrared heating panels not only provides an optimal infusion window and reproducible laminates, but also the desired homogeneous laminate properties including optimum mechanical properties in the flow direction [1, 4].

10.3 Evaluation of GF/APA-6 composite processing with Fibre Bragg Gratings

10.3.1 Experimental procedures

Materials

The previously described work used 1k glass filament tows woven into 8 Harness satin (8HS) fabric, whereas in practice 1k fabrics are not often used for vacuum infusion of large composite parts, such as windmill turbine blades. Reasons are that lay-up of the many relatively thin layers required for such a preform is very laborious and the permeability of this fabric is low, which can prevent full infusion of a part. Instead, a coarse 5 mm wide 12k tow plain woven glass fabric (RP0840 from Ten Cate Advanced Composites, Netherlands) with 840 g/m^2 and high permeability was used that allowed fast infusion. The aminosilane-based (8207) fibre sizing was equal as of the 8HS glass fabric. Before lay-up the fibres were dried overnight in a vacuum oven at ~100°C. The APA-6 matrix was prepared as described in Section 8.3.1 with the aid of the mini mixing unit (Bronk Industrial B.V. Netherlands).

Specimen preparation

The vacuum bag lay up for liquid moulding is shown in Figure 10.3.

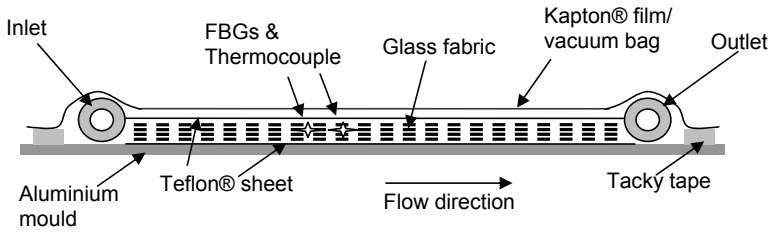

Figure 10.3: Schematic view of laminate build-up for vacuum bagging.

The glass fabric preform was positioned on a 1.5 mm thin aluminium plate measuring 35 by 35 cm^2, of which the bottom surface was painted mat black for enhanced infrared heating. On top of this plate, a 30 x 30 cm^2 Teflon sheet (125 µm thickness) was taped with 0.075 mm thin blue Flashtape2 (Aerovac, UK) and tacky tape (SM5142, Schnee-Morehead, USA) was placed along the edges of the aluminium plate. 4 glass fabric plies of 25 x 30 cm were placed symmetrically, and on two opposing sides of the preform, metal springs connected to aluminium tubes were placed as runners to ensure line infusion. Another layer of Teflon is added on top to ensure easy release of the 25 µm thin polyimide bagging film (Kapton® 100HN, GE Polymershapes HiFi Snij-Unie, Netherlands).

The optic fibre with two strain gratings and temperature sensor, and a thermocouple were cleaned with ethanol and then taped to the surface of the second glass fabric layer with the aid of small polyimide tapes (Tesa 51408, RS, Netherlands). The FBGs were placed parallel to the flow direction and the temperature FBG is placed next to the strain FBGs. A K-type thermocouple (NiCr-Ni: GG220-2K-0.1M, Rössel Temperature Sensors and Systems,

Netherlands) is placed next to the thermal FBG sensor, see Figure 10.4. The sensors were positioned relatively close to the inlet, such that in the unlikely event of incomplete infusion, the chances for measuring useful data are relatively high and the expensive optic fibre is not wasted.

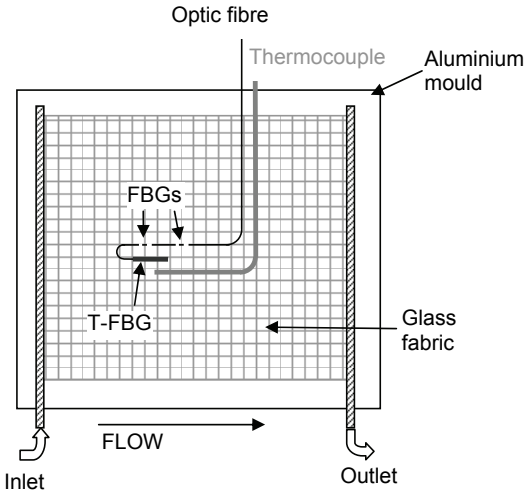

Figure 10.4: Schematic view of sensor positioning.

A total of three laminates were prepared: two laminates with 4 mm long gratings and one with 8 mm gratings. The gratings in the laminate were positioned in the direction of a fibre tow (position *A* in Figure 10.5) or in a valley between two fibre bundles: position *B* in Figure 10.5[1]. The laminates are designated accordingly: laminate 4A has 4 mm FBGs which are positioned according to A in Figure 10.5, etc. This resulted in the laminates 4A, 4B and 8B.

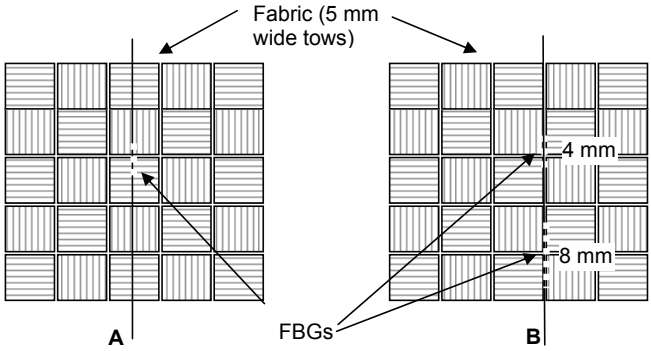

Figure 10.5: Two variations for positioning of optic fibre in dry fabric reinforcement.

[1] How the fabric layer was positioned on top of the optic fibre, could not be determined with certainty.

Test set-up

First, vacuum pressure was applied to the laminate by closing the inlet and connecting the outlet to a vacuum pump and air-tightness was checked. Then, the assembly was placed between two 5000 W infrared heating panels (Watlow, USA) at a distance of 50 mm of the heating elements both above and below. The inlet and outlet are connected to the buffer vessel and a vacuum pump, resp. with silicone rubber hoses (Rubber BV, Netherlands), see also Figure 10.1. The optic fibres contained three 4 mm or 8 mm long Draw Tower Gratings (FOS&S, Belgium) with Bragg wavelengths of 1542nm and 1546nm for the strain sensors and 1550nm for the temperature sensor, and were prepared as the optic fibres in the previous chapters. The optic fibres and thermocouples were connected to the FBGScan616 interrogator (FOS&S, Belgium) and Keithley data logging device, resp. The data acquisition interval was 5 seconds.

First, the dry preform was exposed to a heating cycle from room temperature to 130°C to 180°C and back to room temperature, to calibrate the FBG thermal sensor (FBG T-sensor). Then, the preform was heated to 130°C, and at this temperature, the glass fibres were flushed with nitrogen gas for at least 10 minutes at 100 mbar to ensure that all moisture was removed that could disrupt the polymerisation process.

500 ml of activator-initiator-monomer mixture was prepared in the Mini Mixing Unit at 110°C under a nitrogen protective environment and subsequently injected into the buffer vessel: a Woulff bottle on an electrically heated plate at 110°C and not 130°C. The lifetime of the mixture at 110°C is better than at 130°C [2]. The mixture was subsequently degassed for 5 minutes at 250 mbar. Then, the (closed) inlet hose of the laminate was connected to the buffer vessel through a heated mandrel to ensure that during flow, the mixture would not cool down and solidify in the hose. When everything was set in place, the inlet hose was opened and infusion of the laminate took place within 15-20 seconds. As soon as the resin reached the outlet, the inlet was closed and the infrared heating panels were set to 180°C. After ~1 hour, the heating panels and the vacuum pump were switched off, the panel was allowed to cool down to the ambient air of ~23°C and the vacuum bag was removed.

Data analysis

The strain and temperature developments as registered by the gratings were calculated from the wavelength shifts in a similar fashion as described in Section 4.3.4.

10.3.2 Results and discussion

Application of vacuum pressure

Upon application of vacuum pressure (from 1012 to ~5 mbar) the wavelengths of the strain gratings in the laminates shift, see Figure 10.6. The temperature FBG sensors do not show

any response to pressurisation of the laminate, which indicates that the encapsulated gratings do not experience any strains. The staggering nature of the '4B' curves is caused by the manual touching of the preform while making it airtight, i.e. fastening the tacky tape, etc. It seems to take some time before the FBG wavelength signal is stabilised, which can be attributed to the non-elastic (visco-elastic) deformation of the fabric during pressurisation [5-7].

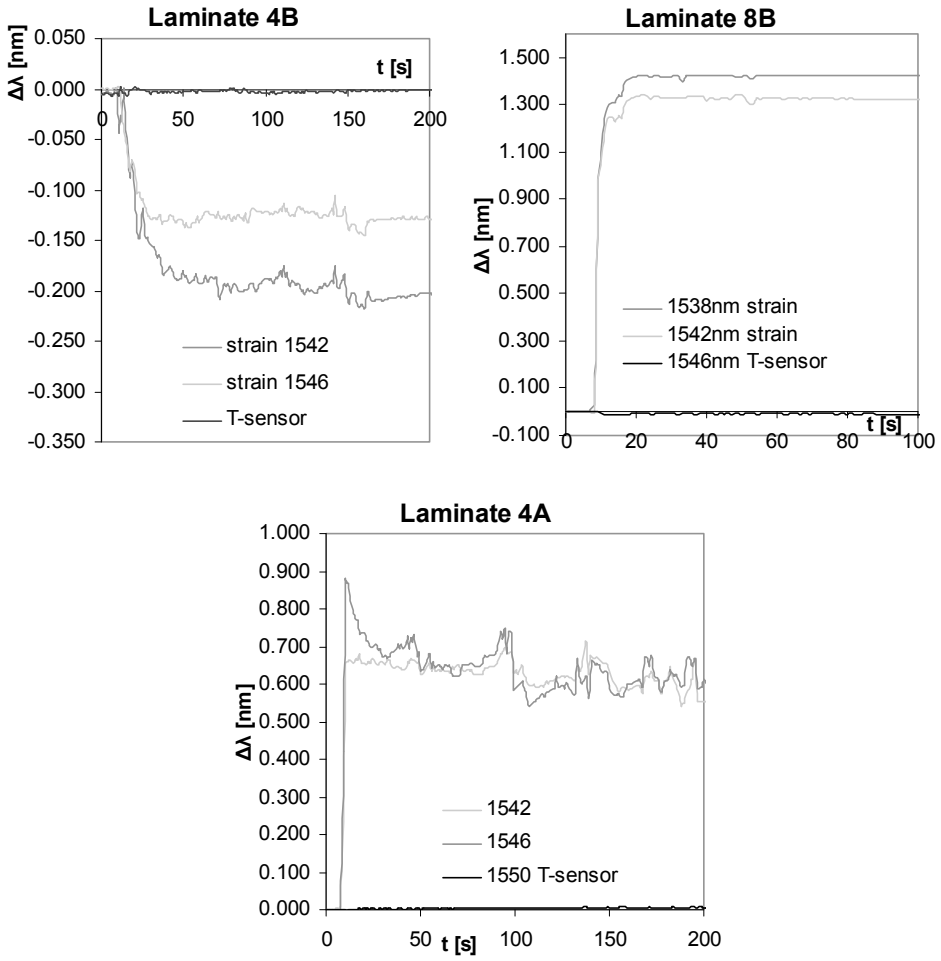

Figure 10.6: Response to vacuum pressure of FBGs embedded in dry preforms 4B and 8B.

Opposed to laminate 4B, laminates 4A and 8B showed a positive wavelength shift (corresponding to a tensile strain) upon application of vacuum pressure. The difference in tensile and compressive response is not likely related to local fabric effects, since both

gratings show the same strain direction, and therefore it seems related to the deformation of the fabric layers to which the optic fibre is attached. The seemingly contradictive response between the 'B'-laminates may be related to the fabric layer position on top of the optic fibre. In laminate 4B it can be that the upper layer also has a B-position relative to the optic fibre resulting in a compression, while for the 8B laminate the upper layer can have position 'A' resulting in a tensile response. In position 'B' tow nesting can occur [6], which may result in a compressive deformation of the optic fibre. In position 'A' spreading of tows and bending of the optic fibre at tow crossover points [6] may result in tensile deformation.

Besides the strain direction, the strain magnitude also varies significantly between the laminates. Apparently, the optic fibres attached to the fabric layers respond dissimilar to the vacuum application. Where this difference comes from is unknown, but may be related to either inhomogeneous deformation of the glass fabric during pressurisation, or the fixation of the optic fibre to the glass fabric with small tapes, which could be a little different for each optic fibre. Why this could have such a significant effect is unknown, but other methods for standardised embedding of optic fibres are investigated further at TU Delft [8].

The variation in strain response between the two strain gratings in one optic fibre was observed for almost every test. This behaviour was found representative for FBGs embedded between layers of dry fabric (in coarse as well as the finer 8HS fabric) when subjected to pressure variations [9], which may be caused by local deformation effects, such as tow nesting, tow spread, embedding and entwining of fibres, etc [6]. These effects may cause the optic fibre to straighten, compress or bend. To value the FBG response correctly, these mechanisms need to be understood and the exact location of the grating needs to be known. Because it is already difficult to identify the exact location of the gratings within the 'free' optic fibre, it is almost impossible to know the exact position when embedded in the fabric reinforced laminate and the extent of deformation of the fabric where the grating is located. Research on deformation mechanisms in dry fibres has received attention only recently [6-8, 10], and it is expected that in the future more understanding of these phenomena becomes available.

This discussion shows that it is assumed that the FBGs' response is related to a combination of fabric and local deformation effects, and these effects are seemingly not reproducible. The topic of dry fibre deformation effects is beyond the scope of this thesis, where the aim is to identify 'global' residual strain development through the thickness and not on a tow (micro)level. Therefore, the output of the two strain gratings is regarded more on a qualitative rather than quantitative level, to assess the residual strain formation during processing of a composite.

FBG response during processing

Several steps can be identified during the manufacturing process of GF/APA-6 laminates, see Figures 10.7 and 10.8 for laminate 4B (the part between 5 and 45 minutes in Figure 10.7 is enlarged in Figure 10.8). The reference wavelength, λ_B^0 in Eq. (4-10), is taken around room temperature, when the laminate was under vacuum pressure (~3 mbar) and had endured a preliminary heating cycle.

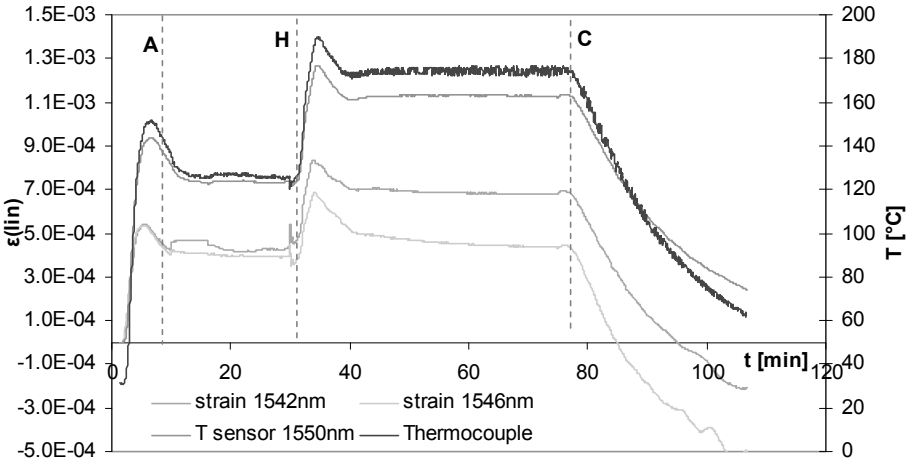

Figure 10.7: Strain and temperature response during processing of GF/APA-6 laminate 4B.

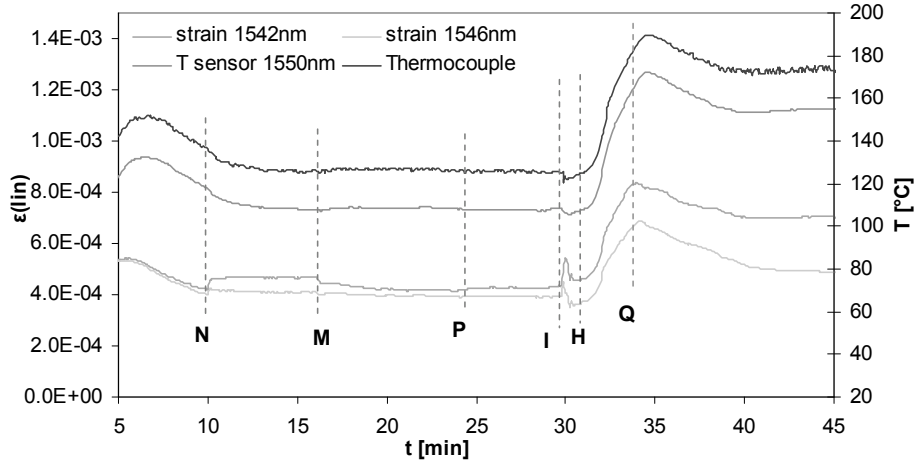

Figure 10.8: Representative part of the polymerisation cycle in Figure 10.7.

Between time = 0 min and point *A*, the preform is heated to the infusion temperature of 130°C. The infrared heating panels unfortunately showed an overshoot to the set temperature, which explains the thermal peak just before *A*. The temperature sensor shows identical behaviour as the thermocouple, indicating good functionality.
The calculated strains should remain zero upon exposure to thermal variations in the absence of other external mechanical strains. However, in Figure 10.7 a clear strain development is visible during heating. Since the optic fibre is embedded in a fabric under pressure, it is mechanically locked between the fabric layers. Friction between the glass reinforcement and optic fibre makes that any displacement of the glass fabric is sensed by the optic fibre due to strain transfer between the two. In this manner, the coefficient of thermal expansion of the dry fabric can be determined and values in the range 4 - $5*10^{-6}$ m/m°C were found, which agree well for E-glass fibres [11].
Between points *N* and *M*, the glass fibres were flushed with nitrogen gas at 103 mbar. The minor pressure change caused a small shift in Bragg wavelengths. At point *P* the pressure was slowly decreased to 250 mbar, which did not seem to effect the strain gratings much. At point *I* the laminates were infused with the APA-6 mixture, which was slightly colder than the glass fibres. The FBGs show a clear response when the flow front passes, which can be related to a pressure gradient caused by this flow [10]. However, flow went so fast in the thin laminates (infusion times of 15-20 seconds), that in this case it is not useful to monitor the flow pattern as in Section 6.4.2.
After the infusion process, the two strain gratings respond differently from each other. This can be attributed to variations in local fibre volume fraction in the close vicinity of the gratings. When a grating is for example surrounded by a higher (liquid) matrix fraction, more relaxation of the previously developed strains can take place after infusion. This effect seems most significant for the 1546nm grating.
At point *H* the infused laminate is heated to the polymerisation temperature. Again, the heating panels caused a thermal overshoot, masking the exothermal temperature rise due to polymerisation and crystallisation. Before the peak temperature is reached, the FBG strain sensors already detect shrinkage (point *Q*), which might indicate that polymerisation and/ or crystallisation has already started, causing shrinkage of the matrix. This behaviour could however also be caused by a thermal lag of the thermocouple and FBG T-sensor.
At point *C*, the heating panels were switched off and the laminate was allowed to cool down. It is clear that a compressive residual strain is present after cooling. This can be related to matrix effects, such as polymerisation and crystallisation shrinkage, since in Figure 10.7 during the isothermal polymerisation step between points *H* and *C*, both strain gratings show a minor decrease in tensile strain, whereas the temperature remains the same. This effect is indicated by the arrows in region *S* in the following Figure:

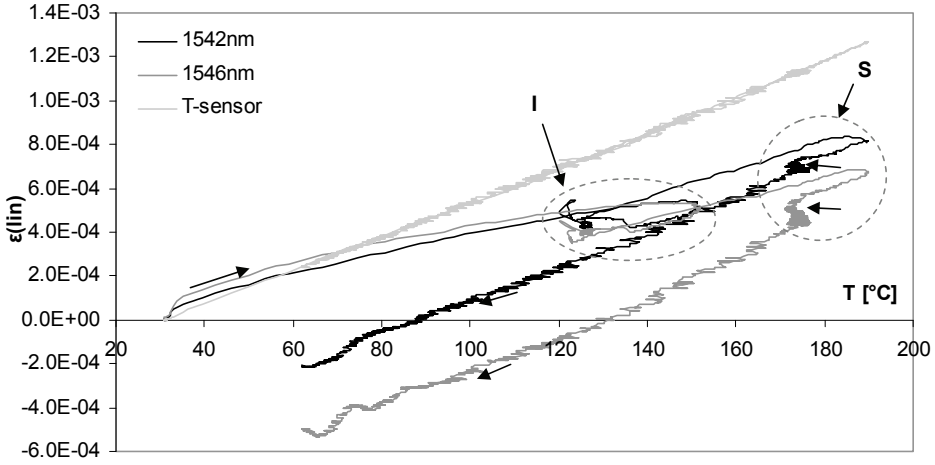

Figure 10.9: Development of strain with temperature during processing of GF/APA-6 composite.

In Figure 10.9 it is again clear that the strain responses of both gratings start to differ during infusion (indicated by *I*), although the response curves of the two gratings are similar in shape. The arrows in region *S* indicate compressive strain formation, which may be attributed to polymerisation and crystallisation of the APA-6 matrix. The coefficients of thermal expansion during cooling are also relatively similar: $7.8*10^{-6}$m/m°C and $8.9*10^{-6}$m/m°C for the 1542nm and 1546nm gratings (between 160 and 110°C), resp.
As expected, the temperature sensor responds linearly to the temperature variations. The slope of the curve is ~$8.0*10^{-6}$m/m°C, which is consistent with the value mentioned in [12].

While the strain and temperature curves for laminate 8B qualitatively resemble those of laminate 4B, for laminate 4A the FBG responses are somewhat different as shown in Figures 10.10 and 10.11, which include the split peak signals of the 1546nm grating. The infrared heating panels did not show a thermal overshoot here, and the reference wavelength was taken at vacuum pressure before the heating cycle[2].

[2] This resulted in the most clear display of the graphs.

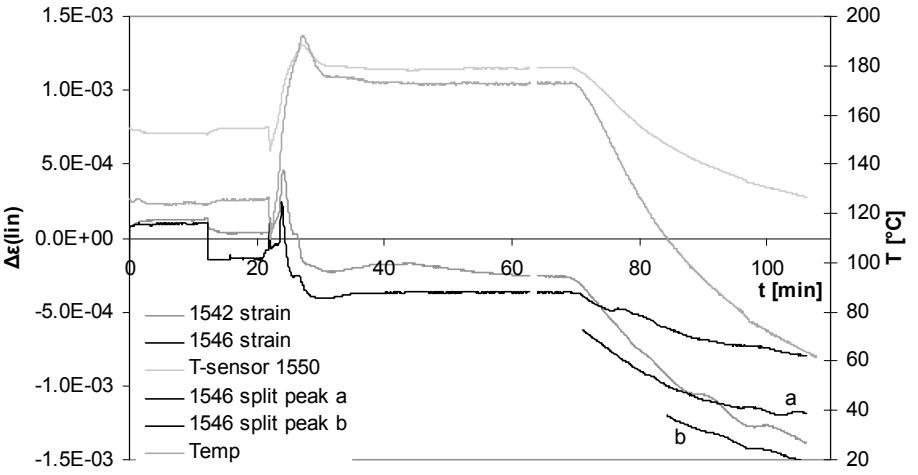

Figure 10.10: Processing cycle for laminate 4A, including split peaks.

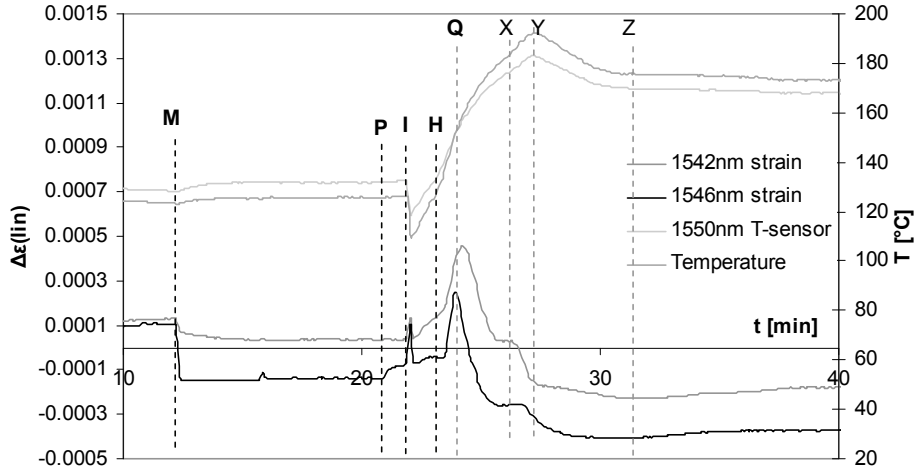

Figure 10.11: FBG and thermocouple response during processing of GF/APA-6 laminate 4A.

Nitrogen flushing had already started at t = 10 min and was stopped at point *M*. Only the 1546nm grating shows an increase due to the pressure rise from 5 to 250 mbar at point *P*, and this is also the one responding most significantly to the pressure differences during nitrogen flushing. Upon infusion (*I*), both gratings show a peak of one data point after which they seem to continue to adapt to the pressure difference.

During heating from point *H* onwards, something happens at point *Q*: when the temperature is 155-160°C, the strains start to decrease even though the temperature is still increasing. This was also observed for laminate 4B, but here it occurs much earlier. It is unlikely that

polymerisation has already started 1.5 min after infusion at these temperatures and therefore it is expected that the tensile strain is relaxed that was previously caused by vacuum application. The temperature curves show a bending point at *X*, i.e. a steeper increase in temperature, which can indicate an exothermal temperature rise due to polymerisation. Why this corresponds to a plateau in strain development is unknown, but it might be that the onset of polymerisation brings the relaxation to a halt. After the strain plateau at point *X*, a further strain decrease is visible, which corresponds roughly to the point *Q* for laminate 4B and might be caused by polymerisation shrinkage. Between points Y and Z, the strain gratings seem to follow the temperature profile again. After point Z the strains rise slowly again, which cannot be accounted for since it is not matched by thermal behaviour.

Peak splitting

The reflected wavelength spectra of the optic fibres are shown in Figure 10.12 for laminate 4B. The peaks correspond to the highest reflected power of the wavelength signals and are therefore used for strain calculations. For laminate 4A similar spectra are obtained, while laminate 8B shows tremendous peak splitting after cooling, see Figure 10.13.

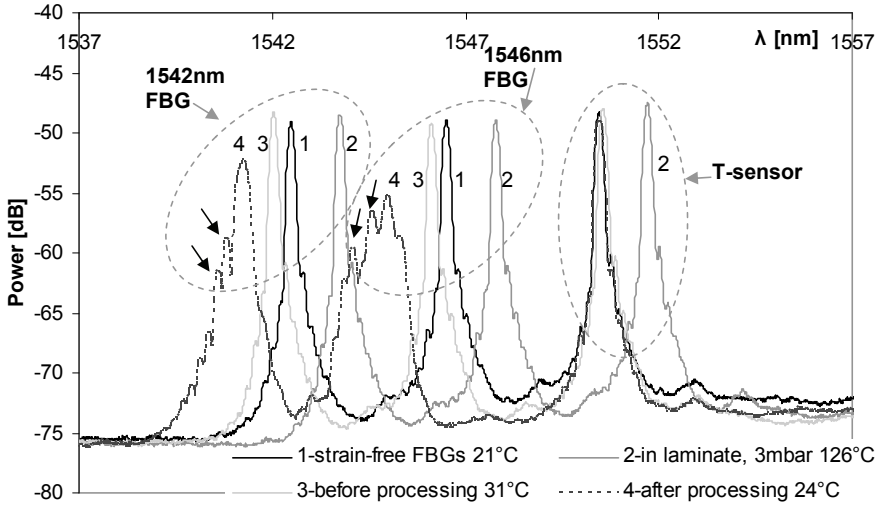

Figure 10.12: Optic fibre spectra during processing for laminate 4B.

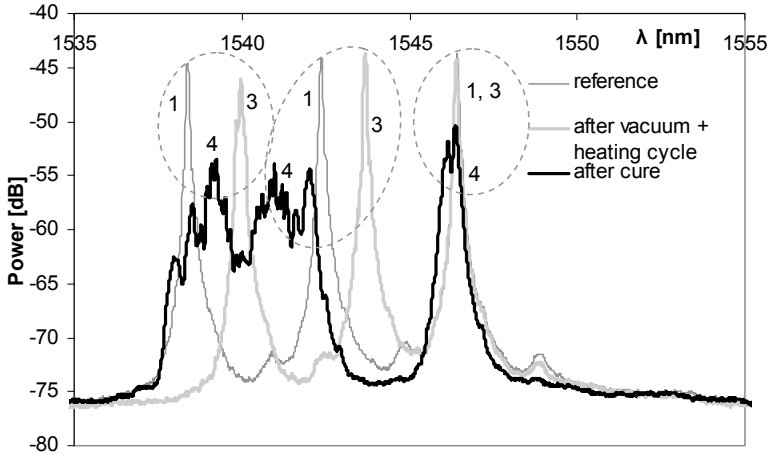

Figure 10.13: Wavelength spectra for laminate 8B.

The spectrum for the optic fibre with two strain FBGs and one encapsulated temperature FBG (T-sensor) at 21°C and no vacuum is given by curve 1. Three neat peaks can be identified. When the optic fibre is embedded in the vacuum-bagged dry preform and heated (curve 2), the curve shifts to the right, resulting from a combination of thermal expansion of the dry glass fabric and the optic fibre itself. After the heat cycle (curve 3), the strain sensors indicate a residual strain (compressive for 4B and tensile for 8B) relative to the strain-free state of curve 1. This can be explained by the combined effect of vacuum bagging and non-elastic behaviour of the glass fabric during the heating cycle resulting in an increased packing density of the fabric, which is detected as a residual strain.

After the processing cycle and demoulding of the laminate, the spectrum of curve 4 shows 'splitting' of the wavelength peaks of the strain FBGs (indicated by the arrows), while the peak wavelength for the temperature sensor has returned to its original wavelength at room temperature, as expected. This peak splitting started around the temperature of 70°C during cooling, which is close to the assumed glass transition temperature (T_g) of the APA-6 matrix. For laminate 4A peak splitting occurred during the entire cooling cycle (i.e. at 170°C and 110°C as visible in Figure 10.10), similar to laminate 8B (Figure 10.13), but for the latter the most peaks were recorded in the temperature range of 80-70°C, again close to T_g. It remains to be investigated whether the relation between peak splitting and T_g is significant. The peak splitting of the 8mm grating was so severe, that at one point no primary peaks could be identified anymore.

Peak splitting was described in Chapter 4 and occurs due to strain variations perpendicular (birefringence) or parallel to the length of the grating. More significant peak splitting is observed for the gratings that are believed to be surrounded by a higher APA-6 matrix

fraction, such as the 1546nm grating in laminate 4B. This can be explained by local stiffness variations along the grating, caused by resin pockets or the appearance of voids. Due to the increased length of the 8mm gratings, they show a much higher sensitivity to strain variations along the length of the grating when embedded in a laminate, resulting in tremendous peak splitting, see Figure 10.13. Here, it is also clear that the temperature grating was not strain-free after cure, and hence corrections were made for that.
For all laminates this peak splitting resulted in a staggering or 'wobbly' strain curve during cooling (see Figures 10.7 and 10.10 after ~85 minutes), which can be explained as follows: the FBG interrogator software is capable of identifying the different split peaks, but when the peaks are too close or too similar, the registered wavelength jumps back and forth between the two peaks and a staggering strain curve can be observed. This behaviour was also observed for other composites during cooling after cure [9].

Strain contributions
To assess the final residual strain after production of a GF/APA-6 laminate as determined with FBGs, it must be taken into account that application of vacuum pressure, heat cycling of dry fabric, the accompanying relaxation, and the production cycle all influence the final result. In Figure 10.14 the strain contributions for these steps are shown for the two strain gratings in laminates 4A and 4B. The final strain values that are given in the Figure represent the residual strain with respect to the embedded optic fibre in the absence of any strains, i.e. no vacuum pressure and at room temperature. For laminate 8B, the absence of a clear peak due to peak splitting made that no residual strain values could be identified after processing, but vacuum application resulted in a very high tensile response of 0.133 and 0.110% for the 1542 and 1546nm gratings, resp., see also Figure 10.6, while the heat cycle gave an additional tensile response of 0.047 and 0.017%.
The effects of vacuum application on the direction and magnitude of the wavelength shift have already been discussed with Figure 10.6. These effects seem to be countered (or 'relaxed') a little by the thermal cycling step of the dry preform. The compressive strain effect of the liquid moulding process is more significant for laminate 4A than for laminate 4B. This may be explained by the additional strain relaxation of laminate A during the earlier stages of the processing cycle, the origin of which may be related to the tow spreading effect during vacuum application (sensed as a tensile strain by the grating), that wants to return to their original shape. In the case of 'nesting', which is assumed to be the dominant effect for 'B', a lower tendency for relaxation exists [6].

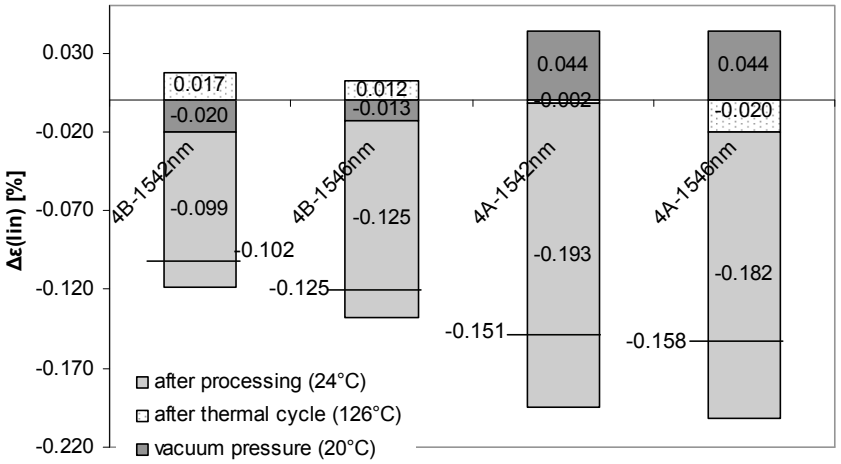

Figure 10.14: Strain contributions per processing step for laminates 4B and 4A.

From Figures 10.9 and 10.14, it seems that the largest portion of the residual strain consists of thermal contraction from the processing temperature to room temperature, when full polymerisation has taken place and the positions of the reinforcing fibres are 'frozen' and no more relaxation can occur. The contribution of thermal contraction to the final residual strain can be estimated with Eq. (6-1). The temperature difference ΔT is estimated to be ~150°C (between the point where strain starts building up, which in this case is the processing temperature ~174°C, and room temperature), and the CTE's for laminate 4B during cooling are estimated from Figure 10.9: 7.8 and 8.9*10^{-6} m/m°C. Combined, this gives a thermal strain of 0.11 - 0.13%, which is fairly close to the measured values. For laminate 4A, the CTE's are ~9.5 and 4.8*10^{-6}m/m°C for the 1542 and 1546 nm gratings, respectively, which correspond to strain value estimations of 0.13 and 0.06%. These values are significantly lower than the values reported in Figure 10.14, which may be related to the additional compressive strain contribution of the visco-elastic relaxation during the processing heating cycle.

The low CTE for the 1546nm grating in laminate 4A is similar to that of the dry fabric and may be caused by the presence of a void around the grating. This particular grating was reported to show tremendous peak splitting, see Figure 10.10, which supports the idea of a void along a part of the grating. For the residual strain calculation in Figure 10.14 the wavelength of one of the split peaks was taken, which was assumed to represent a part of the grating that was surrounded by impregnated laminate.

It can be mentioned that in general many pinholes and voids were observed in APA-6/GF laminates with coarse glass fabric. Usually polymerisation starts at the (hotter) fibre surface,

and in the many resin-rich areas between the fibre bundles polymerisation + crystallisation occurs outside-in consuming the still-liquid resin from the resin pocket centre, leaving a void due to the significant volumetric shrinkage associated with the polymerisation + crystallisation process. This is shown in a C-scan of similar laminates, where the dark lines indicating that the lowest quality/ voids are concentrated in the resin pockets at the interface between two fibre tows.

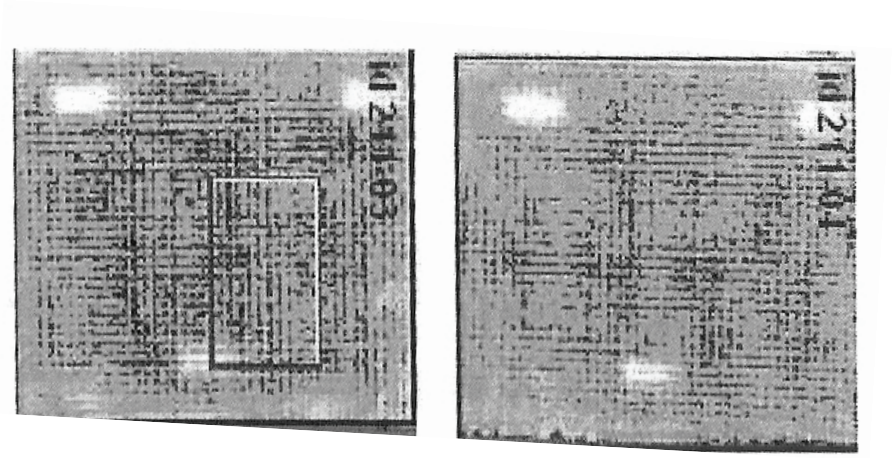

Figure 10.15: C-Scan images of GF/APA-6 laminates.

10.4 Thermal cycling

10.4.1 Experimental procedure

To identify an effect of thermal treatment on strain development in the GF/APA-6 laminates with FBGs, the laminates were exposed to a thermal cycle consisting of heating with ~50°C/min to 160°C (with an overshoot to 170-180°C), keeping the laminate at that temperature for ~1 hour, and cooling down to room temperature with ~5°C/min. Unfortunately, it was not possible to heat to the expected strain-free temperature (crystal melting temperature) of ~220°C, due to limited capacity of the infrared heating panels and heat resistance of the consumables.

The unpacked laminates were replaced on the aluminium mould with the black painted bottom surface. Due to the relatively low annealing temperature (160°C), it was not expected that extensive oxidation of the laminate occurred and therefore it was not surrounded by an inert atmosphere. No annealing test could be performed with laminate 4A, because the optic fibre fractured beyond repair during unpacking.

10.4.2 Results and discussion

Peak splitting effects

The FBG spectra at various points during the thermal cycle are shown in Figure 10.16 for laminates 4B and 8B: just before the annealing cycle, at the heating overshoot peak temperature of 183°C for laminate 8B, at the end of the more than 60 minute isothermal treatment of ~160°C, and after cooling back to room temperature.

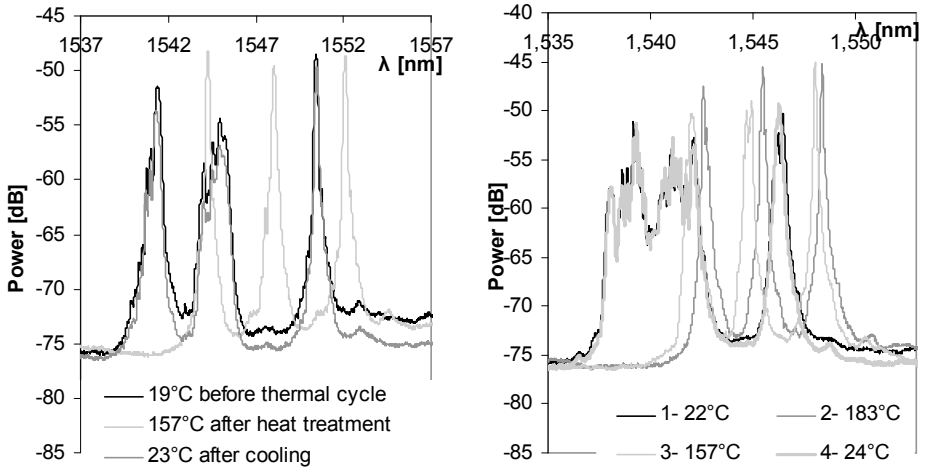

Figure 10.16: FBG spectra during thermal treatment for laminates 4B (left) and 8B (right).

As can be seen in Figure 10.16 most of the peak splitting has disappeared at 157°C. This signifies that the gratings experience a homogeneous strain field, which can be caused by relaxation of the fabric and low stiffness of the polymer matrix at these high temperatures. After cooling a similar spectrum is obtained as before the thermal cycle, which indicates that the strains and their variations along the length of the grating are identical as before.

It was observed that during heating the peak splitting started to disappear above ~55°C in laminate 4B and was completely removed at 140°C, see Figure 10.17. Similar behaviour was observed for laminate 8B, although it must be noted that the temperatures where peak splitting disappeared were difficult to establish due to the fast heating rate of the IR panels.

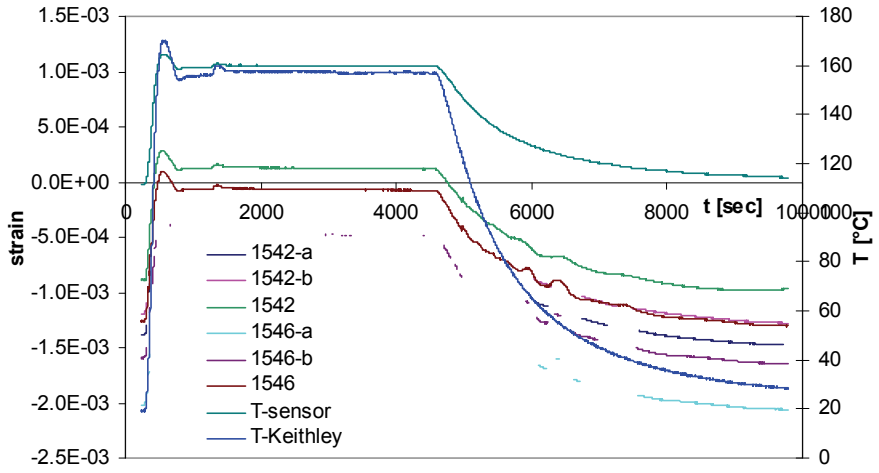

Figure 10.17: Strain profiles per wavelength peak for laminate 4B during annealing.

During cooling after the thermal treatment, significant peak splitting was observed again at 65°C in laminate 4B, while for laminate 8B a single split peak was already observed at 150°C, but most significant peak splitting was also observed from 70-65°C onwards. These temperatures correspond roughly to the glass transition temperature of APA-6 (T_g), which implies that the matrix must possess a certain stiffness to cause peak splitting.

Thermal effects

The strain variation with temperature of laminate 4B is shown in Figure 10.18 together with the polymerisation cycle from Figure 10.9 for comparison, with equal reference wavelength.

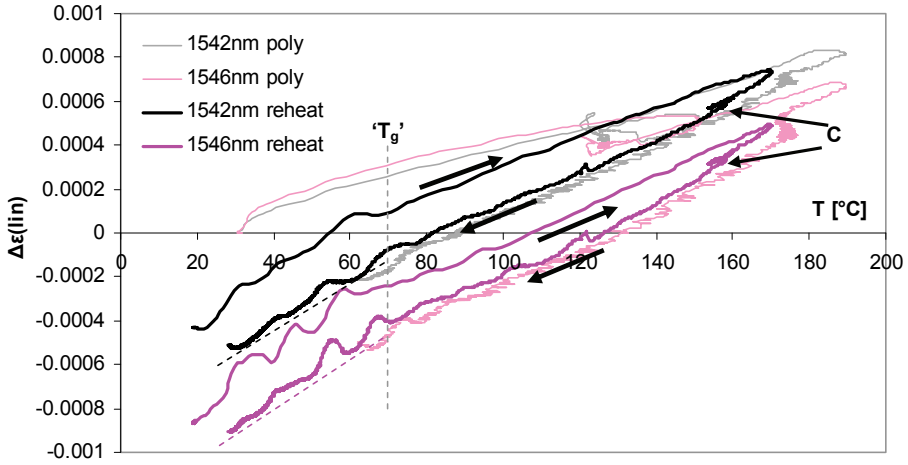

Figure 10.18: Strain curve during annealing (reheat) of laminate 4B and processing cycle (poly).

During cooling after the annealing step, the FBG response is almost identical to the cooling cycle of the polymerisation curve, which is similar behaviour as for the unreinforced APA-6 in Section 9.2. Why the heating curves lie at higher strain values can be explained by the high heating rate: the infrared panels heat so rapidly that the T-sensor in the metal capillary may not be able to respond correspondingly. This means that in Eq. (4-10), the factor $(\Delta\lambda)_T$ is lower as should be, resulting in too high strain values. During the slow cooling from points *C*, this effect is negligible.
A minimal residual compressive strain relative to the starting point could be identified for laminate 4B after the thermal cycle (-0.003 and -0.008%), but these values fall within the accuracy limit of the test set-up. For laminate 8B, an effect of the thermal cycling could not be established in more detail due to the severe peak splitting, but based on Figure 10.16, it is assumed that this effect is insignificant.

The 'wobbly' or staggering nature of the strain curves at temperatures below the line indicated with *'T_g'* in Figure 10.17 was also observed during cooling in the manufacturing cycle, see Figures 10.7 and 10.10 and was attributed to peak splitting and the FBGScan software. Here also, peak splitting is most severe below 'T_g', which may be caused by the higher APA-6 modulus below this temperature, resulting in an inhomogeneous strain field around the grating. The slopes of the curves as indicated by the dotted lines below *'T_g'* increase, implying a more dominant effect of the APA-6 matrix on thermal contraction of the laminate. This corresponds to the development of APA-6 Youngs' modulus in the same temperature region as determined by Van Rijswijk [1], which is higher below this temperature and will therefore have a more pronounced effect on the thermal expansion behaviour and strain development.
Why this transition was not observed for the optic fibres embedded in pure resin in the previous chapter can be explained by the presence of the transcrystalline layer around the optic fibre: at the glass transition, only the amorphous phase becomes soft and not the crystalline phase. Since a relatively large fraction of the crystalline phase exists around the optic fibre, softening of the amorphous phase is hardly detected by the gratings. Around the optic fibre embedded in the glass fabric reinforced APA-6 laminate, there is little 'room' for forming such a transcrystalline layer, due to the close presence of the glass reinforcement and the interaction of the APA-6 polymer with the glass fibre surfaces [13]. Therefore, it is expected that a relatively larger portion of amorphous polymer phase is present in the area surrounding the optic fibre in the composite. The dilatometry test results in the previous chapter also showed a transition around this temperature (corrected for the temperature shift caused by the dilatometer), which can be related to the amorphous phase in the 'bulk' polymer.

10.5 Microstructural properties of GF/APA-6 composites

For GF/APA-6 composites the relation between degree of crystallinity and polymerisation temperature is much more pronounced than for virgin APA-6, since the thermal behaviour is different due to the presence of the fibres, and crystal nucleation can occur at the fibre surface [1]. Therefore, the microVickers hardness test and DSC are employed for GF/APA-6 laminates to investigate the relations between polymerisation temperature, degree of crystallinity and melting peak temperature, and hardness and microstructural heterogeneity.

10.5.1 Experimental procedures

Materials

The thin laminates that were used for the microVickers hardness test were made earlier with fine glass fabric: 1k tow E-glass fibres woven into an 8-harness satin weave (SS0303, 300 g/m^2, supplied by Ten Cate Advanced Composites, Netherlands). 12 plies were stacked symmetrically to obtain a 2 mm thick laminate. The laminates were manufactured non-isothermally, i.e. with the resin at 110°C and the glass fibres at the polymerisation temperature, as described earlier.

Specimen preparation

The specimens for microVickers hardness testing were cut from the centre of the laminates and embedded, grinded and polished similar as described in Section 8.4.1. The specimens for DSC testing consisted of disc-shaped samples of ~5 mg that were punched out from the laminate and before testing, they were dried overnight in a vacuum oven at 50°C.

Test set-up

The microVickers hardness test set-up is described in Section 7.3.3. At least 10 indentations were made in resin-rich areas randomly distributed over the laminate cross-section. The averages and standard deviations of the measurements are calculated.

For the DSC tests, two specimens were tested for each polymerisation temperature with the same equipment and thermal cycle as described in Section 9.3.1. The fibre mass present in the sample needs to be corrected for and therefore the specimen is combusted after the DSC test and the fibre mass m_f was determined with a Mettler AE240 balance. Corrections are made for the monomer content m_{mon} as in Section 9.3.1 by weighing the sample before (m_s) and after (m_s') DSC testing and the difference ($m_s - m_s'$) is m_{mon}. The mass fraction of polymer w_m contributing to the crystal melting enthalpy is then:

$$w_m = \frac{m_s - m_f - m_{mon}}{m_s} \qquad (10\text{-}1)$$

The degree of crystallinity can be calculated with:

$$X_c = \frac{1}{w_m}\left(\frac{\Delta H_c}{\Delta H_0}\right) \qquad (7\text{-}2)$$

Where ΔH_0 is equal to 190 J/g for APA-6.
The degree of conversion (DoC) is determined by:

$$DoC = \frac{m_s - m_f - m_{mon}}{m_s - m_f} \qquad (10\text{-}2)$$

10.5.2 Results and discussion

In Figure 10.19 the microVickers hardness results are presented for the GF/APA-6 laminates produced at different polymerisation temperatures (T_{pol}).

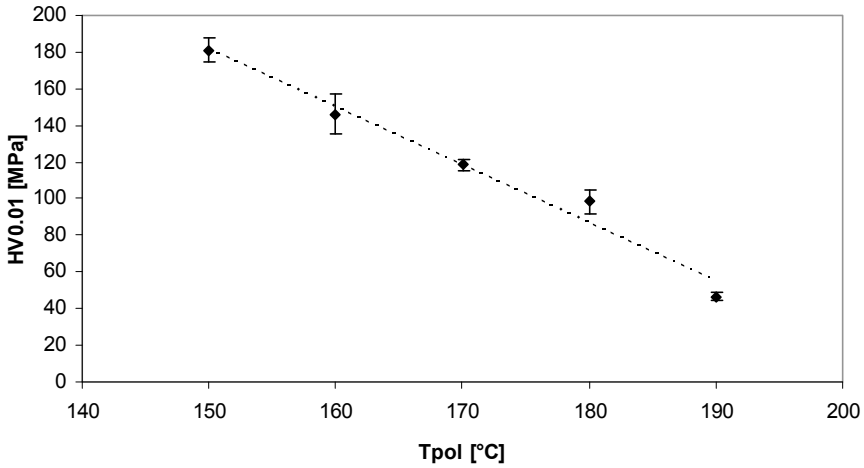

Figure 10.19: MicroVickers Hardness for GF/APA-6 manufactured at various temperatures.

A clear relation is found between microVickers hardness and processing temperature for GF/APA-6 laminates: upon increasing processing temperature, the microVickers hardness drops significantly. This can be related to a decreasing degree of crystallinity, which was also found to decrease significantly upon increasing processing temperature, see Figure 10.20.

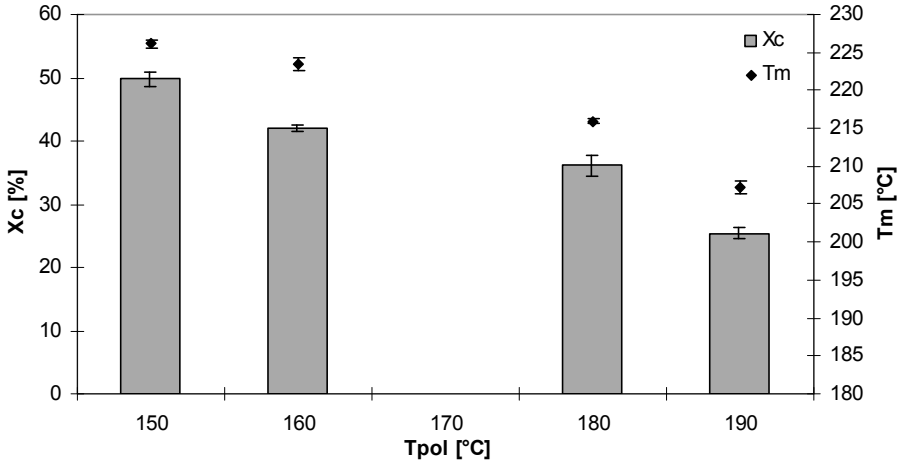

Figure 10.20: Degree of crystallinity (X_c) and peak melting temperature T_m for GF/APA-6 composites manufactured at various temperatures.

The melting peak temperature also decreases upon increasing processing temperature, indicating a less neat crystallisation process. In contrast with the pure APA-6 specimens, the variation in microVickers hardness value is less, though the values are comparable. This indicates that the microstructure of the composite matrix is more homogeneous compared to the pure APA-6. The homogeneity can be explained by the relatively homogeneous temperature in the composite laminates, due to the small thickness and the heat-absorbing effect of the glass reinforcement. In addition, the crystals are likely to nucleate at the glass fibre surfaces where impingement with other crystals can occur, preventing them from becoming very large as in the virgin APA-6 (in the order of 200 µm as observed by Baten [14] and van Rijswijk [1]).

The relations between processing temperature, degree of crystallinity and melting peak temperature are more significant for the composites than for the pure APA-6, see Section 9.3, but are exactly as found by van Rijswijk [1] with similar degree of crystallinity values. When the microVickers hardness is plotted against the degree of crystallinity as in Figure 10.21, a linear relation is found with linear regression (R^2 = 0.99):

$$Xc = \frac{HV + 98}{5.6} \qquad [\%] \qquad (10\text{-}3)$$

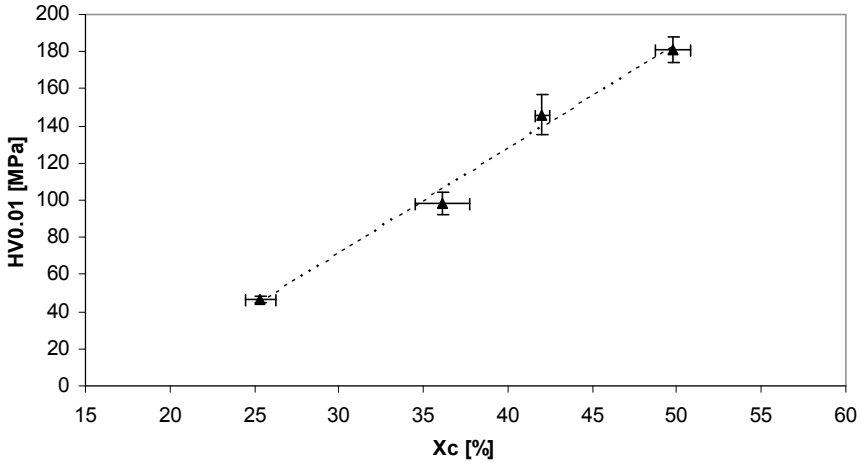

Figure 10.21: Relation between degree of crystallinity and microVickers hardness for GF/APA-6 composites.

Why a relation between microVickers hardness and degree of crystallinity can be found for the APA-6/GF composites and not for the pure APA-6 and the CF/PPS composites from Chapters 9 and 7, resp., can be attributed to the larger difference in crystallinity values between the different specimens, i.e. a difference of 25% compared to 5%. Apparently, a 5% difference in degree of crystallinity cannot be distinguished sufficiently with the microVickers hardness test or with the DSC test. It may therefore be concluded that the microVickers hardness test can be a useful tool for assessing large variations in degree of crystallinity of the produced laminates, especially since the method is much faster than the DSC test.

10.6 Conclusions & recommendations

Optic fibres with fibre Bragg grating (FBG) sensors were used to study the strain development in 2 mm thin GF/APA-6 laminates during the manufacturing process based on isothermal infusion at 130°C and curing at 180°C. The FBGs response showed pressure and temperature variations caused by deformation of the dry glass fabric, as well as passing of the flow front. The FBG sensors can be used to identify the thermal expansion and contraction of the laminate both before and after impregnation and curing of the matrix. In addition, the glass transition was recognised around ~70°C a thermal treatment, after analysis of the Bragg wavelength peak splitting behaviour and differences in temperature-strain slopes. It proved difficult to identify the matrix liquid to solid transition (gel point) due to polymerisation/ crystallisation and to estimate the associated residual strain formation. Thermal contraction upon cooling from the processing temperature is believed to present the

largest part of the final compressive residual strain values. Annealing for 1 hour at 160°C was not found to result in significant additional strain in the GF/APA-6 laminates.
Different grating lengths and optic fibre positions were investigated, which resulted in a great variation in FBG response. Though it proved difficult to identify the exact position of the gratings, the positioning of the optic fibre seemed to have a great influence on the FBG results. This may be related to variations the (local) deformation of the reinforcing fabric. The FBGs showed the presence of local non-homogenous strain fields around the optic fibre, which may be related to the presence of voids and variations in matrix fraction. 4 mm long gratings are recommended for further investigations, because the 8 mm long gratings presented such severe peak splitting, that no primary peaks could be identified for strain calculations.

A clear relation was found between microVickers hardness and the processing temperature for glass fibre reinforced APA-6 laminates, which was related to the crystallinity. With higher processing temperatures the degree of crystallinity and peak melting temperature decrease, similar to the microVickers hardness.

References

1. van Rijswijk, K., Thermoplastic Composite Wind Turbine Blades. 2007. PhD thesis Aerospace Engineering, Delft University of Technology, Delft. 249 pages.
2. Teuwen, J.J.E., Gillis, J.H.A.M., Bersee, H.E.N., Optimisation of infusion temperature for anionic polyamide-6 composites, in AIAA. 2008.
3. Gillis, J.H.A.M., Heating methods for the production of thick APA-6/ glass laminates. 2007. MSc thesis Aerospace Engineering, Delft University of Technology, Delft. 74 pages.
4. Teuwen, J.J.E., Unpublished results on isothermal processing of GF/APA-6 laminates. 2008. PhD thesis Aerospace Engineering, Delft University of Technology, Delft.
5. McGuinness, G.B., Bradaigh, C.M.O., Development of rheological models for forming flows and picture-frame shear testing of fabric reinforced thermoplastic sheets. Journal of Non-Newtonian Fluid Mechanics, 73(1-2): 1-28, 1997.
6. Somashekara, A.A., Bickerton, S., Bhattacharyya, D., Exploring the non-elastic compression deformation of dry glass fibre reinforcements. Composites Science and Technology, 67(2): 183-200, 2007.
7. Weimer, C., Zur nähtechnischen Konfektion von textilen Verstärkungsstrukturen für Faser-Kunststoff-Verbunde. 2002. PhD thesis Instituet fuer Verbundwerkstoffe, TU Kaiserslautern, Kaiserslautern. 161 pages.
8. Balvers, J.M., Bersee, H.E.N., Beukers, A., Integration of fiber bragg gratings in woven fabrics: influences of preform compaction and flow-front propagation, in FPCM-9. 2008: Montréal, Québec.
9. Balvers, J.M., Monitoring the RTM process with FBGs - Progress report. 2008, Delft University of Technology: Delft. p. 61.
10. Bickerton, Walbran, Govignon, Observations of stress and laminate thickness variations in LCM processes, in ICCM-16. 2007: Kyoto.
11. JPS_Composite_Materials. Products. [cited 2009 March]. Available from: http://www.jpscompositematerials.com/products.htm.
12. Belasting meten met optische rekstroken, in Kunststof Magazine. 2007. p. 30-34.
13. Spruiell, J., Janke, C., A review of the measurement and development of crystallinity and its relations to properties in neat poly(phenylene sulfide) and its fiber reinforced composites. 2004, Oak Ridge National Laboratory: Oak Ridge. p. 80.
14. Baten, E.M., Microstructural Variations in Thick-Walled Anionic Polyamide-6 Composites. 2006. MSc thesis Aerospace Engineering, Delft University of Technology, Delft. 80 pages.

Chapter 11: Thick Glass Fibre Reinforced Anionic Polyamide-6 Laminates

11.1 Introduction

The previous chapter showed that thin GF/APA-6 laminates can be successfully manufactured with reproducible properties. Up to now it remains unknown if this material can be processed into thick composite structures, such as windmill turbine blades. The aim is to develop the technology for successful manufacturing of thick GF/APA-6 composite laminates, in terms of complete infusion, full polymerisation and homogeneous properties. Previous chapters showed that thermal behaviour during manufacturing of the composite controls this, and is also responsible for residual strain formation through the thickness. Therefore, the goal of this chapter is to investigate the effects of temperature variations on residual strain formation and matrix properties through the thickness with the experimental techniques presented in the previous chapters: fibre Bragg gratings and microVickers hardness, resp. Preliminary investigations into the manufacturing of thick GF/APA-6 laminates are reported first.

11.2 Investigations into manufacturing of thick GF/APA-6 laminates

To scale up the previously described resin infusion process for thin laminates into thick composite structures for windmill turbine blades, several parameters need to be considered: infusion or flow behaviour, thermal behaviour and variation of material properties through the thickness.

The first trials to manufacture thick (>20 mm) glass fibre reinforced laminates with vacuum infusion of APA-6 were carried out in 2005-2006 by Baten and Gillis *et al* [1, 2] under the joint supervision of Teuwen, van Rijswijk and Parlevliet. Since the Infrared heating panels used in the previous chapter were not yet available, a hot platen press was used for heating. Also, the common procedure at that time was to have the dry fibres already at the polymerisation temperature (180°C) during infusion with the relatively cold (110°C) APA-6 mixture [3].

11.2.1 Infusion

First of all, it must be made sure that full infusion of the preform takes place and that this occurs in a practical time space. Flow behaviour during liquid moulding is related to the viscosity of the matrix, the pressure difference, the permeability of the preform, the gel time, and the dimensions of the structure. Vacuum assisted infusion is preferred for its relatively low manufacturing costs and flexibility. However, full vacuum causes the caprolactam to boil,

causing many voids in the final structure [3]. Therefore, infusion occurs at a vacuum pressure of ~250 mbar also for thick laminates.

It was found impossible to fully infuse a 20 mm thick laminate of 200 x 200 mm^2 with the regularly used 8HS fabric [1]. This was related to the low flow velocity caused by the poor fabric permeability, even though the viscosity of the matrix is extremely low at the infusion temperature: ~10 mPa.s. Before the flow front reached the outlet, polymerisation had already started and the viscosity increased to such an extent that the liquid flow was stopped. Hence the coarse plain weave fabric was chosen with higher permeability, but equal fibre sizing. Several thick laminates with dimensions 200 x 200 mm^2 were successfully produced in that fashion and thicknesses of 12 mm (20 fabric layers), 25 mm (40 layers) and even 50 mm (80 layers) were achieved. Full infusion was observed to take place for these laminates in 40-90 seconds, while for the smaller ones with fine 8HS fabric, this was 2-5 minutes [1]. The thermocouples placed throughout the laminate were able to register the passing of the flow front owing to the lower temperature of the liquid resin with respect to the reinforcing glass fibres. For the thicker laminates (25 and 50 mm), it was found that the flow front started close to the mould plate (later referred to as 'bottom'), which is explained by the contact between the inlet spiral and the mould, see Figure 11.1.

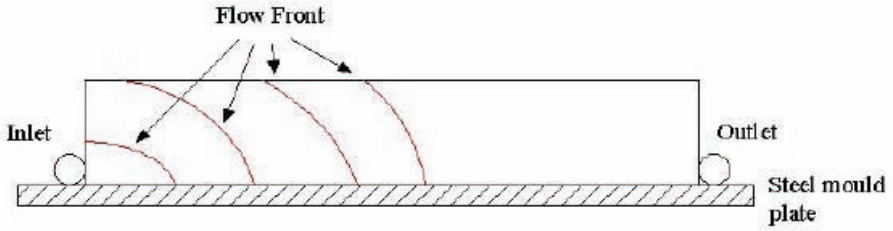

Figure 11.1: Schematic view of flow front progression in thick GF/APA-6 laminates, from [1].

11.2.2 Thermal behaviour

Regarding the dimensions of the preform, a full 60 m long windmill turbine blade remains to be infused, but the aim for the near future is the production of a 10 cm thick laminate. With the epoxy resin based systems that are commonly used for windmill turbine blades, this thickness poses great challenges with respect to the internal heat generated by the exothermal reaction. In the centre of such a laminate, the temperature increase can be such that temperatures above the degradation point are reached. To prevent this, very slow curing systems are used and curing of a blade usually takes 10-12 hours [4]. It was already explained that crystallisation and crystal melting presents a self-regulating thermal system for

APA-6 composites. Whether this is applicable to thick laminates can be seen in the following Figure where a representative thermal profile for a thick laminate is given:

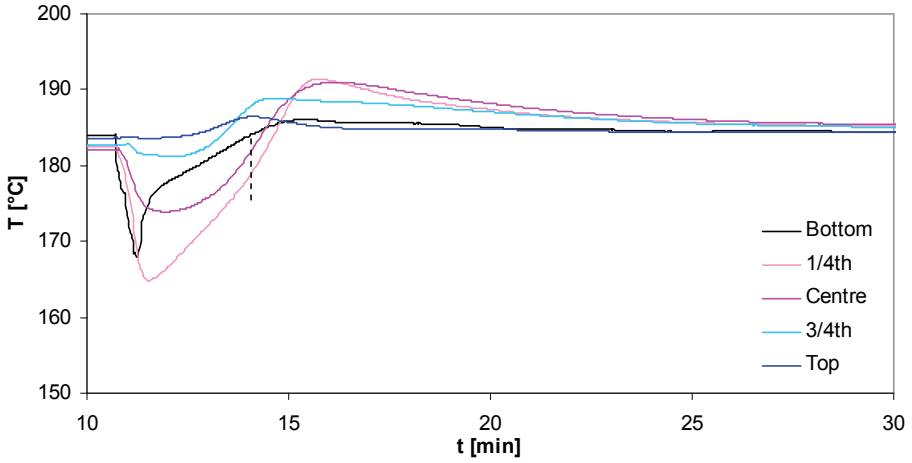

Figure 11.2: Temperature development through the thickness of a 25 mm thick GF/APA-6 laminate.

A few observations can be made based on this Figure:

- No clear distinction between the polymerisation and crystallisation exotherm is visible, i.e. only one exothermal peak is observed. This is consistent with the observations for laminates produced at 180°C by van Rijswijk [3] and in Section 10.3.
- The thermocouples were located closer to the outlet than the inlet, because usually the polymerisation front goes from the outlet towards the inlet, leaving many voids at the inlet. The thermocouples closer to the mould plate ('Bottom') show a more drastic temperature decrease due to the passing of the cold resin compared to the thermocouples at the top, meaning that the resin at the top has gained more heat from the glass fibres due to the longer flow path, which is consistent with Figure 11.1.
- The slope increase of the heating curve after infusion, indicates that the laminate is self-heating. This implies that polymerisation has already started before the mould temperature is reached (for the thermocouple located at 1/4th of the laminate thickness this is ~177°C, see line).
- Since the resin at the top of the laminate has reached the polymerisation temperature earlier than the bottom area, the exotherm peak due to polymerisation is also observed earlier: 3½ min compared to 5 min at the bottom.
- The exothermal peaks closer to the centre of the laminate reach the highest peak temperature. This can be attributed to the heat insulating properties of the composite: the generated heat cannot dissipate.

- The maximum peak temperature for this laminate is 192°C, which is only 10°C above the mould temperature of 182°C. This is higher than the 5°C difference previously reported [3], but it corresponds well to the value found for laminate 4A in Section 10.3. It is still much lower than the exothermal temperature increase in pure resin, due to the heat absorption by the glass fibres. For a 50 mm thick laminate the peak temperature was also ~190°C. This means that the self-regulating system due to (re-)crystallisation prevents the matrix from overheating in thick laminates.
- The exotherm peaks are reached sooner at the top surface and the bottom than in the centre, which indicates that polymerisation occurs outside-in. This may cause entrapment of voids in the centre of the laminate. Also, matrix polymerisation shrinkage at the centre cannot be refilled with liquid resin from the surfaces when these have already polymerised. However, examination of the laminate cross-section showed that voids caused by matrix shrinkage in the large resin pockets in the coarse fabric were evenly distributed through the thickness, see Figure 11.3.

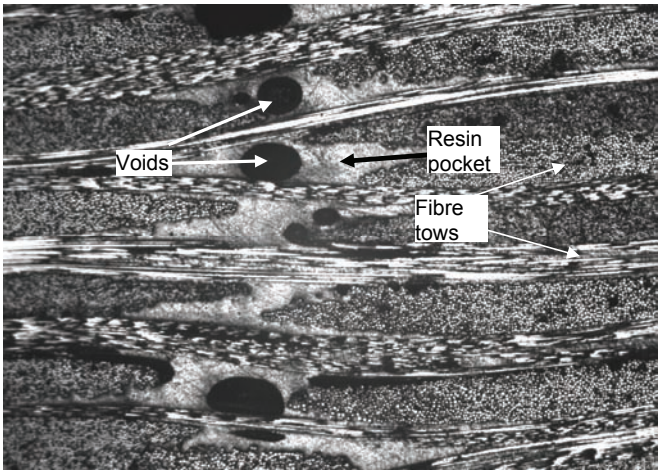

Figure 11.3: Micrograph of GF/APA-6 laminate cross-section.

- It must be mentioned that the centre of a 50 mm thick laminate preform could not be heated to the desired mould temperature of 180°C (but only to 168°C) due to heat losses. However, due to the additional polymerisation heat and the better thermal conductivity of the added matrix, the polymerisation temperature could be reached, see Figure 11.4.

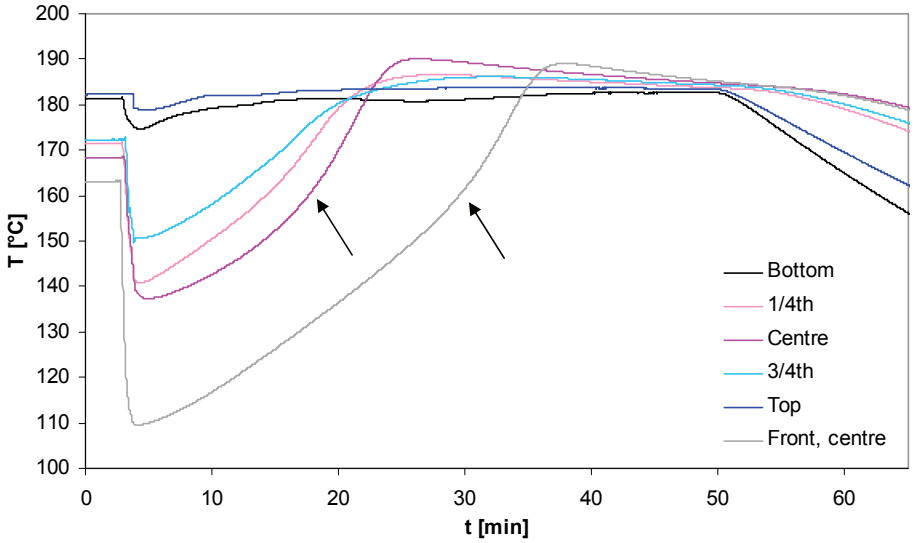

Figure 11.4: Thermal behaviour during manufacturing of a 50 mm thick GF/APA-6 laminate.

- Due to the temperature difference of the flowing matrix between the outlet and the inlet, polymerisation starts significantly later at the inlet area. Therefore, it may be concluded that polymerisation occurs from outlet to inlet as well as outside-in. The explanation for the low temperature at the inlet is that the glass fibres have cooled down significantly due to more flow of the cold resin passing the glass fibres compared to the outlet.
- From the two thermocouples located at the centre plies, it seems that polymerisation already started at ~160°C causing exothermal self-heating (indicated by the arrows).

11.2.3 Material properties through the thickness

The non-homogeneous temperature distribution is likely to affect the matrix properties through the thickness. These were tested by separating the thick laminate by every 10 plies, which was achieved by placing Kapton® films between every stack of 10 fabric layers, similar to the PSL technique described in Chapter 3. After polymerisation, separation of these plies resulted in several 1.5 mm thick laminates that could subsequently be tested. Tests were conducted on specimens taken from the outlet area.

The degree of conversion (DoC) measured with the extraction method [3] was found to vary greatly (between 5% and 10% variation) for all laminates, but no clear trend could be identified [1]. Average DoC values ranged from 78 to 87%, with the least amount of scatter found for the 50 mm thick laminate. These DoC values are low compared to the average ~92% found for the 8HS fabric reinforced laminates produced at similar temperatures [1, 3]. This can be attributed to the coarse fabric with the large resin pockets, where due to the

tremendous matrix shrinkage voids appear, see Figure 11.3. During generation of these voids the local internal pressure drops below the evaporation pressure of caprolactam, causing the voids to be filled with caprolactam vapour [3]. This caprolactam vapour no longer participates in the polymerisation reaction and results in a lower degree of conversion.
Differential Scanning Calorimetry (DSC) results showed a similar trend as the DoC: the degree of crystallinity varied greatly (± 5%) through the thickness for all laminates, while average values were around 38%, which is consistent with the results for thin laminates [3], see also Section 10.5. The peak melting temperature T_m also showed much variation through the thickness, and was found to lie in the range of 215-220°C. The T_m of the 50 mm laminate was however higher: between 220°C and 227°C. This difference may be related to the lower cooling rates for the thicker 50 mm laminate, which can function as an annealing step resulting in enhanced crystal lamellar thicknesses giving higher peak melting temperatures.
Interlaminar shear testing (short beam shear) of the separated laminates showed no clear variation in mechanical properties through the thickness and here, the amount of data scatter was small, indicating homogeneous fibre/matrix adhesion.
Preliminary microVickers hardness testing showed a minor trend of increased hardness values at the surfaces of the laminate, i.e. at the top and bottom. This can be explained by the metal press plates acting as heat sink, resulting in lower peak temperatures and hence higher crystallinity levels (see also Section 8.2), but this will be investigated in more detail later.

11.2.4 Adapted manufacturing parameters

Based on the previously described results regarding temperature inhomogeneities, and most importantly the fact that a thick 50 mm laminate could not be heated to the desired polymerisation temperature before infusion, further attempts were carried out using a test set-up with Infrared heating panels [2]. Optimisation of the manufacturing process was based on 25 mm thick laminates with 40 plies and width and length 220 mm, resp. A mat black painted aluminium tool plate was found most suitable to transfer the heat to the laminate.
In order to reach a more homogeneous temperature distribution throughout the entire laminate and consequently ensure more homogeneous material properties, the laminate was infused at 110°C and then heated to the polymerisation temperature of 180°C. This resulted in the following temperature profile, where the peak at ~16 min of the thermocouple ‘on top laminate’ is caused by the thermal overshooting of the IR panels and is not a polymerisation peak:

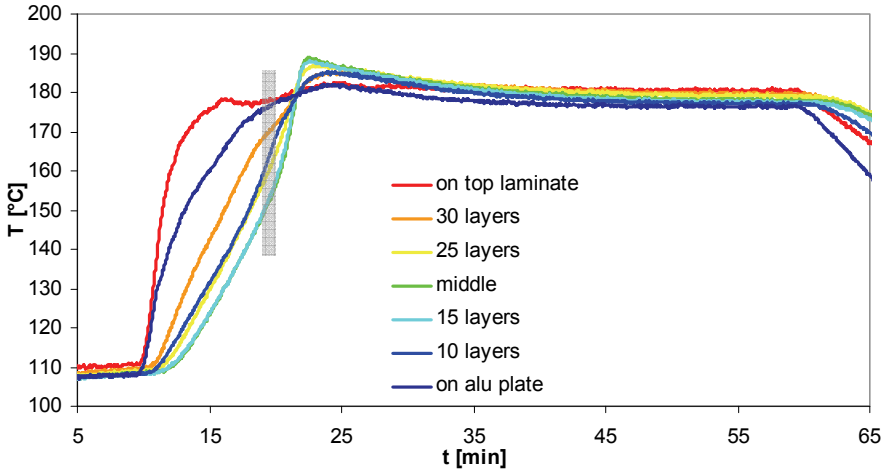

Figure 11.5: Thermal behaviour of an isothermally infused 25 mm GF/APA-6 laminate subsequently heated to the polymerisation temperature.

The temperature distribution is significantly different through the thickness of the laminate compared to Figure 11.2. Polymerisation seems to start in the non-surface plies before the mould temperature is reached, as indicated by the grey area, and at this point the temperatures range from ~150-180°C. The peak exothermal temperature is highest for the centre ply (189°C). One remarkable difference with Figure 11.2 is that the peak temperature is reached for the centre ply first, and progresses towards the laminate surfaces. This indicates an inside-out polymerisation front, which is desired in terms of void distribution (they cannot become trapped in the centre) and residual strains. The time to reach the thermal polymerisation peak between the centre plies and the surface plies differs ~2 minutes, which is somewhat longer than for the other laminate. The variation in peak temperature is similar (~7°C).

For this laminate, the degree of conversion showed equal values with similar scatter as for the previous laminates, but the interlaminar (short beam) shear strength is significantly higher, viz. average 32 ± 3 MPa compared to 24 ± 2 MPa for the non-isothermally cured 25mm laminates. This can be attributed to the low infusion temperature: no filtering of the activator due to interaction with the fibre sizing can take place during matrix flow from the inlet to outlet, since the temperature is still below its deblocking temperature of 160°C. Only when the matrix reaches temperatures above 160°C, the activator is capable of interaction with the fibre sizing. In addition, at the high polymerisation temperature of 180°C, the polymer chains initiated at the fibre surface can reach longer lengths and interpenetrate to a larger extent with the bulk matrix, increasing the fibre-matrix interface strength [3].

11.3 Detection of strain development through the thickness with FBG sensors

The isothermal manufacturing process of a thick GF/APA-6 laminate was investigated with FBG sensors, to monitor the flow behaviour and strain formation. In addition, the laminate was exposed to an annealing cycle.

11.3.1 Specimen preparation and test set-up

40 layers of RP0840 glass fabric were symmetrically stacked on top of a 3 mm thick 350 x 350 mm^2 aluminium plate with black painted surface. Optic fibres and thermocouples were positioned between the following layers (from bottom to top): 1-2, 10-11, 20-21, 30-31 and 39-40, see Figure 11.6.

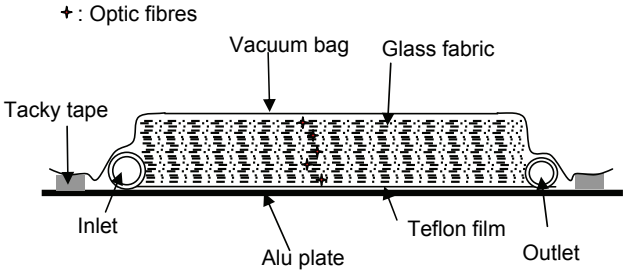

Figure 11.6: Schematic view of laminate build-up.

The optic fibres and thermocouples were cleaned with ethanol before they were positioned between the fabric layers and fixed with small polyimide tapes as in Figure 10.4. Optic fibres were placed in the centre of the fibre bundles (position *A* in Figure 10.5), parallel to the flow direction. Preparation of the vacuum bag was as described in Section 10.3.1, with the difference that the inlet and outlet springs were of a larger diameter to ensure flow through the thickness.

After checking that the set-up was airtight, the laminate was placed between the infrared heating panels and exposed to a heating cycle consisting of heating from 30°C to 130°C, then holding for some time, further heating to 180°C, and cooling down to 130°C again.

The APA-6 mixture was prepared in the MMU at 110°C and degassed in the buffer vessel, as in Section 10.3.1. The hose between the buffer vessel and the inlet was heated to 130°C as well as the dry fabric preform. Nitrogen flushing occurred at 144 mbar pressure, while infusion took place at 250 mbar.

Some of the FBG temperature sensors did not remain airtight during the process, and in that case the thermal cycle was used to calibrate the sensors with the data from the thermocouple, after which the thermocouple readings were used to predict the wavelengths

of the temperature gratings during the manufacturing process. Strain calculations based on the FBG results are similar as in Chapter 10.
The thick laminate was also exposed to an annealing cycle similar to that for the thin laminate: heating to 158 ± 2°C with the infrared heating panels, holding for ~90 minutes and cooling back to room temperature.

11.3.2 Results and discussion

Thermal behaviour

The thermal behaviour during processing (after nitrogen flushing) is shown in Figure 11.7, where the time at the start of infusion (point *I*) was t = 23 min.

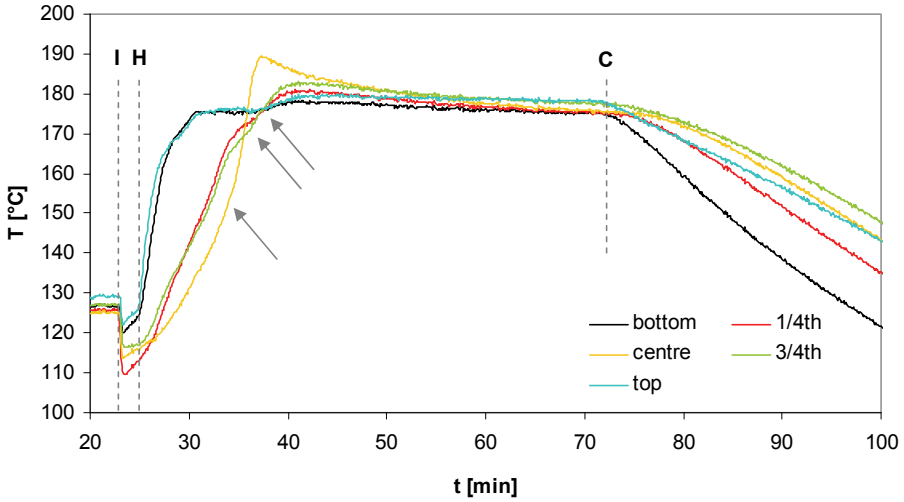

Figure 11.7: Thermal behaviour during manufacturing of a 24 mm thick GF/APA-6 laminate.

At point *H* the infrared panels were set to the mould temperature of 180°C, while at *C* the infrared panels were switched off and the laminate was allowed to cool down to room temperature.

The thermal behaviour resembles very much that of Figure 11.4 for a similar laminate. The onset of the polymerisation exotherms are indicated by the arrows. During polymerisation the temperatures through the thickness are very close. Here also the polymerisation front seems to go from the centre plies towards the outer plies, with the characteristic that polymerisation starts sooner in the centre and at lower temperatures compared to the plies closer to the surface. The peak temperatures are reached earlier in the centre (~38 min) than in the outer plies (~42 min), with the highest temperature in the centre and decreasing towards the outer

surfaces (bottom – 179°C, 1/4th – 181°C, centre – 189°C, 3/4th – 183°C, top – 180°C). The bottom plies cool fastest, since the aluminium plate conducts the heat and aids in cooling down. The top plies cool more slowly due to upward convection of the hot air (the plate is manufactured horizontally). Again, no separate exothermal crystallisation peak is visible, due to the high processing temperature where crystallisation occurs slowly leading to an elongated temperature peak.

FBG results

As with the thin laminates, the flow front during infusion could not be established with the FBG sensors nor with the thermocouples, since the infusion went very fast through the coarse fabric. The residual strain contributions from vacuum pressure, heating cycle and processing cycle are shown in Figure 11.8 for all gratings.

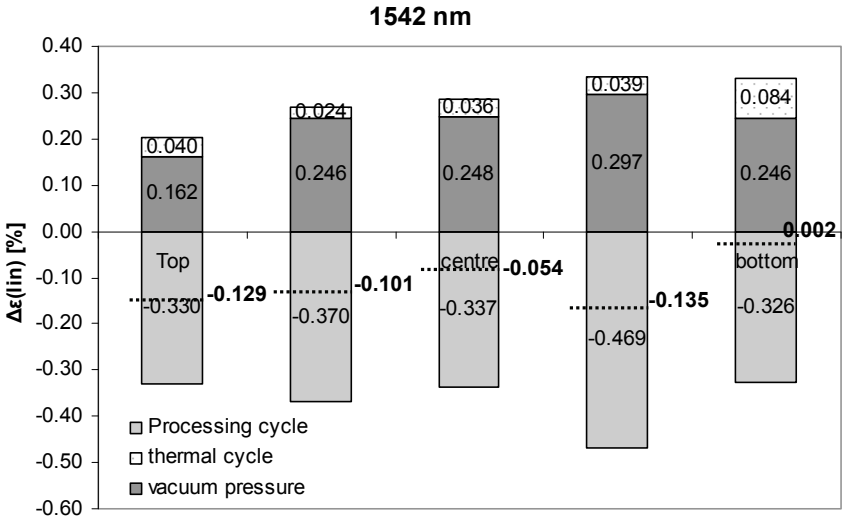

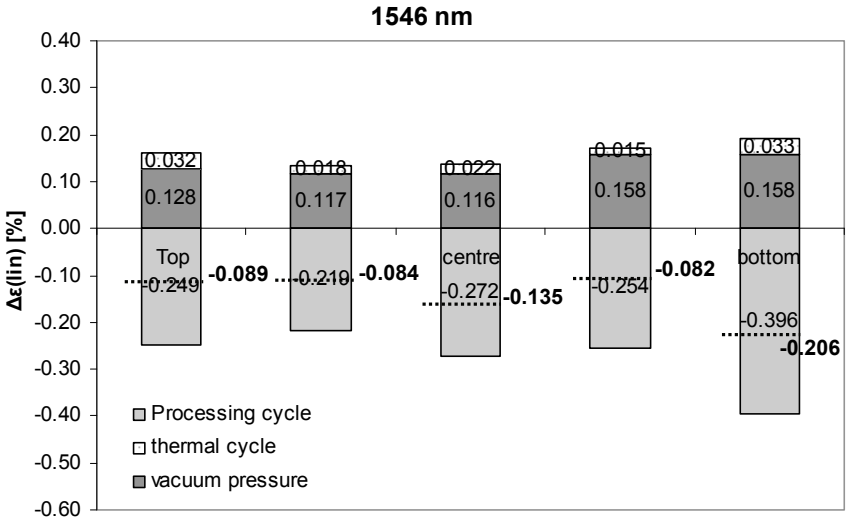

Figure 11.8: FBG responses to the various processing steps.

All gratings showed a tensile strain due to vacuum application similar as for the thin laminate 4A, but the strain is much higher, corresponding to a wavelength shift in the order of 1.5 – 3 nm. For all gratings, the visco-elastic response of the glass fabric caused a gradual strain increase upon application of vacuum pressure, similar to Figure 10.6. The 1542nm gratings always showed a much higher jump than the 1546nm gratings. An explanation for this behaviour has not yet been found. It may be related to the way they are placed inside the laminate, i.e. there is no bulky temperature sensor or thermocouple in the direct neighbourhood as is the case for the 1546nm gratings; hence their response is likely to be dominated by the glass fabric only, but this was not observed for the thin laminates in the previous chapter.

The FBGs closest to the surface plies show the most significant residual strain effect due to the thermal cycle, which may be related to the higher thermal expansion of the polyimide foil and aluminium mould and friction between these and the glass fibres.

Not only vacuum application, but also the effect of the heating cycle is much more significant for the thick than for the thin laminate. This may be attributed to enhanced deformation of the glass fabric in the thick laminate. When more glass fabric layers are stacked on top of each other, there is relatively more room for compaction and more deformation of the fabric is indeed observed.

Moreover, the polymerisation cycle also results in a much higher compressive residual strain contribution as for the thin laminates. This can be related to additional fabric relaxation during heating after infusion, as seen for laminate 4A in Figure 10.11. The strain and thermal

behaviour in the thick laminate are shown in Figure 11.9 for the FBGs located in the centre of the laminate, where the designated letters have equal meaning as earlier. The reference wavelengths λ_B^0 are taken before embedding of the optic fibre between the glass layers.

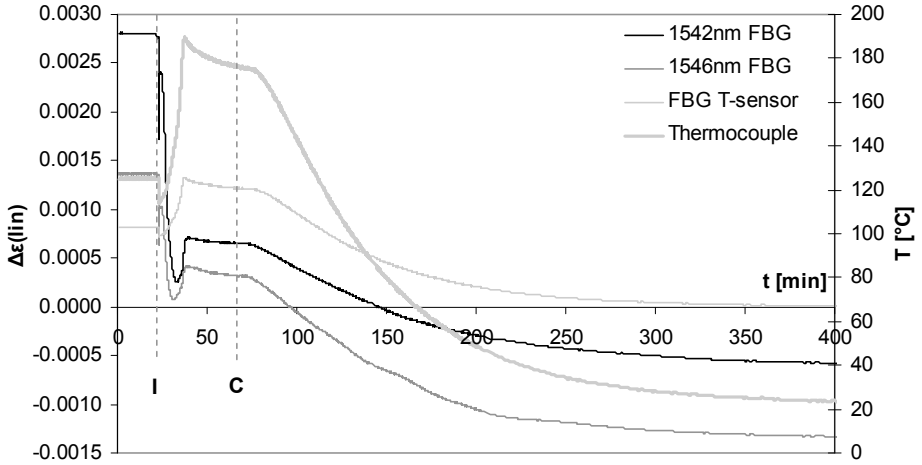

Figure 11.9: Strain and temperature response in the centre plies of thick GF/APA-6 laminate.

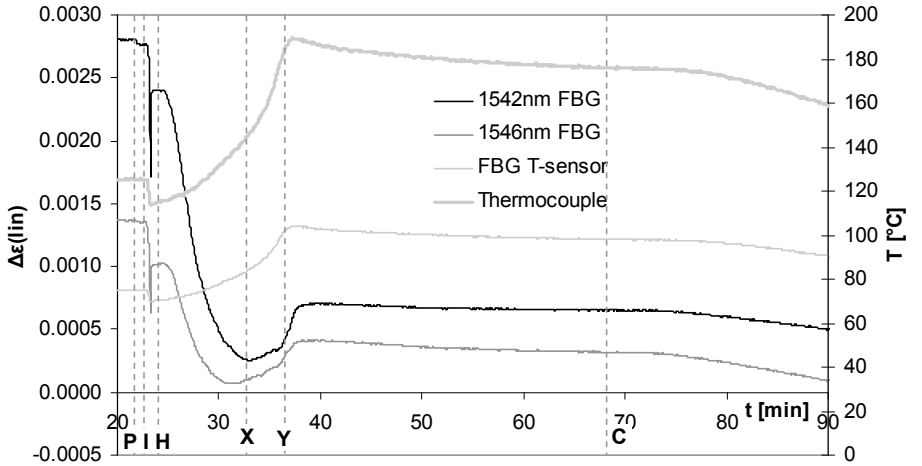

Figure 11.10: Magnification of Figure 11.9.

At point *P* where the vacuum pressure is decreased from 3 to 250 mbar, the strain gratings respond with a minor relaxation of the tensile strain that was previously built-up due to vacuum pressure and the heating cycle. At point *I* infusion takes place, as the resin is still cooler than the dry glass fibres despite the heated inlet hose. The thermal sensors show a

mild temperature drop, whereas the strain gratings show a sharp downward peak consisting of one data point, after which the strain levels remain roughly constant at a lower value than before infusion, indicating strain relaxation. When the infused laminate is heated at point *H*, further relaxation takes place to a level where the strains almost reach zero and the difference between the two gratings is minimised. It seems that the effect of vacuum application is diminished, but why this occurs precisely during heating is unknown, although it can be related with thermal expansion of the liquid matrix. Assumedly in the thick laminate there is a much lower fibre packing density, due to which the optic fibre is more or less detached from the glass fabric after resin infusion and resin thermal expansion. Therefore, the gratings no longer sense deformation of the glass fabric when surrounded by liquid matrix that is incapable of transferring strains to the optic fibre. This state remains until the polymer matrix starts to polymerise, which is assumed to occur in the area around point *X* because an additional temperature rise due to exothermal polymerisation + crystallisation can be seen, and strain transfer to the optic fibre is possible again. This implies that X can be the gel point. It appears that after this point the gratings follow the thermal expansion behaviour of the infused laminate. After reaching the peak temperature at *Y*, the laminate centre ply cools down very slowly to the dwell temperature.

In the following Figure, the strain development for all gratings is displayed. In both graphs *X* and *Y* represent the regions where the 'gel points' and peak temperatures were found, resp.

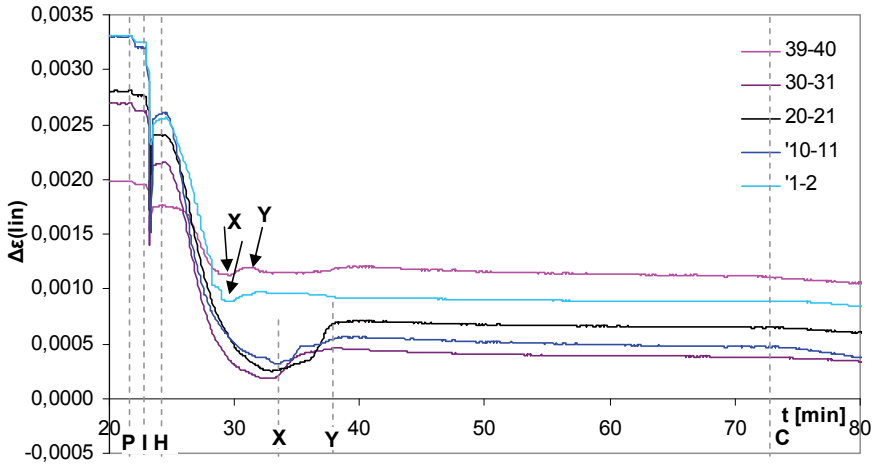

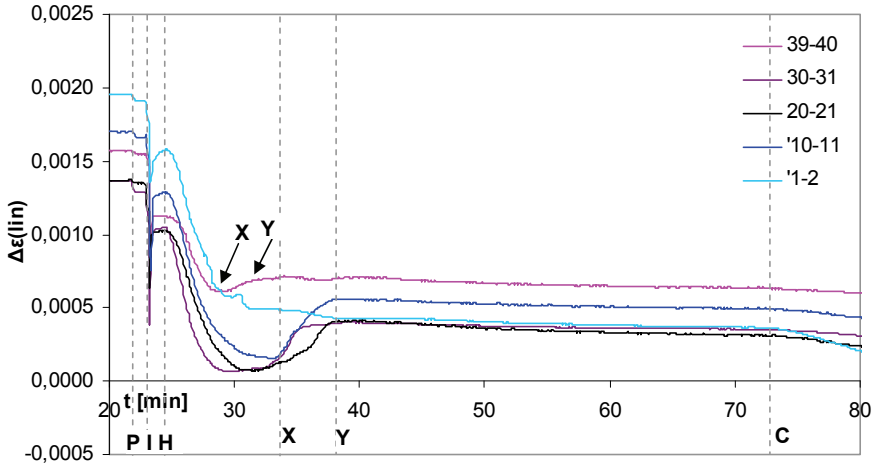

Figure 11.11: Strain development with time for 1542nm (upper figure) and 1546nm (lower) gratings through the thickness of a thick GF/APA-6 laminate.

The strain behaviour during the processing cycle is fairly similar for all gratings: they show some strain relaxation due to infusion, but during heating the relaxation is most pronounced. For the centre plies the strain relaxation is almost complete (close to zero), contrary to the surface plies, which can be related to a larger influence of the reinforcing fibres or the tool. After reaching point *X*, strain relaxations stops and the thermal behaviour of the laminate is followed, which occurs later for the plies closer to the centre, implying outside-in polymerisation. The surface plies reached the mould temperature very early compared to the inner plies and therefore it seems that polymerisation (point *X*) starts earlier compared to the inner plies, contrary to what was assumed for the thermal behaviour of Figure 11.7, where the peak temperatures for the surface plies could be caused by the exotherm of the adjacent layers. In Figure 11.11 it is difficult to establish the polymerisation peak temperature for the surface plies, since the heat was easily dissipated to the surroundings.
The strain behaviour seems different from that of the thin laminates, where the gratings were observed to follow more the thermal expansion behaviour of the glass fibre reinforcement and likely also that of the aluminium tool plate. Apparently, the thickness of the laminate ensures that the FBG sensors in the centre plies detect more matrix-dominated behaviour, such as the ‘gel point’, and an overruling effect of the tool thermal expansion is absent.

Strain vs. temperature
In Figure 11.12 the strain development with temperature is shown for the 1542nm and 1546nm gratings:

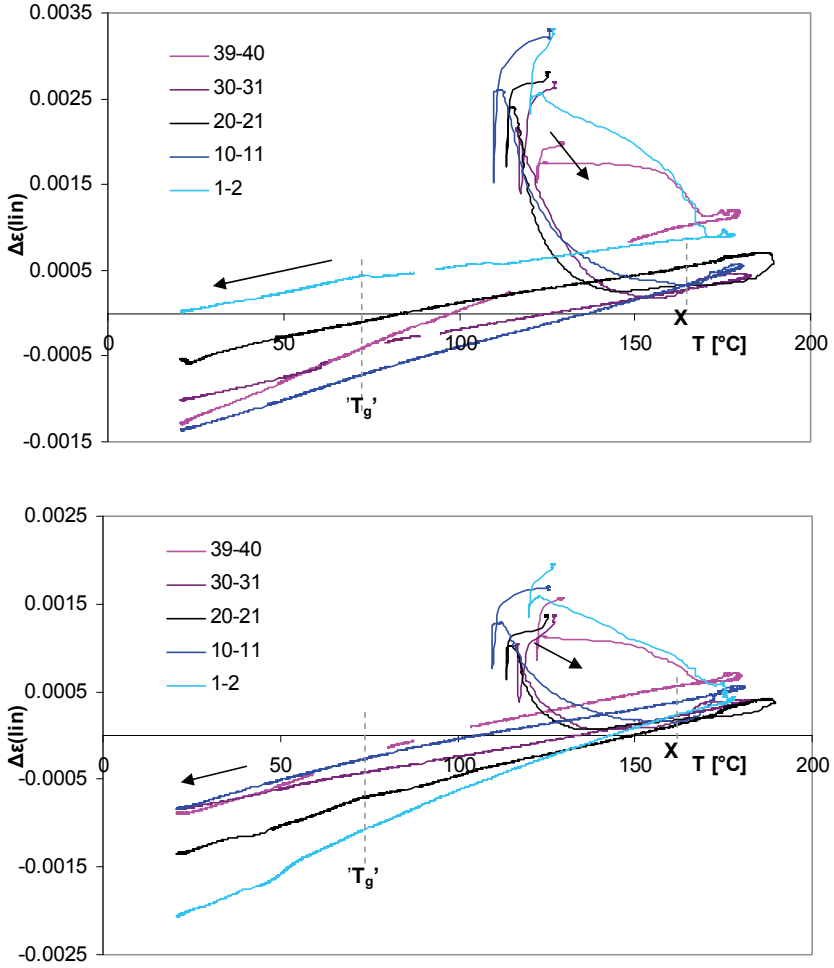

Figure 11.12: Strain development with temperature for 1542nm gratings (upper) and 1546m, gratings (lower figure).

Figure 11.12 clearly shows the relaxation effect during heating (viewing direction is indicated by the arrows). Around point *X*, a tensile strain starts to develop, which is related to the thermal expansion of the laminate. Why the FBG senses the laminate thermal expansion from this point onwards is related to the ability of the matrix to transfer strains.
In pure APA-6 the strain onset started after reaching the peak temperature, see Figures 8.15 and 8.16, which is different from the thick composite. Also, the temperature at which point X is observed lies around 160-170°C, which is lower than the 'gel point' found for the pure resin, which was related to crystallisation. If it is assumed that strain transfer to the optic fibre

is possible only when crystallisation occurs, then apparently crystallisation is enhanced (viz. the crystallisation temperature is lower) by the presence of the reinforcing fibres. Why this was not detected in the thin laminates can be attributed to the dominating thermal expansion effect of the fibres or tool plate. Similar to the thin laminates is that, as in Figure 10.16, a change in slope is visible close to *'T_g'* around 70°C, which is most clear for the 1546nm gratings.

Peak splitting of the FBG wavelength spectrum was observed for all laminates after cooling, but was least severe for the grating in the centre plies and most severe for the 1546nm grating closest to the bottom plate, see Figure 11.13. Apparently, the interaction with the aluminium mould plate caused a very inhomogeneous strain state around the gratings. The most extensive peak splitting was generally observed around 60-70°C, which is close to the glass transition temperature. Some of the split peaks corresponded to the Bragg peak before embedding in the dry fabric, which implies that a void partially surrounded the grating, leaving that grating area in a strain-free state.

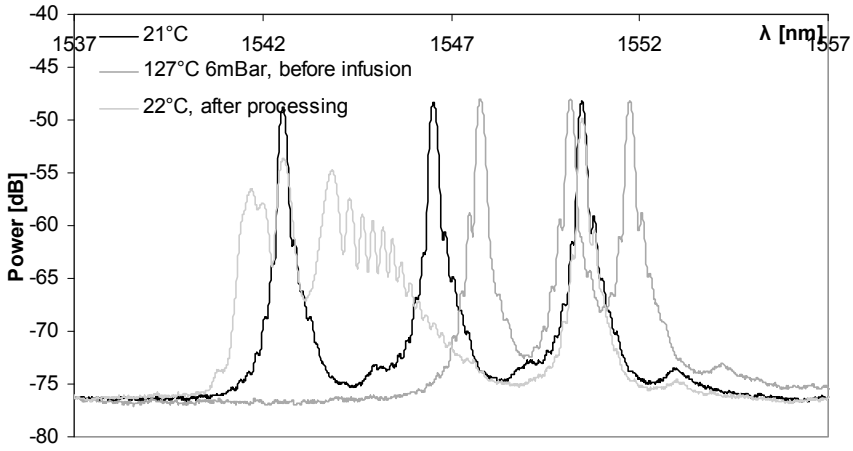

Figure 11.13: FBG spectrum for optic fibre in between plies 1 and 2.

What is remarkable in Figures 11.12 and 11.8, is that the strain development of the two gratings within each optic fibre seem to be mirrored. This is visible more clearly in the following figure, where the strain contributions of the thermal contraction between point *C* and room temperature are displayed. It may be that the gratings within one optic fibre influence each other, in the way that if one experiences a higher compressive strain, the other experiences a strain in the other direction.

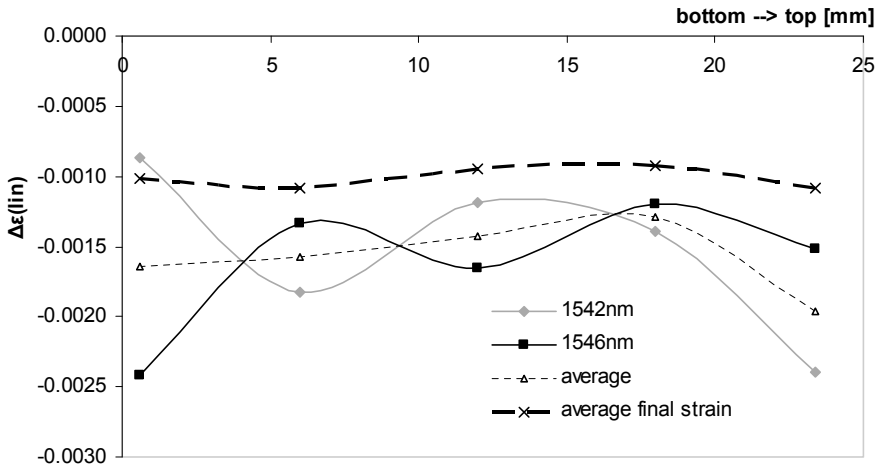

Figure 11.14: Thermal contraction contributions to final residual strains.

The thermal contraction comprises only half to 2/3rd of the processing strains in Figure 11.8. During heating to the polymerisation temperature, the visco-elastic relaxation of deformations caused by vacuum application apparently provides another significant contribution.
If the thermal contraction strain values of the two gratings per location are averaged, the dotted line is the result, which indicates a minimum strain at 3/4th depth of the laminate and a maximum compressive strain at the top plies. However, if the total residual strain values (consisting of vacuum application, thermal cycling of the dry fibres, thermal expansion, visco-elastic relaxation and thermal contraction) from Figure 11.8 are averaged, a fairly horizontal line is obtained, which indicates that no significant strain gradient is present in the thick laminate after manufacturing. This can be explained by the high dwell temperature at which the strains can still be relaxed, which is aided by the presence of voids. The final residual strain values are comparable the those of the thin laminates, which implies that scaling up from thin to thick GF/APA-6 laminates does not result in a significant difference in residual strains after manufacturing.

During thermal cycling of the thick laminate no additional residual strains were formed, similar to the pure APA-6 and thin laminate, as is illustrated in Figure 11.15. Peak splitting was observed to disappear around 60-100°C and reappear upon cooling at 137-90°C, but was again most severe in the glass transition area at ~50-70°C.

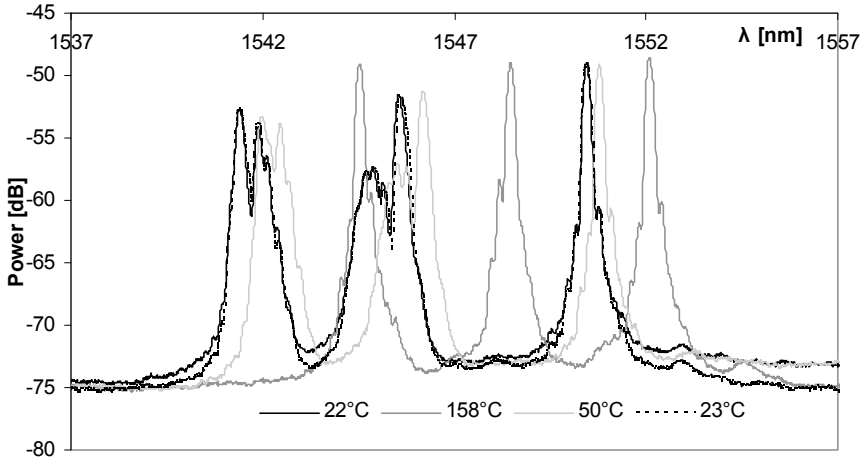

Figure 11.15: FBG Spectra during thermal cycling of thick laminate, layers 30-31.

11.4 MicroVickers hardness testing of a thick GF/APA-6 laminate

11.4.1 Experimental procedure

A 24 mm thick laminate was infused at 110°C and then heated to 180°C with the infrared heating panels as described in Section 11.3.1. The temperature profile of this laminate is shown in Figure 11.5. A section was cut from the centre of the thick laminate, not embedded, but grinded and polished, similar as in Section 7.3.3, where also the microVickers hardness test set-up was described. At least ten indentations were made in every 10th layer starting at the top surface. The averages and standard deviations of the measurements are calculated. No DSC results are available for this thick laminate.

11.4.2 Results and discussion

In Figure 11.16 the average microVickers hardness results are shown through the thickness.

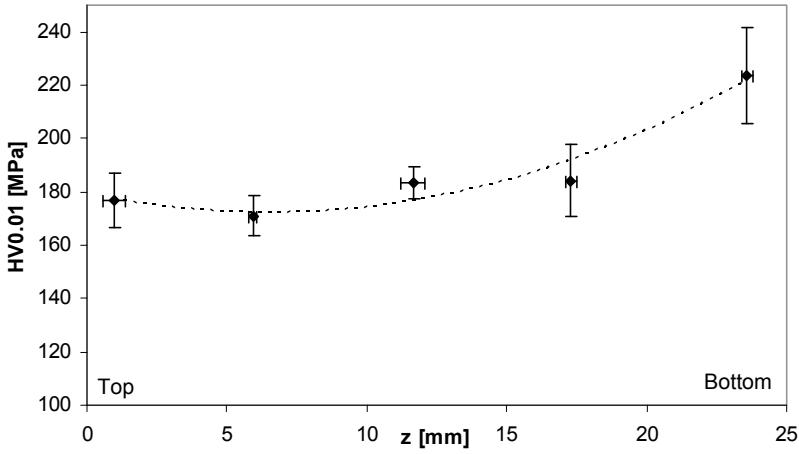

Figure 11.16: MicroVickers hardness through the thickness of a thick GF/APA-6 laminate.

It can be seen in Figure 11.16 that apart from the bottom layers, the microVickers hardness is relatively homogeneous through the thickness. This constancy can be attributed to the relatively constant temperature during the dwell period enabling further (secondary) crystallisation. Using Eq. (10-3) from the previous Chapter, the hardness values correspond to degrees of crystallinity ranging from 49 – 48 – 50 – 50 - 58% from top to bottom, which shows that only a significant difference in crystallinity exists close to the aluminium mould plate. This may be caused by the aluminium plate acting as a heat sink, keeping the polymerisation temperature lower resulting in a higher degree of crystallinity. The variation for this point is also rather large, which correlates to the extreme peak splitting observed for the gratings close to the mould plate in the previous Section, indicating that a large heterogeneity in material structure is present. For the non-isothermally produces laminates in Section 11.2 also no significant variation in crystallinity or hardness was observed [1]. It must be noted that the hardness values in Figure 11.16 and calculated crystallinity values thereof are very high compared to those in Section 10.5.2 and the variance is also larger, which can be related to a different operator, see Section 7.3.3.

11.5 Concluding remarks

Successful manufacturing of thick GF/APA-6 laminates with homogeneous properties through the thickness and in flow direction was achieved with isothermal infusion followed by rapid heating to the polymerisation temperature with infrared heating panels. Flow permeability of the reinforcing fabric proved very important for full infusion of a thick laminate: Up to 50 mm thick laminates were successfully infused with a 12k tow plain weave fabric,

while 3k tow 8HS weave fabric proved unsuitable for infusion of thick laminates. The main disadvantage of the 12k tow fabric is that large resin pockets between the fibre tows exist, which result in many polymerisation shrinkage voids.

The self-regulating temperature mechanism of the APA-6 matrix, based on crystallisation and crystal melting, proved successful in controlling the peak temperature in the laminate centre plies, even in a 50 mm thick laminate. An acceptable exothermal temperature rise of ~10°C was observed for all thick laminates. However, even though the peak temperature profile indicates inside-out polymerisation, the fibre Bragg strain gratings showed outside-in polymerisation due to the longer heating time (> 5 min) of the centre plies compared to the surface plies. Except for the surface plies adjacent to the tool plate, this did not seem to result in significant variations in residual strain nor in matrix properties through the thickness as detected with FBGs and microVickers hardness testing, resp.

In a thick laminate, the FBGs' response seems to be more dominated by visco-elastic relaxation of the reinforcing glass fabric and the matrix behaviour compared to thin laminates. It even seems possible to detect the onset of strain transfer of the polymer matrix for the gratings not located close to the laminate surface. The residual strain values found for the thick laminate are similar to those of 2 mm laminates and annealing was not found to affect the residual strains. Hence it can be concluded that scaling up of GF/APA-6 composites in the thickness direction does not yield major difficulties, nor causes major differences in processing behaviour, strain development and material properties.

References

1. Baten, E.M., Microstructural Variations in Thick-Walled Anionic Polyamide-6 Composites. 2006. MSc thesis Aerospace Engineering, Delft University of Technology, Delft. 80 pages.
2. Gillis, J.H.A.M., Heating methods for the production of thick APA-6/ glass laminates. 2007. MSc thesis Aerospace Engineering, Delft University of Technology, Delft. 74 pages.
3. van Rijswijk, K., Thermoplastic Composite Wind Turbine Blades. 2007. PhD thesis Aerospace Engineering, Delft University of Technology, Delft. 249 pages.
4. www.gurit.com. Prime 20LV technical datasheet. 2008 [cited 2 December 2008]; V4.

Chapter 12: Conclusions and Recommendations

12.1 Introduction

The goal of this thesis was to develop experimental techniques that enable the study of residual strain formation in novel thick thermoplastic composite structures manufactured with resin infusion of a reactive polymer. This chapter presents the outcomes of the efforts to reach that goal.

Conclusions based on a literature survey on residual strain formation in this type of composites are discussed in Section 12.2, with special focus on polymer matrix properties. Section 12.3 summarises the results of investigations into suitable experimental techniques, including recommendations for use with new polymer matrices, such as anionic polyamide-6 (APA-6). Conclusions regarding residual strain formation in this thermoplastic and its composites will be described in Section 12.4, together with recommendations for further research on thick composites with an APA-6 matrix.

12.2 Process-induced residual strains in thick thermoplastic composites

A review of the published literature showed that the most important parameter for residual strain formation during processing of continuous fibre reinforced composites is shrinkage of the polymer matrix from the point where the polymer has sufficient stiffness for strain transfer. In composites manufactured with a reactive polymer matrix, this consists of polymerisation (cure) shrinkage from the gel-point and thermal contraction during cooling from the cure temperature. The polymer thermal contraction depends on properties such as the degree of cure or/ and crystallinity, which in turn is dependent on the thermal behaviour during processing. Therefore, temperature variations in thick laminates proved to be the prime factor for residual strain variations through the thickness. Another contribution is provided by the tool-part interaction (mismatch in thermal contraction between the tool and the composite).

12.3 Experimental techniques

12.3.1 Fibre Bragg gratings in a curing polymer

It was shown that one test set-up, namely an optic fibre with a separate temperature and strain grating positioned in a curing resin, can be used to determine a multitude of polymer properties that could otherwise only be tested with several techniques, such as Differential

Scanning Calorimetry (DSC), Dynamic Mechanical Analysis (DMA) and Thermal Mechanical Analysis (TMA). Besides the thermal behaviour, the curing polymer properties that could be established are the gel point, the vitrification point and contributions of curing shrinkage and thermal contraction to residual strain formation. The point that could not be established with certainty was the glass transition temperature.

Recommendations

It was observed that optimal strain transfer from the shrinking polymer to the grating in the optic fibre core is very important and this can be achieved by removing the optic fibre coating around the gratings. However, this renders the optic fibre even more fragile, and chemical groups at the optic fibre surface can deactivate the APA-6 initiator, reducing the conversion and fibre-matrix adhesion [1, 2]. These effects on the polymerisation behaviour are unwanted, and therefore it is recommended to establish optimal strain transfer between the optic fibre core and the polymer with an optic fibre coating that provides chemical bonding between the two, and does not influence the shrinkage behaviour of the polymer significantly. Ideally, this would be the same coating as used for the reinforcing fibres in the reinforced polymers.

Two different grating lengths were investigated, but it is difficult to recommend a certain length. The 8 mm long gratings for example, showed a much stronger response to strain variations in the sense that the absolute wavelength shifts are much higher than for the 4 mm gratings. Where this difference comes from, is not yet understood. After manufacturing however, the 8 mm gratings showed more severe peak splitting compared to the 4 mm gratings, making it difficult -if not impossible- to determine a residual strain value. Therefore, a trade-off must be made based on sensitivity and data reliability.

Polarisation filters are available on the market that could separate the peaks originating from strain variations in the parallel (0°) or perpendicular (90°C) direction and aid in assessing the origins of the split peaks. This can be useful for future tests to identify the exact strain field around the grating.

12.3.2 Embedded FBGs in composites

Optic fibres with Bragg gratings were embedded in thick and thin composites during liquid resin infusion to identify residual strain development in a non-destructive manner. The FBGs were able to register the thermal behaviour and strains induced by non-elastic deformation of the glass fabric caused by pressure variations and passing of the flow front. The matrix gel point was difficult to identify, but the glass transition temperature could be established. The FBG sensors can be used to identify the thermal expansion and contraction of the laminate both before and after impregnation and curing of the matrix, including a tool effect.

A great variation in FBG response was observed during processing, which can be related to fabric deformation behaviour and positioning of the optic fibre. The FBGs showed significant peak splitting caused by the presence of local non-homogenous strain fields around the optic fibre, which may be related to microbending, the presence of voids, and variations in matrix fraction. This makes it difficult to quantify residual strains in composites. Also in composites, the 8 mm gratings showed severe peak splitting to such an extent that strain values could not be determined properly.

Recommendations for further investigations with FBGs

Based on the results, more research is clearly needed to establish fundamental knowledge regarding the FBG response in relation with processing effects in composites. Apparently, the positioning of the optic fibre and the (local) deformation behaviour of the fabric during pressurisation have great influence on the FBG results. Further research will be carried out at Delft UT by Balvers *et al* [3, 4] on the FBG's strain response due to flow and pressure variations. As a start, unidirectional composites could be studied with optic fibres, to exclude the microbending, nesting and tow spreading effects in fabric reinforced laminates.

To investigate the microbending effect and the strain within the woven fibre tows in one fabric layer, the optic fibre can be co-woven into a fibre tow. This can be achieved by replacing a co-woven nylon fibre or tow, which is slightly larger in diameter than the optic fibre, with an optic fibre that is glued to the nylon fibre end. The nylon fibre or tow is then pulled though the fabric until the optic fibre is woven into the fabric [5]. It might also be of interest to study the spectrum of a very long grating as used by Eum *et al* [6], to assess the local strain field variations in an entire roving in the laminate.

The encapsulated FBG shows a linear relation with temperature until 200°C, which means that after proper calibration it can be used as temperature sensor, instead of thermocouples. However, due to its size it is still intrusive, and the metallic sleeve renders it unsuitable for new heating techniques such as microwave and induction heating. In addition, fast heating rates can compromise the accuracy. Therefore, it is recommended to search for another solution when other heating methods for curing of composites are investigated.

The glue for sealing the optic fibre inside the ferrule is also not resistant to caprolactam, the monomer for APA-6. Therefore, it is recommended to look for another high-temperature and chemically resistant glue that can be cured at low temperatures.

12.3.3 Polymerisation shrinkage behaviour: Volumetric dilatometry

A volumetric dilatometry test based on the buoyancy principle was found suitable to determine the volumetric polymerisation shrinkage during the entire processing cycle. This information is useful for determination of the resin amount necessary for the right fibre

volume fraction and to validate the FBG results. The technique using a silicone bag was further developed for study of thermosetting polyurethane (turane) and anionic polyamide-6 (APA-6) polymers.
The volumetric shrinkage behaviour could be established from the polymerisation start onwards and was compared with the thermal behaviour. For room temperature curing polymers such as the turane, reproducible shrinkage values were obtained, but at the higher polymerisation temperatures needed for APA-6, the silicone bag introduced significant sources of error due to oil absorption, which could not be adequately compensated for. No thermal transitions, such as the gel point, could be identified. The calculation of the shrinkage is based on many assumptions and measurements of other test parameters, which can introduce significant sources for error. Therefore, this method is only recommended as a tool to obtain estimates for the total shrinkage of polymers and not for use in a quantitative analysis. In addition, trends related to temperature effects can be assessed.
Compared to the fibre Bragg gratings, this test method showed a higher response due to polymer thermal expansion and contraction and the thermal behaviour was different due to dissimilar heat transfer properties of the test set-up. Dilatometry seems more suitable for detection of the polymer density variations, whereas the FBG results are clearly related to the stiffness properties and hence strain transfer capabilities of the polymer.

Recommendations
To prevent the error due to oil absorption, it is recommended to use an elastomer that is impermeable to the heating fluid and is resistant to caprolactam. In addition, it must possess sufficient elasticity to accurately follow the contours of the shrinking polymer mixture. The thermal expansion behaviour of the (empty) silicone bag during the entire thermal cycle must be recorded to provide values for m_{bal}^{bag} in Eq. (C-5) which is aided by the use of standardised bag dimensions and monitoring of the bag temperature with a thermocouple. At the time of this research, such bags were unfortunately not available.

12.3.4 Thermal cycling: FBGs and linear dilatometry
Strain relaxation behaviour caused by a thermal treatment was investigated with embedded fibre Bragg gratings and compared to results obtained with linear dilatometry (TMA) and DSC. For the turane polymer, the FBGs registered significant strain relaxation due to postcuring which started in the same temperature range as found with DSC. In addition, the strain-free point was found and coefficients of thermal expansion compared well with those obtained by the linear dilatometry tests, and therefore it is assumed that the FBG technology provides reliable results. Identification of glass transition temperatures (T_g) was difficult in the unfilled polymers, whereas in the composites this transition was visible as a change in

temperature-strain slope due to a more dominating effect of the matrix on the strain behaviour below the T_g. In addition, the peak splitting that was introduced by inhomogeneous strain fields around the grating during processing, disappeared above the assumed T_g.
In the absence of strain relaxation, the strain curve during thermal cycling was observed to repeatedly retrace the processing strain curve, which implies that the FBGs provide stable results.

12.3.5 Matrix property variations: MicroVickers hardness

The microVickers indentation technique was presented as a tool to study variations in polymer matrix hardness through the thickness, which can be related to properties such as crystallinity and degree of cure. This was achieved in woven fabric reinforced laminates, because resin pockets between the fibre tows provide sufficient room for indentations using the smallest available load of 10 gram.
Hardness variations were successfully studied in composites with three different polymer matrices: a melt-processed semi-crystalline polyphenylenesulfide (PPS), a resin infused thermosetting polyurethane (turane) and a resin infused semi-crystalline anionic polyamide-6 (APA-6). A relation was found between microVickers hardness and degree of crystallinity in the semi-crystalline composites. The experimental method to determine the crystallinity of the composite as proposed in this paper, based on Differential Scanning Calorimetry and Thermal Gravimetric Analysis, proved unable to distinguish between crystallinity variations below 5%, which was around the variation through the thickness as observed in thick melt processed CF/PPS laminates. One procedure established for the microVickers hardness test on the other hand, showed a significant variation through the thickness for the same specimen and is therefore considered more reliable to identify variations in matrix properties through the thickness. The microVickers hardness test was capable to identify a tool effect on the composites' matrix properties, and a variation in microstructure homogeneity. Therefore, it is concluded that this is a useful technique to quickly assess variations in polymer matrix properties caused by thermal variations during processing.

Recommendations

The microVickers hardness test cannot be used as a tool to quantify polymer matrix properties, because of the subjectivity of the hardness test operator. The diagonals of the indented area are determined manually, and it turned out that this results in different hardness values for the same specimen as measured by different persons. In metals this is not a problem, because the light reflection is such that usually a clear micrograph of the indentation is obtained and a pattern recognition software is capable of automatic determination of the diagonals. This prevents the error introduced by manual control. The

light reflectivity of polymers is much less, especially of transparent thermoset and amorphous thermoplastic polymers, rendering the automatic determination of the indented area impossible. It is likely that improved optics and pattern recognition software will be available in the future for hardness testing of polymers, making that this problem will soon belong to the past. It is therefore recommended to manufacturers of hardness testing equipment, to make it suitable for automatic determination of the microVickers hardness of polymers.

12.4 Anionic Polyamide-6 and its composites

12.4.1 Pure anionic polyamide-6 (APA-6)

Both the FBG and volumetric dilatometry tests showed significant shrinkage for APA-6 polymerised at temperatures between 160°C and 180°C. For example, back at room temperature the shrinkage estimations are in the order of -2 to -3% linear strain and 15-20 % volumetric shrinkage, with higher processing temperatures resulting in higher values in both tests. This was related to the proportionally higher thermal contraction upon cooling from the processing temperature to room temperature, which can be attributed to the postponed effect of crystallisation.

The volumetric dilatometry test showed that polymerisation shrinkage as well as the development of a polymerisation exotherm already started during heating from the infusion temperature (110°C) to the polymerisation temperature. For lower polymerisation temperatures (160°C), the largest shrinkage contribution is provided by the polymerisation and crystallisation before the exothermal peak temperature is reached. The thermal contraction during cooling was relatively small due to high degrees of crystallinity and conversion. For polymerisation temperatures of 175°C and higher, a large variety of dilatometry curves was observed, which was related to the competing kinetics of polymerisation, branching, and (secondary) crystallisation.

The onset of strain transfer was detected by FBGs during cooling from the exothermal peak temperature at the (melt) crystallisation temperature of 185 ± 3°C, which was attributed to crystal nucleation at the optic fibre surface. Further investigations of the optic fibre – APA-6 interface showed poor fibre-matrix adhesion, which can be related to the Ormocer® coating, although the fibre did seem to introduce a transcrystalline zone, which in general increases the adhesion. In addition, many shrinkage voids around the optic fibre were observed in the centre of a specimen cured at 175°C, which indicates outside-in polymerisation. The voids can also be caused by residual caprolactam in the centre of the specimens, which explains the lower degree of conversion and resulting relatively high coefficient of thermal expansion, as determined with DSC and linear dilatometry and FBGs, resp. During thermal cycling, no strain-free temperature, strain relaxation or thermal transitions could be identified with the

FBGs, even though the linear dilatometry test showed recrystallisation behaviour of the 180°C polymerised specimen.
For pure APA-6 no significant relation was found between the processing temperature and the degree of crystallinity and melting peak temperature, which was reflected by a relatively constant microVickers hardness. It seemed that only the heterogeneity, as observed by a large variation in hardness and crystallinity values, increased with increasing processing temperature.

A polymerisation temperature of 160°C is recommended for polymerisation of unfilled APA-6, because the least shrinkage was observed for this polymerisation temperature. In addition, it seems that most of the shrinkage occurs in the still-liquid state, such that replenishment and strain relaxation can still occur. Polymerisation starts very quickly during the heating stage and the smaller the temperature difference between infusion and polymerisation, the more homogeneously polymerisation will occur throughout the specimen. However, still outside-in polymerisation is observed for this temperature, which enables void formation.

12.4.2 Glass fibre reinforced APA-6 composites

Laminates with thicknesses ranging from 2 mm to 50 mm have been successfully manufactured with a highly permeable coarse fabric to ensure fast and full infusion of thick laminates, see Figure 12.1. The main disadvantage of the 12k tow fabric is that large resin pockets exist between the fibre tows, which result in polymerisation shrinkage voids that are detrimental for the mechanical properties. The most homogeneous temperature distribution and properties within a GF/APA-6 composite laminate were achieved by isothermal infusion of the preform at 110 – 130°C and subsequent fast heating to the polymerisation temperature of 180°C with infrared heating panels.
The self-regulating temperature mechanism of the APA-6 matrix, based on crystallisation and crystal melting, in combination with the heat absorbance of the glass fibres, proved successful in controlling the peak temperature in the centre of thick laminates. An acceptable exothermal temperature rise of ~10°C was observed for all laminates.
The glass transition was recognized around ~70°C during cooling from the processing temperature. Annealing for 1 hour at 160°C was not found to result in significant strain variations in the thin nor thick GF/APA-6 laminates.
A clear relation was found between microVickers hardness and the processing temperature for glass fibre reinforced APA-6 laminates, which was related to the crystallinity: with higher processing temperatures the degree of crystallinity and peak melting temperature decrease, similar to the microVickers hardness.

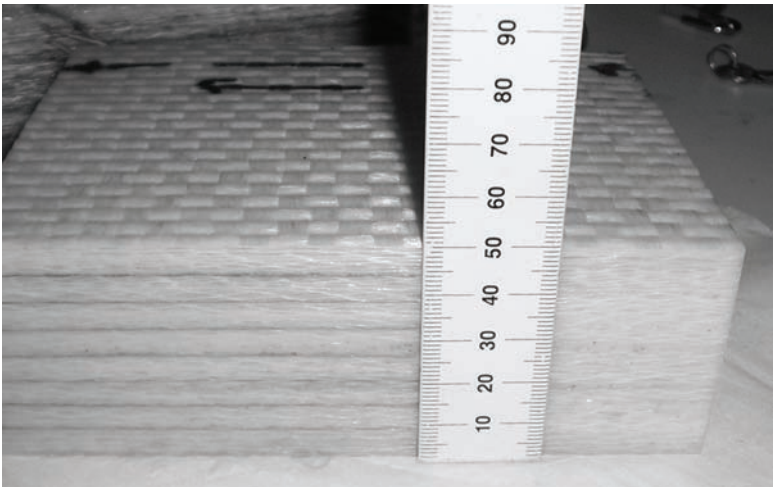

Figure 12.1: 50 mm thick GF/APA-6 laminate.

In a thick laminate, the FBGs' responses seem to be more dominated by visco-elastic relaxation of the reinforcing glass fabric and the matrix behaviour than in thin laminates, where the fabric deformations provided the largest strain contribution during the processing cycle. While in thin laminates it was difficult to identify the gel point due to polymerisation /crystallisation, in the thick laminate this onset of polymer matrix strain transfer could be established for the gratings not located close to the laminate surface. Only a small influence of polymerisation and crystallisation was observed on the final residual strains, similar as for the composite-tool interaction.
Even though the peak temperature profile indicates inside-out polymerisation in the thick composites, the fibre Bragg strain gratings showed outside-in polymerisation due to the longer heating time (> 5 min) of the centre plies compared to the surface plies. Except for the surface plies adjacent to the tool plate, this did not seem to result in significant variations in residual strain nor in matrix properties through the thickness as detected with FBGs and microVickers hardness testing, resp. This can be explained by the high dwell temperature at which the strains can still be relaxed, which is aided by the presence of voids.
The residual strain values found for the thick laminate are similar to those of 2 mm laminates. Hence it can be concluded that scaling up of GF/APA-6 composites in the thickness direction does not yield major difficulties, nor causes major differences in processing behaviour, strain development and material properties.

12.4.3 Recommendations for further research on thick APA-6 composites

The aim for every thick composite product is to have homogeneous properties through the thickness, including known homogeneous residual strain distributions, without the defects

generated by the composite to relieve the residual stresses, such as fibre waviness, transverse cracking, deformations and voids. For APA-6 composites this aim is not yet reached and further development is necessary.
The results showed that the polymerisation starts too early: before a homogeneous temperature distribution is reached inside the APA-6 specimen or composite, the surface already starts to polymerise, which results in outside-in polymerisation with the entrapment of voids as a result. Two ways can be pursued to obtain inside-out polymerisation: the polymerisation rate and initiation time can be lowered by changing the initiator and activator, such that the complete composite structure has reached the polymerisation temperature before polymerisation starts. The heat accumulation in the centre plies can increase the reaction rate there locally, and with the appropriate polymerisation and crystallisation kinetics, inside-out polymerisation and crystallisation can be achieved.
The other way is to realise an inside-out heating profile. This can be accomplished with induction heating of additives or reinforcing fibres (metal or carbon) or by resistive heating of a metal mesh embedded in the composite. Preliminary investigations by Gillis [7] showed that metal meshes between every 10 plies can result in a relatively homogeneous temperature distribution. Another possibility is microwave heating, because the caprolactam monomer is very responsive to microwaves. Microwave curing of epoxy was shown to be faster and resulting in a higher degree of cure than regular thermal curing, depending on the reinforcing fibre type [8].

The high matrix shrinkage of APA-6 during polymerisation and crystallisation is the main source for development of voids in the resin pockets that are intrinsically present in coarse fabrics, such as the 12k tow plain weave used in this thesis. This is one of the reasons why test methods for determination of curing shrinkage are required: when the amount of shrinkage before the matrix flow stops is known, it is possible to establish the amount of resin necessary to produce a laminate without voids and with the desired fibre volume fraction. The established amount of resin can be delivered to the preform with, for example, additional resin and pressure [9]. Additional pressure can be achieved with the Quickstep® or flexible injection technology [10].
Modification of resin systems, such as the rubber-modified Nyrim®, or by the addition of inorganic fillers such as nano-particles, can reduce the shrinkage. This will also lower the thermal contraction mismatch between the tooling and the composite, which can pose great challenges for large composite structures, such as windmill blades [11]. Another advantage is a possible improvement in mechanical performance. However, resin modification usually results in several disadvantages for processing, such as a significant viscosity increase,

filtering of particulate fillers by the reinforcing fibres, or deterioration of the fibre-matrix adhesion [12].

Other forms of fabric/ reinforcement can also be investigated to obtain the desired fibre volume content, where it is important that a suitable fibre sizing is used [2]. For example, in the wind-mill and aerospace industry many non-crimp fabrics are applied.

References

1. Choudhury, P.K., Yoshino, T., On the pH response of fiber optic evanescent field absorption sensor having a U-shaped probe: An experimental analysis. Optik - International Journal for Light and Electron Optics, 114(1): 13-18, 2003.
2. van Rijswijk, K., Thermoplastic Composite Wind Turbine Blades. 2007. PhD thesis Aerospace Engineering, Delft University of Technology, Delft. 249 pages.
3. Balvers, J.M., Monitoring the RTM process with FBGs - Progress report. 2008, Delft University of Technology: Delft. p. 61.
4. Balvers, J.M., Bersee, H.E.N., Beukers, A. Integration of fiber bragg gratings in woven fabrics: influences of preform compaction and flow-front propagation. in FPCM-9, Montréal, Québec, 2008.
5. Jung, K., Kang, T.J., Cure monitoring and internal strain measurement of 3-D hybrid braided composites using fiber Bragg grating sensor. Journal of Composite Materials, 41(12): 1499-1519, 2007.
6. Eum, S., Kageyama, K., Murayama, H., Uzawa, K., Ohsawa, I., Kanai, M.Igawa, H. Resin Flow Front Monitoring for VARTM using Fibre Bragg Gratings. in ICCM-16, Kyoto, Japan, 2007.
7. Gillis, J.H.A.M., Heating methods for the production of thick APA-6/ glass laminates. 2007. MSc thesis Aerospace Engineering, Delft University of Technology, Delft. 74 pages.
8. Scriggia, N., Hawley, M.C., Thermal, morphological, and electrical characterization of microwave processed natural fiber composites. Composites Science & Technology, 67(9): 1986-1991, 2007.
9. Garstka, T., Ersoy, N., Potter, K.D., Wisnom, M.R., In situ measurements of through-the-thickness strains during processing of AS4/8552 composite. Composites Part a-Applied Science and Manufacturing, 38(12): 2517-2526, 2007.
10. Causse, P., Ruiz, E., Trochu, F. Consolidation of Curved Composite Parts Manufactured by Flexible Injection. in 9th International Conference on Flow Processes in Composite Materials (FPCM-9), Montréal, Canada, 2008.
11. Gardiner, G., Wind Blade Manufacturing, Part II: Are thermoplastic composites the future?, in High Performance Composites. 2008.
12. Vlasveld, D.P.N., Parlevliet, P.P., Bersee, H.E.N., Picken, S.J., Fibre-matrix adhesion in glass-fibre reinforced polyamide-6 silicate nanocomposites. Composites Part A: Applied Science and Manufacturing, 36(1): 1-11, 2005.

Appendix A: Derivation of Volumetric Shrinkage from Linear Shrinkage

A.1 Isotropic shrinkage of a cylinder

Assume a cylinder consisting of isotropic material with starting length l_0 and radius r_0. Due to polymerisation or thermal contraction these dimensions will change to length l_e and radius r_e in an isotropic fashion. δ_l is the linear shrinkage fraction and υ is the volumetric shrinkage fraction according to:

$$\delta_l = \frac{l_e - l_0}{l_0} = \frac{r_e - r_0}{r_0} \qquad \text{(A-1)}, \qquad \upsilon = \frac{V_e - V_0}{V_0} \qquad \text{(A-2)}$$

Rewriting Eq. (A-1) gives:

$$l_e = l_0(\delta_l + 1) \qquad \text{(A-3)} \quad \text{and} \qquad r_e = r_0(\delta_l + 1) \qquad \text{(A-4)}$$

Furthermore,

$$V_0 = \pi \cdot r_0^2 l_0 \qquad \text{(A-5)} \quad \text{and}$$

$$V_e = \pi \cdot r_e^2 l_e = \pi \cdot r_0^2 (\delta_l + 1)^2 \cdot l_0(\delta_l + 1) = \pi \cdot r_0^2 l_0 (\delta_l + 1)^3 \qquad \text{(A-6)}$$

Eq. (A-6) is the result when replacing r_0 and l_0 in Eq. (A-5) with Eqs. (A-3) and (A-4). Using Eqs. (A-5) and (A-6) in Eq. (A-2), this gives:

$$\upsilon = \frac{\pi \cdot r_0^2 l_0 (\delta_l + 1)^3 - \pi \cdot r_0^2 l_0}{\pi \cdot r_0^2 l_0} = (\delta_l + 1)^3 - 1 \qquad \text{(A-7)}$$

A.2 Isotropic shrinkage of a cube

Assume a cube consisting of isotropic material with starting side lengths l_0. Due to polymerisation or thermal contraction these lengths will change to length l_e in an isotropic fashion. Again, δ_l is the linear shrinkage fraction and υ is the volumetric shrinkage fraction, which following Eqs. (A-1) and (A-2) and combined with Eq. (A-3) result in:

$$V_0 = l_0^3 \qquad \text{(A-8)}, \qquad V_e = l_e^3 = l_0^3(\delta_l + 1)^3 \qquad \text{(A-9)}$$

and:

$$\upsilon = \frac{l_0^3(\delta_l + 1)^3 - l_0^3}{l_0^3} = (\delta_l + 1)^3 - 1 \qquad \text{(A-10)}$$

A.3 Anisotropic shrinkage of a cube or beam

Assume a cube or beam consisting of anisotropic material with starting side lengths a_0, b_0 and c_0 and volume V_0. Due to polymerisation or thermal contraction these lengths will anisotropically change to lengths a_e, b_e, c_e with fractions δ_a, δ_b, δ_c, resulting in an end volume V_e. Besides Eq. (A-2), the following equations apply:

$$V_0 = a_0 \cdot b_0 \cdot c_0 \qquad \text{(A-11)}, \qquad V_e = a_e \cdot b_e \cdot c_e \qquad \text{(A-12)}$$

$$\delta_a = \frac{a_e - a_0}{a_0}, \qquad \delta_b = \frac{b_e - b_0}{b_0}, \qquad \delta_c = \frac{c_e - c_0}{c_0} \qquad \text{(A-13)}$$

Rewriting gives:

$$a_e = a_0(\delta_a + 1), \qquad b_e = b_0(\delta_b + 1), \qquad c_e = c_0(\delta_c + 1) \qquad \text{(A-14)}$$

Combining with Eq. (A-2) this gives:

$$\upsilon = \frac{a_0 b_0 c_0 \cdot (\delta_a + 1)(\delta_b + 1)(\delta_c + 1) - a_0 b_0 c_0}{a_0 b_0 c_0} = (\delta_a + 1)(\delta_b + 1)(\delta_c + 1) - 1 \qquad \text{(A-15)}$$

Appendix B: Preparation of FBG Temperature Sensors

B.1 Background

Preparation of strain-free sensors can be achieved by encapsulating one grating. The 40 mm long stainless steel capillary with inner and outer diameters 0.6 mm and 1.0 mm, resp. from Section 4.3.3 was selected from many available capillary materials, such as flexible fused silica coated with a polyimide layer and steel tubes with different diameters, for the following:

- Optic fibres inside the silica capillaries demonstrated stick-slip behaviour, possibly caused by static attraction or friction between the Ormocer® coating of the optic fibre and the inner side of the capillary. Moreover, these capillaries are very fragile and brittle.
- Due to the high thermal conductivity of the metal tubes, temperature variations are dissipated quickly compared to the thermally insulating silica. However, the trapped air inside the metal tube is still insulating and may present a source for thermal lag.
- Usually a polymer matrix (as studied in this research) adheres better to metal than to polyimide coated surfaces. Lack of bonding between the investigated polymer and the capillary may reduce heat as well as bulk strain transfer.
- During embedding of a capillary-surrounded fibre grating in fabric reinforced composites with high pressures (for example during hot platen press forming of the laminates, RTM or autoclaving), a flexible capillary will follow the irregular surface of the fabric, resulting in microbending or fracture of the capillary, due to which the grating is not strain-free. The selected metal capillaries possess sufficient stiffness or rigidity to prevent microbending. None of the available silica tubes (various diameters) were resistant to the pressures exerted by the hot platen press; they fractured without exception.

B.2 Preparation

The steel capillaries were cut and the extremities were grinded to remove burrs and sharp edges that could harm the optic fibres. The capillaries were cleaned by immersion in ethanol and drying them thoroughly for a few hours to the air. One side of all capillaries was sealed with adhesive (Epotek® 353ND, from Gentec, Belgium) by dipping while capillary forces forced the adhesive inside the capillary. The capillary was suspended vertically with the adhesive at the lower extremity, which was cured at 80°C for 60 minutes[1] in a convection oven.

[1] Higher temperatures are possible to speed up the curing process of the glue, however, the wires and connectors can only withstand a prolonged temperature of maximum 80°C.

The gratings within the optic fibre were located by means of a heated metal wire, when the optic fibre was connected to a FBGScan 616 (FOS&S, Belgium). The fibre was cut (cleaved) at 10-15 mm distance from the grating such that a proper reflected peak was achieved by the clean cut at the fibre end. At ~10 mm from the other end of the grating, a tiny polyimide tape was placed around the optic fibre to identify the location where the capillary should be attached to the optic fibre to ensure a strain-free grating. This way, the optic fibre is approximately centred and the tape also prevents the fibre from direct contact with the (sharp) edge of the capillary.

After cleaning with ethanol, the optic fibre ends with gratings were carefully placed inside the capillary. The capillaries were taped vertically into place on a home-made jig with the optic fibres also suspended vertically. Glue was applied with a needle to seal the transition between the capillary and the optic fibre and this was again left to cure inside an oven at 80°C for 60 minutes. The other bare gratings in the optic fibre below were taped to the jig to prevent glue from dripping onto the strain gratings.

Following cure of the adhesive, the capillary seals were visually inspected for porosities and checked for liquid tightness by suspending them into baths of cold and hot water. The strain gratings showed a sudden increase due to the temperature difference, and then a gradual increase in wavelength due to the absorption of moisture of the Ormocer® fibre coating (see Figure B.1). The gratings that were encapsulated by the capillaries showed a somewhat more gradual change in temperature, but no wavelength change due to the moisture absorption, since water ingress was prevented.

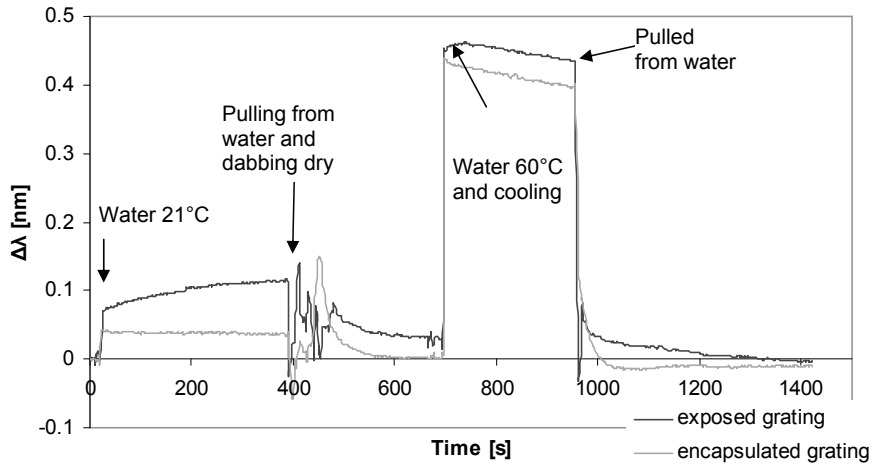

Figure B.1: Wavelength response to immersion in cold and hot water.

In the case that the adhesive accidentally touched the grating, a clear difference in Bragg wavelength before and after curing could be observed.

B.3 Analysis of error sources

The wavelength shift value $\Delta\lambda_B$ is dependent on the Bragg wavelength λ_B, as in Eq. (4-4). But in Equation (4-10) this is not the case. The variation in peak Bragg wavelengths λ_B can be in the order of 25-30 nm during the matrix shrinkage tests, and therefore for every measurement, $\Delta\lambda$ should actually be recalculated based on the Bragg wavelength for that particular measurement. The sum of all these steps can then be used to calculate the total strain. When the calculations are based on one initial reference Bragg wavelength, the maximum error in wavelength shift can be estimated:

> In Equation (4-10), the factor (1-P) equals 0.78 for the gratings used here and $(\alpha_n+\alpha_f)$ in Eq. (4-8) is usually 6.27 x 10^{-6} °C^{-1}. For a temperature difference ΔT of 100°C and a mechanical strain $\Delta\varepsilon$ of 0.01, and a Bragg wavelength of 1525 nm, the wavelength shift $\Delta\lambda_B$ is 12.88 nm. For a Bragg wavelength of 1565 nm, $\Delta\lambda_B$ is 13.22 nm, resulting in a difference of 340 pm.

This translates to a linear strain $\Delta\varepsilon$ variation of 0.03%, which can be neglected.

A much smaller difference in wavelength shift (~50 pm) can also be expected due to dis- and reconnection of the optic fibre to the interrogator due to polarisation effects of the light source and is therefore also neglected.

Appendix C: Derivation of Equations for Volumetric Dilatometry Test

The buoyancy force F_{bouy} acts against the force of gravity exerted on an object (F_g). When this force is equal or higher, the specimen will float. If the object has sufficient mass it will sink, or it can be suspended for example to a mass balance to register any variations in the object dimensions, which in turn have an effect on the buoyancy force. This can be shown with the following free-body diagram:

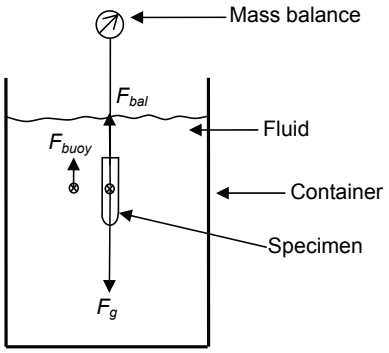

Figure C.1: Free-body diagram of forces acting on a suspended specimen in a fluid.

Since the specimen experiences no acceleration in this set-up, i.e. it does not move up or down, the sum of all forces acting on the specimen must be zero:

$$F_g - F_{bouy} - F_{bal} = 0 \qquad \text{(C-1)}$$

where F_{bal} is the force exerted on the mass balance.
Since the magnitude of the buoyancy force is equal to the weight of the displaced fluid, it is dependent on the volume of the submersed object and the density of the surrounding fluid:

$$F_{buoy} = \rho_{fl} V_{tot} g \qquad \text{(C-2)}$$

where ρ_{fl} is the density of the fluid, V_{tot} is the total volume of the submersed specimen and g is the gravitational constant, which on earth is 9.81 m/s^2.

With $F_g = m_s g$ (where m_s is the mass of the entire submersed specimen in air), the force as registered by the balance (output is given as mass, m_{tot}^{bal}) will be:

$$F_{bal} = m_s g - \rho_{fl} V_{tot} g = m_{tot}^{bal} g \tag{C-3}$$

With division by g, this results in: $$V_{tot} = \frac{m_s - m_{tot}^{bal}}{\rho_{fl}} \tag{C-4}$$

When using the test set-up as described in Section 5.2, the total volume of the submersed object V_{tot} consists of the volumes occupied by the silicone bag and plug, and the polymer.

$$V_{tot} = V_{bag} + V_{pol} = \frac{m_{bag} - m_{bag}^{bal}}{\rho_{fl}} + \frac{m_{pol} - m_{pol}^{bal}}{\rho_{fl}} \tag{C-5}$$

where the subscripts 'bag' and 'pol' designate the silicone bag and polymer system under investigation, respectively. In addition,

$$m_s = m_{bag} + m_{pol} \quad \text{and} \quad m_{tot}^{bal} = m_{bag}^{bal} + m_{pol}^{bal} \tag{C-6}$$

The volumetric shrinkage $\Delta\varepsilon_{vol}$ of the curing polymer is given by:

$$\Delta\varepsilon_{vol} = \frac{\Delta V_{pol}}{V_{pol}^0} = \frac{V_{pol}^1 - V_{pol}^0}{V_{pol}^0} \tag{C-7}$$

Using the contribution of the polymer in Eq. (C-5), this gives:

$$\Delta\varepsilon_{vol} = \frac{\frac{1}{\rho_{fl}^1}\left(m_{pol}^1 - m_{pol}^{bal,1}\right) - \frac{1}{\rho_{fl}^0}\left(m_{pol}^0 - m_{pol}^{bal,0}\right)}{\frac{1}{\rho_{fl}^0}\left(m_{pol}^0 - m_{pol}^{bal,0}\right)} \tag{C-8}$$

Superscripts *0* and *1* denote the parameters at the reference point of the test and at any given time *1*, resp. The mass of the polymer is assumed not to change during the test: $m_{pol}^1 = m_{pol}^0$, which can be easily determined in air with a mass balance after curing. The

output given by the balance that registers the submersed mass m_{tot}^{bal}, consists of the submersed bag mass and submersed polymer mass (Eq. C-6). The submersed bag mass can also be determined by using an empty bag. Therefore, $m_{pol}^{bal} = m_{tot}^{bal} - m_{bag}^{bal}$. Using this in Eq (C-8) gives:

$$\Delta\varepsilon_{vol} = \frac{\frac{1}{\rho_{fl}^{1}}\left(m_{pol}^{1} - m_{tot}^{bal,1} + m_{bag}^{bal,1}\right) - \frac{1}{\rho_{fl}^{0}}\left(m_{pol}^{0} - m_{tot}^{bal,0} + m_{bag}^{bal,0}\right)}{\frac{1}{\rho_{fl}^{0}}\left(m_{pol}^{0} - m_{tot}^{bal,0} + m_{bag}^{bal,0}\right)} \qquad \text{(C-9)}$$

In the case when the density of the fluid does not change, for example when the fluid temperature remains constant, $\rho_{fl}^{1} = \rho_{fl}^{0}$, this equation simplifies to:

$$\Delta\varepsilon_{vol} = \frac{m_{tot}^{bal,0} - m_{tot}^{bal,1} + m_{bag}^{bal,1} - m_{bag}^{bal,0}}{m_{pol}^{0} - m_{tot}^{bal,0} + m_{bag}^{bal,0}} \qquad \text{(C-10)}$$

In addition, when assuming that the submersed bag mass does not change either during the test, i.e. $m_{bag}^{bal,1} = m_{bag}^{bal,0}$, this equation further simplifies to:

$$\Delta\varepsilon_{vol} = \frac{m_{tot}^{bal,0} - m_{tot}^{bal,1}}{m_{pol}^{0} - m_{tot}^{bal,0} + m_{bag}^{bal,0}} \qquad \text{(C-11)}$$

Acknowledgements

As most people know, clichés do not really apply to me. So, no ‘last but not least’, but first and most importantly: THANK YOU, Tjitte, for standing by my side and giving me the support and listening ear when I needed them most! I’d love to remain your favourite nerd for many more decades to come.

The world of thermoplastic composites is small and everybody nowadays knows Harald Bersee, which was not yet the case when I first met him almost a decade ago. He easily convinced me to join the pioneering DPCS group for a PhD, even though it took us more than a year of friendly bickering to settle on the subject for this thesis. Harald, many thanks for all the support and discussions, you made me proud to be a former DPCS member. My dear promoter, Adriaan Beukers, many thanks for your support, discussions and friendly words when I needed them.

Luckily I was not the only PhD student around, and I am really grateful for the discussions, laughs, tears, sweat, holidays, conferences, and drinks (in random order) I shared with my former colleagues Kjelt, Darko, Julie, Simon, Tahira, Giovanni, Teun, Witchuda, Jordy, Valeria, Ton, Rogier and Ab. Thank you Kale, for welcoming me to ‘Cottonball Lab’ and transforming me into DeeDee. Also thanks for choosing a great successor, who together with the occasionally visiting Léontine changed the room into ‘girl power’. Special thanks goes to the DPCS staff for their assistance and availability for a chat and cheering remarks; Lisette, Otto and Sotiris. Thank you Frans for opening the gym and letting us blow off some steam and work some sweat instead of polymer fumes.

This book would not have been possible without the help of my beloved students. I’d like to thank Wouter van der Werf, David Brassard and Florian Sayer for their help with the microVickers testing (which was not at all tedious, right?), Cindy Lavallée for her rewarding never-ending stream of questions, Jing^2 for her lovely three-month burst of efficient goal-getting, Amos Yeo and Marian Gutierrez-Roca for their exploring work on microcracking and new thermoplastic composites, Eelco Baten and Jac Gilles for their thick-laminate pioneering work, Marcel van Elst and Jordy Balvers for introducing me to FEM and process simulations and of course Pieter Verburg for testing my coaching capabilities and the shrinkage tests development. These students as well as my colleagues certainly inspired me to one of my propositions…

A researcher understands quickly that (s)he is helpless without the aid of some good technicians. Sebastiaan Lindstedt and Marc van Dongen, I am grateful for your never-ceasing help and useful ideas. I completely understand the love-hate relationship between

you and the equipment, but you made me often happy with equipment that simply worked! Thank you Frans and Serge for your help and explanations on microscopy and NDE. I would also like to thank Michel, Ed, Herman & Kees for their never-ending assistance and bright fixture and tooling solutions, which also applies to Hans, Fred, Berthil, Dylan, Niels, and Bob. Thanks to Ed I gave my first-ever interview in DEMO Magazine! I also deeply appreciated the assistance on the microVickers and microscopy equipment lend by Eric Peekstok from Materials Science & Engineering. A special thanks goes to Ben Norder of the group Nano-Structured Materials at DelftChemTech, for the help with polymer analysis and introducing some good ol' jazz, such as of your namesake Ben Webster. We still have some of your delicious recipes on our menu! Thanks also to Stephen Picken, Gerard de Vos, Piet and Eduardo Mendes of this same group, and Max and Plamen for being there for a chat.
I would not have taken the job if this would have been a fully academic exercise, and I was happy to work with some inspiring people from some companies: I acknowledge the pioneering work of Willem van Dreumel and Robert Lenferink of Ten Cate Advanced Composites in the area of thermoplastic composites for aerospace. I also want to express my thanks to Eli Voet and the team of FOS&S in Belgium for their assistance and explanations with the fibre Bragg gratings. In addition, Ron Verleg and Jasper Bouwmeester from DSM Composite Resins are thanked for their support with the thermosetting polyurethane. I have also greatly appreciated the help with vacuum infusion and the turane stuff received by Maarten Labordus from Lightweight Structures BV.
Vielen Dank, Christian Weimer, for offering me a job at Eurocopter Germany I simply could not refuse and for introducing piracy into my life. Also many thanks for pushing me to finally finish this diss, which simply enhanced my discipline. That this new job is so great is also due to my great bunch of colleagues who made me feel at home in Munich almost immediately. Since now I have no excuses left, I will finally join you for skiing.
Tsja lieve familie, die geweldige stad en baan hebben mij en Tjitte verleid tot het verhuizen naar 900 km verder zuidoost, maar die afstand heeft niet weggenomen dat het altijd heerlijk voelt hoe jullie supertrots op me zijn en ik hoop dat jullie dat nog heel lang mogen blijven! Dat is zeker een heel grote en warme steun in de rug. Ik ben heel dankbaar en blij dat jullie dit mogelijk hebben gemaakt.
Concluding, I'd like to say thank you to all the friends, family, colleagues, acquaintances, business relations, and anyone I might have forgotten (Irene, René), who supported and encouraged me throughout this work. It was great to know you had the faith in me to finish this, and in front of you is the proof that your support and faith did not go wasted!
Thank you!

Patricia

Munich, February 2010

About the Author

Patricia Pauline Parlevliet was born on 24th July 1978 in Leidschendam, the Netherlands. In 1996 she graduated from the Alfrink College in Zoetermeer, after which she was enrolled as a Materials Science and Engineering student at Delft University of Technology.
Having a great interest in Formula 1 racing and aircraft (at the age of ten she wanted to become an air traffic controller), she chose to specialise in lightweight fibre reinforced polymers. This resulted in an internship at Stork Fokker Aerospace in Hoogeveen, where she investigated microcracking resistance of new thermoplastic aerospace composites and effects of resistance welding on composite material properties. She graduated in 2003 as Master of Science at the chair of Polymer Materials and Engineering with work on the fibre-matrix adhesion in fibre reinforced nanocomposites. This was followed by a doctoral research at the faculty of Aerospace Engineering, on residual strains in thick thermoplastic composites, of which the results are presented in this thesis.
Since April 2008 she is employed by Eurocopter Germany as project manager in composite technologies, such as out-of-autoclave technologies for thermoplastic and thermoset composites. This brought her to Munich in Germany, where she now lives.

Publications

Journal articles

1. Parlevliet, P.P., Bersee, H.E.N., Beukers, A., *Residual Stresses in Thermoplastic Composites - A Study of the Literature - Part I: Formation of Residual Stresses.* Composites Part A: Applied Science and Manufacturing, 37(11): 1847-1857, 2006.

2. Parlevliet, P.P., Bersee, H.E.N., Beukers, A., *Residual Stresses in Thermoplastic Composites - A Study of the Literature - Part II: Experimental Techniques.* Composites Part A: Applied Science and Manufacturing, 38(3): 651-665, 2007.

3 Parlevliet, P.P., Bersee, H.E.N., Beukers, A., *Residual Stresses in Thermoplastic Composites - A Study of the Literature - Part III: Effects of Thermal Residual Stresses.* Composites Part A: Applied Science and Manufacturing, 38(6): 1581-1596, 2007.

4. Parlevliet, P.P., van der Werf, A.W., Bersee, H.E.N., Beukers, A., *Thermal Effects on Microstructural Matrix Variations in Thick-Walled Composites.* Composites Science and Technology, 68(3-4): 896-907, 2008.

5. Parlevliet, P.P., Bersee, H.E.N., Beukers, A., *Measurement of (Post-)Curing Strain Development with Fibre Bragg Gratings.* Polymer Testing, Article in press, 2010.

6. Parlevliet, P.P., Bersee, H.E.N., Beukers, A., *Shrinkage Determination of a Reactive Polymer with Volumetric Dilatometry.* Polymer Testing, Accepted for publication, 2010.

7. Vlasveld, D.P.N., Parlevliet, P.P., Bersee, H.E.N., Picken, S.J., *Fibre-matrix adhesion in glass-fibre reinforced polyamide-6 silicate nanocomposites.* Composites Part A: Applied Science and Manufacturing, 36(1): 1-11, 2005.

Conference Proceedings

1. Parlevliet, P.P.*, et al. Fibre-matrix adhesion in glass-fibre reinforced nylon-silicate nanocomposites*, in International Workshop on Thermoplastic Matrix Composites 2003, Gallipoli, Italy, 2003.

2. Parlevliet, P.P., Bersee, H.E.N. *Effects of Impact Modifiers on Mechanical and Microcracking Properties of PPS Composites*, in 25th Jubilee International SAMPE Europe Conference 2004. 2004. Paris EXPO, Porte de Versailles, Paris, France: SAMPE.

3. Parlevliet, P.P., Bersee, H.E.N., Beukers, *A. Residual Stresses in Thermoplastic Composites: Experimental Techniques*, in 15th International Conference on Composite Materials, Durban, South Africa, 2005.

4. Parlevliet, P.P., Bersee, H.E.N., Beukers, A. *Effects of Processing Conditions on Residual Stresses in Thermoplastic Composites*, in Composites Europe 2005, Barcelona, Spain, 2005.

5. Parlevliet, P.P., Bersee, H.E.N., *Analysis of Microstructural Matrix Variations in Thick-Walled Composites*, in 12th Eurocopean Conference on Comnposite Materials, Biarritz, France, 2006.

6. Parlevliet, P.P., Bersee, H.E.N., *Manufacturing Issues of Thick-Walled Vacuum Infused Composites*, in SAMPE Europe International Conference (SEICO 2007), Paris, France, 2007.

7. Parlevliet, P.P., Bersee, H.E.N., Beukers, A., *Process Monitoring with FBG Sensors during Vacuum Infusion of Thick Composite Laminates*, in 16th International Conference on Composite Materials, Kyoto, Japan, 2007.

8. Parlevliet, P.P., Bersee, H.E.N., *Measurement of Polymerisation Shrinkage of Matrices for Liquid Moulding,* in 17th International Conference on Composite Materials, Edinburgh, UK, 2009.

9. Dumont, F., Parlevliet, P.P., Weimer, C., *Manufacturing Process Simulation Tools for Faster Out-of-Autoclave Industrialisation of Composites Parts,* in 2nd International Carbon Composites Conference, Arcachon, France, 2009.

Book Sections

1. Parlevliet, P.P., Bersee, H.E.N., *Effects of Additives on Mechanical and Microcracking Properties of PPS/CF Composites*, in "Cetex®" - Thermoplastic Composites "From Scratch to Flight", Bersee, H.E.N. and Koelewijn, A.J., Editors. 2006, Delft University of Technology: Delft. p.63-68.

2. Parlevliet, P.P., Bersee, H.E.N., *Analysis of Through-the-thickness Matrix Variations in Thick-Walled Composites*, in "Cetex®" - Thermoplastic Composites "From Scratch to Flight", Bersee, H.E.N. and Koelewijn, A.J., Editors. 2006, Delft University of Technology: Delft. p.78-87.

Patents and more publications coming soon…